Advances in Material Research and Technology

Shadia Jamil Ikhmayies *Editor*

Advances in Energy Materials

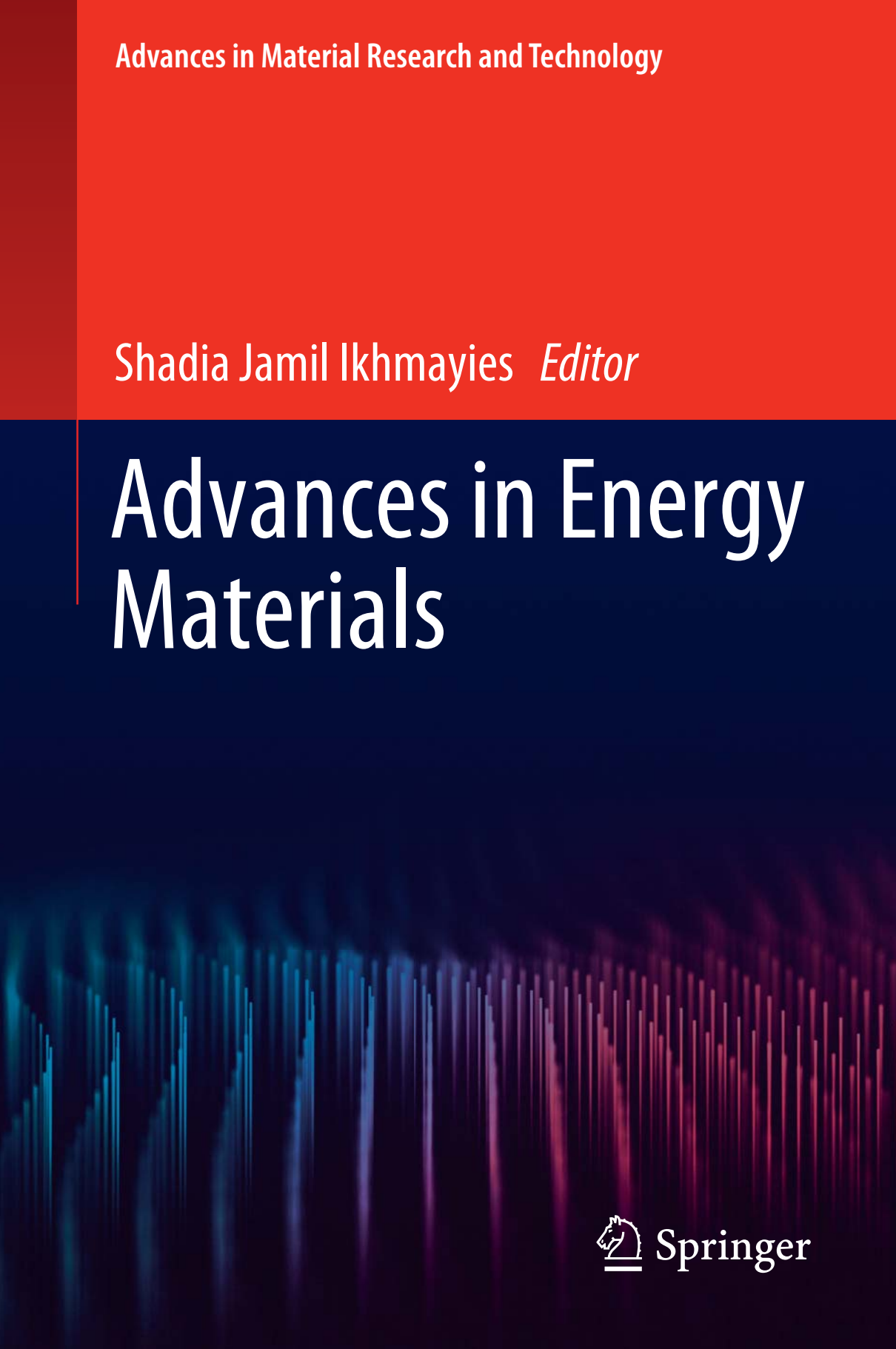

Springer

Advances in Material Research and Technology

This Series covers the advances and developments in a wide range of materials such as energy materials, optoelectronic materials, minerals, composites, alloys and compounds, polymers, green materials, semiconductors, polymers, glasses, nanomaterials, magnetic materials, superconducting materials, high temperature materials, environmental materials, Piezoelectric Materials, ceramics, and fibers.

More information about this series at http://www.springer.com/series/16426

Shadia Jamil Ikhmayies
Editor

Advances in Energy Materials

Springer

Editor
Shadia Jamil Ikhmayies
Jabal El-Hussain
Amman, Jordan

ISSN 2662-4761 ISSN 2662-477X (electronic)
Advances in Material Research and Technology
ISBN 978-3-030-50107-5 ISBN 978-3-030-50108-2 (eBook)
https://doi.org/10.1007/978-3-030-50108-2

This Springer imprint is published by the registered company Springer Nature Switzerland AG
The registered company address is: Gewerbestrasse 11, 6330 Cham, Switzerland

Preface

Energy materials are those materials that can be used in any technology to produce, enhance, generate, convert, transmit, utilize, or store energy. They include materials used in photovoltaics, fuel cells, batteries, supercapacitors, thermoelectrics, hydrogen technologies, and phase change materials. Energy materials are key roadblocks to improve performance in a number of important energy technologies including energy storage in batteries and supercapacitors, and energy conversion through solar cells, fuel cells, and thermoelectric devices. Since energy is a key issue of the modern society, and the world-wide demand for energy is growing, this great challenge can be meet by using sustainable, efficient, and renewable energy sources. Hence, the development of energy materials is necessary for the development of energy production, conversion, transmission, and storage technologies. That is, without continuous advancement of energy materials and developments of new ones, it is not possible to increase the performance of energy technologies. So, continuous research is necessary to accelerate the advances in energy materials, to have energy technologies of higher performance and lower cost, and to increase the efficiency and improve the sustainability of energy systems.

This book presents recent research on energy materials from various aspects, synthesis of energy materials to energy storage devices, focusing on materials that can potentially be used in the production of solar cells. It discusses in detail the latest synthetic methods, processes, characterization methods, and applications of materials like perovskite materials, metal sulfides, metal oxides, nanomaterials, and phase change materials. The book contains nine chapters which include fundamental and recent applied research on the design of different energy materials used in different forms of renewable energy conversion, harvesting, storage, and utilization. Materials scientists, chemists, physicists, materials and renewable energy engineers, people in industry, in addition to graduate and undergraduate students in physics, chemistry, and different branches of engineering will benefit from this book. This book supplies the reader with the basic knowledge of applied research and innovation and provides with the relevant information on the materials used in energy technologies, including background information on the technology itself.

The first three chapters of the book share a relationship with the materials that are used in the manufacture of solar cells. The first chapter entitled "Studies on Synthesis and Various Characteristics of Green Materials for Energy Conversion Applications" by Ranjana Jha et al. focuses on the green materials, where various green materials and their synthesis techniques have been discussed in details. The primary focus of this chapter is to use green materials for energy devices. The second chapter entitled "Advancement in $CdIn_2Se_4$/CdTe Based Photoelectrochemical Solar Cells" by Subhash Chander deals with the preparation of cadmium indium chalcogenide thin films from aqueous medium by the simple and cost-effective spray pyrolysis method, and the consequent use of the produced films in heterojunction solar cell applications. The third chapter entitled "Cadmium Sulfide Thin Films by Chemical Bath Deposition Technique" by M. S. Aida and S. Hariech describes the usefulness of chemical bath deposition (CBD) technique—which is a low cost method—to produce high quality thin films of cadmium sulfide for large-scale applications. The fundamentals of CBD were described with emphasis on growth mechanisms and the influence of key parameters on the films.

The fourth chapter entitled "Development of the Concept of a Spheroidal Shape Anode for a Solid Oxide Fuel Cell" by Bogdan Vasyliv and Viktoriya Podhurska presents a calculation of stress and strain distributions in the YSZ–NiO spheroidal shape anode-substrate for a solid oxide fuel cell (SOFC) under the pressure of an operating environment using the finite element analysis. The authors compared the features of the spheroidal shape anode with those of the cylindrical shape anode. They also suggested the radii ranges for the cylindrical and spheroidal parts of the anode ensuring its improved deformation resistance and more uniform stress distribution.

The next two chapters share a relationship with nanomaterials based photovoltaics. The fifth chapter entitled "Advances in Nano-Materials Used in Photovoltaic/Thermal Systems" by Ali H. A. Al-Waeli and Hussein A. Kazem presents classifications of PV/T systems, principles, and performance. The chapter provides a case study of three different PV/T systems which are; nanofluid and nano-phase change material (nano-PCM) based PV/T, a water-based PV/T with a PCM tank, and water-based PV/T with water tank. The findings show overall improvement in thermophysical properties as nanoparticles are added to the base fluid (water) and phase change material (PCM). Moreover, highest performance is attributed to the nanofluid and nano-PCM based PV/T system. The sixth chapter entitled "Si Quantum Dots for Next-Generation Solar Energy Harvester" by Mrinal Dutta focuses on the progress and growth of Si quantum dots (QDs) based photovoltaic devices with the synthesis techniques as well as the broad range emission properties of these Si QDs. The author discussed the issues related to p-type and n-type doping of these QDs, reported the performances of several photovoltaic devices, and discussed several routes for optimizing the performance of these Si QD cells.

The seventh and eighth chapters are related to perovskite materials and their use in energy harvesting and energy storage. The seventh chapter entitled "Progress in Growth and Development of Perovskite Single Crystals and Their Potential Use in

the Future Devices" by Mrinal Dutta and Aishik Basu Mallick provides recent research and elaborated discussion on the growth of perovskite single crystals by different growth techniques, and the fascinating properties of these perovskites single crystals. In addition, the authors focus on the applications of these single crystals in energy harvesting and high energy radiation detection. The eighth chapter entitled "Perovskite Oxides as Advanced Energy Materials for Solid Oxide Fuel Cell and Supercapacitor Applications" by P. Muhammed Shafi presents a detailed explanation of the crystallographic structures and physiochemical properties of the ABO_3-type perovskite oxides (where A and B are cations of different atomic and mass numbers). It focuses on the applications toward anionic as well as cationic storage mechanism for the supercapacitor electrodes and towards all the three components (cathode, anode, and electrolyte) of solid oxide fuel cells (SOFCs).

Finally, the ninth chapter entitled "Phase Change Materials" by Rabab Jarrar discusses the main types of Phase change materials (PCMs) with their advantages and disadvantages. It presents some of the efforts made to overcome the disadvantages during the last three decades and those made to improve their performance and to demonstrate their most common thermal applications.

Amman, Jordan Shadia Jamil Ikhmayies

Contents

Studies on Synthesis and Various Characteristics of Green Materials for Energy Conversion Applications

Ranjana Jha, Medha Bhushan, and Rekha Bhardwaj

Abstract Energy has become one of the major concerns of the twenty-first century because of the social progress and development in human standard of living. The requirement for energy is increasing constantly, even though conventional combustion-based energy will keep on playing a leading role in gathering our demands in near future. The impending scarcity, rising price and increasing environmental pollution of fossil fuels are approaching humans to build up sustainable, low-cost and clean energy. Sustainable development is integrity of multidiscipline thought combining social, environmental and economical aspects to build a liveable human system. The sustainable development can be done by synthesizing green materials. Green materials hold exceptional physical and chemical properties and are found in nature in plenty, non-toxic and cost-effective. This chapter focuses on green materials originating from the principles to reduce or eliminate the hazardous substances in synthesis of chemical products. At fundamental level, researches in green materials create alternatives to conventional materials or process that present an ecological benefit. So, it deals with the description of cost-effective and low-temperature-based synthesis which involves handling of non-toxic elements. Green materials can be useful for a variety of fields such as in science and technology for energy, construction of buildings, pollution management, engineering applications and materials science. Green materials can be synthesized with the aim of energy production.

Keywords Sustainable development · Green materials · Synthesis · Characteristics · Clean energy

R. Jha (✉)
Research Lab for Energy Systems, Department of Physics, Netaji Subhas University of Technology, New Delhi 110078, India
e-mail: drranjanajha@gmail.com

M. Bhushan · R. Bhardwaj
Research Lab for Energy Systems, Department of Physics, Netaji Subhas Institute of Technology, University of Delhi, New Delhi 110078, India

S. J. Ikhmayies (ed.), *Advances in Energy Materials*,
Advances in Material Research and Technology,
https://doi.org/10.1007/978-3-030-50108-2_1

List of Abbreviations

ZnO	Zinc oxide
TiO_2	Titanium dioxide
MoO_3	Molybdenum trioxide
NiS	Nickel sulphide
ZnS	Zinc sulphide
g-C_3N_4	Graphitic carbon nitrides
I_{sc}	Short-circuit current
V_{oc}	Open-circuit voltage
I	Current
V	Voltage
P_{max}	Maximum power
MPP	Maximum power point
I_{mp}	Maximum current
V_{mp}	Maximum voltage
LED	Light-emitting diode
OCV	Open-circuit voltage
P_{ej}	Power
j	Current density
$P_{ef,max}$	Maximum power
j_{mp}	Current density at maximum point
V_{mp}	Voltage at maximum point
η_{PCE}	Efficiency
PCE	Photovoltaic conversion efficiency
I_{LED}	Particular value of current for which its efficiency is maximum
V_{LED}	Particular value of voltage for which its efficiency is maximum
φ_T	Total power radiated by the LED
P_{LED}	Electrical power ($I_{LED} \cdot V_{LED}$) supplied to it
FF	Fill factor
j_{ph}	Short-circuit photocurrent
V_{oc}	Open-circuit voltage
P	Power
SQ limit	William Shockley and Hans Queisser limit
HER	Hydrogen evolution reaction
OER	Oxygen evolution reaction
PEC	Photoelectrochemical cell

1 Introduction

There are limited resources on earth such as wood, ore and minerals that are vanishing rapidly. The processes of converting them into useable products deplete the essential elements and pollute the environment which affects the ecosystems of many animals and plant species. It is an urgent problem of reversing this issue. According to report released by World Energy Council, global energy demand will increase from year to year. In fact, the demand for energy will double by the year 2060. However, primary energy demand will be in its peak until the year 2030. This primary energy source includes energy derived from coal, oil and gas. Coupled with environmental concern like global warming, the adoption of emerging energy sources is beginning to encroach into the dominance of the primary energy source. Generally, these emerging energy sources are referred as alternative energy resources which are not derived from fuel and coal. Such alternative energy resources include, but not limited to, solar energy, hydroelectric energy and wind energy. Therefore, it is the goal of each inventor and researcher to design efficient energy devices where maximum useful energy can be extracted. Sustainable development is a widespread concept of modern culture. The idea has seemed to be vital strength in growth by conserving natural resources. The development of novel and superior quality materials is one of the largely used efforts in setting up this concept. On the whole, sustainable development is globally recognized dictate and it consists of non-toxic and eco-friendly mechanized resources and equipments. Green synthesis, manufacture and method optimization, play significant role in sustainable development but also testing, performance evaluation and reliability are very important [1]. Future growth in these resources will significantly depend on assurance with sustainable training in research and equipments. “Sustainability” is a great deal than a current catchphrase, though the exercise of the word has definitely enlarged in rate of recurrence, the perception itself is barely new, and it is one of the motivations or thoughts that drives us to write this chapter.

1.1 Why Sustainable Environment?

Sustainability is related to all features of the entity such as constructing eco-friendly homes and providing organic food, and use of renewable energy that look after its own resources. The idea of sustainable progress was crucial and made familiar first in 1987 report “Our Common Future” prepared for the World Commission on Environment and Development. Sustainable ecology, standard of living or a society is one that supports itself and its environment.

Sustainability composed of three major factors, environmental protection, social development and economic development, each of them depends on each other.

1. **Environmental Protection**

Supporting and creating a sustainable ecology take part in important role on ecological safety and security. Relations with surroundings are called as "sustainable" only if it does not devastate the surroundings and resources given by it. Environmental protection involves the assessment of use of resources that affects the environment. The negative effects for environment should be minimized.

2. **Social Development**

Human and social welfare is an integral part of sustainability. The one who has knowledge about sustainability and if its significance can be effectively transferred to them, those are attracted more towards sustainability. It should be ensured that creature should have access to basic resources, so that their health is being protected. Human being can enjoy a good quality of life within a sustainable environment.

3. **Economic Development**

Sustainability devoid of economic growth cannot be succeeded. In order to encourage persons, community and society to put in resources in sustainable development, there must be a number of incentives for lasting return. Financial accomplishment is quite a prejudiced concept.

The basic confront of sustainability consequently is to dissociate the value of living and human being aspirations from energy and material intensities to accomplish them.

1.2 Various Strategies to Create Sustainable Environment

Sustainable surroundings do not represent living with no luxuries but somewhat being conscious of resource expenditure in a way that continues their supply for the future and lowering needless wastage. Environmental skill is the study regarding finding ways to guide a sustainable life. There is a variety of strategies to create sustainable environment:

- Using green material for energy conversion devices.
- Installing and developing energy-efficient devices.
- If we are conserving the energy, it itself means generating source of energy.
- Reducing domestic energy uses.
- Turning off the lights and electronic appliances or devices if not using.

1.3 What Are Green Nanomaterials?

Green nanomaterials are the new material synthesized using the principles and practices of green chemistry. Green chemistry is a set a chemical philosophy that encourages to reduce or eliminate the use and generation of hazardous substances and to use

natural sources, un-hazardous solvents and energy-efficient processes in the synthesis of nanomaterials. In today's developing and challenging environment, green nanomaterials fulfil growing demand for energy, devices and extensive range of applications in various sectors with improved quality. Green materials are synthesized in required shape and size with better properties such as physical, chemical and optical properties that gives better performance according to the demands [2, 3]. There are various green materials such as metal oxides (ZnO, TiO_2, MoO_3), metal sulphides (ZnS and NiS) and graphitic carbon nitride.

1.3.1 Green Materials for Energy Generation

Metal Oxides

Zinc Oxide

Zinc oxide (ZnO) is a multidimensional material due to their unique chemical, structural and physical properties. On the basis of morphology, ZnO can be classified into new materials with potential applications. ZnO can arise into 1-D, 2-D and 3-D structures. 1-D structures include nanorods, nanotubes, nano-needles etc. 2-D structures are nano-sheet, nano-plates and 3-D structures are nano flower, snowflakes, etc. [4]. Due to their unique morphology, ZnO nanoparticles are used in various applications such as solar cell, LED, supercapacitor and batteries. ZnO is a wide band gap semiconductor. It has two most stable states, hexagonal and cubic phases [5]. ZnO is classified into two groups II and IV in the periodic table. ZnO has high excitonic binding energy 60 meV [6]. It has low charge transfer resistance, large surface area, high electron mobility, at room temperature. ZnO shows strong luminescence; thus, it can be used as photo-anode in solar cell, such as electrode in LED and batteries [7]. ZnO is also used in converter, sensors and energy generator, because ZnO has high piezoelectric constant, hardness and rigidity. ZnO has wide band gap 3.37 eV, and its prospective effects were observed on the electrical conductivity and optical absorption properties of the materials [8]. It is an excellent emitter of UV light and absorber and shows high electrical conductivity. Due to these properties, ZnO is used as photo-anode in PEC and DSSC [9].

Titanium Dioxide

Titanium dioxide (TiO_2) is a non-volatile, less soluble, stable compound. It has less thermal conductivity and shows perverse characteristics. TiO_2 has three stable states, anatase, brookite and rutile, and their crystal structure is tetragonal, orthorhombic tetragonal, respectively. Anatase and rutile phases occur naturally and are easily synthesized in the laboratory [10]. Brookite phase is unstable and very difficult to synthesize, at low scientific interest. TiO_2 is amphoteric material, even through less basic than acidic. Each phase has its own importance. Rutile phase is more compact and has high refractive index and higher density than the anatase phase. Titanium dioxide is non-toxic and eco-friendly material. Due to their excellent morphology

and low energy band gap, highly crystalline materials are used in various industrial applications. Titanium dioxide is used as photo-anode in various types of solar cell. Titanium dioxide has high dielectric constant and high electrical resistance and shows excellent electro-catalytic properties; due to these properties, TiO_2 is used in gas sensor, corrosion protective layer, etc.

Molybdenum Oxide

Molybdenum oxide is the one important class of transition metal oxide. Molybdenum oxide has several phases. Different phases of molybdenum dioxide depend upon the concentration of precursors used during synthesis process, reaction time, temperature, etc [11]. Molybdenum dioxide is reduced to (MoO_{3-x}, $2 < x < 3$) and fully stoichiometric molybdenum trioxide (MoO_3), accompanied by Mo^{4+} ions oxidized to Mo^{5+} and Mo^{6+}, and its colour varies from dark blue to light yellow and green/blue [12]. Molybdenum dioxide has excellent melting point, chemical stability and high conductivity, because MoO_2 has multiple valences which are induced by sufficient amount of oxygen vacancies. Thus, these properties make it good candidate of electrode in energy conversion devices [13].

Metal Sulphides

Nickel Sulphide

Nickel sulphide is the important constitute of metal sulphides and has many phases such as NiS, $Ni_{3+X}S_2$, Ni_3S_2, Ni_7S_6, Ni_7S_2, Ni_3S_4 and NiS_2 [14]. Out of these phases, nickel sulphide has two prominent phases, β-NiS rhombohedral phase and α-NiS hexagonal high temperature phase. Nickel sulphide has unique optical and electrical properties, and it has low charge transfer resistance, high conductivity, long cycle life, high theoretical capacity. Due to these properties, nickel sulphide has many applications in energy conversion devices. Each phase of nickel sulphide has its own applications such as NiS_2 used as counter electrode in various types of solar cell and Ni_3S_2 used as electrode in supercapacitor, lithium-ion batteries and so on [15].

Zinc Sulphide

Zinc sulphides have two most stable states: one is hexagonal phase named as wurtzite, and second state is cubic phase known as zinc blende. It has a large exciton energy (40 meV) [16]. ZnS is a multifaceted wide-gap semiconductor that shows superior chemical stability against hydrolysis and oxidation [17]. It is non-toxic unlike other chalcogenide compounds including cadmium sulphides, selenides, etc [18]. Zinc sulphide has wide energy band gap which is the highest value of the II-IV group semiconductor [19]. In ambient atmosphere, ZnS has two polymorphs: cubic zinc blende (ZB) and hexagonal wurtzite (WZ) [20]. Both the phases of zinc sulphide can be used in energy conversion devices such as solar cell, batteries and LED [21]. As one of the most important semiconductors, ZnS with its wide and direct band gap energy of 3.7 eV has been known for a long time as a multifaceted and superior

phosphor host material [22]. ZnS has high theoretical and specific capacitance, high cyclic stability, areal capacitance; due to these properties, ZnS is used as anode materials for electrochemical devices such as supercapacitor and lithium-ion batteries. But it is also advantageous due to natural presence in abundance of S and Zn and low cost [23].

Graphitic Carbon Nitride

Graphitic carbon nitride belongs to carbon nitride family. It can be synthesized by the polymerization of melamine, dicyandiamide or cyanamide, and shows semiconductor properties such as high mobility of charge carrier, large surface area, highly stable and high theoretical capacity. Due to these properties, it can be used as electrode in supercapacitor, batteries, solar cell [24, 25].

2 Synthesis of Green Energy Materials

2.1 Various Methods for Synthesis of Nanomaterials

2.1.1 Two Approaches for the Synthesis of Nanomaterials

(i) **Bottom-Up Approach**

The main aim of this approach is to synthesize uniform shape, size and distribution of all the particles. It starts from atomic level to nanoscale level. It can be done in solutions such as chemical vapour deposition and sol-gel. This method is generally used for the synthesis of metallic nanoparticles. Bottom-up approach is more advantageous than top-down approach in nanofabrication, because it produces less defects, better short- or long-range order and homogeneous nanostructures. A disadvantage of this approach is that the production of large scale is very difficult and also chemical purification of nanoparticles is essential. The schematic illustration is shown in Fig. 1.

(ii) **Top-Down Approach**

This approach is based on the bulk materials to make smaller, miniaturizing or breaking down of solid materials into smaller particles by applying external forces. In this method, many thermal, chemical and physical processes are used for the formation of nanoparticles. This technique is a cost-effective technique, and we can easily control the shape and size of nanoparticles. The main disadvantage of this technique is impossible to get perfect surface, edges due to cavities and roughness in nanoparticles. The schematic illustration is shown in Fig. 1.

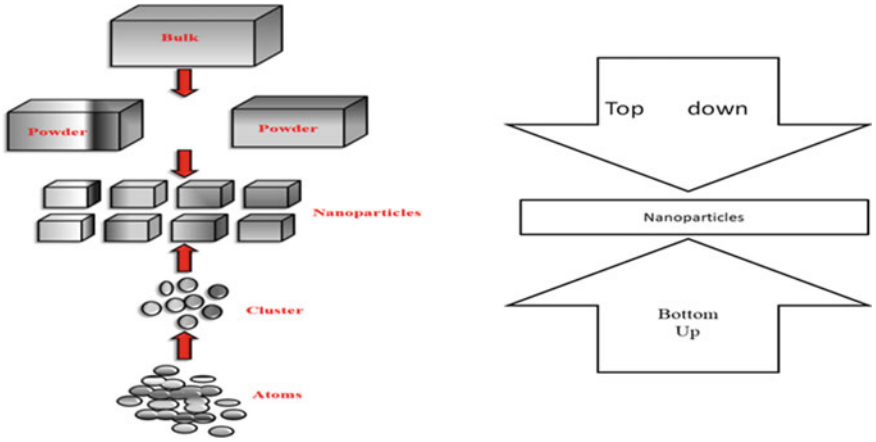

Fig. 1 Schematic illustration of the bottom-up and top-down technique

2.1.2 Hydrothermal and Solvothermal Methods

Hydrothermal and solvothermal methods are common methods which are used for synthesis of inorganic nanoparticles. Hydrothermal/solvothermal synthesis carried out in a pressurized vessel is known as autoclave. If water is used as a solvent, this method is knows as hydrothermal method. If variety of solvent is used except water, then the method is known as solvothermal method. Advantages of these methods are that we can easily control the size, shape and crystalline phase of the nanoparticles by changing the reaction conditions such as temperature, pressure, reaction time, solvents ratio and pH. The schematic illustration is shown in Fig. 2.

2.1.3 Co-precipitation Method

Co-precipitation method is a very simple method for the synthesis of nanoparticles. This method is generally used for the synthesis of fluoride, oxide or nanophosphors. In co-precipitation method, two types of solutions are required: one is cation and other is anion. For cation and anion solutions, we use nitrate, chloride, acetate, etc., used as precursors, and distilled water, ethanol, cyclohexane, N,N-dimethyl formaldehyde, etc., used as solvents. The cation and anion solutions are prepared separately, and after that, precipitating agent is added drop-wise into another solution with constant stirring which results in the formation of the desired compound. The main advantage of this method is that large amount of nanoparticles can be easily synthesized in a short time. Also, kinetic factor only helps to control the growth rate which limits the particle size distribution. The schematic illustration is shown in Fig. 3.

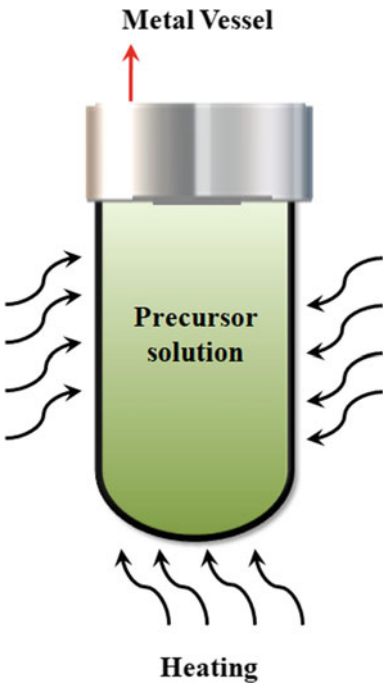

Fig. 2 Schematic illustration of the conventional hydrothermal method

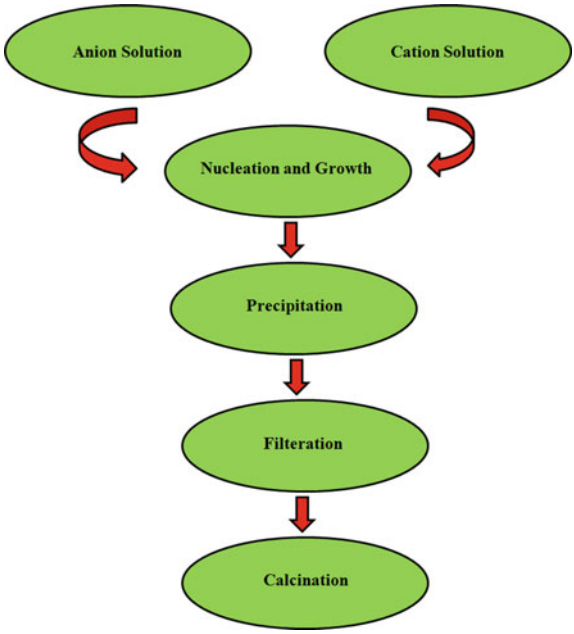

Fig. 3 Schematic illustration of the co-precipitation method

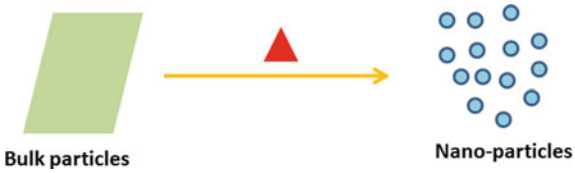

Fig. 4 Schematic illustration of the thermal decomposition method

2.1.4 Thermal Decomposition Method

Thermal decomposition or thermolysis is a decomposition of precursors (metal oxides, sulphides, etc.) in the presence of hot suitable surfactant. The decomposition may be driven by light or heat. In this method, yield is more than the other methods. This process is endothermic process, but there are some limitations such as controlling nanoparticle size and poor uniformity of the particles. The schematic illustration is shown in Fig. 4.

2.1.5 Sol-Gel Method

This is the most reliable method for the production of uniform particle size distribution. It is a wet-chemical technique which is generally used for synthesis of ceramics nanoparticles. Metal alkoxides, nitrates and metal chlorides are used as precursors. These precursors along with chelating agent and surfactant dissolve in de-ionized water or other suitable solvent. Prepared solution is heated continuously with constant stirring until solvent is transformed into sol, which will later get converted into gel. This technique is simple and cost-effective, and it produces highly pure and uniform nano-structured particles at low temperature. The schematic illustration is shown in Fig. 5.

2.1.6 Microwave Synthesis

The basic principle of the microwave synthesis is the heating of materials by microwave dielectric heating. This method depends on the capability of the materials (reagent or solvent) to absorb microwave and convert it. Microwave radiations are directly applied to the reactions not to the vessel, which increase the rate of reactions and control the reaction parameters. In this synthesis technique, lower amount of energy and lesser time is required. Less byproducts are formed in this process. Limitation of this technique is choice of reactants. The schematic illustration is shown in Fig. 6.

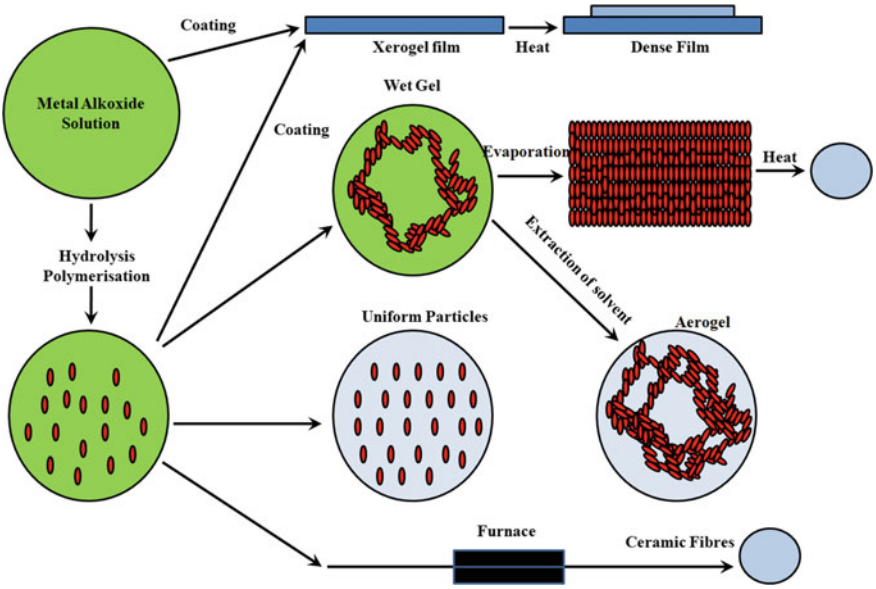

Fig. 5 Schematic illustration of the sol-gel method

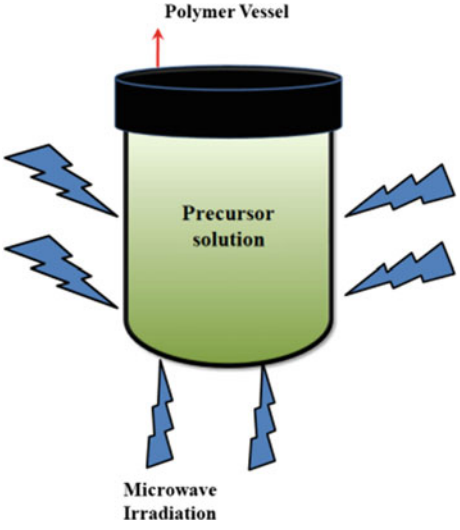

Fig. 6 Schematic illustration of the microwave-assisted synthesis

2.1.7 Micro-emulsion Technique

Micro-emulsion method is defined as macroscopically uniform, optically translucent and thermally stable and isotropic dispersions constituting components, i.e. non-polar phase (generally hydrocarbon, liquid or oil), polar phase (generally water)

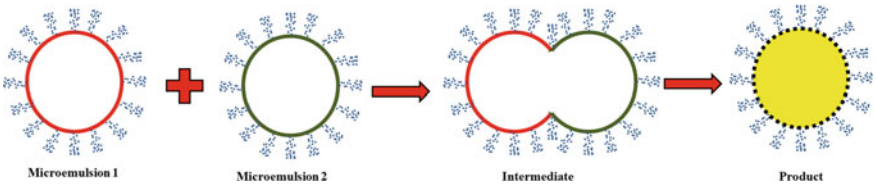

Fig. 7 Schematic illustration of the micro-emulsion technique

and surfactant. Surfactant molecules create interfacial layer separating organic and aqueous phase. Micro-emulsion consists of mono-dispersed spherical droplets (5–100 nm), water-in-oil and oil-in-water depending upon the surfactant. The nano-droplet size can be varied by reaction parameters, e.g. types of stabilizer, surfactant, temperature and pressure. The schematic illustration is shown in Fig. 7.

2.2 Different Green Precursors Required for Synthesis of Green Materials

Nickel nitrate, nickel chloride, zinc acetate, thiourea, sulphur, L-cysteine, thioacetamide, titanium butoxide, titanium tetrachloride, molybdenum hex hydrate, urea, de-ionized water, aqueous ammonia, CTAB, PVP, trisodium citrate, ethylene glycol, etc., are required for the synthesis of green nanomaterials. Different green precursors for synthesis of green materials are given in Table 1.

2.3 Different Reaction Conditions

There are several reaction conditions such as temperature, pressure and concentration of the precursors, reaction time and solvents, which affects structural, optical, electrical and magnetic properties of the nanomaterials as discussed in Tables 2, 3 and 4.

3 Basic Characteristics of Green Materials

3.1 Structure and Morphology

Morphology of the green nanoparticles affects the efficiency of energy conversion devices. Various nanostructures or morphology such as 1-D nanorods, nanotubes and nanowires exhibits excellent charge transport properties which increase the

Table 1 Different green precursors required for synthesis of green materials

Green material	Precursors	Method	References
Nickel sulphide	Nickel nitrate, nickel chloride used as nickel source Thiourea, thioacetamide used as sulphur source	Hydrothermal, microwave, co-precipitation methods	[26] [27] [28]
Zinc sulphide	Zinc nitrate, zinc acetate used as zinc precursors Thiourea, thioacetamide used as sulphur source	Hydrothermal, microwave, micro-emulsion	[29] [30]
Zinc oxide	Zinc nitrate, zinc acetate used as zinc precursors Lithium hydroxide used as oxidizing agent	Co-precipitation method Sol-Gel	[31, 32] [14]
Titanium dioxide	Titanium butoxide, titanium tetrachloride	Hydrothermal method Co-precipitation method	[33] [34]
Molybdenum dioxide	Molybdenum hex hydrate	Sol-gel and hydrothermal methods	[35] [36]
Graphitic carbon nitride	Urea	Thermal decomposition Hydrothermal method	[37] [38]

Table 2 Effect of temperature

Green material	Effect of temperature	References
Nickel sulphide	Formation of different phases of nickel sulphide like NiS_2 and Ni_3S_2	[39]
Zinc sulphide	Phase change from cubic to hexagonal wurtzite phase	[40]
Zinc oxide	Different morphologies of zinc oxide observed (triangular, rose-like petal structure)	[41]
Titanium dioxide	Flower-like, nanosheet-like structure observed in ZnO	[42]
Molybdenum oxide	Band gap reduced from 3.67 to 3.36 eV	[43]
Graphitic carbon nitride	Band gap reduced from 2.85 to 2.47 eV	[44]

Table 3 Effect of molarity

Green material	Effect of molarity	References
Zinc sulphide	Band gap reduces from 3.69 to 3.36 eV	[45]
Nickel sulphide	Different morphologies like spheres, cubes and rods found	[46]
Zinc oxide	Increases non-uniformity of ZnO nanoparticles	[47]
Titanium dioxide	Conductivity of the TiO_2 nanoparticles varies	[48]
Molybdenum oxide	Crystallite size of MoO_2 decreases	[49]

Table 4 Effect of different precursors

Green materials	Effect of different precursors	References
Molybdenum dioxide	Growth rate of nanoparticles increases	[50]
Zinc oxide	Different morphologies like nanorods and nanoprism found	[51]
Zinc sulphide	Increases grain size	[52]
Nickel sulphide	Formation of different phases	[53]
Titanium dioxide	Increases the porosity of the nanostructure	[54]
Graphitic carbon nitride	Enhancement of electrochemical properties	[55]

Table 5 Different morphologies of green materials and its applications

Green material	Morphology	Application	References
Nickel sulphide	Nano-flower	Supercapacitor	[57]
Nickel sulphide	Microspheres	Sodium-ion batteries	[58]
Nickel sulphide	Cubes	Dye-sensitized solar cell	[59]
Zinc sulphide	Polyhedral	Li–Na-ion batteries	[60]
Zinc sulphide	Microsphere	Photocatalytic	[61]
Zinc oxide	Tripods	Solar cell	[62]
Zinc oxide	Nano-tower	Optical/electrical applications	[63]
Titanium dioxide	Nanorods	Solar cell	[64]
Titanium dioxide	Beads	Quantum dot co-sensitized solar cell	[65]
Molybdenum oxide	Grains	Solar cells	[66]
Molybdenum trioxide	Hexagonal rod	Catalytic ozonation	[67]
Graphitic carbon nitride	Nanosheets	Photocatalysis	[68]
Graphitic carbon nitride	Nanorods	Solar cell	[24]

charge/discharge rate [56]. Three-dimensional mesoporous nano-/macro-spheres which have large surface area provide more catalytic active sites and increase electron transfer rate, which improve the efficiency of solar cell and supercapacitor as given in Table 5.

3.2 Optical Properties

Optical properties of a material are defined as the interaction of materials with different incident radiations such as photons, electric field and high energy electrons. Optical properties of the nanomaterials depends upon the dimensions of the materials. If the size of the particle increases, energy band gap of materials decrease, for

Table 6 Parameters affecting the optical properties of green materials

Green material	Parameters affecting optical properties	References
Zinc oxide	Particle size decreases from 11 to 3.4 nm, and energy band gap of the materials changes from 3.53 to 3.65 eV	[69]
Nickel sulphide	Particle size varies from 30.51 to 42.09 (reaction temperature increases), and energy band gap varies from 4.8 to 2.8 eV	[70]
Graphitic carbon nitride	Increase in doping varies the band gap from 2.6 to 2.52 eV	[71]
Zinc sulphide	Concentration of precursor changes, and band gap varies from 3.73 to 3.64 eV	[72]
Titanium dioxide	By varying the temperature, band gap varies from 0.33 to 0.18 eV	[73]
Molybdenum dioxide	By varying the temperature, band gap varies from 3.67 to 3.36 eV	[43]

example optical absorption and emission shift to the higher energies for quantum dots. Optical property of the nanomaterials depends upon the various parameters, shape, size, surface characteristics and other variables including doping using surfactant, etc., as given in Table 6.

3.3 Electrical Properties

The properties of the materials like conductivity and resistivity come under the category of electrical property. Electrical property of the materials depends upon the morphology, size and surface of the nanomaterials; e.g. if the diameter of nanowire is decreased, electrical conductivity of the material is increased as given in Table 7.

Table 7 Parameters affecting the electrical properties of green materials

Green material	Parameters affecting electrical properties	References
Nickel sulphide	Temperature increases; conductivity decreases	[74]
Zinc sulphide	Increase in crystallinity of the ZnS increases conductivity	[75]
Zinc oxide	Increases in temperature decrease the resistivity	[76]
Titanium dioxide	Increase in temperature decreases the conductivity	[77]
Molybdenum dioxide	Increase in effective mass increases the resistivity	[78]

Table 8 Parameters affecting the magnetic properties of green materials

Green material	Parameters affecting magnetic property	References
Zinc oxide	When temperature increases, magnetic property changes from paramagnetic to ferromagnetic	[79]
Nickel sulphide	At room temperature, nickel sulphide shows weak ferromagnetism	[80]
Zinc sulphide	Crystallization atmosphere changes magnetic susceptibility	[81]

3.4 Magnetic Properties

Magnetic nanoparticles are those particles which are affected by the magnetic field applied. These particles contain elements like nickel, zinc, carbon, etc. Magnetic property depends upon the size and morphology of the particles, for example ferromagnetism disappears and transforms into super-paramagnetic materials in some cases when particles come in the range of nanoscale as given in Table 8.

4 Basic Operation for Energy Conversion Devices

The main characteristics of the operation of a solar cell, LED, battery with respect to voltage, electrical current are described in this section.

4.1 Current–Voltage Characteristics

Solar Cell I–V Characteristic Curves

The operational properties of a solar cell under a substantial incident illumination using the basic model are studied. The excitation by light generates more number of electrons and holes in carrier bands that result in the division of the related Fermi levels. By controlling the voltage V that exists between the two contacts of the solar cell, the amount of recombination can be changed. I–V characteristic curves are essentially a graphical illustration of the process of a solar cell or module summing up the correlation between current and voltage in the present conditions of irradiance and temperature. I–V curves as shown in Fig. 8 offer knowledge requisite to construct a solar system that can work as close up to its most favourable peak power point (MPP) as probable. Knowing I–V characteristics and maximum power of solar cell is vital in deciding device's performance and efficiency of solar cells.

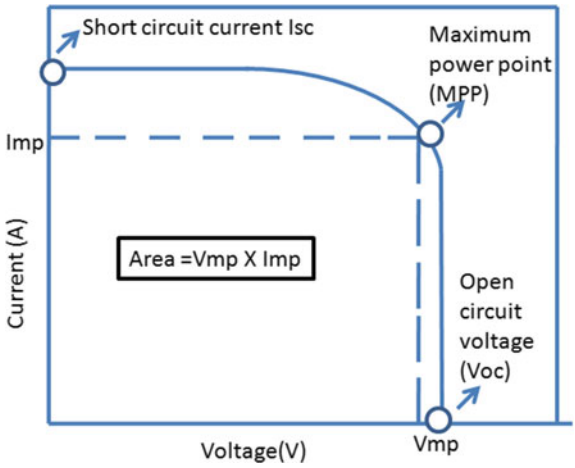

Fig. 8 *I–V* characteristics of solar cells

I–V Characteristics of LED

In order to emit any wavelength of light, LEDs need a current to flow in the course of it, since LEDs are current-dependant device. In LEDs, output light intensity is dependent directly to the forward current flowing in the LED.

To protect LEDs from excess current flow, it should be made current limited by means of a series resistor since LEDs are connected in a forward bias condition in a power supply. LED should not be connected to a battery or power supply directly since it can destroy instantaneously because high current will pass across it and burn it out. The I–V curve is shown in Fig. 9.

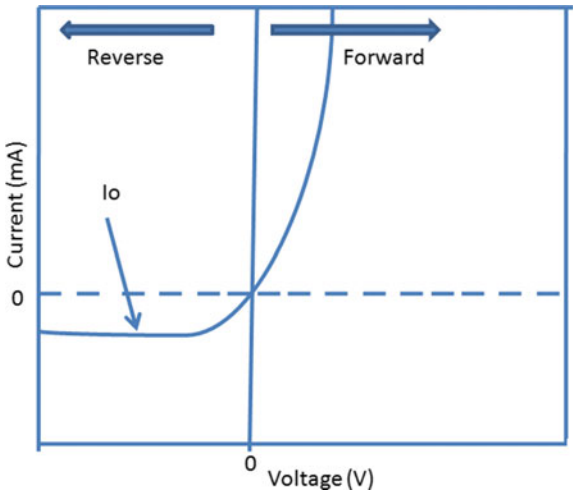

Fig. 9 *I–V* characteristics of LEDs

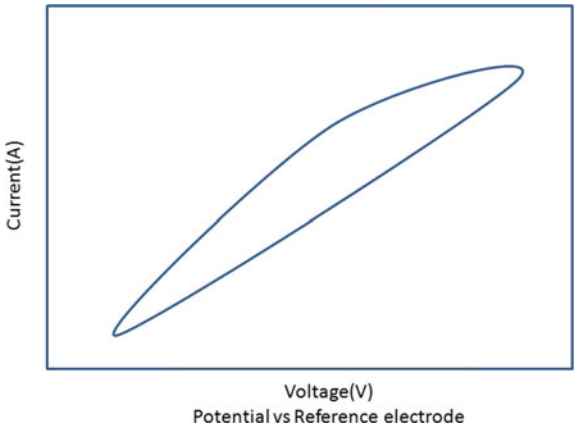

Fig. 10 *I–V* characteristics of batteries

I–V Characteristics of Battery

A battery is a collection of voltaic cells. It is a device that converts chemical energy to electrical energy through electrochemical reactions. A battery characterizes a small voltage. Alongside the quantity of cells associated in series, chemistry produces the open-circuit voltage (OCV), which is approximately 5–7% higher on a wholly charged battery. I–V characteristics of battery are shown in Fig. 10.

4.2 Power Conversion Efficiency

The main application of solar cell is to serve as a power supply unit that produces electricity from sunlight or from ambient light in indoor applications. The central feature to assess the solar cell performance is the electrical power that can be extracted from the available radiation level. The electrical power at a given voltage operation point of the solar cell, P_{ej}, has the value shown in (Eq. 1):

$$P_{ej} = jV \tag{1}$$

The power is zero at both open- and short-circuit conditions. In between the extreme cases of low power lies the maximum power point (MPP) at which voltage (V_{mp}) the solar cell should be operated for electricity production. The maximum power provided by the photovoltaic device is represented in (Eq. 2):

$$P_{ef,}\mathrm{max} = j_{\mathrm{mp}}\, V_{\mathrm{mp}} \tag{2}$$

For the characterization of energy converter devices, the main figure of merit is the maximum conversion efficiency of the solar cell, that is, the PCE that consists of the electrical power supplied at MPP with respect to the incoming photon energy

(Eq. 3):

$$\eta_{\mathrm{PCE}} = \frac{j_{\mathrm{mp}}}{\varphi} V_{\mathrm{mp}} \tag{3}$$

The PCE depends on the operation conditions that need to be defined. The PCE of a solar cell is usually reported under simulated standard terrestrial spectrum AM 1.5G which bears an integrated power of $\phi = 1\ \mathrm{kWm^{-2}} = 100\ \mathrm{mWcm^{-2}}$. This type of illumination is usually denominated as "1Sun."

The η (efficiency) of LED is the function of current passing across it. For every LED, there is a value of I_{LED} for that efficiency is found to be maximum. The efficiency gets decreased when the operational temperature is increased.

This expression associates the current in photodiode $I(m)$ kept back at a distance m from the axis of cone to the total power radiated φ_{T} emitted by the LED.

The efficiency η is given by (Eq. 4):

$$\eta = \frac{\phi_{\mathrm{T}}}{P_{\mathrm{LED}}} \tag{4}$$

where φ_{T} represents the total power emitted by LED and $\mathrm{P_{LED}}$ denotes the electrical power ($I_{\mathrm{LED}} \cdot V_{\mathrm{LED}}$) applied to it [82].

4.3 Analysis of Fill Factor

The efficiency increases when the short-circuit photocurrent j_{ph} and open-circuit voltage V_{oc} increase, but η_{PCE} also depends critically on the MPP. The form of the j–V curve decides that at what voltage value the electrons are extracted as electric current. At lower voltage value, extraction of electrons is easy, and the current is computed by quantum yield of the absorber. Though, a higher voltage produces a current opposite to the photocurrent, and ultimately the power decreases. If the point is close to V_{oc}, then the operational voltage and current are much larger if V_{mpp} occurs at low voltage close to $V_{\mathrm{oc}}/2$. The parameter that tracks this property is the fill factor (FF) defined as (Eq. 5):

$$\mathrm{FF} = \frac{j_{\mathrm{mp}}}{j_{\mathrm{ph}}} \frac{V_{\mathrm{mp}}}{V_{\mathrm{oc}}} \tag{5}$$

The fill factor depends on the form of the j–V curve (Fig. 11), determining the MPP and exerting a large influence on PCE of the solar cell. If the FF is higher, the fall in current at higher voltage can be delayed, and the electrons can be extracted at high voltage while the current is closer to $j_{\mathrm{ph.}}$ For a good-quality diode attribute, the power P should increase linearly at the lower voltage.

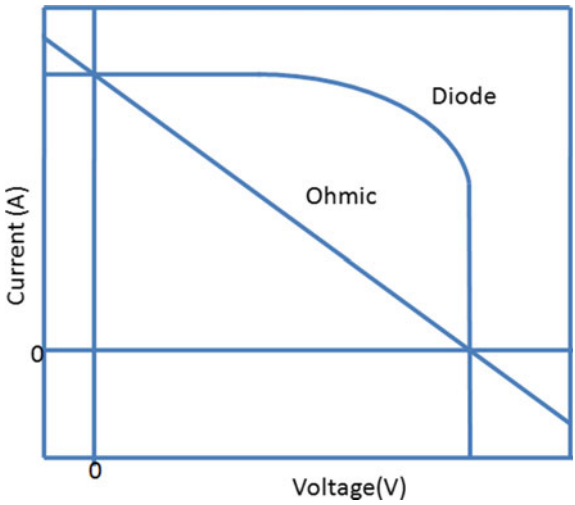

Fig. 11 Analysis of fill factor

4.4 Efficiency Limits

Efficiency limits were firstly computed by William Shockley and Hans Queisser in 1961. The conversion efficiency of solar cell is the fraction of conversion of power from sunlight to the electrical energy under standard test conditions (STCs). The modern SQ limit computation is a maximum efficiency of 33% for any kind of single junction solar cells. The original estimation by Shockley and Queisser was 30% for silicon solar cells. Recent solar cell's conversion efficiencies differ by the energy band gap of the semiconductor material used in the fabrication process [83].

5 Various Applications of Green Energy Materials

A solar cell or photovoltaic cell is a semiconductor device that converts the light energy (certain wavelength) into electrical energy by photovoltaic effect. Solar cell consists of absorption of photon, producing electron–hole pairs in a semiconductor and charge-carrier separation. At present, three types of solar cells are available, first-generation, second-generation and third-generation solar cells. First-generation solar cells are made up of crystalline silicon wafers, and this technique is the oldest technique and high power efficient technique. Second-generation solar cells are thin-film technologies such as copper–indium–gallium–selenides (CIGS), gallium arsenide (GaAs) and cadmium telluride (CdTe). Third-generation solar cells are less commercial and consist of organic materials such as carbon nanotube and titanium dioxide.

5.1 Dye-Sensitized Solar Cells (DSSCs)

Dye-sensitized solar cell is a third-generation solar cell. Dye sensitized solar cells consist of semiconductor photo anode (e.g. titanium dioxide, zinc sulphide etc.), counter electrode (e.g. nickel sulphide, platinum, titanium disulphide etc.) and electrolyte (e.g. iodine). Photoanodes are coated on substrates such as ITO/FTO, sensitized with organic dyes for e.g. N3 that can absorb quantum dots (CdS, PbS etc.). Electrolytes are injected between sensitizer and counter electrode which collects electrons from the external circuit. Performance of the DSSCs depends upon the properties (morphology, electrical, magnetic, etc.) of the semiconductor materials such as large surface area required for absorption of dye which increases the charge transport rate. This is an alternative of the silicon solar cell, because dye-sensitized solar cell is cost-effective, less toxic and semi-transparent, and has high flexibility and good performance [84].

5.2 Quantum Dot-Sensitized Solar Cells (QDSSCs)

QDSSC is a third-generation solar cell. QDSSC is a potential candidate for next-generation solar cells due to unique optoelectronic features such as high light, moisture stability and thermal stability. QDSSC is similar to DSSC, and dye is replaced by new absorbing material, quantum dot. Titanium dioxide, zinc oxide, etc., are used as photo-anode because they have large surface area, unique morphology, high charge transport rate. Zinc sulphide is used as quantum dot because zinc sulphide has a large band gap which is depending on the size of zinc sulphide particle [85]. Nickel sulphide and platinum are used as counter electrode because they have low charge transfer resistance, high cyclic stability, unique morphology which helps in the collection of electron from the external circuit.

The process of developing the DSSC versus QDSSC is deduced by the type of sensitizer used, which is either an inorganic nanoparticle (QDs) or dye (DSSCs). The superior optoelectronic properties of QDs, such as size dependent tunable energy band gap and carrier multiplication (i.e. MEG multiple exciton generation effect), enhance the performance of QDSSCs [86, 87]. CdS and CdSe have been studied as semiconducting material for QDSSCs. But these are toxic in nature because of the presence of Cd in it. So, there is a need of green material for QDSSCs.

5.3 Hydrogen Evolution Reaction

Water splitting consists of two reactions: one H_2 (hydrogen evolution reaction) and O_2 (oxygen evolution reaction). Production of hydrogen evolution and oxygen evolution occur through water electrolysis process. Hydrogen evolution depends upon the

desorbing of the molecules coming from cathode surface. These reactions generally occur on noble metals such as Pt, Rh or Ru, because in HER and OER a large number of electrons and protons are required. But these noble metals cannot be directly used because of very high cost. So instead of using these noble metals we use nickel sulphide, zinc sulphide, etc., because these materials have large surface area, higher intrinsic activity and higher exchange current density.

Reason of Metal Sulphides in QDSSCs

Metal oxides can cause photocorrosion under band gap excitation, such as ZnO. So, they are not active water splitting because of photocorrosion. Hydrogen production can be improved by using metal sulphides with oxides. The reason is that metal sulphides on the surface of metal oxides play a vital role in the separation of e^-/h^+ pairs and enhance the performance of hydrogen evolution [88].

In contrast, other metal oxides such as MoO_3 [89] and TiO_2 [90] possess superior photocatalytic activity for hydrogen generation. MoO_3 on surface of polyimide significantly enhances the photocatalytic activity for hydrogen evolution, which ascribes to increase light absorption and the suppression of radiative recombination of photogeneration of e^-/h^+ pairs.

5.4 Supercapacitor

Supercapacitor is a high-capacity capacitor which has high capacitance than the normal capacitor. Supercapacitors consist of anode, electrolyte and cathode. The anode (nickel sulphide, zinc sulphide, zinc oxide) and cathode materials have high cyclic stability, low charge transfer resistance, large surface area, high theoretical capacity. For increasing the cyclic stability of the electrode materials, we mix some amount of carbonaceous materials. Generally, two types of supercapacitor are available depending upon the mechanism of supercapacitor: one is pseudosupercapacitor, and other is electric double-layer capacitors. Electric double-layer capacitor is ascribed due to charge separation along with accumulation of electrolyte, and pseudosupercapacitor originates from reversible faradic reaction. Nickel sulphide has high theoretical capacity, low charge transfer resistance, high cyclic stability; due to these properties, nickel sulphide is used as electrode in electrochemical devices such as supercapacitor and lithium-ion batteries.

5.5 Batteries

Electrochemical energy sources which convert chemical energy into electrical energy are called as battery, which consist of more than one cells. A cell consists of cathode (nickel sulphide, zinc sulphide, zinc oxide), electrolyte, separator and anode. The main function of the electrolyte is to allow ions to move between the electrodes

and terminals. Usually, two types of batteries are available: one non-rechargeable battery and rechargeable batteries like lithium-ion, sodium-ion batteries, etc. These batteries are very useful because of high energy density, and low maintenance. The main disadvantages of these batteries are poor cyclic stability, long charging times, slow charging rate. Nickel sulphide, zinc sulphide and molybdenum dioxide are used as electrode in charge storage devices.

5.6 Light-Emitting Diodes (LEDs)

LED is a semiconductor device that emits visible light when electric current passed through it. If electric energy is applied, then inter-band transition takes place resulting in luminescence which is called as electroluminescence. When a voltage is applied in the metal nanoparticles, placed in ITO/FTO substrate through proper electrode system. Then electronic transition takes places in metal nanoparticles which help to emit light. The colour of the emitted light depends upon the energy difference between valence band and conduction band of the materials.

6 Conclusions and Future Perspectives

In this chapter, the importance of sustainable environment, green materials, has been discussed. Use of green or non-toxic materials and green technology is an effective tool for the alternative of green energy generation. Green nanomaterials would provide an influential route for energy device fabrication. The primary focus of this chapter is to use green materials for energy devices. Various green materials and its synthesis techniques have been discussed in detail. Significant progress has been reported for various green materials with properties and its potential applications. The green materials can be applied as components in various energy conversion and storage devices such as solar cells, hydrogen evolution reaction, supercapacitors and batteries. Researchers have investigated the physical and chemical properties of green materials. Potential applications of the green materials are recommended to provide insight into the wide spectrum to which their properties such as optical, electrical and magnetic can be utilized. Environmental issues we face every day cannot be solved overnight, but with increasing discoveries in green nanotechnology, the goal can be achieved significantly very soon.

Acknowledgements The authors are grateful to the vice chancellor of Netaji Subhas University of Technology (formerly Netaji Subhas Institute of Technology) for financial support.

References

1. Russo, D., & Rizzi, C. (2014). High performance and optimum design of structures and materials. *Computers in Industry, 65*(3), 1.
2. Jessop, P. G., Ahmadpour, F., Buczynski, M. A., Burns, T. J., & Ii, N. B. G. (2015). Opportunities for greener alternatives in chemical formulations. *Green Chemistry, 17,* 2664.
3. Lu, Y., & Ozcan, S. (2015). Green nanomaterials: On track for a sustainable future. *Nano Today, 10*(4), 1.
4. Parihar, V., Raja, M., & Paulose, R. (2018). A brief review of structural, electrical and electrochemical properties of Zinc Oxide Nanoparticles. *Reviews on Advanced Materials Science, 53*(2), 119.
5. Becheri, A., Dürr, M., Lo Nostro, P., & Baglioni, P. (2008). Synthesis and characterization of zinc oxide nanoparticles: Application to textiles as UV-absorbers. *Journal of Nanoparticle Research, 10*, 679.
6. Kołodziejczak-Radzimska, A., & Jesionowski, T. (2014). Zinc oxide—from synthesis to application: A review. *Materials Basel, 7*(4), 2833.
7. Sirelkhatim, A., Mahmud, S., Seeni, A., Mohamad Kaus, N. H., Ann,L. C., et al. (2015). Review on zinc oxide nanoparticles: Antibacterial activity and toxicity mechanism. *Nano-Micro Letters, 7*, 219.
8. Agarwal, H., Kumar, S. V., & Rajeshkumar, S. (2017). A review on green synthesis of zinc oxide nanoparticles – An eco-friendly approach. *Journal of Energy Resources Technology, 3*(4), 406.
9. Ghosh, M., Kurian, M., Veerender, P., Padma, N., Aswal, D. K., Gupta, S. K., et al. (2010). Photovoltaic Properties Of ZnO Nanoparticle Based Solid Polymeric Photoelectrochemical Cells. *AIP Conference Proceedings, 1313,* 394.
10. Haider, A. J., Jameel, Z. N., & Al-Hussaini, I. H. M. (2019). Review on: Titanium dioxide applications. *Energy Procedia, 157,* 17.
11. Zeng, L., & Cheng, C. (2009). A literature review of the recovery of molybdenum and vanadium from spent hydrodesulphurisation catalysts: Part II: Separation and purification. *Hydrometallurgy, 98,* 10.
12. Smedley, P. L., & Kinniburgh, D. G. (2017). Molybdenum in natural waters: A review of occurrence, distributions and controls. *Applied Geochemistry, 84,* 387.
13. Zhan, Y., Liu, Y., Liang, Z., Hongru, G., Yanxian, W., Shuangshuang, H., et al. (2018). Phase-controlled synthesis of molybdenum oxide nanoparticles for surface enhanced Raman scattering and photothermal therapy. *Nanoscale, 10,* 5997.
14. Li, B., Zheng, M., Pang, H., & Li, B. (2016). High performance electrochemical capacitor materials focusing on nickel based materials. *Inorganic Chemistry Frontiers, 3,* 175.
15. Gervas, C., Mlowe, S., Akerman, M. P., Ezekiel, I., Moyo, T., & Revaprasadu, N. (2017). Synthesis of rare pure phase Ni_3S_4 and Ni_3S_2 nanoparticles in different primary amine coordinating solvents. *Polyhedron, 122,* 16.
16. Lai, C.-H., Lu, M.-Y., & Chen, L.-J. (2012). Metal sulfide nanostructures: synthesis, properties and applications in energy conversion and storage. *Journal of Materials Chemistry, 22*(1), 19.
17. Bredol, M., & Kaczmarek, M. (2010). Potential of nano-ZnS as electrocatalyst. *The Journal of Physical Chemistry A, 114*(11), 3950.
18. Mal, J., Nancharaiah, Y. V., van Hullebusch, E. D., & Lens, P. N. L. (2016). Metal chalcogenide quantum dots: biotechnological synthesis and applications. *RSC Advances, 6*(47), 41477.
19. Arbi, N., Ben Assaker, I., Gannouni, M., Kriaa, A., & Chtourou, R. (2015). Experimental investigation of the effect of Zn / S molar ratios on the physical and electrochemical properties of ZnS thin films. *Materials Science in Semiconductor Processing, 40*, 873.
20. Zhao, H., Liu, W., Zhu, J., Shen, X., Xiong, L., Li, Y., et al. (2015). Structural transition behavior of ZnS nanotetrapods under high pressure. *High Pressure Research, 35*(1), 9.
21. Wang, X., Huang, H., Liang, B., Liu, Z., Chen, D., & Shen, G. (2013). ZnS nanostructures: Synthesis, properties, and applications. *Critical Reviews in Solid State and Materials Sciences, 38,* 57.

22. Uzar, N., & Arikan, M. (2011). Synthesis and investigation of optical properties of ZnS nanostructures. *Bulletin of Materials Science, 34*(2), 287.
23. Du, X., Zhao, H., Zhang, Z., Lu, Y., Gao, C., Li, Z., et al. (2017). Core-shell structured ZnS-C nanoparticles with enhanced electrochemical properties for high-performance lithium-ion battery anodes. *Electrochimica Acta, 225*, 129.
24. Safaei, J., Mohammed, N., Mohamad, N., Mohamad, F., Soh, M., et al. (2018). Graphitic carbon nitride (g-C3N4) electrodes for energy conversion and storage: a review on photoelectrochemical water splitting, solar cells and supercapacitors. *Journal of Materials Chemistry A, 6*, 22346.
25. Zhao, Z., Sun, Y., & Dong, F. (2015). Graphitic carbon nitride based nanocomposites: a review (2015). *Nanoscale, 7*(1), 15.
26. Rajan, K., Mani, N., Archana, J., Thangaraju, D., Arivanandhan, M., Hayakawa, Y. (2014). Shape controlled synthesis of hierarchical nickel sulfide by the hydrothermal method. *Dalton Transactions, 43*, 17445.
27. Salavati-Niasari, M., Banaiean-Monfared, G., Emadi, H., & Enhessari, M. (2013). Synthesis and characterization of nickel sulfide nanoparticles via cyclic microwave radiation,. *Comptes Rendus Chimie, 16*(10), 929.
28. Ryu, H., Ha Ryu, C., Ji, S., Ahn, I., Ahn, J., Ahn, H., & Kim, K. (2014). Electrochemical properties of the NiS powder prepared by co-precipitation method for lithium secondary battery. *Journal of Nanoscience and Nanotechnology, 14*(10), 7943.
29. Thi Quynh Hoa, T., Vu, L., Canh, T., Nguyen Ngoc, L. (2009). Preparation of ZnS nanoparticles by hydrothermal method. *Journal of Physics: Conference Series, 187*, 12081.
30. Liu, J., Ma, J., Liu, Y., Song, Z., Sun, Y., Fang, J., et al. (2009). Synthesis of ZnS nanoparticles via hydrothermal process assisted by microemulsion technique. *Journal of Alloys and Compounds, 486*(1), L40.
31. Sharma, D., & Jha, R. (2017). Transition metal (Co, Mn) co-doped ZnO nanoparticles: Effect on structural and optical properties. *Journal of Alloys and Compounds, 698,* 532.
32. Hasnidawani, J. N., Azlina, H. N., Norita, H., Bonnia, N. N., Ratim, S., & Ali, E. S. (2016). Synthesis of ZnO nanostructures using sol-gel method. *Procedia Chemistry, 19,* 211.
33. Mali, S. S., Betty, C. A., Bhosale, P., & Patil, P. (2011). Hydrothermal synthesis of rutile TiO_2 with hierarchical microspheres and their characterization. *CrystEngComm, 13,* 6349.
34. Rathod, P. B., Nemade, K. R., & Waghule, S. A. (2015). Study of structure and optical for chemically synthesized titanium dioxide nanoparticles. *International Journal of Chemical and Physical Sciences, 4,* 491.
35. Méndez-Vivar, J. (1991). Synthesis of molybdenum oxides by the sol-gel method. *Inorganica Chimica Acta, 179,* 77.
36. Angamuthuraj, C., & Chandra Bose, A. (2012). Hydrothermal synthesis of molybdenum oxide microbelts. *AIP Conference Proceedings, 1447*, 311.
37. Praus, P., Svoboda, L., Ritz, M., Troppova, I., Sihor, M., & Kocí, K. (2017). Graphitic carbon nitride: Synthesis, characterization and photocatalytic decomposition of nitrous oxide. *Materials Chemistry and Physics, 193,* 438.
38. Dai, H. (2013). Synthesis and characterization of graphitic carbon nitride sub-microspheres using microwave method under mild condition. *Diamond and Related Materials, 38,* 109.
39. Kumar, N., Natarajan, R., & Athinarayanan, S. (2013). Temperature evolution of nickel sulphide phases from thiourea complex and their exchange bias effect. *Journal of Solid State Chemistry, 208,* 103.
40. Shaikh, A. Z., & Sonawane, P. S. (2016). Effect of temperature on different properties of ZnS nanocrystals prepared by chemical method. *IOSR Journal of Applied Physics, 8*(3), 99.
41. Gopal, V. R. V., & Kamila, S. (2017). Effect of temperature on the morphology of ZnO nanoparticles: A comparative study. *Applied Nanoscience, 7,* 75.
42. Zhao,Y. (2015). Effect of annealing temperature and element composition of titanium dioxide/graphene/hemin catalysts for oxygen reduction reaction. *RSC Advances, 5*(101), 82879.

43. Kumar, A., & Pandey, G. (2017). Synthesis, characterization, effect of temperature on band gap energy of molybdenum oxide nano rods and their antibacterial activity. *Journal of Inorganic and Organometallic Polymers and Materials, 3*(4), 81.
44. Liu, J., Zhang, T., Wang, Z., Dawson, G., & Chen, W. (2011). Simple pyrolysis of urea into graphitic carbon nitride with recyclable adsorption and photocatalytic activity. *Journal of Materials Chemistry, 21,* 14398.
45. Ponnuswamy, V. P. S. S. V. (2018). Influence of thiourea on the synthesis and characterization of chemically deposited nano structured zinc sulphide thin films,. *Journal of Materials Science: Materials in Electronics, 29,* 7739.
46. Thangwane, C. S., Xaba, T., & Moloto, M. J. (2017). The formation of the mixed morphology of nickel sulfide nanoparticles derived from substituted benzimidazole dithiocarbamate nickel (ii) complexes. *Chalcogenide Letters, 14,* 407.
47. Winkler, N., Wibowo, R. A., Kautek, W., Dimopoulos, T. (2019). Influence of the aqueous solution composition on the morphology of $Zn_{1-x}Mg_xO$ films deposited by spray pyrolysis. *Journal of Materials Chemistry C, 7*, 3889.
48. Lourduraj, S., & Williams, R. V. (2017). Effect of molarity on sol – gel routed nano TiO_2thin films. *Journal of Advanced Dielectrics, 7,* 1.
49. Knauss, M., Tolea, F., Valeanu, M., Diamandescu, L., Trotta, R., Wood, K., et al. (2018). Mechanochemical synthesis and characterization of molybdenum dioxide-hematite nanostructures with different molarities. *Journal of Minerals and Materials Characterization and* Engineering, *06*, 587.
50. Drake, T. L. (2016). Vapor deposition of molybdenum oxide using bis (ethylbenzene) molybdenum and water. *Journal of Vacuum Science and Technology, 34*, 1.
51. Urgessa, Z. N., Oluwafemi, O. S., & Botha, J. R. (2012). Effect of precursor concentration on the growth of zinc oxide nanorod arrays on pre-treated substrates. *Physica B: Condensed Matter, 407,* 1543.
52. Rao, A. V. K. G. (2017). Structural and Optical Properties of ZnS Thin Films by SILAR Technique obtained by acetate Precursor. *IOP Conference Series: Materials Science and Engineering*, 2221.
53. Buchmaie, C., Glänzer, M., Torvisco, A., Poelt, P., Wewerka, K., Kunert, B., et al. (2017). Nickel sulfide thin films and nanocrystals synthesized from nickel xanthate precursors. *Journal Materials Science, 52,* 1.
54. Ahn, K. H., Ho-Lee, Y., Kim, M., Shik Lee, H., Suk Youn, Y., Kim, J., & Woo Lee, Y. (2013). Effects of Surface Area of Titanium Dioxide Precursors on the Hydrothermal Synthesis of Barium Titanate by Dissolution–Precipitation. *Industrial & Engineering Chemistry Research, 52*(37), 13370.
55. Lee, H. L., Sofer, Z., Mazánek, V., Luxa, J., Chua, C. K., & Pumera, M. (2017). Graphitic carbon nitride: Effects of various precursors on the structural, morphological and electrochemical sensing properties. *Applied Materials Today, 8,* 150.
56. Wang, Y., Song, Y., & Xia, Y. (2016). Electrochemical capacitors: mechanism, materials, systems, characterization and applications. *Chemical Society Reviews, 45,* 5925.
57. Cao, H., Wang, X., Chen, X., Liu, H., Zheng, J., & Zhou, W. (2017). Hollow cubic double layer structured Cu7S4/NiS nanocomposites for high-performance supercapacitors. *Journal of Materials Chemistry A, 5–39,* 20729.
58. Bi, R., Zeng, C., Huang, H.-W., Wang, X., & Zhang, L. (2018). Metal-organic frameworks derived hollow NiS2 spheres encased in graphene layers for enhanced sodium-ion storage. *Journal of Materials Chemistry A, 6,* 14077.
59. Zhang, C., Deng, L., Zhang, P., Ren, X., Li, Y., & He, T."Hydrothermal Synthesis of NiS_2 Cubes with High Performance as Counter Electrodes in Dye-Sensitized Solar Cells," (2017). *International Journal of Electrochemical Science, 12*, 4610.
60. Li, J., Yan, D., Zhang, X., Hou, S., Lu, T., Yaoa, Y., et al. (2017). ZnS nanoparticles decorated on nitrogen-doped porous carbon polyhedra: a promising anode material for lithium-ion and sodium-ion batteries. *Journal of Materials Chemistry A, 5*(38), 20428.

61. Waghadkar, Y., Arbuj, S., Shinde, M., Ballal, R., Rane, S. B., Gosavi, S., et al. (2018). Hydrothermally synthesized zinc sulphide microspheres for solar light-driven photocatalytic properties. *Journal of Electronic Materials, 47,* 2687.
62. Yan, L., Uddin, A., Wang, H. (2015). ZnO tetrapods: Synthesis and applications in solar cells review article. *Nanomaterials and Nanotechnology, 5*, 19.
63. Chang, Y. C. (2014). Ni-doped ZnO nanotower arrays with enhanced optical and field emission properties. *RSC Advances, 4,* 56241.
64. Chen, C., Ye, M., Lv, M., Gong, C., Guo, W., & Lin, C. (2014). Ultralong Rutile TiO_2 Nanorod Arrays with Large Surface Area for CdS / CdSe Quantum Dot-sensitized Solar Cells. *Electrochimica Acta, 121,* 175.
65. Zhou, R., Zhang, Q., Uchaker, E., Lan, J., & Cao, G. (2014). CdSe quantum dot co-sensitized solar cells. *Journal of Materials Chemistry A, 2*(8), 2517.
66. Li, Y., Yu, H., Huangab, X., Wuab, Z., & Chen, M. (2017). A simple synthesis method to prepare a molybdenum oxide hole-transporting layer for efficient polymer solar cells. *RSC Advances, 7,* 7890.
67. Manivel, A., et al. (2015). Synthesis of MoO_3 nanoparticles for azo dye degradation by catalytic ozonation. *Materials Research Bulletin, 62,* 184.
68. Miao, J., Xu, G., Liu, J., Lv, J., & Wu, Y. (2017). Activation of carbon nitride solids by protonation: Morphology changes, enhanced ionic conductivity, and photoconduction experiments. *Journal of Solid State Chemistry, 246,* 186.
69. Hammad, T. M., Salem, J. K., & Hammad, T. M. (2009). The effect of surfactants on the particle size and optical properties of precipitated ZnO nanoparticles. *Journal of Material Science, 63*(17), 1489.
70. Rozue, R. R. A., Shally, V., Dharshini, M. P., & Jayam, S. G. (2015). Structural and Optical properties of Nickel Sulphide (NiS) nanoparticles. *International Journal of NanoScience and Nanotechnology, 6*(1), 41.
71. Hu, S., Li, F., Fan, Z., Wang, F., Zhao, Y., & Lv, Z. (2014). Band gap-tunable potassium doped graphitic carbon nitride with enhanced mineralization. *Dalton Transactions, 44,* 1084.
72. Agbo, P. E., Nwofe, P. A., Odo, L. O., & Ikwo, N. (2017). Analysis on energy bandgap of zinc sulphide (ZnS) thin films grown by solution growth technique. *Chalcogenide Letters, 14*(8), 357.
73. Mukherjee, S., et al. (2017). Tuning the band gap in titanium dioxide thin films by surfactant mediated confinement and patterning of gold nanoparticles. *The Journal of Physical Chemistry C, 121*(39), 21311.
74. Rao, K. D. M., Bhuvana, T., Radha, B., Kurra, N., Vidhyadhiraja, S., Kulkarni, G. U. (2011). Metallic conduction in NiS_2 nanocrystalline structures. *The Journal of Physical Chemistry C, 115*(21), 10462.
75. Mosiori, C. C., Njoroge, W., & John, O. (2014). Electrical properties of zinc sulphide thin films grown by chemical bath deposition. *Thin Film Characterization, 5*(9), 2343.
76. Halim, A. A. A., Hashim, H., Rusop, M., Mamat, M. H., & Zoolfakar, A. S. (2008). Study on electrical properties of zinc oxide thin film. *AIP Conference Proceedings, 1733,* 12.
77. Yildiz, A., Lisesivdin, S. B., Kasap, M., & Mardare, D. (2008). Electrical properties of TiO_2 thin films. *American Chemical Society, 354,* 4944.
78. Kumar, S. (1993). Electrical and optical properties of molybdenum trioxide thin films. *Bulletein of Material Science, 16*(3), 187.
79. Jayakumar, O., Atomic, B., Mohapatra, M., & Atomic, B. (2006). Magnetism in Mn-doped ZnO nanoparticles prepared by a co-precipitation method. *Nanotechnology, 17*(5), 1278.
80. Yin, P., Han, X., Zhou, C., Xia, C., Hu, C., & Sun, L. (2015). Large-scale synthesis of nickel sulfide micro / nanorods via a hydrothermal process. *International Journal of Minerals, Metallurgy, and Materials, 22*(7), 762.
81. Sapra, S., Nanda, J., Anand, A., Bhat, S., & Sarma, D. (2003). Optical and Magnetic Properties of Manganese-Doped Zinc Sulfide Nanoclusters. *Journal of Nanoscience and Nanotechnology, 3,* 392.

82. Shur, M., Gaska, R., Dobrinsky, A., & Shatalov, M. (2014). Deep Ultraviolet Light Emitting Diodes: Physics, Performance, and Applications. *ECS Transactions, 61,* 53.
83. Shockley, W., & Queisser, H. J. (1952). Detailed Balance Limit of Efficiency of pn Junction Solar Cells. *Acta Crystallographica, 5*(6), 860.
84. Thomas, S., Deepak, T. G., Anjusree, G. S., Arun, T. A., Nair, S. V., & Nair, A. S. (2014). A review on counter electrode materials in dye-sensitized solar cells. *Journal of Materials Chemistry A, 2*(13), 4474.
85. Mehrabian, M., Mirabbaszadeh, K., & Afarideh, H. (2014). Solid-state ZnS quantum dot-sensitized solar cell fabricated by the Dip-SILAR technique. *Physica Scripta, 89*(8), 085801.
86. Roduner, E. (2006). Size matters: why nanomaterials are different. *Chemical Society Reviews, 35*(7), 583.
87. Tao, L., Xiong, Y., & Shen, W. (2014). High performance PbS quantum dot sensitized solar cells via electric fi eld assisted in situ chemical deposition on modulated TiO_2 nanotube arrays. *Nanoscale, 6,* 931.
88. Kudo, A., & Miseki, Y. (2009). Heterogeneous photocatalyst materials for water splitting. *Chemical Society Reviews, 38*(1), 253.
89. Ma, C., Zhou, J., Cui, Z., Wang, Y., & Zou, Z. (2016). In situ growth MoO_3 nanoflake on conjugated polymer: An advanced photocatalyst for hydrogen evolution from water solution under solar light. *Solar Energy Materials and Solar Cells, 150,* 102.
90. Yu, L., Shao, Y., & Li, D. (2017). Direct combination of hydrogen evolution from water and methane conversion in a photocatalytic system over Pt/TiO_2. *Applied Catalysis B: Environmental, 204,* 216.

Advancement in $CdIn_2Se_4$/CdTe Based Photoelectrochemical Solar Cells

Subhash Chander

Abstract Many binary and ternary chalcogenide semiconductor materials (viz CdS, CdSe, CdTe, CdZnTe, $CuInS_2$, $CuInSe_2$, Bi_2CdS_4, $CdIn_2Se_4$, etc.) have been used to develop photoelectrochemical (PEC) solar cells for the sustained and efficient capture of solar energy conversion. Because thin-film solar cell technologies are a capable tactic for global and planetary-photovoltaics and offer a wide variability of picks in terms of device designing and fabrication. Cadmium indium selenide ($CdIn_2Se_4$) has obtained very little consideration as a potential material for photoelectrochemical cells. The manufacturing of thin-film-based heterojunction solar cells done by using some chemical and physical techniques such as sputtering, pulsed laser deposition, and evaporation. In spray pyrolysis technique (Fig. 1), a desired equimolar aqueous solution of cadmium chloride, indium trichloride, and selenourea in appropriate volumes can be taken onto preheated substrates (amorphous or conducting substrates viz. ITO, FTO, quartz, etc.). The preparative parameters (substrate temperature, solution concentration, quantity of solution) should be optimized by a PEC method in order to get high-quality stoichiometric films. The optimization of preparative parameters of the photoactive semiconducting electrode by the photoelectrochemical method is a new, reliable, and unique technique in the field of thin-film technology. So, this chapter deals with the preparation of cadmium indium chalcogenide thin films from aqueous medium by cost-effective and simple spray pyrolysis and consequently use of these films in heterojunction solar cell applications. It also extensively describes the physiochemical properties of $CdIn_2Se_4$ thin film as a potential window layer to the photoelectrochemical solar cells.

Keywords Energy materials · $CdIn_2Se_4$ thin films · PEC solar cells · Recent progress

S. Chander (✉)
Department of Chemical Sciences, Indian Institute of Science Education and Research (IISER) Mohali, Knowledge City, Sector 81, SAS Nagar, Mohali, India
e-mail: sckhurdra@gmail.com

S. J. Ikhmayies (ed.), *Advances in Energy Materials*,
Advances in Material Research and Technology,
https://doi.org/10.1007/978-3-030-50108-2_2

1 Introduction

The solar energy is radiant energy produced by the sun, and every single day, the sun radiates, or sends out, an enormous amount of energy. The sun radiates more energy in one second than people have used since the beginning of time; this energy comes from within the sun itself. The solar energy moves to the earth planet at a speed of 1.86×10^5 miles per second, the speed of light. Solar energy is also absorbed by plants, the land, and the oceans. The public and world governments remained largely indifferent to the possibilities of solar energy until the oil shortages [1]. Today, people use solar energy to heat buildings and water and to generate electricity. Hence, considering the industrial demand for reliable and a variety of new scientifically based future technologies, thin-film studies have made tremendous advances in the last decade. The advancements in the heterojunction solar cells have developed in several new areas of research in the field of solid-state physics and chemistry [2].

There has been a growing interest during the past few decades in metal chalcogenide thin films because of their promising applications such as solar cell, light-emitting diode, thermoelectric coolers, optoelectronic devices, and photoelectrochemical-based devices. To realize these applications, it is one of primary importance to grow high-quality thin films and characterize their fundamental properties. The fabrication of thin-film-based heterojunction solar cells has been done by using some chemical and physical techniques such as sputtering, pulsed laser deposition, and evaporation. All these techniques have their own merits and demerits, but spray pyrolysis technique has been attracting a great deal of attention to deposit semiconducting thin films owing to its simplicity and low cost. So, this chapter deals with the preparation of cadmium indium chalcogenide thin films from aqueous medium by cost-effective and simple spray pyrolysis and, consequently use of these films in heterojunction solar cell applications. The optimization of preparative parameters of the photoactive semiconducting electrode by the photoelectrochemical method is a new, reliable, and unique technique in the field of thin-film technology [3]. The p-n junction-based single-crystalline silicon solar cells have been favored due to their high efficiency (more than 25%), and the rigorous prerequisite of very decorative configurations (for the realization of high efficiency) stalemates a severe inadequacy that the industrial cost would be an extreme level. In recent years, heterojunction-based photovoltaic devices have earned significant consideration owing to their lower industrial cost, in spite of their comparatively small power conversion efficiency. A number of methods/techniques can be employed to fabricate heterojunction-based solar cell devices [4]. Thin-film solar cells (TFSC) are an encouraging methodology for terrestrial and space photovoltaics and offer a wide variety of choices in terms of device designing and fabrication [5]. A range of substrates (flexible or rigid, metal, or insulator) can be used for deposition of different layers (contact, buffer, absorber, reflector, etc.) exhausting diverse flexible techniques which allowed tailoring and engineering of the layers for enhancement in the performance of the solar cell device. Thin-film-based methods are not so energy-concentrated as compared to silicon-based technologies and are flexible for bunch

processing, which results in a reduction in the total cost of the device. Recent studies reveal that there is rapid advancement in the synthesis and design of bulk semiconducting chalcogenide-based thin films for solar cell applications [6–9]. A thickness of 2–4 μm of direct bandgap semiconductors (GaAs, CIGS, and CdTe) for the thin-film-based photovoltaic cells is enough for light absorption while crystalline silicon needs around 200–300 μm to absorb all the incident radiation. Owing to the narrower layer generated, this commands to the more rapidly processing moves and yield-lessening the principal cost. Solar cells made from these materials have demonstrated module efficiencies of over 12% and are currently manufactured globally. Copper indium gallium selenide and cadmium telluride based solar modules are having power conversion efficiencies comparable to silicon-based solar modules designed and developed, and their stability has also been well tested [10]. The maximum obtained efficiency of these single crystalline silicon and thin-film-based solar cells is limited to around 25%, which is less than the maximum hypothetical efficiency limit of 33% as predicted by Shockley and Queisser for a single p-n junction solar cell [11]. But efforts on n-$CdIn_2Se_4$/p-CdTe heterojunction solar cells fabricated by low-cost and straightforward chemical spray pyrolysis technique have given less coverage. This technique has some advantages over others like easy to vary the precursor's concentration and substrate temperature for controlling stoichiometry and adherence of the deposited layers. So, this chapter will be a milestone in the field of $CdIn_2Se_4$/CdTe thin-films based electrochemical solar cells by incorporating research work done so far.

2 Significance of $CdIn_2Se_4$ Material

The interest in the semiconductor–liquid junction has evolved parallel to develop solid-state junctions. Even though there have been both academic advances and market expansion in solar cell technologies in modern years, there persists a need for enhanced efficiency, reduced-cost processing, and increased process yields. The binary and ternary semiconducting materials can be grown on different types of substrates employing the spray pyrolysis method [12–14]. The binary and ternary chalcogenide materials (viz. CdS, CdSe, CdTe, CdZnTe, $CuInS_2$, $CuInSe_2$, Bi_2CdS_4, $CdIn_2Se_4$, etc.) have been used to develop photoelectrochemical (PEC) solar cells for the sustained and efficient capture of solar energy conversion [15–20]. Cadmium indium selenide ($CdIn_2Se_4$) is an n-type ternary semiconducting compound material belongs to the II-III-VI group and has tetragonal and cubic structures with the lattice constant of 5.823 Å [21, 22]. It was first produced by Hahn et al. [23], while $CdIn_2Se_4$ crystals were prepared by Nitsche [24] employing the chemical transport method. It is widely used in optoelectronic devices, nonlinear optics, semiconducting devices, radiation detectors, laser materials, thermoelectric devices, solar energy converters, etc. [25–27]. This material has been effectively utilized as a window layer owing to its light-moving property with a thin direct bandgap and low electrical resistivity to

make different electronic and electro-optical devices. One of its proficient applications is in thin-film heterojunction solar cells or as a photoelectrode in the PEC cells. The efficient operation of solar energy is the best encouraging approach to tackle the concern related to the energy crunch. Consequently, effective solar energy conversion into functional photovoltage by PEC cells has stimulated tremendous research attempts.

3 Advancement in $CdIn_2Se_4$ Thin Films

The compound $CdIn_2Se_4$ material has given a little consideration as a potential material for the PEC cells owing to its optical absorption property, narrow optical bandgap (1.73 eV), and a low electrical resistance [28–31]. Great intense studies on $CdIn_2Se_4$ thin films have been made in recent years due to their exciting and proposing tailored properties that extend the possibility of implementing innovative applications in many modern applications such as solar energy conversion, nonlinear optics, and optoelectronic devices [32, 33]. The fundamental needs of good thin-film photoelectrode for PEC cells are low resistivity and large grain size, where later one leads to lessening the grain boundary area of thin films with vital outcomes for efficient energy conversion. The low resistivity of photoelectrode is required to minimize the series resistance of PEC cells. $CdIn_2Se_4$ thin films can be fabricated by a number of physical and chemical processes viz slurry pasting technique [32], sol-gel [34], thermal evaporation [35], pulsed electrodeposition [36], spray deposition [28, 37], potentiostatic cathodic electrodeposition [38], and laser ablation technique [39] where every method has their own merits and demerits. The spray pyrolysis technique is one of the most used processes since it is relatively inexpensive and convenient for extensive area deposition and provided quality films having good photovoltaic activity, high crystallinity, low electrical resistivity, and high thermoelectric power [40]. In spray pyrolysis technique (Fig. 1), a desired equimolar aqueous solutions of cadmium chloride, indium trichloride, and selenourea in appropriate volumes can be taken onto preheated substrates (amorphous and conducting substrates viz. ITO, FTO, quartz, etc.). The preparative parameters (substrate temperature, solution concentration, quantity of solution) should be optimized by a PEC method in order to get high-quality stoichiometric films.

After fabrication of high-quality $CdIn_2Se_4$ thin films, one can be post-treated by various treatment and then subjected to different characterization tools viz. X-ray diffraction (XRD), scanning electron microscopy (SEM) coupled with energy dispersive analysis by X-rays (EDAX), atomic force microscopy (AFM), UV-Vis spectrophotometer, and source meter (i.e., electrometer) in order to investigate structural, surface morphology (along with compositional), topography, optical, electrical, and photovoltaic properties. The optical, photophysical, and photoluminescence properties of thin $CdIn_2Se_4$ films are reported by different research groups across the world [41–47].

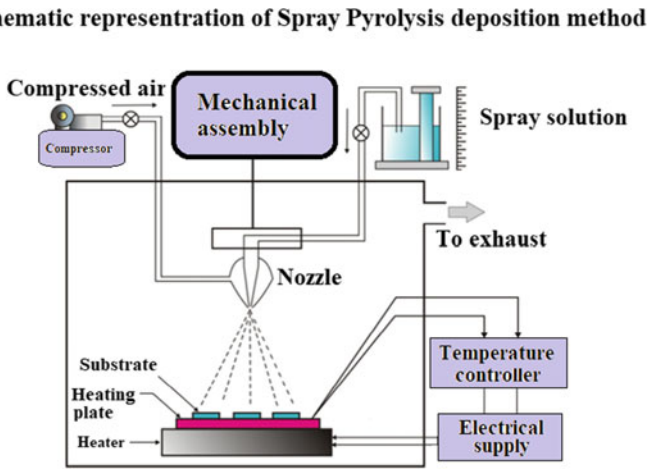

Fig. 1 Schematic representation of the spray pyrolysis deposition method

The photoactive cadmium indium selenide ($CdIn_2Se_4$) thin films are electrochemically synthesized by Ahn et al. [12] at ambient temperature. The films found to be nanocrystalline in nature and have 1:2:4 elemental chemical stoichiometric ratio for Cd, In, and Se. Irregularly shaped islands having 400–500 nm in sizes and composed of a large number of small spherical grains were verified from the atomic force microscopy and the scanning electron microscopy images. The physical properties of thin $CdIn_2Se_4$ films are investigated by Dalchiele et al. [13], where the films were grown by electrodeposition technique. The photoelectrochemical measurement in the presence of 1 M poly-sulfide electrolyte revealed the device conversion efficiency of 0.42% under the light illumination intensity of 80 mW/cm^2. Salem et al. [14] prepared stoichiometric bulk ingot material of the quaternary $CdGaInSe_4$ by direct fusion of the constituent elements in vacuum-sealed silica tubes. All the films exhibited n-type conduction and ohmic behavior with metallic films of Au, Cd, In, Ag, and Sb. The optical constants of $CdIn_2Se_4$ thin films within the spectral range of 500–2000 nm are studied by El-Nahass [21], who also evaluated the refractive index, absorption index, absorption coefficient, and forbidden energy gaps. Adpakpang et al. [29] synthesized $CdIn_2Se_4$ powder via an aqueous chemical reduction where they used Se metal, $InCl_3$, and $CdCl_2{\cdot}2.5H_2O$ as precursors, $NaBH_4$ as a reducing agent, and water as a solvent. The $CdIn_2Se_4$ phase was observed in some preparative conditions with $In(OH)_3$ contaminating phase. Though, $In(OH)_3$ impurity had disappeared when the reaction temperature was 130 °C with a reaction time of 30 min while the particle size was found to be around 10 nm.

Neumann et al. [48] studied infrared reflectivity of $CdIn_2Se_4$ single crystals at room temperature in the wavenumber range from 180 to 4000 cm^{-1} for the polarization directions E_c and E. The spectra reveal two vibrational modes with nearly the same frequencies for both polarization directions. It is concluded that these modes are sphalerite-like in nature and their frequencies are primarily determined by the

properties of the In-Se bond. Guerrero et al. [49] prepared samples of $CdIn_2Se_4$ by the melt-and-anneal technique followed by annealing at 500 °C. The films found to have p-structure and also calculated the deformation potentials of the valence and conduction bands. The degree of crystallinity increases with increasing the annealing temperature, while the elemental compositional analysis confirmed the nearly stoichiometric nature of the films. The allowed direct and indirect optical transitions, and both values of energy gaps were also decreased with increasing annealing temperature. Hady et al. [50] studied the structural, optical, thermoelectric power measurement for several pre-annealed thin $CdIn_2Se_4$ films having different thicknesses. Their results showed that the pre-annealed films are n-type semiconductors, whereas free charge carrier concentrations were used to calculate the free charge carrier mobility from which the grain boundary potential barrier has also been evaluated. Trykozko et al. [51] prepared $CdIn_2Se_4$ crystals by means of chemical transport reactions using iodine as a transport agent. They measured the reflectance of $CdIn_2Se_4$ at room temperature and at liquid nitrogen temperature within the range of 1.5–20 eV using synchrotron radiation. The effects of temperature and pH on the formation of thin $CdIn_2Se_4$ films are investigated by Ruanthon et al. [34] where they fabricated the films by sol-gel dip-coating method using cadmium, indium, selenium precursors which were dissolved in the different solvents (ethanol, hydrochloric acid, and acetic acid) to form metal alkoxides. The precursor solutions were mixed together in the N_2 atmospheric condition, and then, these metal alkoxides were hydrolyzed by adding water and consequently poly-condensed by adding ethylene glycol to become gels. These thin films were annealed at various temperatures in the N_2 atmosphere and characterized by SEM. Their results indicated that $CdIn_2Se_4$ thin films fabricated by the reaction at room temperature with pH4 and annealed at 450° in nitrogen atmosphere are suitable for photovoltaic applications. Girija et al. [52] have fabricated cadmium indium selenide thin films on glass substrate employing chemical bath technique at different temperatures of 40 °C, 60 °C, and 80 °C. They tailored the properties to the compound itself in order to find the potential applications for optoelectronic devices. The films were found to have a cubic phase while presence of elemental constituents was confirmed by EDAX. Their optical studies revealed that the films have a direct transition with energy bandgap ranging from 1.55 to 2.28 eV.

Mahalingam et al. [38] reported the effect of deposition potential on the microstructural parameters (crystallite size, strain, and dislocation density) where they deposited thin $CdIn_2Se_4$ films on ITO coated substrates at various deposition potentials using potentiostatic electrodeposition technique. The prepared films found to have polycrystalline nature with the preferential orientation of (200) diffraction peak. They observed the stoichiometric behavior of well-defined composition at a deposition potential of −950 mV and films exhibited direct bandgap value within the range of 1.66–1.75 eV, which was varied with the deposition potential. Nikale and coworkers [27] deposited well adherent and stoichiometric semiconducting n-$CdIn_2Se_4$ thin films spray pyrolysis technique. The films found to have good photoactive and photoactivity, while XRD patterns show the polycrystalline nature with a cubic crystal structure. The crystallinity and texture coefficients were increased with the optimized solution concentration, whereas surface morphology study reveals non-uniformity

of distributed grains that having different grain sizes. The lowest resistivity and activation energy achieved for films deposited at 12.5 mM concentration were about 3.9 $\times$ 10^1 Ω cm and 6.8 meV, respectively, where grown films showed n-type conductivity. Salim and co-authors [35] have grown $CdIn_2Se_4$ thin films employing thermal evaporation technique using pre-synthesized ingot material. They observed that the as-deposited films have amorphous nature, but the amorphous-to-crystalline phase transition occurred at an annealing temperature of 200 °C as well as films showed stoichiometric behavior as confirmed by EDAX analysis. The optical analysis of the optical absorption coefficient revealed the existence of direct and indirect optical transitions.

The microstructural and electrical properties of $CdIn_2Se_4$ thin films have been investigated by Sudha and co-workers [36], where they grow the films by pulsed electrodeposition technique. Their AFM results showed that the as-deposited films were well-adherent with uniformly grains distribution over the surface of the substrate as well as films were highly transparent in the visible range having more than 80% average transmittance. The direct optical bandgap was varied from 3.12 to 3.77 eV and decreased with the duty cycle of the deposition process.

In 2017, Bhalerao and co-workers [31] had electro-synthesized the thin $CdIn_2Se_4$ films and have (photo)electrochemically explored using current–voltage and capacitance–voltage characteristics along with photoresponse, speed response, and electrochemical impedance studies. The improved photoconversion efficiency can be justified by hypothetical modeling of energy band illustration and equivalent circuited model of impedance spectra of the PEC cells. Very recently, Degdas and Peksoz [53] deposited cadmium indium selenide thin films on ITO coated substrates using electrodeposition technique at a constant deposition voltage of −0.95 V. They used $CdCl_2$, $InCl_3$, and H_2SeO_3 precursors, while the Se concentration was enhanced from 5 to 35 mM by a step of 5 mM as well as HCl was used to adjust the pH of the electrolytes. They investigated the effect of concentration of Se source on film thickness, surface morphology, film composition, crystallinity, donor density, mobility, and optical band gap. They found that the film thickness was increased from 247 to 374 nm with the concentration of Se source, whereas Se concentration causes a significant variation of surface morphology and elemental compositions of the films. All the films have a tetragonal crystalline phase, while the energy bandgap is ranging from 1.98 to 2.23 eV. The Hall-effect analysis confirmed the n-type semiconducting nature and donor density which is found within the range of -1.3×10^{17} cm^{-3} and -4.1×10^{18} cm^{-3}, whereas the mobility increased with the increasing of Se atomic percentage which might be due to decrease in the donor concentration.

4 Photoelectrochemical (PEC) Solar Cells

The formation of a practical PEC cell is to convert the sunlight into electricity, and the most vital element is the long-term stability of the solar device which shows sufficient power conversion efficiency. This type of cell has consisted of a semiconductor

photoelectrode, an electrolyte, and a counter electrode, as demonstrated in Fig. 2. The spacing from the photoelectrode to the counter electrode can be kept around 5 mm. The band bending of semiconductor photoelectrode may occur when both electrodes are immersed in the electrolyte. The electron transfer can take place only from the electrolyte into the conduction band, while hole transfer into the area of the valance band because these types of transfers can only occur between two states of the same energy, one empty and other filled. Under light illumination, electron-hole pairs are generated in the depletion layer and separated by the electric field present at the interface. The incident energy of the photon should be higher than the energy bandgap of the semiconductor. The electron-hole pairs generated in the bulk of the semiconductor are mostly lost through recombination. If a positive potential is applied to the n-type semiconductor photoelectrode and illuminated, electron-hole pairs are generated, and separated electrons rise to the top of the conduction band and holes in the valence band. This process sets up a counter field under open-circuited conditions. The counter field is at its maximum and is the open-circuited voltage (V_{oc}) which is given by Eq. (1) [54].

$$V_{oc} = \left(\frac{nKT}{e}\right) \ln\left[\frac{I_{ph}}{I_o} + 1\right] \tag{1}$$

Here, I_o is the total output current, I_{ph} is the photon-generated current, n is the junction ideality factor, K is the Boltzmann constant, T is the temperature, and e is the electronic charge. On the other hand, the counter electrode is being in the same electrolyte, the photovoltage acts as a driving force for electrons to move under short-circuit conditions from semiconductor electrode to the counter electrode, and a regenerative cell is formed and is shown in Fig. 3. As discussed by

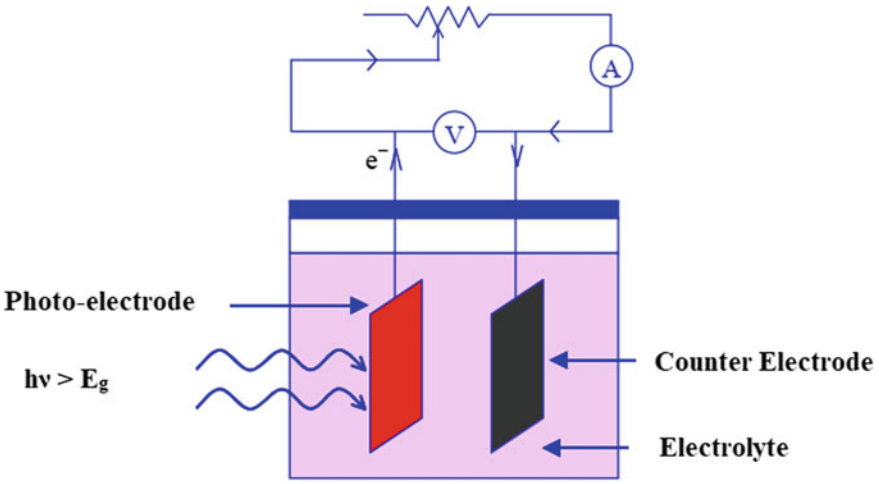

Fig. 2 Conventional schematic representation of the electrochemical photovoltaic cell

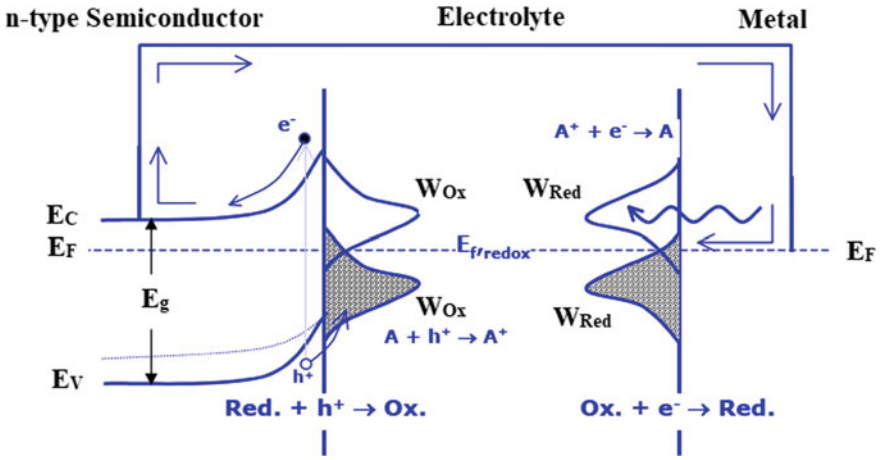

Fig. 3 Direction of current flow and energy band level diagram for a PEC cell having n-type semiconducting material

short-circuited current [55], the electrons pushed to the conduction band glide in the direction of the interior, while the minority carriers (i.e., holes) come to the surface of a semiconducting material where they encountered and reduce into the redox couple form inside the solution. The part is dissolved by holes, transferred to the counter-electrode, and consequently gets diminished. Such diminution is propelled by the external connection from the semiconducting material.

4.1 Prerequisites to Make a PEC Cell

A photoelectrochemical (PEC) cell has consisted of a photoelectrode (made by a semiconducting material), an electrolyte, and a countered electrode, as demonstrated in the above Fig. 2. The following prerequisites are required to achieve excellent performance of the device:

4.1.1 Semiconductor Photoelectrode

One of the most vital components to developing a PEC solar cell is the selection and preparation of semiconducting material, which indicates the modifications in the electrical characteristics of the solar cell device. The semiconducting photoelectrode be supposed to fulfill the subsequent basic requirements as follow:

1. The energy bandgap of semiconducting material ought to be such that the utmost portion of the solar radiation spectrum is utilized. Nearly, all the visible portion

of solar radiation arriving at the earth's surface is focused within the range of 1.65–3.50 eV.
2. The power conversion cell efficiency should be high that varies with the optical absorbance, bandgap energy, diffusion-length, electrical conductivity, recombination of charge carriers, surface-states, etc.
3. The semiconducting photoelectrode has to be stable against erosion when it positioned inside the specific redox-electrolyte. So, the selection of semiconducting materials is highly significant for a PEC cell.
4. The thickness of the semiconducting photoelectrode is supposed to be sufficiently large to absorb the maximum photons of the incident solar radiation.
5. The series and shunt resistances must be small and large (as much as possible), respectively, here ideal value of series and shunt resistances is zero and infinity, respectively.
6. The manufacturing cost and power conversion cell efficiency would be an acceptable range.

4.1.2 Electrolyte

The electrolyte is another critical factor of the PEC cells, and it consists by oxidized and reduced species. These species are ionic species and are required in helping for the transportation of photogenerated holes from the semiconducting photoelectrodes to the countered electrodes. The energy band levels of electrolytes are analogous to the solid-state theory of energy states, and E_f of the redox is equal to the Fermi energy level of the semiconducting material. When the semiconducting photoelectrode is engrossed into the electrolyte, the equipoise position is attained by the electron-exchange at the electrolyte surface. The Fermi level of the semiconducting material adjusts with the other counterparts, which generates a barrier height depending on the solution species types and semiconducting material. The requirements for an electrolyte are as follow:

1. Reduction–oxidation outcomes have to occur suitable to the band edges of the semiconducting material.
2. Rate of charge transfers of oxidized/reduced species have to be elevated at the semiconducting photo and countered electrodes.
3. The oxidized and reduced species along with supporting electrolyte concentration in the solvent have to be suitable to achieve the expected current densities.
4. The optical absorbance/absorption of electrolyte has to be lowest. The electrolyte ought to be non-corrosive to the photo and counter-electrodes.
5. The noxiousness, reactivity, and cost ought to be below as possible.

4.1.3 Countered Electrode

The countered electrode is required to fulfill recreating processes, and the species of electrolytes are oxidized as the electrodes providing no netting chemical variation

in the composition of the electrolytes. The countered electrode is supposed to fulfill the subsequent basic requirements as follow to enhance the performance of a solar device:

1. The countered electrode must be chemically inactive.
2. Charge transfer between the countered electrodes and redox species inside the electrolyte has to be quick.
3. As a countered electrode is engrossed into the electrolyte, the half-cell potential of the countered electrode has to match with the half-cell potential of semiconducting photoelectrode.
4. Countered electrodes ought to be not expensive.

5 Advancement in $CdIn_2Se_4$/CdTe Based Thin Film Solar Cells

5.1 Solar Cell Device Characterization

The solar cell characterization is the current–voltage measurements can be undertaken under simulated sunlight, and the integration of spectral response with the solar spectrum (having condition of AM1.5G and normalized intensity of 100 $mWcm^{-2)}$ may provide information on different photovoltaic parameters viz short-circuit current, open-circuited voltage, fill factor, cell efficiency, maximum power point, and series/shunt resistances. The air mass (AM) number is given by the standard relation (Eq. 2) [56].

$$\text{Air Mass (AM)} = \frac{1}{\cos\theta} \tag{2}$$

Here, θ is the angle of incidence. The radiant power as seen at the surface of the earth is called AM1.5 and most widely used for evaluating solar cells (solar spectral irradiance distribution incident at sea level from the sun at 45° above the horizon). The current–voltage characteristics of a solar cell in the dark and illuminated junctions are demonstrated in Fig. 4.

When the diode is illuminated, the dark current characteristic shifts down by light generated current (I_L), and the characteristic curve describes three essential parameters that give a complete description of a solar cell that is short-circuited current (I_{sc}), open-circuited voltage (V_{oc}), and fill factor (FF). The short-circuited current is obtained when the voltage drop across the junction is zero, which means that under ideal conditions I_{sc} is I_L, but I_{sc} is lower than I_L due to the effect of series and shunt resistances [57]. The maximum power point (MPP) is equal to the area of maximum power rectangle as shown in Fig. 4 on the I–V curve which is the point where maximum power is produced. It is a point on the current–voltage

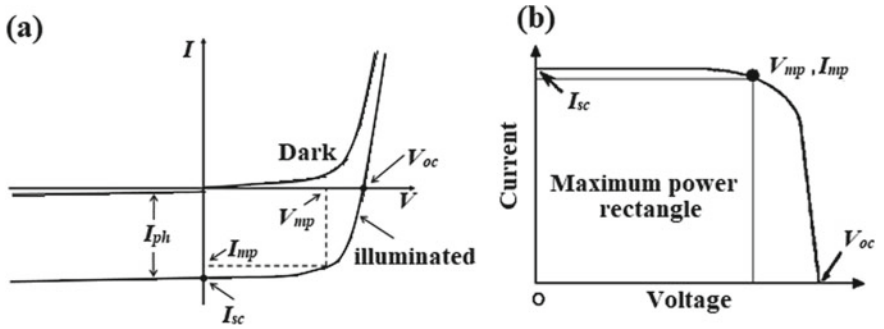

Fig. 4 **a** Current–voltage characteristics of a solar cell in the dark and illuminated and **b** maximum power rectangle

characteristics where the area of the resulting rectangle is largest. The fill factor (as given by Eq. 3) is described as the ratio of the maximum available power to the product of the open-circuited voltage and short-circuit current [58].

$$\mathrm{FF} = \frac{V_{\mathrm{m}} \times I_{\mathrm{m}}}{V_{\mathrm{oc}} \times I_{\mathrm{sc}}} \tag{3}$$

Here, V_{m} and I_{m} are maximum voltage and current (at maximum power point), respectively. Typical commercial solar cells have a fill factor >0.70. Besides power conversion efficiency, it is one of the most significant parameters for the energy yield of a photovoltaic cell. It is well known that the PV cells with a high fill factor have a low equivalent series resistance and a high equivalent shunt resistance, so less of the current produced by light is dissipated in internal losses.

The power conversion efficiency (η) is a measure of the performance of a solar cell which could be determined by the maximum output power of the device as the ratio of power output (P_{out}) to power input (P_{in}), where input power is the sum over all wavelengths which is commonly fixed at 100 mW/cm^2 when solar simulators are used [58].

$$\eta = \frac{P_{\mathrm{out}}}{P_{\mathrm{in}}} \tag{4}$$

$$\eta = \frac{\mathrm{FF} \times V_{\mathrm{sc}} \times I_{\mathrm{sc}}}{P_{\mathrm{in}}} \tag{5}$$

5.2 $CdIn_2Se_4$/CdTe Heterojunction Based Solar Cells

A heterojunction is a junction between two dissimilar crystalline materials, and it can be classified as abrupt and graded corresponding to distances during which the electronic transitions from one material to others are completed near the interface. For abrupt heterojunction, the region is within a few atomic distances, while for graded heterojunction, it is of the order of several diffusion lengths. When photons having energies between two bandgap energies pass through wide bandgap semiconductors, they generate electron-hole pairs in and near depletion regions on the narrow bandgap side of the junction. The built-in-field at the junction separates the holes before recombining in the depletion region and generation of photovoltage. This is known as window effect and firstly reported first by Preston [59] and known as heterojunction window effect, but interest in the heterojunction devices was stimulated by the work of Kroemer and other researchers [60–63]. Though the p-n junction solar cells of single crystalline silicon are preferred because of their high efficiencies of above 25%, the stringent requirement of very elaborate configurations for the realization of high efficiency impasses a serious shortcoming that the manufacturing cost would be very high [64] which leads to the search for low-cost solar cells. In recent years, heterojunction-based solar cells have gained great attention because of their lower manufacturing cost, in spite of their relatively low conversion efficiency [11, 65, 66]. A variety of techniques could be used for the preparation of heterojunction solar cells [67, 68]. Thin-film solar cells (TFSC) are a promising approach for terrestrial and space photovoltaics and offer a wide variety of choices in terms of device designing and fabrication. A variety of substrates (flexible or rigid, metal, or insulator) can be used for the deposition of different layers (contact, buffer, absorber, reflector, etc.) using different flexible techniques those allowed tailoring and engineering of the layers in order to improve device performance [69–79]. But efforts on n-$CdIn_2Se_4$/p-CdTe heterojunction solar cells fabricated by simple and low-cost chemical spray pyrolysis technique have given less coverage. This technique has some advantages over others like easy to vary the concentration of precursors and the substrate temperature for controlling stoichiometry and adherence of the deposited layers. The next paragraph comprises the advancement in the field of $CdIn_2Se_4$/CdTe based electrochemical solar cells.

During the last few years, the conversion efficiencies of PEC cells (also called electrochemical photovoltaic cells) have risen steadily, and a number of systems and reasons to excellent stability have been reported. The $CdIn_2Se_4$ thin films having n-type semiconducting nature are used to $CdIn_2Se_4$/CdTe based thin film solar cells where CdTe thin films are having p-type semiconducting nature and then study the current–voltage, capacitance–voltage, and spectral response characteristics, and consequently, photovoltaic or performance parameters viz junction ideality factor, fill factor, power conversion efficiency, flat-band potential (V_{fb}), and energy bandgap (E_g) can be evaluated using these measurements.

The substrate cleaning plays an essential role in the device fabrication process, and therefore prior to making a device, the required substrates should be successively

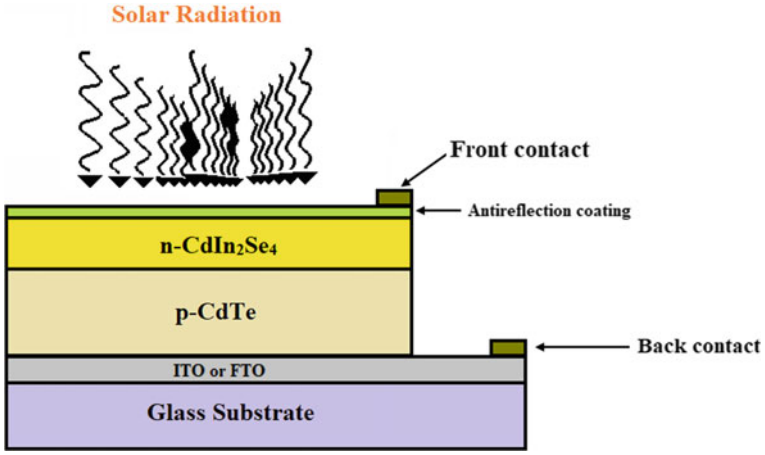

Fig. 5 Typical schematic device structure of $CdIn_2Se_4$/CdTe based electrochemical solar cells in a substrate configuration

cleaned by ultra-sonication in detergent solution, deionized water, ethanol, acetone, and 2-propanol and then should blow-dried with nitrogen and then treated in UV-ozone for 20–30 min. The typical schematic device structure of $CdIn_2Se_4$/CdTe based electrochemical solar cells in substrate configuration is demonstrated in Fig. 5.

The physical properties of thin $CdIn_2Se_4$ films are investigated by Dalchiele et al. [13], where the films were grown by electrodeposition technique. The photoelectrochemical measurement electrode in the presence of 1 M poly-sulfide electrolyte revealed the device conversion efficiency of 0.42% under the light illumination intensity of 80 mW/cm^2. The absorber p-CdTe type thick layer having optimized preparative parameters (viz. substrate temperature of 250 °C, solution concentration of 10 mM, solution quantity of 40 cc, spray rate of 2 cc/min, and pH (10)) was grown onto FTO coated glass by Rajpure's group [30] using spray pyrolysis technique. On the absorber layer, a thin layer of n-$CdIn_2S_4$ having optimized preparative parameters (viz. substrate temperature of 360 °C, solution concentration of 50 mM, quantity of solution of 56 cc, spray rate of 3 cc/min) was grown by same technique (as mentioned above). FTO layer acts as a back contact while the front contact was made with the help of silver paste. A thin layer of TiO_2 was used as an antireflection coating. This developed heterojunction solar cell under illumination was further tested for their current–voltage (I–V), capacitance–voltage (C–V), power output characteristics, and spectral response. They studied the photovoltaic parameters viz. power conversion efficiency, fill factor, series and shunt resistances, junction quality factor in the dark (n_D), and light (n_L) for the n-$CdIn_2Se_4$/p-CdTe heterojunction solar cells. The device exhibited a maximum fill factor of 0.55 and a power conversion efficiency of 0.67%. Their I–V measurements suggested that the forward current in these junctions involved tunneling while the forward current can be explained by a multi-tunneling capture-emission model in which the hole emission process dominates the carrier

transport mechanism. Bhalerao et al. [31] have fabricated (photo)electrochemical $CdIn_2Se_4$ thin-film solar cells using electro-synthesizing technique and analyzed using current–voltage and capacitance–voltage characteristics along with photoresponse, speed response, and electrochemical impedance studies. The PEC performance of the cell showed a good photoresponse, comparatively high short-circuit current, and open-circuited voltage with better stability over the long duration with the lower value of diffusion coefficient and high value of carrier lifetime to support lower recombination rate. The improved photoconversion efficiency can be explained with the help of theoretical modeling of the energy band diagram of the impedance spectra of the PEC cells. The reduced interfacial charge transfer resistance of the PEC cell after illumination is responsible for improving the photocurrent, which has promise for low-cost photovoltaic device fabrication. There is intensive research focused on the progress of $CdIn_2Se_4$ thin film as a window potential layer to the PEC solar cells.

6 Conclusions

The solar energy is radiant energy produced by the sun, and there has been an increasing interest during the past few decades in metal chalcogenide thin films because of their promising applications. The ternary chalcogenide $CdIn_2Se_4$ semiconducting material has received very little attention as a prospective material for photoelectrochemical (PEC) cells, but it may be used for the sustained and efficient capture of solar energy conversion because it offers a wide variety of choices in terms of the device designing and fabrication. The performance of solar cells can be enhanced with the approaches adopted based on the materials layer processed methods and the band alignment. The recent progress in $CdIn_2Se_4$ thin-film material has shown the practicability to develop high-efficiency PV devices as it is stable, eco-friendly, and low cost. The fabrication of $CdIn_2Se_4$ thin-film-based heterojunction solar cells was done by using some chemical and physical techniques. This chapter deals with the preparation of $CdIn_2Se_4$ thin films from aqueous medium by cost-effective and simple spray pyrolysis and consequently use of these films in heterojunction solar cell applications. It also extensively described the physiochemical properties of $CdIn_2Se_4$ thin film as a potential window layer to the photoelectrochemical solar cells. For $CdIn_2Se_4$/CdTe based solar cell technology to reach the commercialization stage, this review also highlighted the significant research progress and the patentability for further improvement in the power conversion efficiency by the understanding of the window layer material and reducing non-radiative recombination centers. The research efforts should be focused on the development of new approaches for synthesizing $CdIn_2Se_4$ thin film as well as the understanding of device mechanisms and operation. The promising candidature of this material remains a reality, and the technology may be enormously useful for the world and society to cater to the current energy demand as a leading contender.

References

1. The University of Colorado Boulder, http://lsa.colorado.edu/essence/texts/solar.html. Accessed on 19 Dec 2019.
2. Nalwa, H. S. (2001). *Handbook of thin films* (1st ed., pp. 1–102). Cambridge: Academic Press, Elsevier.
3. Nikale, V. M., & Bhosale, C. H. (2004). Properties of spray-deposited $CdIn_2Se_4$ thin films for photovoltaic applications. *Solar Energy Materials and Solar Cells, 82*, 3.
4. Green, M. A. (1992). *Solar cells: operating principles, technology, and system applications* (2nd ed., pp. 1–274). Kensington/Sydney: University of New South Wales.
5. Chopra, K. L., Paulson, P. D., & Dutta, V. (2004). Thin-film solar cells: an overview, *Progress in Photovoltaics: Research and Applications, 12,* 69.
6. Hassanien, A. S., & Sharma, I. (2020). Optical properties of quaternary a-Ge_{15-x} $Sb_xSe_{50}Te_{35}$ thermally evaporated thin-films: refractive index dispersion and single oscillator parameters. *Optik, 200,* 163415.
7. Hassanien, A. S., & Sharma, I. (2019). Band-gap engineering, conduction and valence band positions of thermally evaporated amorphous $Ge_{15-x}Sb_xSe_{50}Te_{35}$ thin films: Influences of Sb upon some optical characterizations and physical parameters. *Journal of Alloys and Compounds, 798,* 750.
8. Hassanien, A. S., & Akl, A. A. (2018). Influence of thermal and compositional variations on conduction mechanisms and localized state density of amorphous $Cd_{50}S_{50-x}Se_x$ thin films. *Journal of Non-Crystalline Solids, 487,* 28.
9. Hassanien, A. S., & Akl, A. A. (2018). Optical characteristics of iron oxide thin films prepared by spray pyrolysis technique at different substrate temperatures. *Applied Physics A, 124,* 752.
10. Ushasree, P. M., & Bora, B. (2019). *Solar energy capture materials* (p. 1) (E. A. Gibson, Ed.). Cambridge: Royal Society of Chemistry.
11. Green, M. A., Hishikawa, Y., Dunlop, E. D., Levi, D. H., Hohl-Ebinger, J., & Ho-Baillie, A. W. Y. (2018). Solar cell efficiency tables (version 52). *Progress in Photovoltaics: Research and Applications, 26,* 427.
12. Ahn, J.-H., Cai, G., Mane, R. S., Todkar, V. V., Shaikh, A. V., Chung, H., et al. (2007). Electrochemically deposited photoactive $CdIn_2Se_4$ thin films: Structural and optical studies. *Applied Surface Science, 253,* 8588.
13. Dalchiele, E. A., Cattarin, S., & Musiani, M. M. (1998). Preparation of $CdIn_2Se_4$ thin films by electrodeposition. *Journal of Applied Electrochemistry, 28,* 1005.
14. Salem, A. M., Soliman, W. Z., & Mady, Kh A. (2008). Structural characterization and electrical properties of quaternary $CdGaInSe_4$ thin films. *Physica B, 403,* 145.
15. Chander, S., & Dhaka, M. S. (2017). Optimization of substrates and physical properties of CdS thin films for perovskite solar cell applications. *Journal of Materials Science: Materials in Electronics, 28,* 6852.
16. Purohit, A., Chander, S., Nehra, S. P., & Dhaka, M. S. (2015). Thickness-dependent physical properties of thermally evaporated nanocrystalline CdSe thin films. *Acta Metallurgica Sinica (English Letters), 28,* 1299.
17. Chander, S., & Dhaka, M. S. (2016). Thermal evolution of physical properties of vacuum evaporated polycrystalline CdTe thin films for solar cells. *Journal of Materials Science: Materials in Electronics, 27,* 11961.
18. Chander, S., & Dhaka, M. S. (2015). Preparation and physical characterization of CdTe thin films deposited by vacuum evaporation for photovoltaic applications. *Advanced Materials Letters, 6,* 907.
19. Chander, S., & Dhaka, M. S. (2017). Thermal annealing induced physical properties of electron beam vacuum evaporated CdZnTe thin films. *Thin Solid Films, 625,* 131.
20. Chander, S., & Dhaka, M. S. (2016). Effect of thickness on physical properties of electron beam vacuum evaporated CdZnTe thin films for tandem solar cells. *Physica E: Low-dimensional Systems and Nanostructures, 84,* 112.

21. El-Nahass, M. M. (1991). Optical properties of $Cdln_2Se_4$ thin films. *Applied Physics A, 52,* 353.
22. Khusayfan, N. M. (2012). Optical properties of $CdIn_2Se_4$ thin films in the region of the fundamental absorption edge. *Australian Journal of Basic and Applied Sciences, 6,* 329.
23. Hahn, H., Frank, G., Klinger, W., Storger, A. D., & Storger, G. (1955). Untersuchungen über ternäre Chalkogenide. VI. Über Ternäre Chalkogenide des Aluminiums, Galliums und Indiums mit Zink, Cadmium und Quecksilber. *Zeitschrift für Anorganische und Allgemeine Chemie, 279,* 241.
24. Nitsche, R. (1960). The growth of single crystals of binary and ternary chalcogenides by chemical transport reactions. *Journal of Physics and Chemistry of Solids, 17,* 163.
25. Rajpure, K. Y., Lokhande, C. D., & Bhosale, C. H. (1997). A comparative study of concentration effect of complexing agent on the properties of spray deposited Sb_2S_3 thin films and precipitated powders. *Materials Chemistry and Physics, 51,* 252.
26. Rajpure, K. Y., Mathe, V. L., & Bhosale, C. H. (1999). Photoelectrochemical investigation on spray depositedn-$CdIn_2S_4$ thin films. *Bulletin of Material Science, 22,* 927.
27. Nikale, V. M., Shinde, S. S., Bhosale, C. H., & Rajpure, K. Y. (2011). Structural, morphological and electrical properties of spray deposited $CdIn_2Se_4$ thin films. *Journal of Alloys and Compounds, 509,* 3116.
28. Nikale, V. M., Gaikwad, N. S., Rajpure, K. Y., & Bhosale, C. H. (2003). Structural and optical properties of spray-deposited $CdIn_2Se_4$ thin films. *Materials Chemistry and Physics, 78,* 363.
29. Adpakpang, K., Sarakonsri, T., Isoda, S., Shinoda, Y., & Thanachayanont, C. (2010). Synthesis of $CdIn_2Se_4$ compound used as thermoelectric materials via the solution method. *Journal of Alloys and Compounds, 500,* 259.
30. Nikale, V. M., Shinde, S. S., Babar, A. R., Bhosale, C. H., & Rajpure, K. Y. (2011). The n-$CdIn_2Se_4$/p-CdTe heterojunction solar cells. *Solar Energy, 85,* 1336.
31. Bhalerao, A. B., Wagh, B. G., Deshmukh, R. N. P. R., Shim, J.-J., & Lokhande, C. D. (2017). (Photo) electrochemical analysis of electrosynthesized fibrous cadmium indium selenide ($CdIn_2Se_4$) thin films. *Journal of Photochemistry and Photobiology A: Chemistry, 336,* 69.
32. Tenne, R., Mirovsky, Y., Greenstein, Y., & Cahen, D. (1982). Ternary chalcogenide-based photoelectrochemical cells: II . The n-$CdIn_2Se_4$/aqueous polysulfide system. *Journal of the Electrochemical Society, 129,* 1506.
33. Marinelli, M., de Pascale, T. M., Meloni, F., Mula, G., Serra, M., & Baroni, S. (1989). Theoretical study of cubic versus tetragonal structures of defect zinc-blende semiconductors: $CdIn_2Se_4$. *Physical Review B, 40,* 1725.
34. Ruanthon, A.-A., Sarakonsri, T., & Thanachayanont, C. (2009). Preparation of $CdIn_2Se_4$n-type semiconductor sed as thermoelectric material by sol-gel method. *Functional Materials Letters, 2,* 199.
35. Salim, S. M., Kamal, M., Salem, A. M., & Bahr, T. M. (2012). Characteristic behaviour of thermaly evaporated $CdIn_2Se_4$ thin films. *Journal of Applied Sciences Research, 8,* 2670.
36. Sudha, D., Dhanapandian, S., Manoharan, C., & Arunachalam, A. (2016). Structural, morphological and electrical properties of pulsed electrodeposited $CdIn_2Se_4$ thin films. *Results in Physics, 6,* 599.
37. Nikale, V. M., Shinde, S. S., Babar, A. R., Bhosale, C. H., & Rajpure, K. Y. (2011). Photoelectrochemical performance of sprayed n-$CdIn_2Se_4$ photoanodes. *Solar Energy, 85,* 325.
38. Rawat, K., Manisha, C., & Shishodia, P. K. (2016). Investigation of $CuInSe_2$ thin films deposited by laser ablation method. *Emerging Materials Research, 5,* 259.
39. Mahalingam, T., Thanikaikarasan, S., Chandramohan, R., Chung, K., Chu, J. P., Velumani, S., et al. (2010). Electrosynthesis and studies on cadmium-indium-selenide thin films. *Materials Science and Engineering B, 174,* 236.
40. Perna, G., Capozzi, V., Minafra, A., Pallara, M., & Ambrico, M. (2003). Effects of the indium doping on structural and optical propertiesof CdSe thin films deposited by laser ablation technique. *The European Physical Journal B, 32,* 339.

41. Hady, D. A., El-Shazly, A. A., Soliman, H. S., & El-Shazly, E. A. (1999). Electrical properties of $SnSe_2$ thin films. *Vacuum, 52,* 375.
42. Nakanishi, H., Eudo, S., & Trie, T. (1973). Optical Absorption in $CdIn_2S_4$. *Japanese Journal of Applied Physics, 12,* 1646.
43. Fuentes-Cabrera, M., Dong, J., & Sankey, O. F. (2000). Theoretical study of the structural, electronic and vibrational properties of $CdIn_2Te_4$. *Thin Solid Films, 373,* 19.
44. Nakada, T. (2000). Nano-structural investigations on Cd-doping into Cu(In,Ga)Se_2 thin films by chemical bath deposition process. *Thin Solid Films, 361–362,* 346.
45. Krishna, K. M., Sharon, M., Mishra, M. K., & Marathe, V. R. (1996). Selection of optimal mixing ratios to obtain suitable photoelectrodes from mixed semiconductors using band gap calculations. *Electrochimica Acta, 41,* 1999.
46. Kokate, A. V., Suryavanshi, U. B., & Bhosale, C. H. (2006). Structural, compositional, and optical properties of electrochemically deposited stoichiometric CdSe thin films from non-aqueous bath. *Solar Energy, 80,* 156.
47. Abdel-Aal, A. (2007). The optical parameters and photoconductivity of $Cd_xIn_1Se_{9-x}$ chalcogenide thin films. *Physica B, 392,* 180.
48. Neumann, H., Kissinger, W., Lévy, F., Sobotta, H., & Riede, V. (1989). Electrical and infrared optical properties of $CdIn_2S_4$ single crystals grown by chemical transport. *Crystal Research and Technology, 24,* 1165.
49. Guerrero, E., Quintero, M., & Woolley, J. C. (1990). Temperature variation in direct and indirect band gaps of β-$CdIn_2Se_4$. *Journal of Physics: Condensed Matter, 2,* 6119.
50. Hady, D. A., El-Shazly, A. A., Soliman, H. S., & El-Shazly, E. A. (1996). The thermoelectric power, the dark electrical resistivity and the grain boundary potential barrier in $CdIn_2Se_4$ thin films. *Physica A, 226,* 324.
51. Trykozko, R., & Huffman, D. R. (2009). Reflectance and optical constants of $CdIn_2Se_4$ crystals. *Journal of Applied Physics, 52,* 5283.
52. Girija, K., Thirumalairajan, S., & Mohan, S. M. (2009). Deposition and characterization of cadmium indium selenide thin films by chemical bath technique. *Optoelectronics and Advanced Materials, Rapid Communications, 3,* 60.
53. Degdas, G., & Peksoz, A. (2019). Electrodeposition of In:CdSe precursor thin films in aqueous electrolytes including different selenous acid concentrations as Se source. *Materials Science in Semiconductor Processing, 104,* 104655.
54. Reichman, J., & Russak, M. A. (1981). Photo effects a semiconductor electrolyte interface. In A. J. Nozik (Ed.) *ACS Sys* (vol. 146, p. 359).
55. Zhuiykov, S. (2014). *Nanostructured semiconductor oxides for the next generation of electronics and functional devices: Properties and applications* (pp. 1–49). Cambridge: Woodhead Publishing, Elsevier.
56. Luque, A., & Hegedus, S. (2011). *Handbook of photovoltaic science and engineering* (2nd ed.). London: Wiley.
57. Chander, S. (2016). Dissertation, Mohanlal Sukhadia University Udaipur.
58. Chander, S., Purohit, A., Sharma, A., Arvind, S. P., Nehra, & Dhaka, M. S. (2015). Impact of temperature on the performance of series and parallel connected mono-crystalline silicon solar cell. *Energy Reports, 1*, 175.
59. Preston, J. S. (1950). Constitution and mechanism of the selenium rectifier photocell. *Proceedings of the Royal Society, 202,* 449.
60. Kroemer, H. (1957). Quasi-Electric and Quasi-Magnetic Fields in Non-Uniform Semiconductors. *RCA Review, 18,* 332.
61. Kroemer, H. (1957). Theory of a Wide-Gap Emitter for Transistors. *Proceedings of the IRE, 45*, 1535.
62. Tauc, J. (1957). Generation of an emf in semiconductors with nonequilibrium current carrier concentrations. *Reviews of Modern Physics, 29,* 308.
63. Armstrong, H. L. (1958). On junctions between semiconductors having different energy gaps. *Proceedings of the IRE, 46*, 1307 (1958).

64. Chang, P. C., Fan, Z., Chien, C. J., Stichtenoth, D., Ronning, C., & Lu, J. G. (2006). High-performance ZnO nanowire field effect transistors. *Applied Physics Letters, 89,* 133113.
65. Thundat, T. (2008). Flexible approach pays off. *Nature Nanotechnology, 3,* 133.
66. Wu, J. J., & Wong, D. K.-P. (2007). Fabrication and Impedance Analysis of n-ZnO Nanorod/p-Si Heterojunctions to Investigate Carrier Concentrations in Zn/O Source- Ratio-Tuned ZnO Nanorod Arrays. *Advanced Materials, 19,* 2015.
67. Oku, T., Takeda, A., Nagata, A., Noma, T., Suzuki, A., & Kikuchi, K. (2010). Fabrication and characterization of fullerene-based bulk heterojunction solar cells with porphyrin, cuInS_2, diamond and exciton-diffusion blocking layer. *Journal of Energies, 3,* 671.
68. Fan, B., Maniglio, Y., Simeunovic, M., Kuster, S., Geiger, T., Hany, R., et al. (2009). Squaraine planar-heterojunction solar cells. *International Journal of Photoenergy, 2009,* 1.
69. Chander, S., Purohit, A., Nehra, A., Nehra, S. P., & Dhaka, M. S. (2015). A study on spectral response and external quantum efficiency of monocrystalline silicon solar cell. *International Journal of Renewable Energy Research, 5,* 41.
70. Chander, S., Purohit, A., Sharma, A., Nehra, S. P., Dhaka, M. S. (2015). A study on the photovoltaic parameters of mono-crystalline Silicon solar cell with cell temperature. *Energy Reports, 1*, 104.
71. Chander, S., & Dhaka, M. S. (2016). Optimization of structural, optical and electrical properties of CdZnTe thin films with the application of thermal treatment. *Materials Letters, 182,* 98.
72. Chander, S., & Dhaka, M. S. (2016). Impact of thermal annealing on physical properties of vacuum evaporated polycrystalline CdTe thin films for solar cell applications. *Physica E: Low-dimensional Systems and Nanostructures, 80,* 62.
73. Chander, S., & Dhaka, M. S. (2017). Time evolution to $CdCl_2$ treatment on Cd-based solar cell devices fabricated by vapor evaporation. *Solar Energy, 150,* 577.
74. Chander, S., Purohit, A., Patel, S. L., & Dhaka, M. S. (2017). Effect of substrates on structural, optical, electrical and morphological properties of evaporated polycrystalline CdZnTe thin films. *Physica E: Low-dimensional Systems and Nanostructures, 89,* 29.
75. Chander, S., & Dhaka, M. S. (2017). Enhanced structural, electrical and optical properties of evaporated CdZnTe thin films deposited on different substrates. *Materials Letters, 186,* 45.
76. Chander, S., & Dhaka, M. S. (2018). Enhancement in microstructural and optoelectrical properties of thermally evaporated CdTe films for solar cells. *Results in Physics, 8,* 1131.
77. Matsuura, J., Khatri, I., Lin, T.-Y., Sugiyama, M., & Nakada, T. (2019). Impact of heat-light soaking and heat-bias soaking on NaF-treated CIGS thin film solar cells. *Progress in Photovoltaics: Research and Applications, 27,* 623.
78. Chander, S., & Dhaka, M. S. (2019). Exploration of CdMnTe thin film solar cells. *Solar Energy, 183,* 544.
79. Yan, C., Huang, J., Sun, K., Johnston, S., Zhang, Y., Sun, H., et al. (2018). Cu_2ZnSnS_4 solar cells with over 10% power conversion efficiency enabled by heterojunction heat treatment. *Nature Energy, 3,* 764.

Cadmium Sulfide Thin Films by Chemical Bath Deposition Technique

M. S. Aida and S. Hariech

Abstract In this chapter, we describe the usefulness of chemical bath deposition (CBD) technique to produce high-quality thin films of cadmium sulfide for large-scale applications. In terms of operation, CBD offers unique blend of cost-effectiveness and rapid deposition rate of thin films with controlled morphology and crystallite size. Compared to other expensive thin films deposition techniques, this strategy involves the use of low-cost precursors, solvents and ambient conditions or mild temperature (up to 70 °C). Here, we explain the fundamentals of CBD with emphasis on growth mechanisms in CBD and influence of key parameters like temperature, reaction time, substrates type, and solvent to grow high conformal thin films for technological grade.

Keywords Thin films · Cadmium sulfide · Chemical bath deposition · Films growth mechanism · Semiconductors

1 $B^{II}A^{VI}$ Semiconductors and Metal Chalcogenides

$B^{II}A^{VI}$ semiconductors are chemical compounds composed of two elements, where B is an element of group II of the periodic table such as zinc, cadmium, and mercury and A is an element of group VI: sulfur, oxygen, tellure, and selenium. Hence, the formed binary compounds can be: oxides (ZnO, CdO), selenides (ZnSe, CdSe, HgSe), sulfides (CdS, ZnS, HgS), and tellurides (ZnTe, CdTe, HgTe) [1]. This type of semiconductors materials are also called metallic chalcogenides; their optical,

M. S. Aida (✉)
Department of Physics, Faculty of Science, King Abdulaziz University, Djeddah, Kingdom of Saudi Arabia
e-mail: aida_salah2@yahoo.fr

Center of Nanotechnology, King Abdulaziz University, Djeddah, Kingdom of Saudi Arabia

S. Hariech
Department of Physics, Faculty of Science, University Frères Mentouri Constantine 1, Constantine, Algeria

S. J. Ikhmayies (ed.), *Advances in Energy Materials*,
Advances in Material Research and Technology,
https://doi.org/10.1007/978-3-030-50108-2_3

electrical, and magnetic properties have been intensively studied [1]. Metal chalcogenides semiconductors, with wide optical gap, are of considerable technological interest because their emissions cover the blue and green spectral regions. They found particularly several applications such as optoelectronic devices, lasers and detectors, light emitting diodes (LEDs), nonlinear optical materials, optical fibers, thermal imaging, radiation detectors, third-generation photovoltaic cells, magneto-optical devices, and materials for magnetic storage of information [2–7].

1.1 Metal Sulfides and Cadmium Sulfide (CdS)

The existence of metal sulfides has long been known; since miners have always observed sulfur as the mineralizer of metals. For a long time, chemists have directed their researches in the field of mineralogy as well as that of chemistry. They attempt to reproduce the different minerals in laboratories. Sulfur possesses the property to combine directly with almost all metals. Quite often, the combination takes place with mostly alkali metals, zinc, lead, copper, etc. because of the high affinity between sulfur and these metals [8]. CdS is an interesting semiconductor; it found a wide range of applications in photovoltaics, optoelectronics, catalysis, and biological sensors [9]. CdS possesses excellent structural and optical properties allowing it to be a good candidate as a buffer layer in CdS/$CuInSe_2$ [10], CdS/CdTe [11], CdS/CIGS [12], CdS/CuS [13] and recently in Cu_2ZnSnS_4/CdS thin film solar cells [14], optical filters, gas sensors, [15] thin films transistors [16], semiconductor lasers [17], and photoelectrochemical cells [18]. Various techniques have traditionally been adopted to prepare high quality of metal chalcogenides thin films, each technique has its own limits. For example, solid-state reactions occur only at high temperatures to transition into molten states of solid reagents. However, techniques such as spray pyrolysis, vapor deposition, and vacuum evaporation require high temperatures to allow chalcogenides formation, and in contrast, the chemical methods such as hydrothermal deposition, solvothermic, and chemical bath (CBD) can be used at lower temperatures.

1.2 Chemical Bath Deposition Technique

Thin films chemical bath deposition (CBD) is a very old technique, also called solution growth technique. In 1835, Liebig presented the first report of deposition of silver using this method [19, 20]. Earlier, CBD has been limited to the deposition of lead compounds PbS and PbSe [21]; a wide range of substrates have been successfully used for these deposits; namely porcelain, ebonite, iron, steel … etc. [22]. The range of metal chalcogenide films deposited by CBD has been gradually developed, particularly in the 1980s. In 1982, there were approximately twenty metal chalcogenide, which can be synthesized by this technique. Nowadays, it exceeds 50, mostly

are semiconductors [23]. The reason for this increasing interest is due to the benefits of the attractive CBD technique. After the success of chemical bath CdS films deposition on CdTe (and later on $CuInSe_2$ films) to produce more efficient photovoltaic (PV) cells by comparing to CdS films obtained by thermal evaporation [24–27], CdS become the most studied material prepared by this technique [21].

The first CdS layer deposited by CBD and used in photovoltaic cells was achieved by Birkmire et al. [28] reported that CdS film obtained by CBD leads to 10.6% $CuInSe_2$ based solar cells efficiency which is larger than that of (Cd, Zn) S prepared by evaporation. The reached efficiency record of $CuInSe_2$ cells using CdS prepared by CBD is of 19.8% [29].

CBD technique enjoys several advantages:

- It is relatively simple and safe [30] due to the application over a wide range of easy chalcogenide compounds preparation.
- The flexibility in the substrate choice.
- It is a useful and excellent technique for nanomaterial preparations such as polycrystalline CdS films for optimal photovoltaic devices [24–26].
- It allows the deposition of homogeneous, adherent, and reproducible thin films over a large surface [31].
- It is carried out at low temperatures as well as at relatively high temperatures.
- It is a slow process, in which the reaction time required is sometimes several hours or even tens of hours [32]. This may favor the crystallites size and orientation control [33].

1.3 Chemical Bath Deposition Mechanisms

Chemical deposition of films on solid substrate is achieved by means of reactions occurring in an aqueous solution. It is based on the chemical transformation of precursor through species exchange. If the exchanged species are electrons, the deposition technique is called CBD redox or "electroless deposition." While, if the exchanged species are chemical elements, the technique is called CBD. During CBD deposition, substrates are immersed in diluted solutions containing metal ions (M^{n+}) and a source of chalcogenide (C^{m-}) such as sulfur S^{2-}. The concept of the solubility product (Ksp) is introduced for understanding the CBD deposition mechanisms. The solubility product informs about the salt solubility. Consider a soluble salt (CdS for example) in equilibrium with its saturated aqueous solution:

$$CdS(s) \rightarrow Cd^{2+} + S^{2-} \tag{1}$$

where subscript s represents the solid phase. The CdS dissolves in water producing a few amount of Cd and S ions. The solubility product (Ksp) is the concentrations product of the dissolved ions as defined by the following equation:

$$Ksp = \left[Cd^{2+}\right]\left[S^{2-}\right] \tag{2}$$

Table 1 Solubility products of different compound (at 25 °C) used in CBD deposition

Solid	Ksp	Solid	Ksp
Ag2S	3×10^{-50}	FeS	10^{-18}
AgCl	2×10^{-10}	HgS	6×10^{-35}
AgI	10^{-6}	PbS	10^{-28}
$Cd(OH)_2$	2×10^{-14}	PbSe	10^{-37}
CdS	10^{-28}	SnS	10^{-26}
CdSe	4×10^{-35}	SnS_2	6×10^{-57}
CdTe	10^{-42}	SnSe	5×10^{-34}
Cu_2S	10^{-48}	$Zn(OH)_2$	10^{-16}
CuS	5×10^{-36}	ZnS	3×10^{-25}
$Fe(OH)_2$	5×10^{-17}	ZnSe	10^{-27}

more generally, for the dissolution:

$$MaXb \rightarrow aM^{n+} + bX^{m-} \tag{3}$$

The solubility product of $Ksp = [M^{n+}]^a[X^{m-}]^b$.

The more soluble is the salt, the greater is the solubility product Ksp.

A list of approximate values of Ksp for some semiconductors and related salts encountered in CBD is given in Table 1.

When ions concentrations product exceeds the solubility product Ksp, two events may happen:

- Formation of a precipitate (powder) in the solution. This process is called homogeneous deposition
- Formation of a deposit on solid surface (substrate or the vessel walls). This process is called heterogeneous process. Generally, both processes are concurrent and may be present in the same time but with different rates.

1.3.1 Homogeneous Nucleation

The first stage of powder formation is the individual ions or molecules contact and collision to aggregate and form embryos by coalescence. They are subsequently enlarged by coalescence to form a stable nuclei as shown in Fig. 1.

1.3.2 Heterogeneous Nucleation

In heterogeneous nucleation, the nucleation step is achieved on the solid substrate through embryon ions adsorption onto the substrate. Any substrate immersed in the solution acts as a nucleation center. Generally in a alkaline aqueous solution

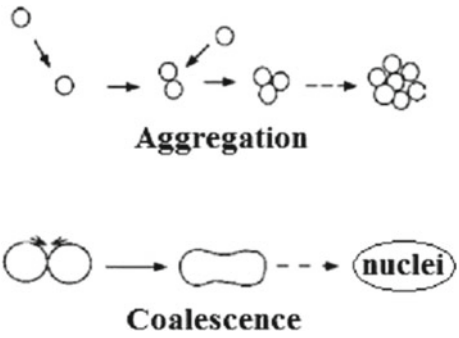

Fig. 1 Particles aggregation and coalescence in solution

commonly used in CBD technique, the metallic ion forms a hydroxide precipitation $Cd(OH)_2$ rather than film formation. To prevent this homogeneous precipitation, the Cd complexation is necessary. Ammonium hydroxide is a commonly used complexant agent. $Cd(NH_3)_4{}^{2+}$ complex is formed according to the reaction:

$$Cd^{2+} + 4NH_3 \rightarrow Cd(NH_3)_4{}^{2+} \tag{4}$$

Films formation on the substrate is based on the chalcogenic ions slow release in the solution, where free metal ions are complexed. The complexing agent should not be too weak to prevent solution precipitation of the hydroxide and not too strong to prevent the film from being deposited. Thereafter, the amount of ammonia to add depends on Cd concentration, solution temperature, and pH [20].

The CBD mechanisms can be achieved through two different processes:

- The compound formation through ionic reactions involving free anions (ion-by-ion mechanism)
- Decomposition of metal complexes (cluster-by-cluster mechanism).

These mechanisms are often unclear due to their complexity and their simultaneous occurring.

1.4 Ion-by-Ion Mechanism

This mechanism is the simplest one, when the ion product $[Cd^{2+}][S^{2-}]$ exceeds 10^{-28} the solubility product of CdS [19], consequently a solid phase of CdS will be formed. The film growth occurs through sequential ionic reactions as follow:

$$Cd(NH_3)_4{}^{2+} \rightarrow Cd^{2+} + 4NH_3 \left(\text{dissociation of complex to free } Cd^{2+} \text{ ions}\right) \tag{5}$$

$$(NH_2)_2CS + 2OH^- \rightarrow S^{2-} + CN_2H_2 + 2H_2O \left(\text{formation of sulphide } S^{2-} \text{ ion}\right) \tag{6}$$

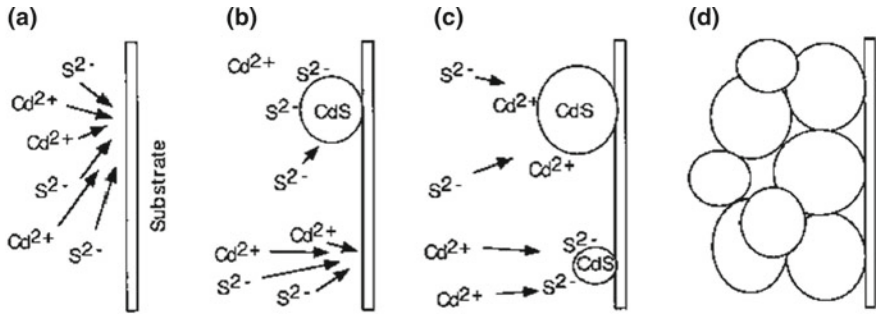

Fig. 2 Schematic drawn of the deposition steps involved in ion-by-ion deposition process

$$Cd^{2-} + S^{2-} \rightarrow CdS \text{ (CdS formation by ionic reaction)} \quad (7)$$

A complex is generally necessary to maintain constant metallic ions concentration in the solution and to avoid the hydroxide precipitating. In this situation, the presence of any solid surface (i.e., substrate, vessel walls) acts as nucleation center.

The adhesion and attraction of species on the substrate is achieved by the Van der Waals force. Once the nucleation step starts on a substrate, the film growth becomes easier, since deposition is easier on a covered surface than on a clean one. Films growth by this process proceeds as follow (see Fig. 2):

A: Cd and S ions diffusion toward the substrate.
B: Nucleation of CdS facilitated by the substrate.
C: Formation of CdS nuclei by adsorption of Cd and S ions incoming from the solution.
D: Subsequent growth of CdS.

1.5 Cluster-by-Cluster Mechanism

If the complexing agent concentration is low to prevent metal hydroxide formation, small amount of $Cd(OH)_2$ can be formed in a colloidal form. The metal hydroxide $Cd(OH)_2$ plays an important reaction intermediates during CBD process. CdS film is then formed by reactions:

$$nCd^{2+} + 2nOH^{-} \rightarrow \left[Cd(OH)_2\right]_n \text{ (formation of } Cd(OH)_2 \text{ cluster)} \quad (8)$$

$$\left[Cd(OH)_2\right]n + nS^{2-} \rightarrow nCdS + 2nOH^{-} \text{ (exchange reaction)} \quad (9)$$

CdS is formed because its precipitation constant Ksp is 10^{-28} is too low by comparison to that of $Cd(OH)_2$ (2×10^{-14}). Moreover, this is due to the free formation energy of CdS that is more negative than that of $Cd(OH)_2$. Thereafter, CdS formation

occurs preferentially on the hydroxide surface rather than to nucleate separately in the solution. Then CdS is homogeneously formed and precipitates in the solution. The film deposition passes first by the hydroxide adhesion on the substrate. Then the hydroxide conversion into CdS forming a primary CdS clusters deposition.

The films are formed via cluster-by-cluster process according the following steps (as depicted in Fig. 3):

A: Hydroxide colloidal particles diffusion to the substrate, where they adhere.
B-C: Reaction with S ions. This reaction results in exchange of the hydroxide by sulfide. This reaction occurs simultaneously on the surface-adsorbed colloids and on the dispersed ones in the solution. The reaction will continue until the total conversion of the hydroxide to sulfide.
D: The primary CdS particles aggregate to form a solid film.

Since in cluster-by-cluster process, films are formed through the colloids, incoming from the solution, sticking on the substrate, the crystallite size cannot vary too much with the film thicknesses. While in the case of ion-by-ion growth process, since the crystal growth occurs through the nucleation on the substrate, the crystal size may increase with increasing deposition time. It is possible that the mechanism may change during the deposition, or both mechanisms occur in parallel.

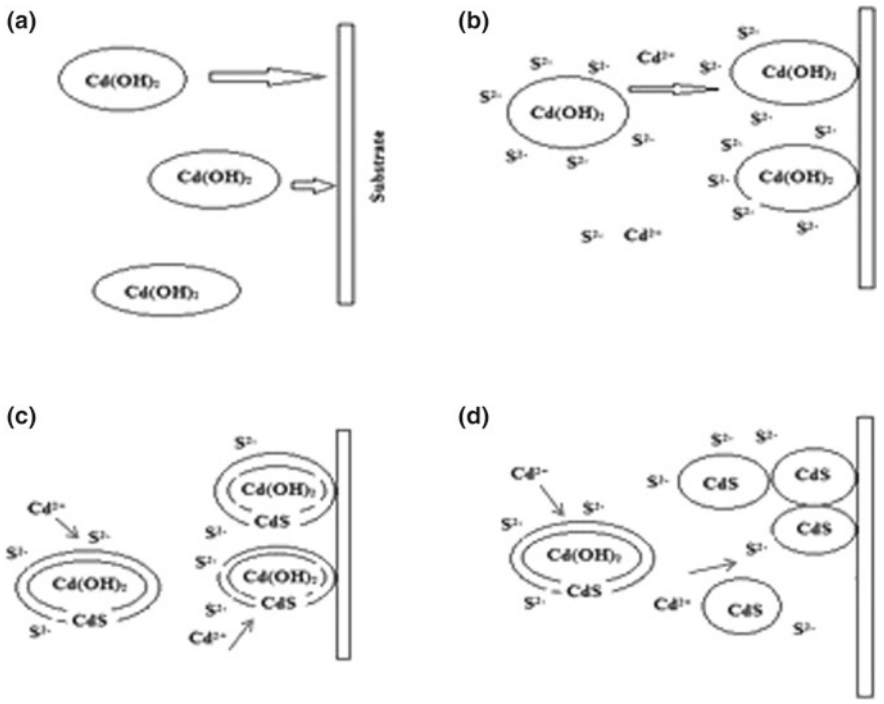

Fig. 3 Schematic diagram of the different steps involved during the cluster-by-cluster deposition mechanism

2 CdS Thin Film Deposition

In this chapter, we focused on the growth mechanism of CdS thin films by chemical bath deposition. Figure 4 depicted a schematic schema of the experimental setup used for CdS thin films deposition. The different processes are regrouped in Fig. 4.

2.1 Deposition Kinetics

The CdS deposition rate variation has been extensively studied, by several authors, as a function of different deposition parameters such as: bath temperature [34], deposition time [34], pH of the solution [35] and thiourea [36] or cadmium concentrations [37]. Due to the different processes occurring during CBD thin film formation, the growth kinetics may widely vary from one deposition condition to another.

Generally, films kinetic growth passes by three periods (as shown in Fig. 5):

- Induction (or incubation) time at the early stage of the process, where no clearly deposit is detectable. This time corresponds to the chalcogenide concentration rising.
- Linear growth. The deposition starts only when the chalcogenide CdS concentration is high enough to permit the nucleation and the subsequent growth. Some studies [38, 39] suggested that, during this step, the chemical process is the rate-limiting growth rather than the diffusion process.

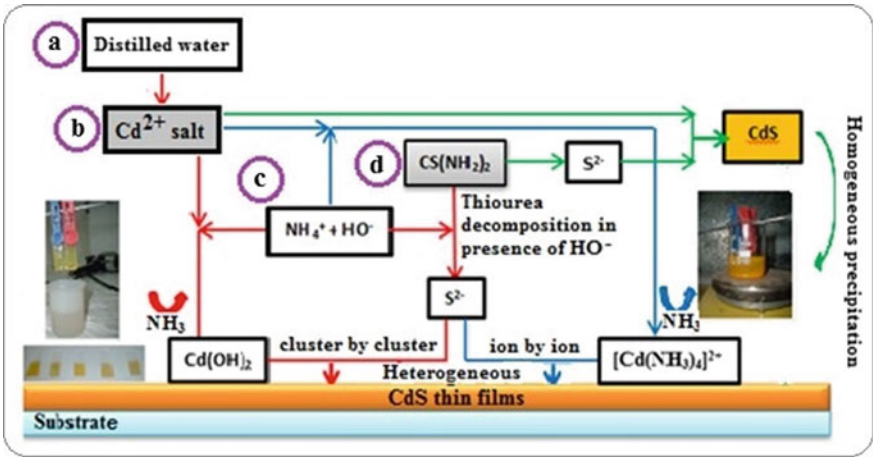

Fig. 4 Diagram of the CBD process. CdS film is formed by a mechanism ion by ion (blue) or a cluster by cluster (red) or both simultaneously. Homogeneous precipitation in solution (green) and heterogeneous precipitation on the substrate (blue and red).

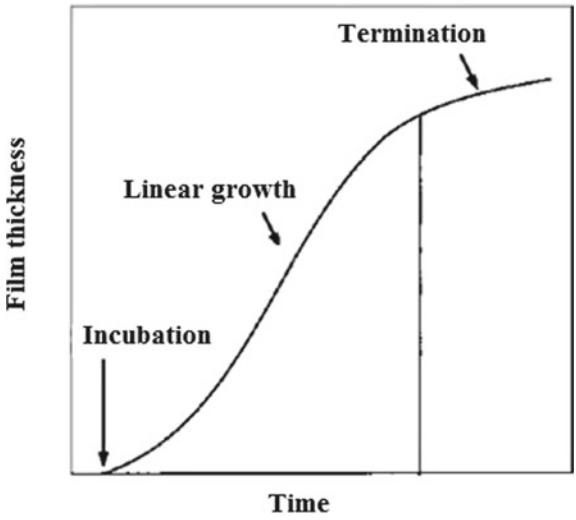

Fig. 5 Variation of film thickness as a function of deposition time using CBD technique

- Termination. During this step, the growth slows down and may stop due to the reactants consumption. The terminal film thickness depends on the deposition parameters.

2.2 Influence of Solution Temperature

The whole investigated temperature range in CdS deposition by CBD technique is ranged between 50 and 90 °C. Lower temperatures do not promote the chemical reactions necessary for film formation, while higher temperatures cause the solution evaporation especially the ammonia generally used as complexing agent. As shown Fig. 6, CdS film thickness and the deposition rate are sensitive to the solution bath temperature. The temperature influence can be divided, at least, in three regions:

- Region I: Low temperatures range (<65 °C): In this range, the deposition rate increases linearly as a function of the temperature bath. This is due to the thermal activation of chemical reaction between species, contributing in films formation. The bath temperature may motivate, the thiourea decomposition, which is responsible for sulfur chalcogenide ion (S^{2-}) production:

$$SC(NH_2)_2 + 2HO^- \rightarrow S^{2-} + CH_2N_2 + 2H_2O \quad (10)$$

and on the other hand, it releases metal ions (Cd^{2+}) by dissociation of complexing compound $Cd(NH_3)_4{}^{2+}$ according to the following equation:

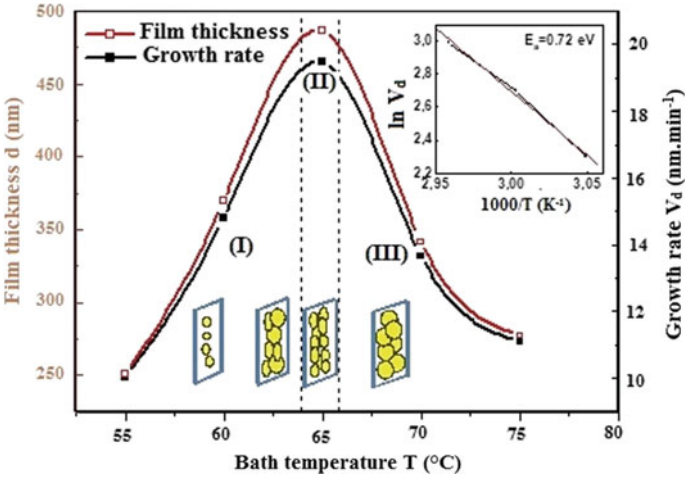

Fig. 6 Variations of CdS thin films thickness and growth rate as a function of bath temperatures

$$Cd(NH_3)_4{}^{2+} \rightarrow Cd^{2+} + 4NH_3 \tag{11}$$

The formation of this compound is an intermediate reaction, necessary to control (Cd^{2+}) ions hydrolysis:

$$NH_4{}^{+} + HO^{-} \rightarrow NH_3 + H_2O \tag{12}$$

$$CdSO_4 \rightarrow Cd^{2+} + SO_4{}^{2-} \tag{13}$$

$$Cd^{2+} + 4NH_3 \rightarrow \left[Cd(NH_3)_4\right]^{2+} \tag{14}$$

Consequently, the obtained free ions Cd^{2+} and S^{2-} react between them by ionic reaction (mechanism ion by ion) to form CdS film:

$$Cd^{2+} + S^{2-} \rightarrow CdS \tag{15}$$

The calculated activation energy of film growth (insert Fig. 2), in this temperature range, is equal to 0.72 eV (~71 kJ/mol), which is close to the formation enthalpy 74.2 kcal/mol of Cd^{2+} [30]. This may suggest that Cd^{2+} ions formation controls the films growth. This comforts the fact that ammonia complexing agent is required for Cd^{2+} ions slow release necessary for films growth control. In this temperature range, the films growth is governed by ion-by-ion process. However, increasing the bath temperature from 55 to 65 °C enhances the thiourea decomposition and Cd^{2+} ions release. This leads to the free ions (Cd^{2+} and S^{2-}) concentrations increase in the bath, which leads to the growth rate increasing.

- Region II (saturation): At 65 °C, the growth rate reaches its saturation due to the fast and complete decomposition of thiourea and cadmium sulfate. The temperature of 65 °C can be considered as the critical temperature corresponding to the appearance of a mixed growth mode where both ion-by-ion and cluster-by-cluster mechanisms contribute in the films formation.
- Region III: (T > 65 °C): At this temperatures range, a fast formation of CdS clusters is observed on the substrate surface as well as in the solution. Once the reactants are depleted, the growth rate is reduced and stops. The films growth, in this temperature range, is achieved through the cluster-by-cluster mechanism. The film formation passes, at the beginning by an intermediate phase $Cd(OH)_2$ production originating from the ammonium hydroxide dissolution according to the following reactions:

$$nCd^{2+} + 2nHO^{-} \rightarrow \left[Cd(OH)_2\right]_n \tag{16}$$

and then by the replacement of HO^{-} by S^{2-} to form at the end the CdS deposit:

$$\left[Cd(OH)_2\right]_n + nS^{2-} \rightarrow nCdS + 2nHO^{-} \tag{17}$$

Increasing the temperature from 65 to 75 °C yields to the growth rate reduction (Fig. 2). This is due to the reactants depletion in the solution due to their consumption. In fact, at very high temperatures (>65 °C), ammonia (NH_3) starts to be evaporated during chemical reactions. The presence of NH_3 in the bath is essential chemical reactions controlling in one hand for colloids creation in the solution prevention on the other hand. Moreover, the evaporation of NH_3 and therefore HO^{-} formation in the solution suggests that film growth is controlled by cluster as a dominant mechanism. Moreover, the reduction of growth rate and film thickness may have other origins such as:

- Dissolution of unstable nuclei adsorbed on film surface,
- Film peeling due to its thickness increase.

This variation shape is an intrinsic characteristic of CBD technique, by comparison to other thin films deposition techniques of [19]. It is well argued that higher deposition rates and higher thicknesses are usually accompanied by powder formation [40].

2.3 Influence of Salt Molarity

CdS film growth is also sensible to the molarity of cadmium source. As reported in Fig. 7 showing, the deposition rate variation as a function of Cd source molarity in this example $CdCl_2$ is the source of Cd. Increasing of $CdCl_2$ molarity causes the

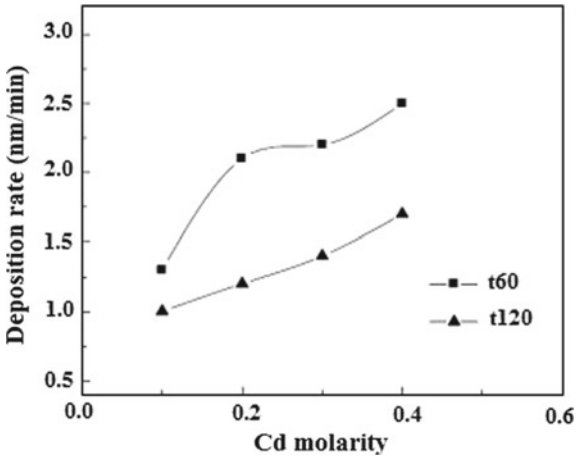

Fig. 7 Variation of the deposition rate as a function of Cd salt molarity for two deposition times

increase of the Cd concentration, which yields growth rate enhancement. Sasikala et al. [41] have deposited CdS thin films using $CdCl_2$ as source of Cd by varying the molarity from 0.1 to 1 M and noticed deposition rate enhancement with the Cd concentration.

2.4 Influence of Cd Salt Source

In CBD deposition, several Cd salts have been used. As can be seen in Fig. 8, the deposition rate is Cd salt dependent. The deposition rate increases with changing the CdS salt nature in the following order $CdCl_2$, $CdSO_4$, $Cd(CO_3)$, and $Cd(CH_3COO)_2$. Few

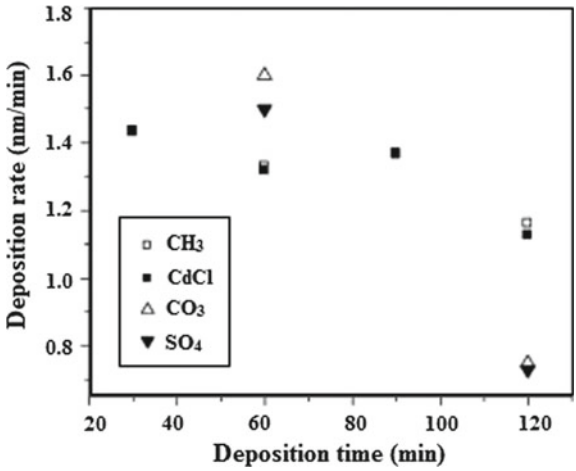

Fig. 8 Variation of CdS films deposition rate as a function of time for different Cd salt sources

Table 2 Stability coefficient of complex formed with different Cd salt source

Salt complex	Stability constant (log scale)
$Cd[SO_4]_3^{4-}$	2
$Cd[CH_3COO]_2$	2.19
$Cd[Cl]_4^{2-}$	2.93
$Cd[I]_4^{2-}$	6.4
$Cd[NH3]_4^{2+}$	7

studies have been devoted to the influence of the Cd salt on CdS thin film properties [42–44]. Khallaf et al. [43] have grown CdS film with four different sources. In their study, they used several Cd salt sources with lower molarity of 0.2 mM, ammonia as complexing agent and solution temperature equals to 70 °C. They ranked, from the lowest to the highest achieved films' thickness, the CdS salts in the following order: CdI_2, $CdCl_2$, $Cd(CH_3COO)_2$, and $Cd(SO_4)$ (Table 2).

The influence of the salt nature on the deposition rate can be explained by considering the stability of Cd complex for each salt. In Table 1, we have reported the stability of some Cd complexes formed in the salt bath during CBD deposition. The rank of complex stability is as following CdI_2, $CdCl_2$, $Cd(CH_3COO)_2$, $CdSO_4$ [43]. This is in the same order as the thickness of the deposited CdS films. The most stable salt releases much slowly Cd ions to contribute in film formation and consequently lower deposition rate.

3 Films Structure and Morphology

3.1 Structural Properties

From structural point of view, the most interesting feature in CdS thin films deposited by CBD is their polymorphism. CdS structure can be either hexagonal (Wurtzite: α-CdS phase), cubic (sphalerite or zinc blende: β-CdS phase), or mixed phase. The distinction between these two phases is difficult; this is due to the fact that several planes in both phases have the same diffraction angle. For example: the (111) in the cubic phase and the (002) plane in the hexagonal one diffract at the same angle 26.6°. Moreover, (110) plane in the hexagonal structure and (220) in the cubic one diffract at the same angle 43.8°. The (004) plane in hexagonal phase and the (222) in cubic phase have the same 53.78° diffraction angle. CdS wurtzite structure is the same as that of ZnO material (Fig. 9). Each elementary cell has two CdS molecules, the two Cd atoms occupy positions (0, 0, 0); (1/3, 2/3, 1/2), and the two S atoms occupy positions (0, 0, 4); (1/3, 2/3, 1/(1 + u)) with $u \approx 3/8$ [35].

In the case of the cubic structure (Zinc blend) (Fig. 10), each elementary cell contains four CdS molecules, whose atoms occupy well-defined positions defined by coordinates: 4 S atoms in positions: (0, 0, 0); (0, ½, ½); (½, 0, ½); (½, ½, 0); 4

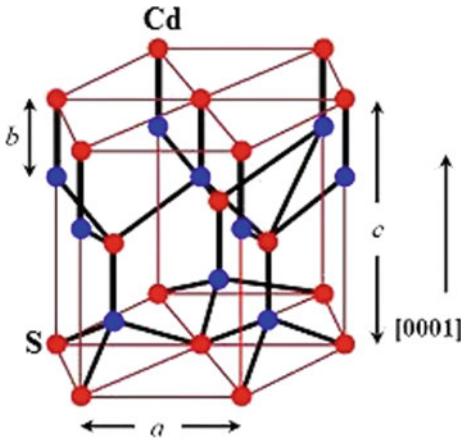

Fig. 9 Structure of CdS (Wurtzite) crystal

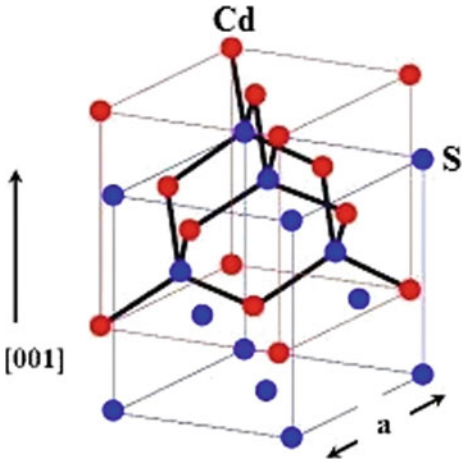

Fig. 10 Zinc blend structure of CdS crystal

Cd atoms in positions: (¼, ¼, ¼); (¼, ¾, ¾); (¾, ¼, ¾); (¾, ¾, ¼). In this structure, each atom Cd has four neighbors S occupying the vertices of a regular tetrahedron.

Certain $B^{II}A^{VI}$ compounds are transformed under the action of high external pressures into the rock salt structure (NaCl), characterized by an octahedral arrangement of the atoms, and although these phases are unstable under normal conditions, they can sometimes remain at low temperatures [45, 46]. On the other hand, under a pressure of 2.6–4.2 GPa, the hexagonal structure is transformed into a rock salt structure. At a higher pressure of 60–86 GPa, the rock salt structure is transformed into a distorted cubic structure of the rock salt [46].

The values of the parameters of CdS network are summarized in the following Table 3.

Table 3 Crystallographic parameters of different crystalline structures of CdS

Compound	Crystalline structure	Network parameters (Å)	Ref.
CdS	Wurtzite (α-CdS)	$a = 4.16$ and $c = 6.75$	[35]
	Zinc blend (β-CdS)	$a = 5.83$	
	Rock salt	$a = 5.32$	
	Distorted rock salt	$a = 3.471$, $b = 4.87$ and $c = 3.399$	

Table 4 Crystallographic structure, grain size, and preferential orientation of CdS thin films produced by different techniques

Technique	Parameters studied	Structure	D (nm)	(hkl)
RF magnetron sputtering	Power (60–120 W)	Hexagonal	–	(002)
	Power RF 75–150 W	Mixed C/H at low pressure	–	C(111)/H(002)
	Substrate temperature: 100–250 °C	Hexagonal at high pressure (150 W)	–	
	Annealing	Hexagonal	–	(002)
Thermal evaporation	Deposition time	Hexagonal	54–62	(002)
		Hexagonal	25	(002)
PLD	Doping par C	Hexagonal	52–72	(002)
ED		Hexagonal	13–25	(002)
Spray	Substrate temperature	Mixte à basse T	10–33	C(111)/H(101)(002)
		Hexagonal with the increase of T	15–30	(101)
CBD	Deposition time	Cubic	26–34	(111)
	Cadmium concentration	Hexagonal	10–12	(002)
	Complexing agent NTA	Hexagonal	–	(002)
	Solution temperature	Cubic	170	(111)
	Substrate nature	Mixed hexagonal/cubic	50–300	(002)/(111)
	Cadmium source	Mixed hexagonal/cubic	–	(002)/(111)

D Grain size, *hkl* Miller indices for the preferential orientation, *PLD* Pulsed laser deposition, *ED* Electrodeposition

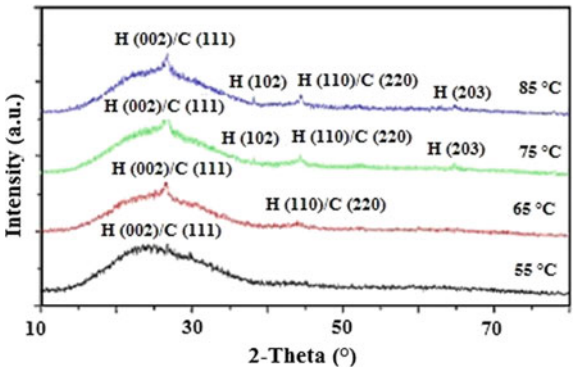

Fig. 11 XRD spectra of CdS films deposited by CBD: at different temperatures. Reprinted with permission from [47]. Copyright © 2007 Elsevier B.V.

Table 4 summarizes the crystalline structure, grain size, and preferential orientation reported in the literature of CdS films deposited by different deposition techniques. In general, the binding in compounds II-VI is ionic as well as covalent but is only ionic in those that have the structure of rock salt.

The crystal structure and physical properties of CdS thin films are sensitive to the method and deposition conditions. Among all these structures of CdS, the hexagonal is the most thermodynamically stable and thus the most common observed. Due to its metastable character, the cubic phase can be transformed into hexagonal under the effect of annealing temperature.

Several studies have confirmed the deposition parameters influence on the structure of CdS films deposited by CBD technique. These include bath temperature, time, the nature and concentrations of the source solutions, the pH of the bath, the nature of the substrate, and sometimes the agitation of the solution [45]. However, at low temperature, CdS films are amorphous with a low crystallinity (hexagonal and/or cubic) which can be improved with increasing temperature or prolonging the deposition time, as shown in Fig. 11 [47]. The increase in temperature also favors the transformation of the cubic structure to the hexagonal one.

The nature of both used cadmium source and complexing agent can be decisive for the structure of the future film [45]. Table 5 reports the influence of Cd source nature on the structure of the deposited CdS films by CBD at various temperatures and baths.

Also, Table 6 shows the influence of used complexing agent on CdS films structure.

Saxena et al. [48] found that the crystal structure is cubic for all CdS films elaborated by CBD whatever the nature of Cd source precursor used in the bath. This was confirmed by their DRX results shown in Fig. 12, which indicates that all films deposited from different source solutions are polycrystalline with an orientation preferential according to the plane (111) where the degree of texturing increases in this order: $CdCl_2$, CdI_2, Cd $(CH_3COO)_2$, $CdSO_4$. It is worth noting that the nature of the substrate and the deposition conditions change the structure as well as the crystallographic orientation of the film.

Table 5 Influence of parameters: Cd source nature, pH values, and bath temperature on the structure crystalline CdS

Cd source	Precursors solution	Bath pH	Deposition temperature T (°C)	Structure crystalline
$CdCl_2$ $CdAc_2$[a]	$NH_4OH/NH_4Cl/Tu$[b]	11	80	Hexagonal amorphe
$CdCl_2$	$NH_4OH/NH_4Cl/Tu$	11.5	>40	Cubic
CdI_2	$NH_4OH/NH_4I/Tu$	–	>60	Hexagonal
$CdSO_4$	NH_4OH/Tu	–	60–85	Hexagonal
$CdSO_4$	$NH_4OH/N_2H_4/Tu$	–	60	Mixed
$CdSO_4$	NH_4OH/Tu	11–12	70	–
$CdAc_2$	$NH_4OH/NH_4Ac/Tu$	–	85	–
$CdAc_2$	$NH_4OH/NH_4Ac/Tu$	9	50–90	Mixed
$CdAc_2$	TEA + NH_4OH/Tu	–	30–85	–
$CdAc_2$	$Na_3C_6H_5O_7/NH_4OH/Tu$	–	50–90	–
$Cd(NO_3)_2$	$NH_4NO_3/NaOH/Tu$	7.8–13.5	20	Cubic

[a]*Ac* Acetate $(CH_3COO)^-$, [b]*Tu* Thiourea $SC(NH_2)_2$, *TEA* Triethanolamine

Table 6 Influence of the nature of Cd complex on the crystal structure of CdS films

Nature of Cd complex	Structure	Refs.
Halide, citrate	Hexagonal	[48]
Nitrate	Hexagonal	[50, 51]
Sulfate, acetate, chlorure, ammonium salt	Cubic	[48]
Triethanolamine	Mixed structure	[48]

Figure 13 represents the XRD diffraction patterns variation as function of deposition time. The absence of peaks in the spectra of film deposited at low time suggests that the deposited films in early stage are amorphous. Increasing deposition time leads to a peak emergence at 28.2° assigned to the (101) plane of the hexagonal structure. Further increase in the deposition time rends the peak assigned to the plane (101), sharper and intense. Moreover, increasing the deposition time engenders the emergence of a peak located at 58.2° originating from (202) diffraction plane in the hexagonal structure. The preferential orientation in CdS is controlled by the nucleation process associated to the low deposition rate [49, 50]. It is reported that (002) and (111) planes are the generally observed preferential orientations in the hexagonal and the cubic structure, respectively [30, 51], in CBD deposited CdS thin films when using ammonia as complexing agent. While, in spray pyrolysis deposited CdS films hexagonal (101) preferential orientation has been reported [52, 53]. The grain sizes, calculated from XRD diffraction analysis, were 26 nm in films deposited during 60 min and 40 nm in films deposited during 120 min.

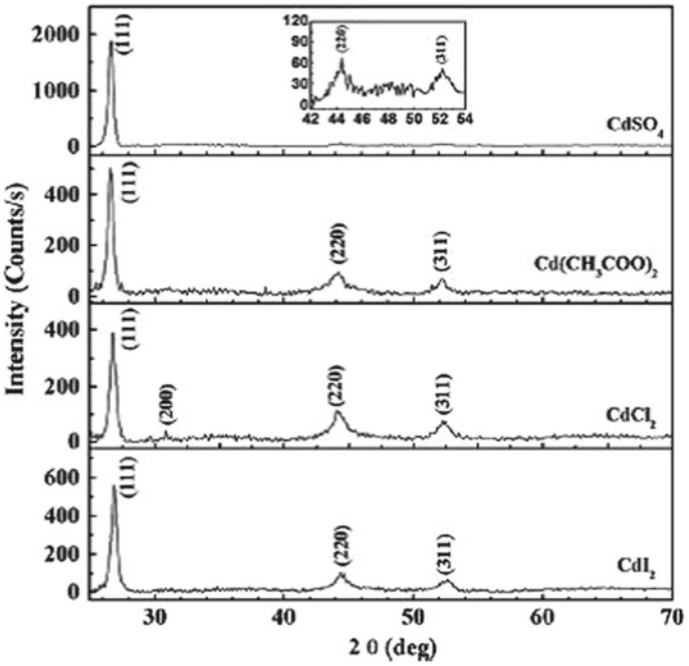

Fig. 12 XRD spectra of CdS films deposited using four different Cd source solutions. Reprinted with permission from [43]. Copyright © 2009 Elsevier B.V.

Fig. 13 XRD diffraction patterns of CdS films prepared with different deposition times

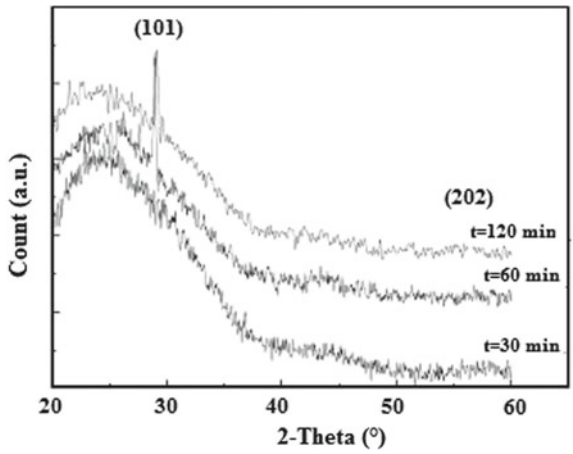

CdS thin film is well known as an important partner to fabricate CdTe or CuInSe2 heterojunction-based solar cells. Despite that CdS in hexagonal phase suffers from the high lattice mismatch with CuInSe2 (1.2%) by comparison to CdS (0.7%) in cubic phase, hexagonal structure is preferred. This is due to its higher stability by comparison to the cubic structure [54, 55]. Several attempts have been made to deposit CdS films with hexagonal structure by changing the deposition parameters such as: Cd source salt [56, 57], solution temperature [47, 58, 59], or thermal annealing [60]. Actually, in CBD process, ammonia plays a key role in the film structure. Using ammonia, as complexing agent generally, leads to cubic, hexagonal, or mixed phase. While, films prepared without ammonia exhibit a hexagonal as well as a mixed phase structures [54]. Hence, using ETA as complexing agent rather than the commonly used ammonia is one procedure to prepare pure hexagonal CdS thin films, which is recommended for photovoltaic applications. It has been claimed that ion-by-ion process leads to a pure hexagonal or a mixture of cubic and hexagonal structure, while cluster-by-cluster process leads only to a pure cubic structure [53, 61].

3.2 Films Morphology

CdS film morphology depends on the deposition. Figure 14a–d shows the AFM images of CdS films morphology variation with the deposition time. As can be seen, the films surface morphology evolves with deposition time. Thirty minutes of deposition time lead to a rough film with a columnar and pyramidal structure. The film morphology becomes smoother and denser after 60 min; the columnar structure becomes ended by a spherical shape. Smooth, dense, and pinhole free film is formed after 90 min of deposition. However, after 120 min of deposition time, pyramidal quantum dots are formed on the film surface with a uniform spatial distribution.

CdS films morphology changes with the molarity of cadmium salt (Fig. 15a–d). The films surfaces become rougher with increasing molarity.

With increasing Cd salt source molarity, the film became rougher (Fig. 15) regardless of the deposition time. The surface roughness increases by a factor of six with increasing the molarity from 0.1 to 0.4 M when using $CdSO_4$ source. In CdS thin films deposited with cadmium acetate molarity as Cd source, Gopinathan et al. [62] reported that the surface roughness increases from 9 to 18 nm with increasing the molarity from 0.4 to 0.5 M. The variation of the surface roughness is the consequence of the variation of the deposition mechanism. Actually, growth mechanism occurs by ion mechanism at low cadmium salt molarity condition and by cluster by cluster when higher cadmium salt is used. For this reason, the quasi-totality of CBD-CdS thin films deposition studies use mainly low molarity of Cd salt [51, 52, 63].

The surface morphology is also sensitive to the salt nature. The AFM images of CdS films deposited with different salts were shown in Fig. 16. The early stage of film growth occurs through 3D mechanism (Volmer–Weber mechanism). This yields films with high surface roughness. If the deposition rate is sufficiently low, the growth

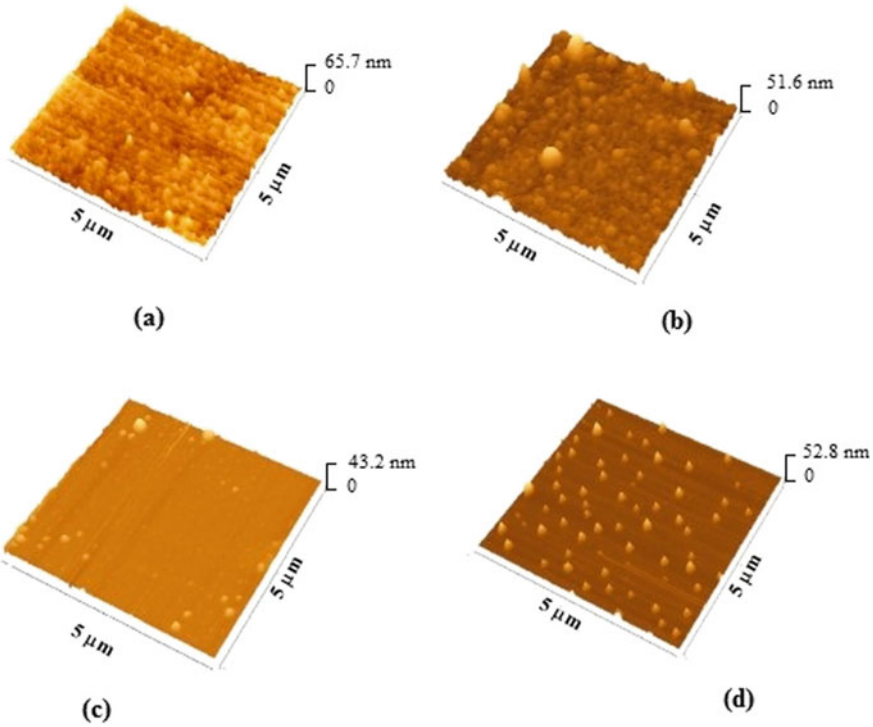

Fig. 14 AFM images of CdS thin films deposited at different times: **a** 30, **b** 60, **c** 90, and **d** 120 min

mechanism will be 2D growth leading to the formation of a smooth surface, and in the termination stage, quantum dots are formed.

These structures have been observed in films deposited with $CdCl_2$ and $Cd(CH_3COO)_2$ (Fig. 16a, b), However, $Cd(SO_4)$ and $Cd(CO_3)$ salts produce rough films (Fig. 16c, d). This difference may originate from the difference in the growth rate of each salt. As mentioned above, CdS formation with $CdCl_2$ and $Cd(CH_3COO)_2$ salts exhibits the lowest deposition rate. This favors the 2D growth at the termination of growth stage. In the case of $Cd(SO_4)$ and $Cd(CO_3)$, the growth rate is too high, and therefore, the solution is consumed before reaching the 2D growth. Khallaf et al. [43] have prepared CdS thin films using two salts $CdSO_4$ and $CdCl_2$. They have noticed that the film deposited with $CdCl_2$ source is smoother than the films deposited with $CdSO_4$.

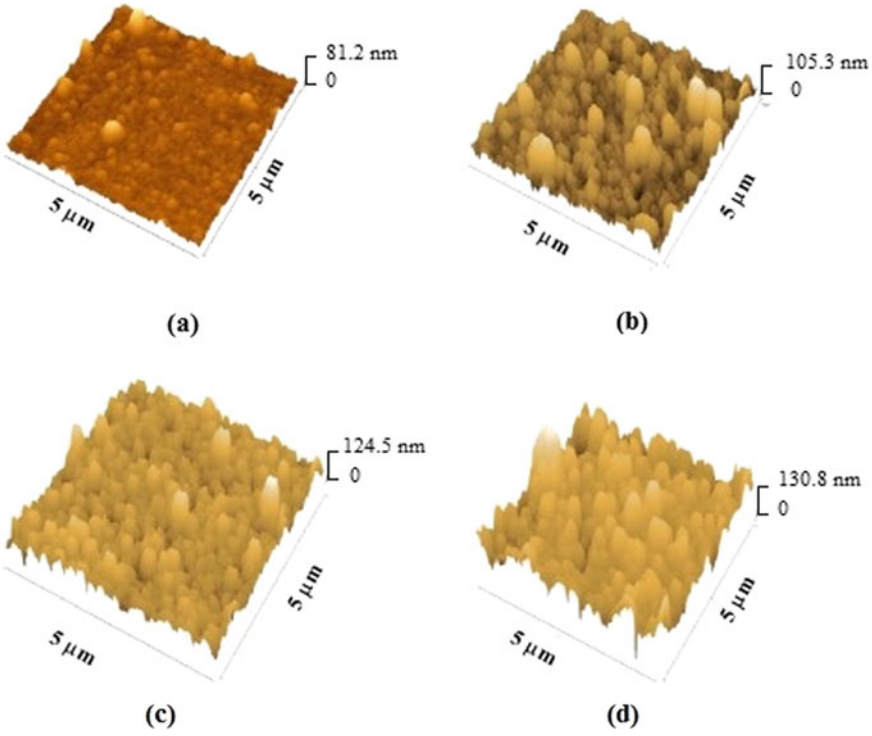

Fig. 15 AFM images of CdS thin films deposited with different salt molarity. **a** 0.1, **b** 0.2, **c** 0.3, and **d** 0.4 M

4 Growth Model

Actually, thin film growth occurs through three models (i) Volmer–Weber model (3-D mode) (ii) Frank–Van der Merwe model (2-D mode) and (iii) Stranski–Krastanov model. A schematic diagram of these models is depicted in Fig. 17. Island growth occurs when the stable nuclei formed on the substrate grow in three dimensions to form islands. This growth mechanism occurs when the deposited atoms are tightly bonded to each other than to the substrate. However, the layer-by-layer or planar growth occurs when the atoms of the deposit are strongly bonded to the substrate than to each other. The Stranski–Krastonov (S-K) growth model is an intermediate combination of the two preceding models. In this case after the formation of one or more monolayer subsequent layer, growth is not favorable leaving the formation of islands. In fact, S-K growth mode is observed when the formed layer increases beyond a critical thickness in a substrate–film lattice mismatched system. With increasing the thickness, the relaxation of film strain is achieved by the formation of islands through elastic relaxation without any dislocation in the islands [64, 65]. This may be the case in our samples, due to the amorphous structure of the used glass substrates.

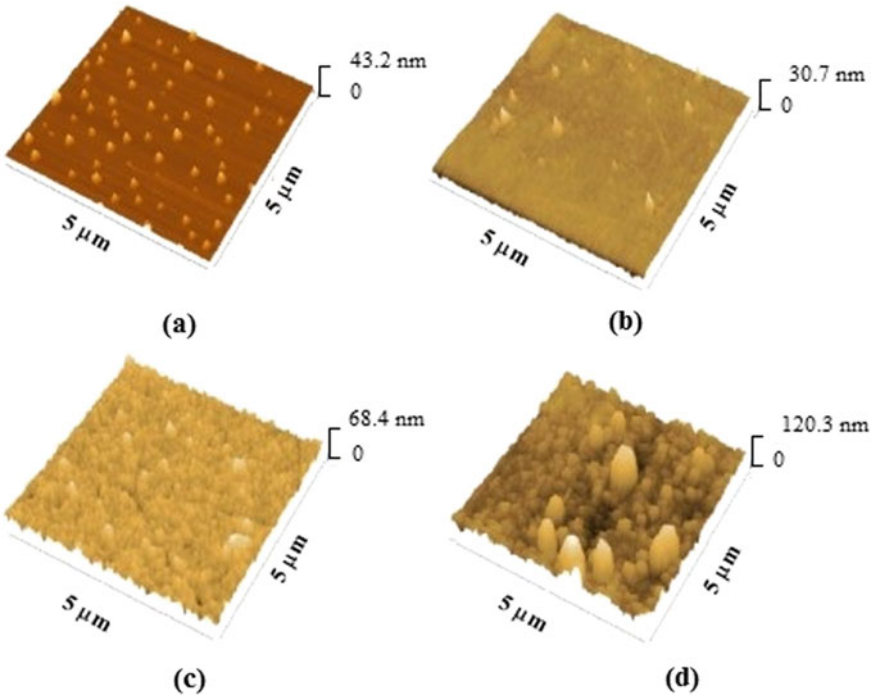

Fig. 16 AFM images of CdS thin films deposited with different Cd salt: **a** $CdCl_2$, **b** $Cd(CH_3COO)_2$, **c** $CdSO_4$, and **d** $Cd(CO_3)$

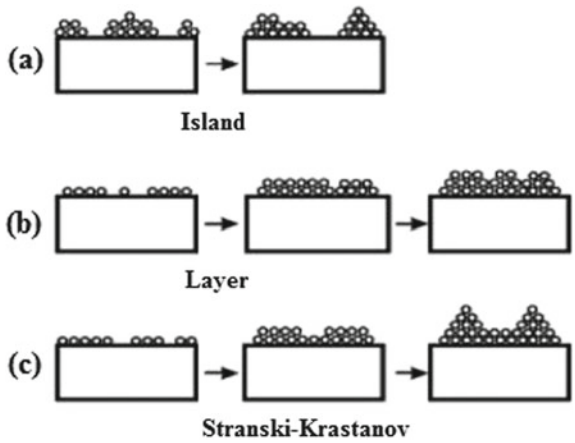

Fig. 17 Different thin film growth models:
a Volmer–Weber,
b Frank–van der Merwe, and
c Stranski–Krastonov

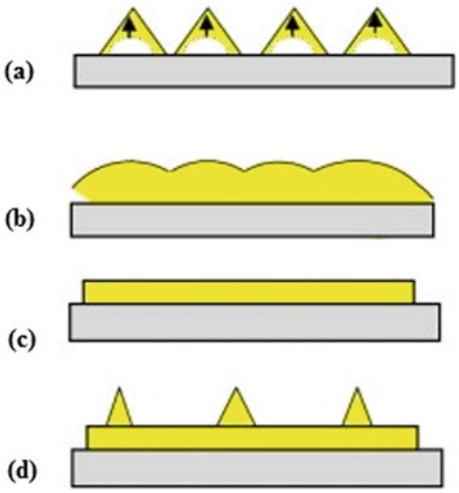

Fig. 18 Schematic diagram of the different steps of film growth. **a** Coalescence and 3D growth, **b** column coalescence and ripening, **c** smooth plane formation, **d** quantum dots formation

Based on the results of AFM images CdS thin film, growth model for CdS thin film prepared by CBD was suggested by Jaber et al. [53]. In this model, the film formation passes through different steps. The different steps of film formation through the suggested model are depicted in Fig. 18.

1. The initial growth stage is achieved by the commonly known nucleation and coalescence followed by a subsequent vertical growth (3-D Volmer–Weber) as shown in Fig. 18a. The obtained films are characterized by a high surface roughness.
2. With increasing deposition time, the grain becomes sharper and unstable due to reduction of number of bonded atoms; thus, the grains reduce their surface energy via their coalescence (Fig. 18b). This phenomenon is called Ostwald ripening [54]. In this step, the surface film roughness is reduced.
3. The most characteristic feature in CBD technique, in contrary to other deposition techniques such as sputtering, thermal evaporation, spray pyrolysis, chemical vapor deposition, is the depletion of the feedstock of incoming species during the film growth. Consequently, the film growth rate is slowed and the film thickness is saturated. This termination stage depends on the starting solution purity and its molarity. The scarce of incoming species causes a larger mobility to the ions on growing surface. By this way, ions can reach the valley site characterized by a lower energy, resulting in valley filling and a flat surface as seen in Fig. 18c.
4. The rarefaction of ions forming the films reduces the nucleation centers on the formed plane; hence, the incoming species migrate on the film's surface to join a stable nuclei which grows vertically to form a pyramidal column or a quantum dot as seen in Fig. 18d.

5 Conclusions

Chemical bath deposition is a cost-effective and simple technique for Cds thin film. It is mainly based on the metallic ions precipitation control in a solution containing sulfide ions. In CBD technique, the film growth can be achieved via two different mechanisms: (i) ion by ion (heterogeneous reaction) or (ii) cluster by cluster (homogeneous reaction). Currently, CdS thin film is mainly deposited by this technique; this method avoids the contact between the user and the hazardous Cd atom. CdS film morphology and structure can be controlled through several parameters such as deposition time, solution bath temperature, Cd salt nature, and molarity.

References

1. Nair, K., & Nair, M. T. S. (1987). Prospects of chemically deposited CdS thin films in solar cell applications. *Solar Cells*, *22*, 103.
2. Theerthagiri, J., Thiagarajan, K., Senthilkumar, B., Khan, Z., Senthil, R. A., Arunachalam, M., et al. (2017). Synthesis of hierarchical cobalt phosphate nanoflakes and their enhanced electrochemical performances for supercapacitor applications. *Chemistry Select*, *2*, 201.
3. Pang, H., Wei, C., Li, X., Li, G., Ma, Y., Li, S., et al. (2014). Microwave-assisted Synthesis of NiS2 Nanostructures for Supercapacitors and Cocatalytic Enhancing Photocatalytic H2 Production. *Applications: A Brief Review Scientific Reports*, *4*, 35771.
4. Theerthagiri, J., Karuppasamy, K., Durai, G., Sarwar Rana, A., Arunachalam, P., Sangeetha, K., et al. (2018). Recent Advances in metal chalcogenides (MX; X = S, Se) nanostructures for electrochemical supercapacitor applications: A Brief Review. *Nanomaterials*, *8*, 256.
5. Xi, C., & Li, J. (2016). Recent advances in optoelectronic properties and applications of two-dimensional metal chalcogenides.*Journal of Semiconductors*, *37*, 051001.
6. Cui, Y., Zhou, Z., Li, T., Wang, K., Li, J., & Wei, Z. (2019). Metal Chalcogenides: Versatile crystal structures and (Opto) electronic applications of the 2D Metal Mono-, Di-, and Tri-Chalcogenide Nanosheets. *Advanced Functional Materials*, *29*, https://doi.org/10.1002/adfm.201970161.
7. Mishra, N., Vasavi, V. G., Milena, D., & Arciniegas, P. (2019). Recent progress on metal chalcogenide semiconductor Tetrapod-Shaped colloidal nanocrystals and their applications in optoelectronics. *Chemistry of Materials*, *31*, 9216.
8. Felder, R. M., & Rousseau, R. W. (Ed.). (1986). *Elementary principles of chemical processes* (2nd ed.). New York, NY: Wiley.
9. Wei, C. M., & Hou, S. S. (2007). Preparation and optical properties of blue-emitting colloidal CdS nanocrystallines by the solvothermal process using poly (ethylene oxide) as the stabilizer. *Colloid and Polymer Science, 285,* 1343.
10. Cui, H. N., & Xi, S. Q. (1996). The fabrication of dipped CdS and sputtered ITO thin films for photovoltaic solar cells. *Thin Solid Films, 288,* 325.
11. Acevedo, A. M. (2006). Thin film CdS/CdTe solar cells: research perspectives. *Solar Energy, 80*, 675.
12. Orgassa, K., Rau, U., Nguyen, Q., Schock, H. W., & Werner, J. H. (2002). Role of the CdS buffer layer as an active optical element in Cu(In,Ga)Se2 thin-film solar cells. *Progress in Photovoltaics, 10,* 457.
13. Ezema, F. I., Hile, D. D., Ezugwu, S. C., Osuji, R. U., & Asogwa, P. U. (2010). Optical properties of CdS/CuS & CuS/CdS heterojunction thin films deposited by chemical bath deposition technique. *Journal of Ovonic Research, 6,* 99.

14. Courel, M., Andrade-Arvizu, J. A., & Vigil-Galán, O. (2015). Loss mechanisms influence on Cu2ZnSnS4/CdS-based thin film solar cell performance. *Solid-State Electronics, 111,* 243.
15. Nazir, A., Toma, A., Shah, N. A., Panaro, S., Butt, S., Sagar, R. R., et al. (2014). Effect of Ag doping on opto-electrical properties of CdS thin films for solar cell applications. *Journal of Alloys and Compounds, 609,* 40.
16. Pradhan, B., Sharma, A. K., & Ray, A. K. (2007). Conduction studies on chemical bath-deposited nanocrystalline CdS thin films. *Journal of Crystal Growth, 304,* 388.
17. Duan, X., Huang, Y., Agarwal, R., & Lieber, C. M. (2003). Single-nanowire electrically driven lasers. *Nature, 421,* 241.
18. Kim, W., Seol, M., Kim, H., Miller, J. B., Gellman, A. J., & Yong, K. (2013). Freestanding CdS nanotube films as efficient photoanodes for photoelectrochemical cells. *Journal of Materials Chemistry, A1,* 9587.
19. Hodes, G. (Ed.). (2002). *Chemical solution deposition of semiconductor films.* New York: CRC Press.
20. Liebig, J. (1835). *Ann. Pharmaz., 14,* 134.
21. Mokrushin, S. G., & Tkachev, Y. V. (1961). Experimental investigation of laminar systems formation of ultrathin cadmium sulfide layers at solution solid. *Kolloidn Zhurnal, 23,* 438.
22. Reynolds, J. E. (1884). On the synthesis of galena by means of thiocarbamide, and the deposition of lead sulphide as a specular film. *Journal of the Chemical Society, 45,* 162.
23. Roy, P., & Srivastava, S. K. (2007). Hydrothermal Growth of CuS Nanowires from Cu−Dithiooxamide, a Novel Single-Source Precursor. *Materials Letters, 61,* 1693.
24. Hodes, G., Albu-Yaron, A., Decker, F., & Motisuke, P. (1987). Three-dimensional quantum-size effect in chemically deposited cadmium selenide films. *Physical Review B, 36,* 4215.
25. Hodes, G., & Albu-Yaron, A. (1988). Size-quantized CdS films in thin film CuInS2 solar cells. *Proceedings of the Electrochemical Society, 88,* 298.
26. Gorer, S., Albu-Yaron, A., & Hodes, G. (1995). Quantum size effects in chemically deposited, Nanocrystalline Lead Selenide Films. *Journal of Physical Chemistry, 99,* 16442.
27. Allen, E. T., Crenshaw, J. L., & Merwin, H. E. (1912). The slphides of zinc, cadmium, and mercury; their crystalline forms and genetic conditions. *American Journal of Science, 34,* 341.
28. Birkmire, R. W., McCandless, B. E., Shafarman, W. N., & Varrin, R. D. (1989). Approaches for high efficiency CuInSe solar cells. *Proceeding of 9th ECPV Solar Energy Conference* (p. 134), Freiberg, Germany.
29. Kazmerski, L. L. (2006). Solar photovoltaics R&D at the tipping point: a 2005 technology overview. *Journal of Electron Spectroscopy and Related Phenomena, 150*, 105.
30. Ramaiah, K. S., Pilkington, R. D., Hill, A. E., Tomlinson, R. D., & Bhatnagar, A. K. (2001). Structural and optical investigations on CdS thin films grown by chemical bath technique. *Materials Chemistry and Physics, 68,* 22.
31. Hiie, J., Dedova, T., Valdna, V., & Muska, K. (2006). Comparative study of nano-structured CdS thin films prepared by CBD and spray pyrolysis: annealing effect. *Thin Solid Films, 511–512,* 443.
32. Zhai, R., Wang, S., Xu, H. Y., Wang, H., & Yan, H. (2005). Rapid formation of CdS, ZnS thin films by microwave-assisted chemical bath deposition. *Materials Letters, 59,* 1497.
33. Prabahar, S., & Dhanam, M. (2005). CdS thin films from two different chemical baths—structural and optical analysis. *Journal of Crystal Growth, 285,* 41.
34. Çetinörgü, E., Gümüş, C., & Esen, R. (2006). Effects of deposition time and temperature on the optical properties of air-annealed chemical bath deposited CdS films. *Thin Solid Films, 515,* 1688.
35. Lai, S., Chang, X., & Fu, C. (2009). Cadmium sulfide quantum dots modified by chitosan as fluorescence probe for copper (II) ion determination. *Microchimica Acta, 165,* 39.
36. Quiebrasa, J. N. X., Puentea, G. C., Moralesa, G. R., Vigila, O., Rodrıguez, G. S., & Acevedo, A. M. (2006). Properties of CdS thin films grown by CBD as a function of thiourea concentration. *Solar Energy Materials and Solar Cells, 90,* 727.
37. Mathew, S., Joseph, S. A., Radhakrishnan, P., Nampoori, V. P. N., & Vallabhan, C. P. G. (2011). Shifting of fluorescence peak in CdS nanoparticles by excitation wavelength change. *Journal of Fluorescence, 21,* 1479.

38. Kitaev, G., Uritskaya, A., & Mokrushin, S. (1965). Kinetics of lead sulfide precipitation from citrate solutions of Thiourea. *Russian Journal of Physical Chemistry, 39,* 1101.
39. Hariech, S., Aida, M. S., Bougdira, J., Belmahi, M., Medjahdi, G., Genève, D., et al. (2018). Cadmium sulfide thin films growth by chemical bath deposition. *Journal of Semiconductors, 39,* 034004.
40. Nair, P. K., Nair, M. T. S., Garcia, V. M., Arenas, O. L., Pena, Y., Castillo, A., et al. (1998). Semiconductor thin films by chemical bath deposition for solar energy related applications. *Solar Energy Materials and Solar Cells, 52,* 313.
41. Sasikala, G., Thilakan, P., & Subramanian, C. (2000). Modification in the chemical bath deposition apparatus, growth and characterization of CdS semiconducting thin films for photovoltaic applications. *Solar Energy Materials and Solar Cells, 62,* 275.
42. Jaber, A. Y. A. A. (2011). *A comparative study of properties of CdS thin films deposited by thermal evaporation and chemical bath techniques* (Ph.D. thesis), Taibah University, KSA.
43. Khallaf, H., Oladeji, I. O., & Chow, L. (2008). Optimization of chemical bath deposited CdS thin films using nitrilotriacetic acid as a complexing agent. *Thin Solid Films, 516,* 5967.
44. Ortega-Borges, R., & Lincot, D. (1993). Mechanism of chemical bath deposition of cadmium sulfide thin films in the ammonia-thiourea system: in situ kinetic study and modelization. *Journal of the Electrochemical Society, 140,* 3464.
45. Baranski, P., Klotchkov, V., & Potykévitch, I. (1978). *Electronique des Semiconducteurs.* Moscow: Mir Moscou.
46. Buckley, R. W. (1973). *Problems associated with the CdS photovoltaic cell* (Ph.D. thesis), University of Durham.
47. Liu, F., Lai, Y., Liu, J., Wang, B., Kuang, S., Zhang, Z., et al. (2010). Characterization of chemical bath deposited CdS thin films at different deposition temperature. *Journal of Alloys and Compounds, 493,* 305.
48. Saxena, N., Kalsi, T., Uttam, P., & Kumar, P. (2018). Morphological evolution in nanocrystalline CdS thin films from flowers to salt rock like structures. *Optical Materials, 84,* 625.
49. Wenyi, L., Xun, C., Qiulong, C., & Zhibin, Z. (2005). Influence of growth process on the structural, optical and electrical properties of CBD-CdS films. *Materials Letters, 59,* 1.
50. Sharama, S. N., Sharma, R. K., Sood, K. N., & Singh, S. (2005). Structural and morphological studies of chemical bath-deposited nanocrystalline CdS films and its alloys. *Materials Chemistry and Physics, 93,* 368.
51. Ximello-Quiebras, J. N., Aguilar-Hernandez, G. C. J., Santana-Rodriguez, G., & Arias-Carbajal Readigos, A. (2004). Physical properties of chemical bath deposited CdS thin films. *Solar Energy Materials and Solar Cells, 82*, 263.
52. Ravichandran, K., & Philominathan, P. (2009). Structural and optical investigations on CdS thin films grown by chemical bath technique. *Applied Surface Science, 255,* 5736.
53. Jaber, A., Alamri, S. N., & Aida, M. S. (2012). CdS thin films growth by ammonia free chemical bath deposition technique. *Thin Solid Films, 520,* 3485.
54. Kaur, I., Pandya, D. K., & Chopra, K. L. (1980). Growth kinetics and polymorphism of chemically deposited CdS films. *Journal of the Electrochemical Society, 127,* 943.
55. Yeh, C. Y., Lu, Z. W., Froyen, S., & Zunger, A. (1992). Zinc-blende–wurtzite polytypism in semiconductors. *Physical Review B, 46,* 10086.
56. Furlong, M. J., Froment, M., Bemard, M. C., Cortes, R., Tiwari, A. N., Krejci, M., et al. (1998). Aqueous solution epitaxy of CdS layers on CuInSe2.*Journal of Crystal Growth, 193,* 114.
57. Lincot, D., Ortega-Borges, R., & Froment, M. (1993). High-resolution transmission electron microscopy study of chemically deposited cadmium sulphide thin films from aqueous ammonia solutions. *Philosophical Magazine B: Physics of Condensed Matter: Statistical Mechanics, Electronic, Optical and Magnetic Properties, 68,* 185.
58. Ileperuma, Q. A., Vithana, C., Premaratne, K., Akuranthilaka, S. N., Mc Gregor, S. M., & Dharmadasa, I. M. (1998). Comparison of CdS thin films prepared by different techniques for applications in solar cells as window materials. *Journal of Materials Science: Materials in Electronics*, *9*, 367.

59. Abd-Lefdil, S., Messaoudi, C., Abd-Lefdil, M., & Sayah, D. (1998). Transparent conducting undoped and indium-doped zinc oxide films prepared by spray pyrolysis. *Physica Status Solidi (a), 168*, 417.
60. Soundeswaran, S., Senthil Kumar, O., & Dhanasekaran, R. (2004). Effect of ammonium sulphate on chemical bath deposition of CdS thin films. *Materials Letters, 58*, 2381.
61. Maliki, H. E., Bernede, J. C., Marsillac, S., Pinel, J., Castel, X., & Pouzet, J. (2003). Study of the influence of annealing on the properties of CBD-CdS thin films. *Journal of Applied Surface Science, 205,* 417.
62. Gopinathan, C., Serveswaran, T., & Mahalakshmi, K. (2011). Studies on CdS nanocrystalline thin films with different S/Cd ratios prepared using chemical bath deposition method. *Advanced Studies in Theoretical Physics, 5,* 171.
63. Chen, H., Li, W., Liu, H., & Zhu, L. (2010). A suitable deposition method of CdS for high performance CdS-sensitized ZnO electrodes: sequential chemical bath deposition. *Solar Energy, 84,* 1201.
64. Shchukin, V. A., & Bimberg, D. (1999). Spontaneous ordering of nanostructures on crystal surfaces. *Reviews of Modern Physics, 71,* 1125.
65. Pinczlits, M., Spingholz, G., & Bauer, G. (1998). Direct formation of self-assembled quantum dots under tensile strain by heteroepitaxy of PbSe on PbTe (111). *Applied Physics Letters, 73,* 250.

Development of the Concept of a Spheroidal Shape Anode for a Solid Oxide Fuel Cell

Bogdan Vasyliv and Viktoriya Podhurska

Abstract Stress and strain distributions in the YSZ–NiO spheroidal shape anode-substrate for a solid oxide fuel cell (SOFC) under the pressure of an operating environment were calculated using the finite element analysis. The features were then compared with ones of the cylindrical shape anode. The radii ranges for the cylindrical and spheroidal (segments of a sphere) parts of the anode ensuring its improved deformation resistance and more uniform stress distribution were suggested. Based on the calculations, an anode of the cylindrical shape with top and bottom convex surfaces (a spheroidal shape anode), with the spheroid to cylinder radii ratio R/R_c in the range from 5 to 20 is suggested. Its specific volume V/S_c is in the range from 1 to 2.5 mm. The stresses in the most dangerous areas (i.e., along the axis and the closed-loop fixing) and maximum strain, caused by the external gas pressure on the anode working surface, are decreased by 10–30% and 20–40%, respectively, as compared to an anode of the cylindrical shape of the same radius and volume features. This increases the lifetime of a solid oxide fuel cell. A three-dimensional curve of intersection of the surfaces of stress distribution in the anode along its axis and the closed-loop fixing was approximated which displays the values of balanced stresses depending on V/V_c and R/R_c parameters. Also, the advantage of the spheroid shaped SOFC anode-substrate over conventional flat one was substantiated using a shape-dependent crack deceleration approach.

Keywords Solid oxide fuel cell · Cylindrical and spheroidal shape anodes · Finite element analysis · Stress and strain distributions · Shape-dependent crack deceleration approach · Lifetime

B. Vasyliv (✉)
Department of Mechanics and Automation Engineering, Lviv Polytechnic National University, 12 S.Bandera str., Lviv 79000, Ukraine
e-mail: mechengin1111@gmail.com

B. Vasyliv · V. Podhurska
Department of Structural Fracture Mechanics of Materials, Karpenko Physico-Mechanical Institute, 5 Naukova str., Lviv 79060, Ukraine
e-mail: podhurskavika@gmail.com

S. J. Ikhmayies (ed.), *Advances in Energy Materials*,
Advances in Material Research and Technology,
https://doi.org/10.1007/978-3-030-50108-2_4

1 Introduction

A solid oxide fuel cell (SOFC) is an electrochemical conversion device that produces electricity directly from oxidizing a fuel. Fuel cells are characterized by their electrolyte material; the SOFC has a solid oxide (ceramic) electrolyte. The advantages of this class of fuel cells include high efficiency, long-term stability, fuel flexibility, low emissions, and relatively low cost. The largest disadvantage is the high operating temperature which results in longer start-up times and mechanical and chemical compatibility issues.

Among the up-to-date versions of the SOFC design, the anode supported one prevails which consists of the thick anode-substrate layer and comparatively thin electrolyte and cathode layers. A porous cermet consisting of two solid phases (nickel one and zirconia stabilized with scandia and ceria (or with yttria), i.e., ScCeSZ–Ni or YSZ–Ni) and pores, is widely used as anode material for a SOFC [1–4]. To reach required electrical conductivity of as-sintered ScCeSZ–NiO or YSZ–NiO ceramic anode, it is subjected to a reduction in a hydrogenous environment at high temperature (usually a few hundred degrees celsius). Due to the reduction of NiO particles, a nickel network is formed in a ceramic (YSZ) skeleton of the anode.

In order to improve the lifetime of a SOFC and to lower the cost of electricity that it produces, researchers work to optimize the structure of its components to prevent degradation of the physical and mechanical properties and improve the structure of the SOFC as layered macrocomposite [5–9]. For this reason, elementary (single) SOFCs of various geometrical shapes (from flat to cylindrical) have been developed.

The operating surface area of an anode of tubular shape [10] is of maximum possible value from the geometrical and structural points of view. However, the length of a tubular SOFC is limited by the stresses which occurred at sealing the environment supply system, as well as caused by the environment pressure.

An anode of truncated cone shape [11] has a large operating surface area, characterized by a high value of the ratio of surface area to volume of the anode, which is however lower by 20–25% than for the anode of tubular shape. Its shape provides connecting the battery of elementary SOFCs in such a way that each next cell by its wider part is imposed on the narrower part of the previous cell. However, to ensure a large operating surface area, the angle at the top corner of the cone should be small (2–10°). In this case, substantial tensile stress arises in a wider part of each cell during the operation, causing the initiation of a network of microcracks at the cell edge that reduces its lifetime.

A flat anode of rectangular shape with a plane work surface [12] is cheaper to manufacture as compared to the abovementioned variants because of using a relatively cheap technology of tape casting. In the same way, thin electrolyte and cathode layers are formed on the anode-substrate. However, an operating surface area of such a SOFC is limited because of the limited thickness of the anode and the stresses arising when assembling elementary fuel cells in a stack. These stresses are not distributed uniformly [13].

Another variant of a flat anode-substrate with a plane work surface is of a round shape (cylindrical anode) [14]. Due to the assembling of elementary fuel cells in a stack, axially symmetric stresses arise in the anode-substrate. However, the diameter of the elementary fuel cell, and consequently, its operating surface area is limited by the thickness of the anode and the ultimate stress along the axis of the cell due to this consolidation scheme. So the cylindrical anode does not provide the required deformation resistance and, consequently, the required lifetime of a SOFC. These factors affect the cost of electricity that it produces and fuel cell performance per unit volume of the anode.

A new improved shape of a SOFC anode has been proposed recently [15]. The anode of such spheroidal shape provides improved resistance to deformation.

The purpose of this work is to determine radii ranges for cylindrical and convex (spheroidal) parts of the SOFC spheroidal shape anode based on stress and strain parameters calculated and substantiate the anode potential to withstand deformation, stress gradient, and crack growth under operational conditions.

2 Methods

2.1 Manufacturing Technique

Traditionally, the anode can be composed of a mixture of ScCeSZ powders (cubic structured zirconia ZrO_2 stabilized with 10 mol% Sc_2O_3 and 1 mol% CeO_2) with addition of 20–50 wt% NiO, or also can be composed of a mixture of YSZ powders (cubic structured zirconia ZrO_2 stabilized with 8 mol% Y_2O_3) with addition of 20–50 wt% NiO. The mixture is compressed under a pressure of 16–20 MPa at a temperature of 20 °C in a cylindrical mold with the concave bottom of the spheroidal shape, with a punch of the same spheroidal shape of its contacting surface. As a result, a cylinder shape pressed body with top and bottom convex surfaces is formed (called a spheroidal shape anode). During 1–4 h of exposure at 800–1250 °C, preliminary annealing of the body is performed which is followed by shrinkage and pore formation, and integrated material structure is formed. Finally, the body is sintered at 1350–1450 °C in air or inert gas during 2–5 h.

2.2 Characterization of the Software Used

To calculate stress and strain parameters of the anodes of the cylindrical and proposed spheroidal shapes by finite element analysis, software for calculating three-dimensional tasks *Mechanical Desktop 6 Power Pack* (MDPP) was used. The MDPP finite element analysis consists of the following steps:

1. Apply fixtures.
2. Apply load.
3. Define material of the part.
4. Analyze (run) the part.
5. View the results.
6. Optimize the part.

1. Applying fixtures. Fixtures let you define fixed restraints. Each restraint can contain multiple faces. The restrained faces are constrained in all directions. You must fix at least one face of the part to avoid analysis failure due to rigid body motion.

When you select faces to fix in the graphics area, the fixture is added to the "Fixtures" folder in the MDPP study tree and a check mark appears next to "Fixtures" in the MDPP wizard.

2. Applying loads. "Loads" lets you apply force and pressure loads to faces of the model. In MDPP, loads can be either force or pressure.

You can apply multiple forces to a single face or multiple faces. For this, you have to select a direction to apply the specified force value to each face in the direction of its normal, and then select the force units and enter the force value. The specified force value is applied to each face. For example, if you select three faces and specify a 50 N force, the program applies a total force of 150 N (50 N on each face). If necessary, select "Reverse direction" to reverse the direction of the force.

The force appears in the "External Loads" folder in the MDPP study tree, and a check mark appears next to "Loads" in the MDPP wizard.

You can apply multiple pressures to a single face or to multiple faces. The program applies pressure loads normal to each face. For this, you have to select "Normal to selected face" to apply the pressure in the direction normal to each selected face, or "Use reference geometry" to apply the pressure in the direction of a selected reference plane (here you need to select a reference plane in the corresponding feature manager design tree), and then select the pressure units and enter the pressure value. If necessary, select "Reverse direction" to reverse the direction of the pressure.

The pressure appears in the "External Loads" folder in the MDPP study tree and a check mark appears next to "Loads" in the MDPP wizard.

3. Assigning material. The response of a part depends on the material assigned to the part. MDPP must know the elastic properties of the material of the part. You assign material to the part by picking a material from a material library. MDPP uses the physical properties of the materials defined in the Mechanical Desktop Material library. Materials can be isotropic, orthotropic, or anisotropic. MDPP supports isotropic materials only.

To assign/modify the material to a part, in the "Material" dialog box, expand the class of materials and select a material.

The material appears in the MDPP wizard and a check mark appears next to "Material". Also, the material appears next to the part's name in the MDPP study tree. If you select a material that does not have a yield strength, a message specifies that the yield strength is not defined.

If the material you want to assign to the part is not in the Mechanical Desktop Material library, you can create a custom material. When you create a custom material, start with an existing material similar to the material you want to create. To create a material, in the "Material" dialog box, in the material tree, select the material on which to base the custom material. Then, select Copy, and in the material tree, select a category in a custom library. You can use the Custom Materials library or a library you created. Select Paste. To rename the material, right click the material and select Rename. Edit properties of the material and click Save. Click Apply.

4. Analyzing the part. MDPP prepares the model for analysis and then calculates displacements, strains, and stresses. To analyze the part, you can use the default mesh settings or change them.

To accept the default mesh settings (default element size and tolerance values), click "Run Simulation". When the simulation is complete, a drawing of the deformed part is displayed. Review the drawing and determine whether the loads and fixtures are applied properly, then click "Continue".

When the simulation is complete, a check mark appears next to "Run" and "Results" in the MDPP wizard.

To change mesh settings, in the "Mesh" Property Manager, adjust the mesh by dragging the slider. Drag the slider to the right for a finer mesh (more accurate) or to the left for a coarser mesh (quicker), then remesh the model. After that, click "Run Simulation" and repeat the abovementioned steps of analyzing the part.

Mesh failure diagnostics. The meshing of a solid model consists of two basic phases. In the first phase, the mesher places nodes on the boundary. This phase is called surface meshing. If the first phase is successful, the mesher starts the second phase where it creates nodes in the inside, fills the volume with tetrahedral elements, and places mid-side nodes on edges.

Failure can occur in either of the two phases. When the meshing of a part fails, MDPP opens the mesh failure diagnostics tool to help you locate and resolve meshing problems. The tool lists the faces and edges that caused the failure. To highlight a face or an edge that failed to mesh, select it from the list.

5. Viewing the results. After completing the simulation, you can view results.

The "Results" folder in the MDPP study tree contains the results for the current geometry, material, fixtures, and loads. MDPP calculates stresses, displacements, deformation, and strains, and places them in the "Results" folder.

To view the stress distribution in the model, click "Show von Mises stress". The equivalent stress (von Mises stress) plot is displayed.

To view the displacement distribution in the model, click "Show displacement". The resultant displacement plot is displayed.

The deformation scale refers to the scale factor that the program uses to scale the deformed shape of the model. The value of the scale factor depends on the model's largest dimension and the calculated deformations.

For example, a scale factor of 50 means that the largest deformation calculated by MDPP is shown as 50% larger than the largest dimension of the smallest boundary box that surrounds the model.

A larger deformation scale factor helps you visualize deflections that are a lot smaller compared to the original dimensions of the model.

6. Optimizing the part. After completing a stress analysis, you can perform an optimization analysis to find the optimal value for one model dimension while satisfying a specified criterion. For example, you can find the optimal length of a part such that the von Mises stresses do not exceed a specified value.

3 Results and Discussion

3.1 The Classic Stress–Strain Approach

Formulation of the task. Stress and strain parameters of the anodes of the cylindrical and proposed spheroidal shapes (Fig. 1) were calculated by the MDPP finite element analysis. Initial conditions were as follows: material of ZrO_2–Y_2O_3–Ni system; average value of the ultimate fracture stress $\sigma_f = 110$ MPa; Young's modulus $E = 1.5 \times 10^5$ MPa; Poisson's coefficient $\nu = 0.3$; the fixing pressure $n = 1$ MPa along the closed-loop fixing of inner radius $R_p = 10.5$ mm; the external gas pressure $p = 1$ MPa on the anode working surface; the radius of the cylindrical part of anodes $R_c = 12$ mm; the spheroid radii, R, were 240, 60, and 36 mm, respectively.

Stress and strain features of the anodes. Corresponding faces of the model were fixed and loads were applied (Fig. 1). Then, the material was assigned and the default mesh setting (default element size and tolerance values) was used to analyze the part. After completing the simulation, we obtained results. Such procedure was repeated for each separate case of spheroid radii and the anode hight starting from 0.5 mm with a step of 0.5 mm.

To compare stress and strain features of the anodes of the cylindrical and spheroidal shapes, the following parameters were calculated:

volume V_c of an anode of the cylindrical shape

$$V_c = \pi \cdot R_c^2 \cdot h \tag{1}$$

where h is a hight of a cylinder;

volume V_s of two convex parts (spherical caps) of an anode of spheroidal shape

$$V_s = \frac{2}{3}\pi \cdot H^2(3R - H) \tag{2}$$

where H is a hight of a convex part (spherical cap) of the anode;

volume V of an anode of spheroidal shape

$$V = \pi \cdot R_c^2 \cdot h + \frac{2}{3}\pi \cdot H^2(3R - H) \tag{3}$$

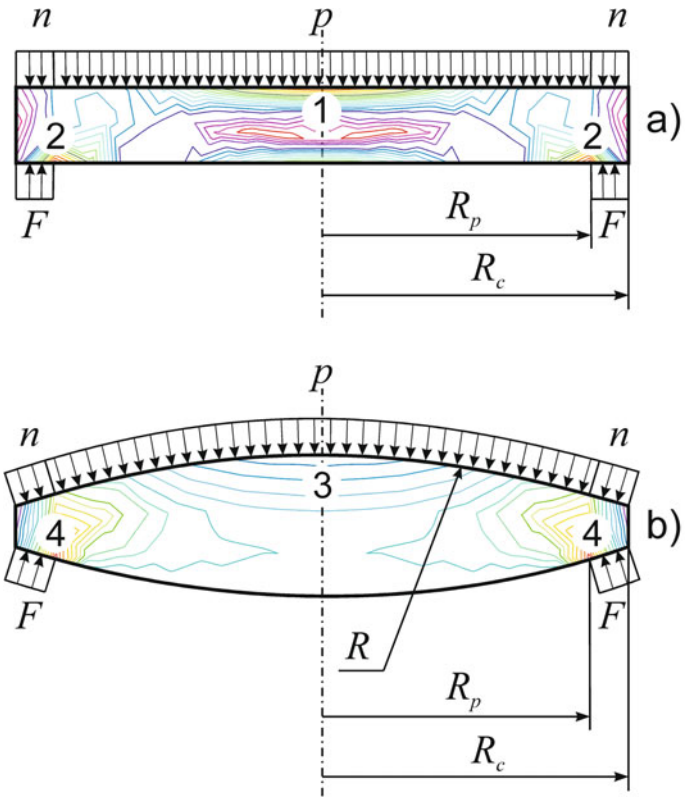

Fig. 1 Diagrams of application of the fixing pressure, n, along the closed-loop fixing of the inner radius, R_p, the external gas pressure, p, on the anode working area, the reaction force, F, along the closed-loop fixing, the stress distribution, σ, along the axis (items 1 and 3), and the closed-loop fixing (2 and 4) in the anode of a cylinder radius, R_c, with **(a)** parallel working surfaces and **(b)** convex ones of a spheroid radius, R

area S_c of the base of the cylindrical part of the anode

$$S_c = \pi \cdot R_c^2 \tag{4}$$

ratios V/S_c and V_c/S_c;

surface area increment ΔS (in %) of an anode of a spheroidal shape

$$\Delta S = 100 \cdot \left(\frac{2R \cdot H}{R_c^2} - 1 \right) \tag{5}$$

ratio V/V_c of the spheroidal shape anode volume to the volume of an anode of the cylindrical shape;

ratio V/V_{c1} of the spheroidal shape anode volume to the volume of an anode of the cylindrical shape, where $V_{c1} = 452$ mm^3 is the calculated volume of the cylindrical anode of radius $R_c = 12$ mm and of hight 1 mm fabricated for industrial applications [7].

The range of values of R/R_c ratio from 20 to 5 corresponds to a noticeable increment of anode surface area ΔS (up to 1%, see Fig. 2). For this range at slight working surface convexity, the ratio V/V_{c1} is small (from 1.31 to 2.20). For the R/R_c range from 3.5 to 5 increment of anode surface area, ΔS is from 1 to 2% but a steep increase of anode volume occurs due to the excessive convexity (V/V_{c1} from 2.20 to 2.75), that does not provide the conditions for reactions to be passed in the fuel cell.

The volumes V and V_c, the area S_c, and V/S_c ratio were calculated as functions of parameters R, R_c ($R_c = 12$ mm) and variable anode hight (its increment step was 0.5 mm). For each partial case, the stress distribution and maximum strain were calculated by finite element analysis. Then, the stresses in the most dangerous areas [i.e., along the axis (items 1 and 3, see Fig. 1) and the closed-loop fixing (2 and 4)] and maximum strain, ε_{max}, along the axis versus V/S_c ratio dependences were plotted (Fig. 3).

The dependences show that for an anode of the cylindrical shape the stresses along the axis are higher than ones along the closed-loop fixing (Fig. 3a, curve 1 contrary to curve 2). In contrast to this, for an anode of spheroidal shape even of slight convexity ($R/R_c = 20$), the stresses along the axis and the closed-loop fixing, caused by the external gas pressure on the anode working surface, are already balanced at the value of V/S_c over 1.5 mm (Fig. 3a, curves 3 and 4), and the maximum strain is decreased by 10–30% as compared to an anode of the cylindrical shape (Fig. 3b, curve 10 contrary to curve 9).

For an anode of spheroidal shape with the ratios of R/R_c in the range from 5 to 20 and V/S_c from 1 to 2.5 mm, the stresses in the most dangerous areas [i.e., along

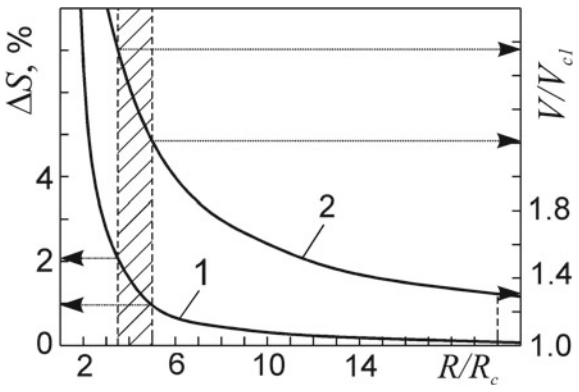

Fig. 2 A graph of calculated values of the area increment, ΔS, of a spheroidal shape anode (curve 1, an ordinate axis is on the left) and the ratio V/V_{c1} of the anode volume to the volume of the in-production cylindrical shape anode of a radius of 12 mm and of 1 mm thickness (curve 2, an ordinate axis is on the right) depending on the spheroid-to-cylinder radii ratio, R/R_c

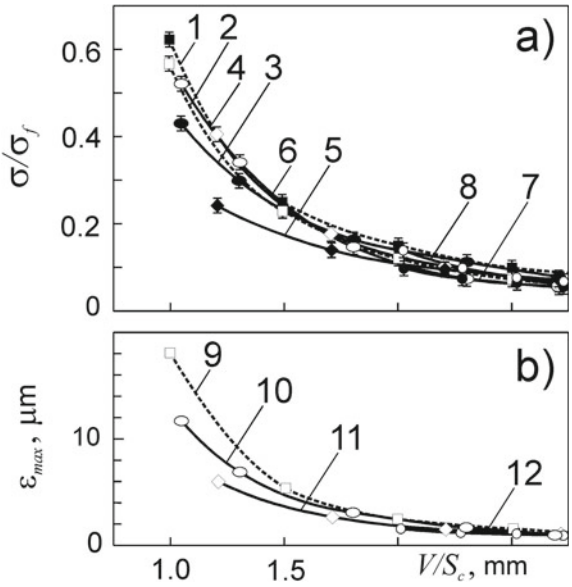

Fig. 3 Change in the values of **(a)** the ordinary to fracture stresses ratio, σ/σ_f, along the axis (curves 1, 3, 5, and 7) and closed-loop fixing (2, 4, 6, and 8) as well as **(b)** maximum strain, ε_{max}, along the axis (9–12) caused by the fixing pressure and the external gas pressure on the anode working surface which are calculated using the finite element analysis, depending on the anode volume to its cylinder base area ratio, V/S_c, for cylindrical shape anodes with parallel (curves 1, 2, and 9) and spheroidal working surfaces having the spheroid to cylinder radii ratio, R/R_c, of 20 (curves 3, 4, and 10), 5 (5, 6, and 11), and 3 (7, 8, and 12), respectively

the axis (items 1 and 3, see Fig. 1) and the closed-loop fixing (2 and 4)], and the maximum strain, caused by the external gas pressure on the anode working surface, are decreased by 10–30% and 20–40%, respectively, as compared to an anode of the cylindrical shape of the same radius and volume features.

Based on the FEA calculations performed for spheroidal anodes with $R_c = 12$ mm and various values of R (Fig. 4), the surfaces of stress distribution along their axes and closed-loop fixing were plotted. As a result of the graphic intersection of these surfaces, a three-dimensional curve was created (Fig. 4, surfaces 1 and 2, respectively, and curve 3). The curve displays the values of balanced stresses depending on V/V_c and R/R_c parameters. A domain of this curve was also defined.

Projections of the curve on the coordinate planes [V/V_c; R/R_c], [σ/σ_f; R/R_c], and [σ/σ_f; V/V_c] were approximated by the corresponding lines (Fig. 4, curves 3′, 3″, and 3‴, respectively). Curve 3′ for the ranges $0.065 < (\sigma/\sigma_f) < 0.460$, $1.20 < (V/V_c) < 1.58$, and $10 < (R/R_c) < 32$ was described by an equation:

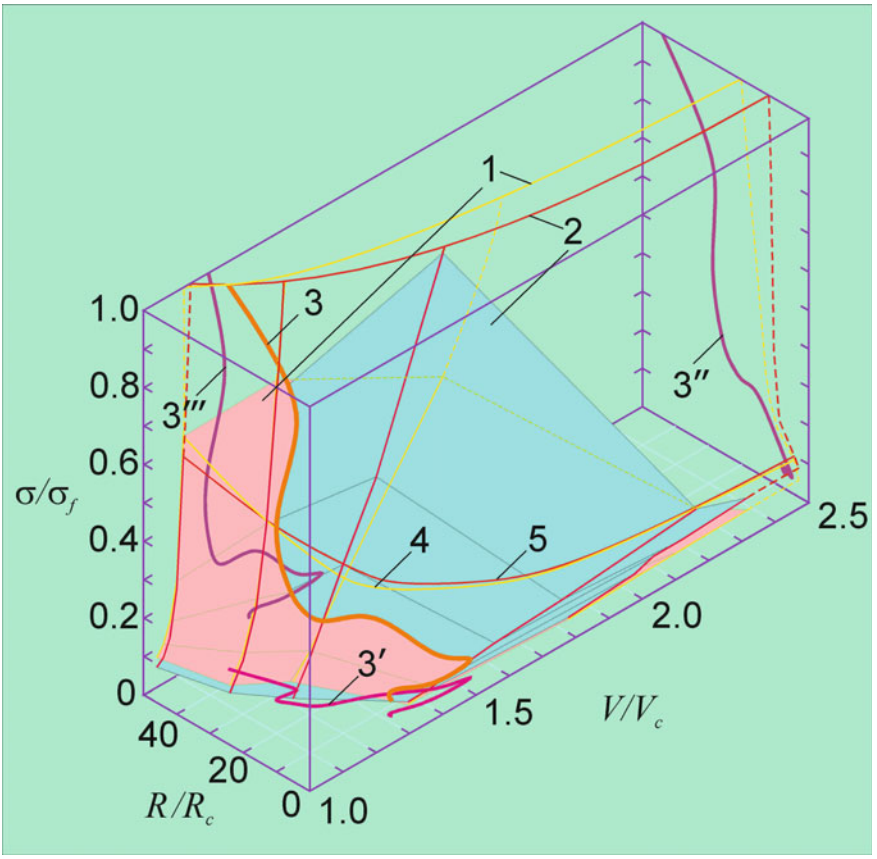

Fig. 4 Surfaces of stress distribution along the axis (surface 1) and closed-loop fixing of anodes (surface 2) as well as their three-dimensional intersection curve (3) with its projections on the coordinate planes [R/R_c; V/V_c], [σ/σ_f; R/R_c], and [σ/σ_f; V/V_c] (curves 3′, 3″, and 3‴, respectively). Curves 4 and 5 (located on surfaces 1 and 2, respectively) show levels of stresses in anodes with a 1 mm thick cylindrical part and a variety of R/R_c (V/V_c) ratios

$$\frac{V}{V_c} = 0.00000547(R/R_c)^5 - 0.0005109(R/R_c)^4 + 0.01829(R/R_c)^3 - 0.313(R/R_c)^2 + 2.525(R/R_c) - 6.1085 \quad (6)$$

Curve 3″ for the ranges $0.065 < (\sigma/\sigma_f) < 0.430$ and $7.5 < (R/R_c) < 22$ was described by an equation:

$$\frac{\sigma}{\sigma_f} = 0.000022(R/R_c)^4 - 0.00126(R/R_c)^3 + 0.0275(R/R_c)^2 - 0.2454(R/R_c) + 0.7774 \quad (7)$$

Curve 3‴ for the ranges $0.065 < (\sigma/\sigma_f) < 0.280$ and $1.20 < (V/V_c) < 1.47$ was described by an equation:

$$\frac{\sigma}{\sigma_f} = 549.26(V/V_c)^4 - 2961.15(V/V_c)^3 + 5973.1(V/V_c)^2 - 5343.51(V/V_c) + 1789.15 \quad (8)$$

Based on Eqs. (1) and (3) for the volumes of the cylindrical and spheroidal shape anodes as well as their ratios, it can be noted that for a certain R/R_c ratio range (approximately from 3 to 50) curve 3′ for anodes with a radius of the cylindrical part $R_c > 12$ mm (see Fig. 4) will be shifted towards lower values of V/V_c while curve 3″ will be shifted towards higher values of σ/σ_f, and curve 3‴ will be shifted towards lower values of V/V_c and higher values of σ/σ_f.

Thus, a spheroidal shape anode allows the stress distribution to be changed and a level of maximum strain in a fuel cell to be lowered. Therefore, it allows resistance to its deformation, and the lifetime of a fuel cell to be increased. This reduces the cost of electricity that the cell produces, and thus increases the efficiency of a solid oxide fuel cell with an anode-substrate of spheroidal shape as compared to the fuel cell comprising an anode-substrate of the cylindrical shape.

3.2 A Shape-Dependent Crack Deceleration Approach

A short history of a chevron profile. Chevron-notched specimens (Fig. 5) are gaining widespread use for fracture toughness testing of ceramics, rocks, high-strength metals, and other brittle materials [16–20]. They are small (5- to 25-mm thick),

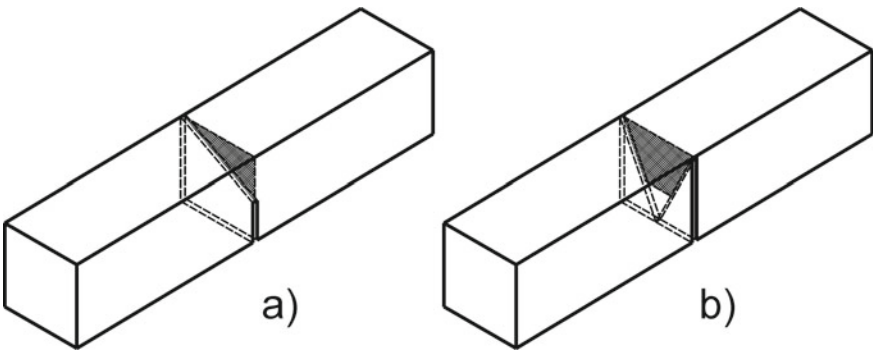

Fig. 5 Various chevron-notched fracture specimen configurations: **(a)** a bend bar with an unsymmetrical chevron notch [17]; **(b)** a bend bar with a chevron notch symmetrical about the center line of the specimen [19]

simple, and inexpensive specimens for determining the plane-strain fracture toughness. Because they require no fatigue precracking, they are also well suited as quality control specimens.

The unique features of a chevron-notched specimen, over conventional fracture toughness specimens, are: (1) the extremely high stress concentration at the tip of the chevron notch, and (2) the stress intensity factor passes through a minimum as the crack grows. Because of the high-stress concentration factor at the tip of the chevron notch, a crack initiates at a low applied load, so costly precracking of the specimen is not needed. From the minimum stress intensity factor, the fracture toughness can be evaluated from the maximum test load. Therefore, a load-displacement record, as is currently required in the ASTM E399 plane-strain fracture toughness (K_{Ic}) test procedure, is not needed.

In 1964, Nakayama [17, 18] was the first to use a bend specimen with an unsymmetrical chevron notch. His specimen configuration is shown in Fig. 5a. He used it to measure fracture energy of brittle, polycrystalline, refractory materials. All previous methods which had been developed for testing homogeneous materials were thought to be inadequate. This specimen is unique in that a crack initiates at the tip of the chevron notch at a low load, then propagates stably until catastrophic fracture. Because of the low load, the elastic stored energy in the test specimen and testing apparatus was small so that the fracture energy could be estimated from the area under a load-time history record.

Tattersall and Tappin [19] in 1966 proposed using a bend bar with a chevron notch symmetrical about the center line of the specimen, as shown in Fig. 5b. They used this specimen to measure the work of fracture on ceramics, metals, and other materials. The work of fracture was determined from the area under the load-displacement record divided by the area of the fracture surfaces.

Pook [20] used the stress intensity factor solution for a three-point bend bar with a straight-through crack [21] and a side-groove correction proposed by Freed and Kraft [22] to obtain approximate solutions for various shape chevron notches. The stress intensity factor for a chevron-notched specimen, K_{CN} was given by

$$K_{\mathrm{CN}} = K_{\mathrm{STC}}\left(\frac{B}{b}\right)^{1/2} \tag{9}$$

where K_{STC} is the stress intensity factor for a straight-through crack in a bar having the same overall dimensions. The unique stress intensity factor solution for a chevron-notched specimen compared to a straight-through crack specimen is illustrated in Fig. 6.

The dashed curve shows the normalized stress intensity factors for the straight-through crack as a function of a/W. This curve is a monotonically increasing function with crack length.

The solid curve shows the solution for the chevron-notched specimen. For $a = a_0$, the stress intensity factor is very large but it rapidly drops as the crack length increases. The minimum value is reached when the crack length is between a_0 and

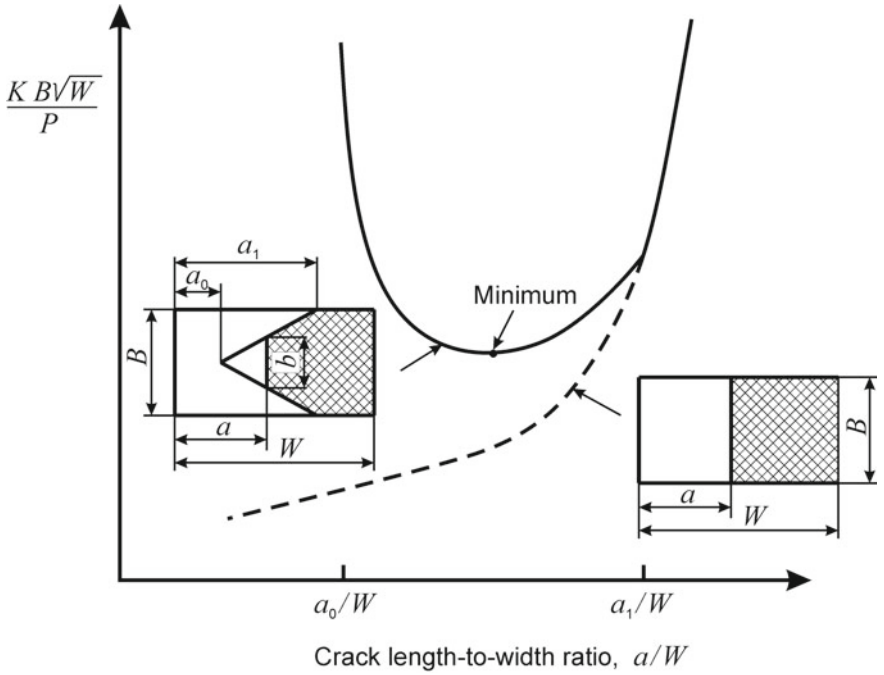

Fig. 6 Comparison of normalized stress intensity factors for chevron-notched and straight-through crack specimens. Here, K is the stress intensity factor and P is the applied load

a_1. For $a > a_1$, the stress intensity factors for the chevron-notched specimen and for the straight-through crack specimen are identical because the configurations are identical.

A concept of variable length of the crack front. We assume that at first approximation, the crack profile of arbitrary shape can be replaced by a similar trapezoidal profile [23]. So there can be a unified approach for estimating the dynamics of crack growth in ceramic parts of various shapes [24] by using developed earlier procedure of crack initiation and propagation in a ceramic specimen with the oblique front of a notch, and corresponding formulae for compliance calibration [24–26].

A compact specimen with a chevron notch monotonically loaded by wedging the edges of a notch on a testing machine (Fig. 7) can be used for modeling the dynamics of crack growth. For this purpose, the notch mouth in a specimen and a loading wedge were sharpened to the same angle β. The proposed loading mode is, to a greater extent, strain-controlled than eccentric tension mode, and guarantees stable crack growth in the case where the load applied to the specimen increases stepwise.

The experimental procedure can be described as follows: A specimen is monotonically loaded by moving the wedge with a speed of 10 μm/s up to the attainment of an empirically specified load level, held for 30–120 s until the initiation of a

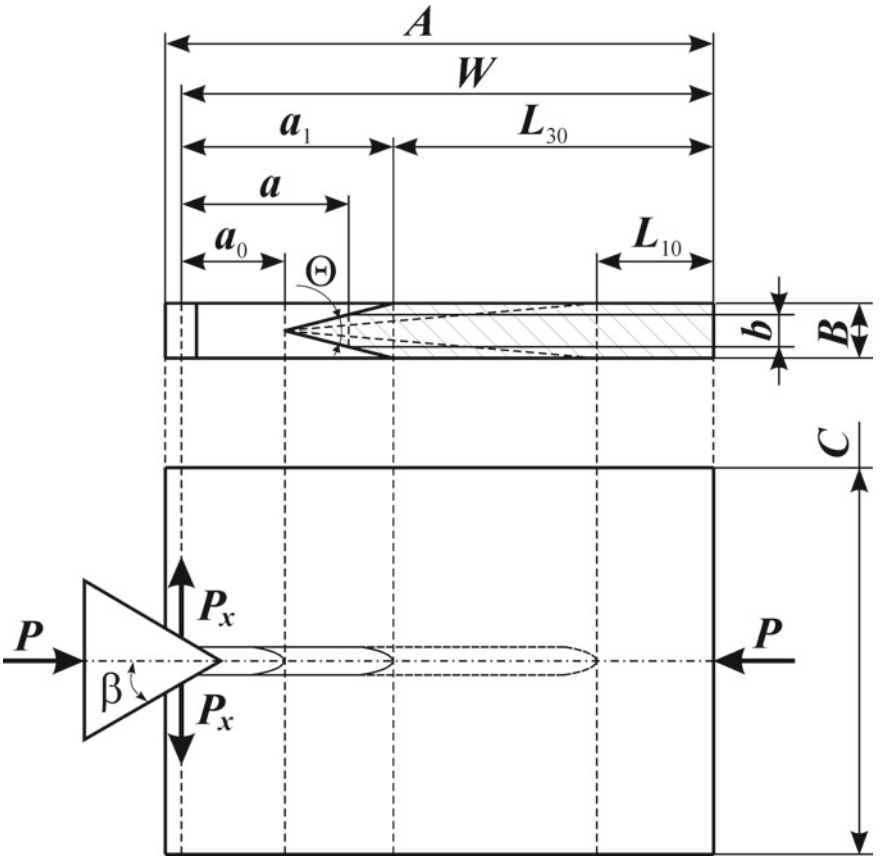

Fig. 7 Schematic diagram of loading a compact chevron-notched specimen. Here, the values of L_{10} and L_{30} correspond to the profile angle θ of 10° and 30°

0.10–0.15 mm long incipient crack, and then unloaded. The procedure is periodically repeated, each time under a higher maximum load guaranteeing the attainment of an increment of crack length of about 0.05–0.25 mm with subsequent termination of the crack growth. In the course of the tests, current values of the crack length, load, and displacements of the notch edges are recorded. The growth of a crack is observed with an optical microscope.

The stress intensity factor K_{CN} at the crack tip in a compact specimen with a chevron notch can be determined by using the formulae [20, 22, 27–29]

$$K_{\mathrm{CN}} = \frac{P_X^{\mathrm{corr}(e)}}{B}\sqrt{\frac{\pi}{W}} \cdot y_{\mathrm{STC}}\left(\frac{\alpha_1 - \alpha_0}{\alpha - \alpha_0}\right)^{0.5} \tag{10}$$

$$y_{\mathrm{STC}} = 16.7\,\alpha^{1/2} - 104.7\,\alpha^{3/2} + 369.9\,\alpha^{5/2} - 573.8\,\alpha^{7/2} + 360.5\,\alpha^{9/2} \tag{11}$$

where $P_X^{\mathrm{corr}(e)}$ is the corrected value of applied load, B is the thickness of the specimen ($1.5\ \mathrm{mm} < B < 4.5\ \mathrm{mm}$), a is the crack length, W is the width of the specimen, $\alpha = a/W$ ($0.2 < \alpha < 0.6$), a_0 is the distance from load line to the tip of chevron notch, $\alpha_0 = a_0/W$ ($0.2 < \alpha_0 < 0.45$) (see Fig. 7);

$$P_X^{\mathrm{corr}(e)} = \frac{k_1 k_2 P}{2(\tan\beta)} \tag{12}$$

where P is the applied load, β is the angle of loading wedge (see Fig. 7),

$$k_1 = \left(\frac{B}{B_0}\right)^{0.5} \tag{13}$$

$B_0 = 1$ mm;

$$k_2 = \lambda_0^n \left(\frac{B}{B_0}\right) \exp\left\{(-1)\left(0.1\alpha_0^2 + \left(\frac{B_0}{B}\right)^{0.5}\right)\left(\frac{\alpha_1 - \alpha_0}{\alpha - \alpha_0}\right)^{0.25}\right\} \tag{14}$$

where n is changed in the range $0.3 < n < 1.2$ and the corresponding value of α_0^n is changed in the range $0.169 < \alpha_0^n < 0.569$ for the experimental curves obtained on the specimens of various thicknesses.

In the case of applying certain load P using the wedging scheme, we can calculate the current value of $K_\mathrm{I} = K_\mathrm{CN}$ for a certain profile with corresponding profile angle θ (Fig. 8c). This angle is an average one for either the concave (Fig. 8a) or convex profile (Fig. 8b), as well as for combined variants.

In general, crack growth behavior depends on the profile angle (Fig. 9). Having calculated the values of the parameter K_I in time, we will obtain the dependence $K_\mathrm{I} = f(t)$ which can be different for different crack profiles (Fig. 10).

Schematically, we can present the main cases of the profile angle θ depending crack growth behavior (Fig. 9a, c, e, g) and fracture (Fig. 9b, d, f, h).

Also, we can present corresponding shapes of the basic K_I–da/dt curve (Fig. 10a, c, e, g) and of $K_\mathrm{I} = f(t)$ curve (Fig. 10b, d, f, h) for the range from threshold (K_Ith) to critical level (K_Ic), for the cases of applying load P causing certain starting value

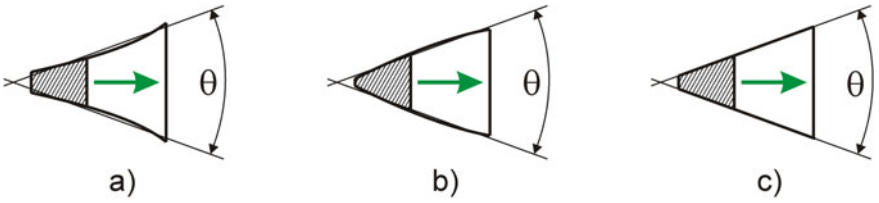

Fig. 8 Diagrams of **(a)** the concave, **(b)** convex, and **(c)** symmetrical chevron profiles in a ceramic part of arbitrary shape, having the same average profile angle θ. For each case, a hatched area corresponds to a crack running along the direction indicated by an arrow

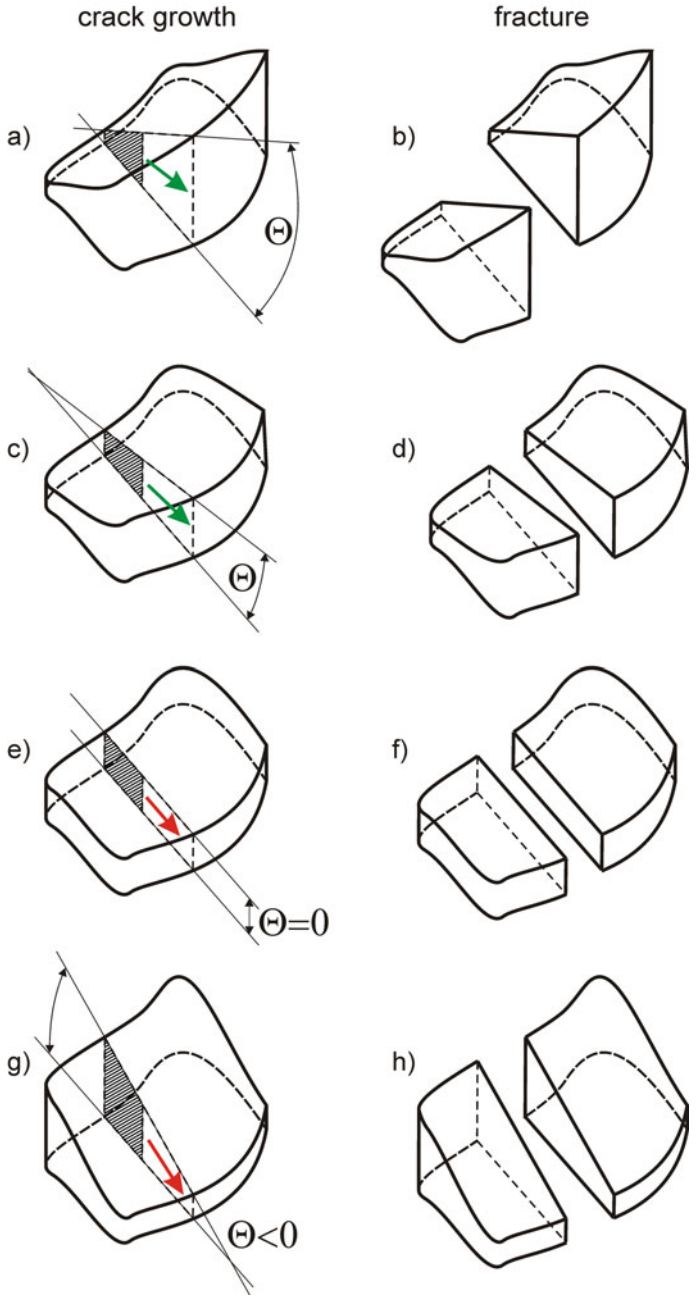

Fig. 9 Diagrams of the crack profiles in a ceramic part of arbitrary shape which correspond to the profile angle θ depending crack growth behavior: **(a**, **b)** crack deceleration, **(c**, **d)** quasi-equilibrium crack growth, and **(e**–**h)** its acceleration. For each case, a hatched area corresponds to a crack running along the direction indicated by an arrow

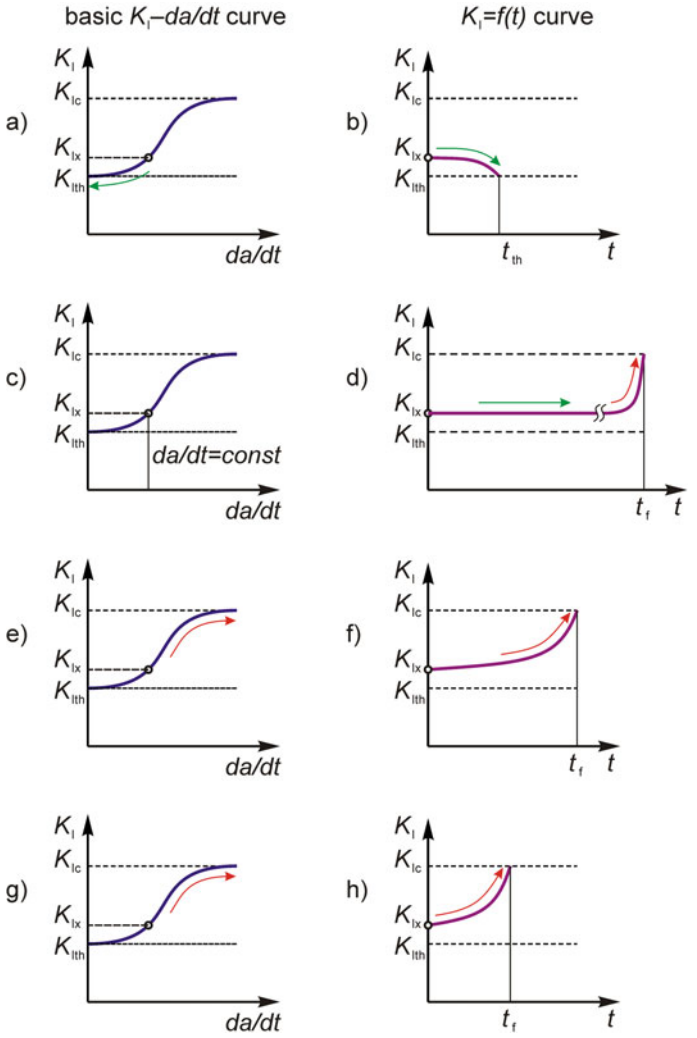

Fig. 10 Basic K_I–da/dt curves **(a**, **c**, **e**, **g)** and $K_I = f(t)$ curves **(b**, **d**, **f**, **h)** for ceramic parts of arbitrary shape which correspond to the profile-depending crack growth behavior: **(b)** crack deceleration, **(d)** quasi-equilibrium crack growth, and **(f**, **h)** its acceleration. The arrows along curves indicate the direction of change of the corresponding parameters while running cracks in the profiles. K_{Ith} and K_{Ic} are the threshold and critical stress intensity factors, respectively, K_{Ix} is a certain starting value of the stress intensity factor, t_{th} is the time during which K_{Ix} to K_{Ith} stress state change occurs, and t_f is the time during which K_{Ix} to K_{Ic} stress state change occurs

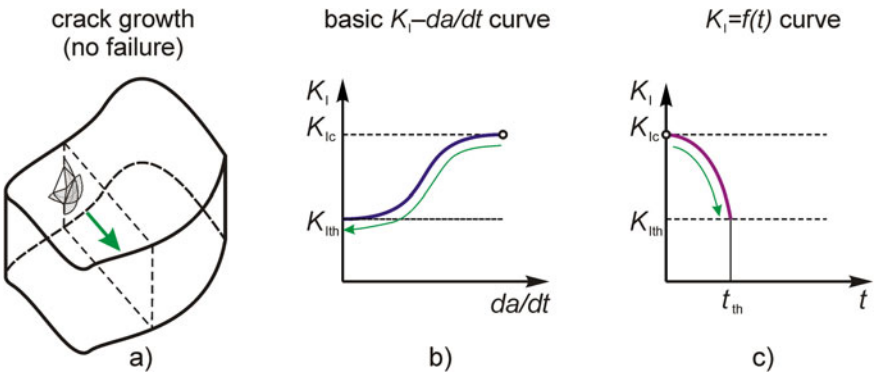

Fig. 11 A diagram of the indentation crack profile in a ceramic part of arbitrary shape, and corresponding basic K_I–da/dt **(b)** and $K_I = f(t)$ **(c)** curves, showing a particular case of the crack deceleration conditions. Hatched areas **(a)** correspond to perpendicular cracks running along the direction indicated by an arrow. The arrows along curves **(b**, **c)** indicate the direction of change of the corresponding parameters while running cracks in the profile. K_{Ith} and K_{Ic} are the threshold and critical stress intensity factors, respectively; t_{th} is the time during which K_{Ic} to K_{Ith} stress state change occurs

K_{Ix}: descending $K_I = f(t)$ curve (Fig. 10b) for comparatively big angles θ (Fig. 9a, b), horizontal one (Fig. 10d) for smaller angles θ (Fig. 9c, d), and then ascending curve (Fig. 10f, h) for rectangular ($\theta = 0$) and especially reverse ($\theta < 0$) profiles (Fig. 9e–h).

As a particular case of the crack deceleration conditions in a ceramic part of arbitrary shape, the indentation crack profile [30, 31] can be presented (Fig. 11a), along with the basic K_I–da/dt and $K_I = f(t)$ curves (Fig. 11b, c).

This profile has the angle $\theta = 180°$ which is the biggest one among the profiles causing the crack deceleration (see Fig. 9). This behavior is demonstrated by a very steep slope of the descending $K_I = f(t)$ curve (Fig. 11c).

Determination of the crack running moment. The abovementioned profile-dependent features of crack advance have been taken into account when constructing multiple M_x–a curves for symmetrical profiles with various profile angles. For this purpose, the crack running moment M_x applied to a specimen with symmetrical chevron crack profile can be determined by transforming Eq. (10):

$$M_X = P_X \cdot a = \frac{K_{CN} \cdot B\sqrt{W} \cdot a}{y_{STC} \cdot \sqrt{\pi}} \cdot \left(\frac{\alpha_1 - \alpha_0}{\alpha - \alpha_0}\right)^{-0.5} \tag{15}$$

where P_x is the eccentric tension load, a is the crack length, $\alpha = a/W$ is the relative crack length, K_{CN} is the stress intensity factor at the crack tip, B and W are the thickness and width of a specimen, respectively, a_0 is the distance from load line to the tip of chevron notch, $\alpha_0 = a_0/W$, a_1 is the distance from load line to the point where chevron notch intersects specimen surface, $\alpha_1 = a_1/W$ (see Fig. 7); y_{STC} is determined according to Eq. (11).

In the beginning, we can analyze the behavior of dimensionless constituents of Eq. (15) to understand the feature of "M_x versus a" dependences. For this reason, let us introduce the following notation:

$$M_X = \frac{K_{\mathrm{CN}} \cdot B\sqrt{W} \cdot a}{\sqrt{\pi}} \cdot k_1 k_2 \tag{16}$$

where

$$k_1 = \frac{1}{y_{\mathrm{STC}}} \tag{17}$$

$$k_2 = \left(\frac{\alpha_1 - \alpha_0}{\alpha - \alpha_0}\right)^{-0.5} \tag{18}$$

Also, we can use additional mathematical operations for this purpose:

$$k_3 = k_1 k_2 = \frac{1}{y_{STC}} \cdot \left(\frac{\alpha_1 - \alpha_0}{\alpha - \alpha_0}\right)^{-0.5} \tag{19}$$

$$k_4 = k_3 a = \frac{a}{y_{\mathrm{STC}}} \cdot \left(\frac{\alpha_1 - \alpha_0}{\alpha - \alpha_0}\right)^{-0.5} \tag{20}$$

Now we can analyze graphically behaviors of corresponding curves (Fig. 12a, c, e). We can see for all three particular cases presented in the figure (the thickness $B = 1$ mm; the width $W = 12$ mm; $\alpha_0 = 0$) that values of k_1 decrease gradually with increasing relative crack length α (curve 1), while values of k_2 increase (curve 2). Thus, we obtain the maximum value of k_3 (the peak of curve 3) corresponding $\alpha = 0.2877$ for all three cases of the profile angle θ, namely 5°, 10°, and 15° (Fig. 12a, c, e).

With increasing the specimen thickness no change in position of curves and their peaks occur except a slight increase in peak values. Also, when the width is increased twice ($W = 24$ mm), the tendencies for the mentioned curves remain the same (a slight increase in peak values) with the same position of the peak of curve 3 ($\alpha = 0.2877$) for all three cases of the profile angle θ (Fig. 12b, d, f).

Similarly to this, at $\alpha_0 = 0$ we can see the peak of k_4 (curve 4) corresponding $\alpha = 0.5016$ for the cases of the profile angle while $\alpha_1 > 0.5016$ (Fig. 12a). The magnitude of maximum k_4 value only depends on the constants in Eq. (15). Also, a sharp kink in line 4 is observed for these cases at the positions corresponding α_1 where the cracks put out of the chevron profiles. It is because of k_2 values which are equal to 1 after curve 2 reaches the position of α_1. When the width is increased twice ($W = 24$ mm), the kink in line 4 is shifted toward lower values of α because of $\alpha_1 < 0.5016$ (Fig. 12b, d, f).

So we can conclude that independently of the profile angle of a specimen, its geometry parameters, and fracture toughness of tested material, the position of maximum

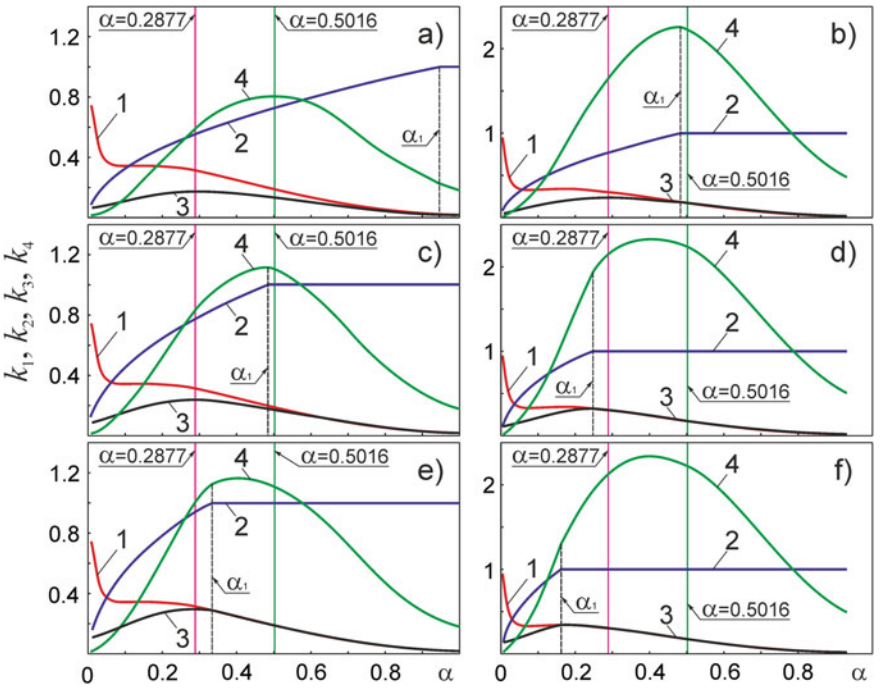

Fig. 12 Dimensionless constituents k_1, k_2, k_3, and k_4 [according to Eqs. (17)–(20)] versus the relative crack length α dependences for analyzing the parameter-depending tendencies of change of the crack running moment M_x for the cases of the specimen width 12 mm **(a**, **c**, **e)** and 24 mm **(b**, **d**, **f)**, and the profile angle θ of 5° **(a**, **b)**, 10° **(c**, **d)**, and 15° **(e**, **f)**. The specimen thickness for all the cases is 1 mm. Curves 1–4 correspond to the constituents k_1–k_4

crack running moment M_x (in case of $\alpha_0 = 0$ and $\alpha_1 > 0.5016$) is strictly at $\alpha = 0.5016$. When $\alpha_0 > 0$, then curve 2 and its kink are shifted towards higher values of α. Respectively, the peaks of curves 3 and 4 are shifted in a similar way. These changes in positions of curves 2–4 are followed by a slight lowering of their peak values.

Now we have to evaluate the conditions of crack growth in specimen profiles of a certain material. In the beginning, we can take into account a range of the fracture toughness K_{Ic} of 1.9–3.4 MPa $m^{1/2}$ for the YSZ–Ni cermet presented in [1]. Assuming the conditions of crack growth when the stress intensity factor K_{CN} is equal to critical one, i.e., $K_{CN} = K_{Ic}$ (for the boundary conditions of the YSZ–Ni cermet behavior we select $K_{Ic} = 1.9$ MPa $m^{1/2}$), corresponding data sets of the crack running moment, M_x, and the actual crack length, Δa, for the YSZ–Ni compact specimens of symmetrical chevron cross sections with the profile angle θ in the range 5°–60° were calculated according to Eq. (15). Then, corresponding dependences were plotted for three particular cases of the specimen thickness, B, equal to 1 mm, 2 mm, and 3 mm (Fig. 13a–c, respectively; the specimen width $W = 12$ mm; $\alpha_0 = 0$).

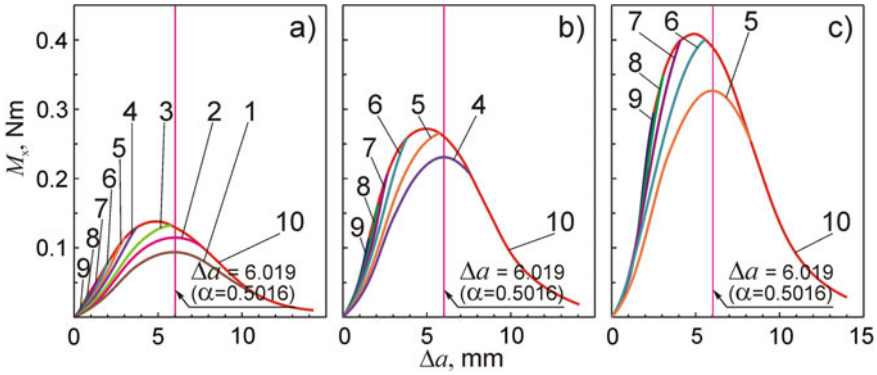

Fig. 13 Crack running moment, M_x, versus the actual crack length, Δa, dependences for chevron notched compact specimens of the thickness 1 mm **(a)**, 2 mm **(b)**, and 3 mm **(c)**. The specimen width is 12 mm, and the distance from the load line to the tip of chevron notch $a_0 = 0$ for all the cases. Curves 1–9 correspond to the symmetrical chevron profile angle θ of 5°, 7.5°, 10°, 15°, 20°, 30°, 40°, 50°, and 60°, respectively. Curve 10 corresponds to the conditions of crack growth behind the chevron profile

It was revealed that the values of M_x increase gradually with increasing the profile angle θ (Fig. 13a–c). The higher is the specimen thickness, B, the higher is the value of M_x. There exist the peaks of M_x corresponding $\alpha = 0.5016$ for the cases of the profile angle while $\alpha_1 > 0.5016$. The magnitude of maximum M_x value only depends on the constants in Eq. (15). In fact, the kinks in "M_x versus Δa" lines corresponding positions of α_1 where the cracks put out of the chevron profiles, are observed for all the cases (Fig. 13a–c). However, in contrast to the abovementioned profiles with $\alpha_1 > 0.5016$, there are no maxima of the curves corresponding to the position of $\alpha = 0.5016$ for the cases of $\alpha_1 < 0.5016$.

Based on the constructed curves one can estimate a safe level of the applied moment for manufactured pieces of a certain geometry, which allows their reliable operation without a risk to be put out of order.

Regularities of the crack retardation kinetics. The shape-dependent crack deceleration approach [24] was used to evaluate the crack growth resistance of SOFC anode-substrate of a certain shape. Diagrams (Fig. 14) of the crack initiated at the edge of an anode-substrate with (a) parallel working surfaces (the profile angle $\theta = 0$) and (b) convex ones ($\theta > 0$) allow modeling crack growth in both the profiles using corresponding parameters of geometry and load.

If accidentally, a crack is initiated at the edge of an anode, it may advance depending on the crack profile geometry and loading conditions. One can evaluate the stress intensity factor K at the crack tip depending on the loading mode. For the case of the external gas pressure $p = 1$ MPa and the fixing pressure $n = 1$ MPa applied to the cylindrical shape anode of radius 12 mm and thickness 1 mm (see Fig. 14), we assume that these forces cause K_{III} mode of crack growth (tearing or out-of-plane shear mode), and this parameter can be defined using approximate

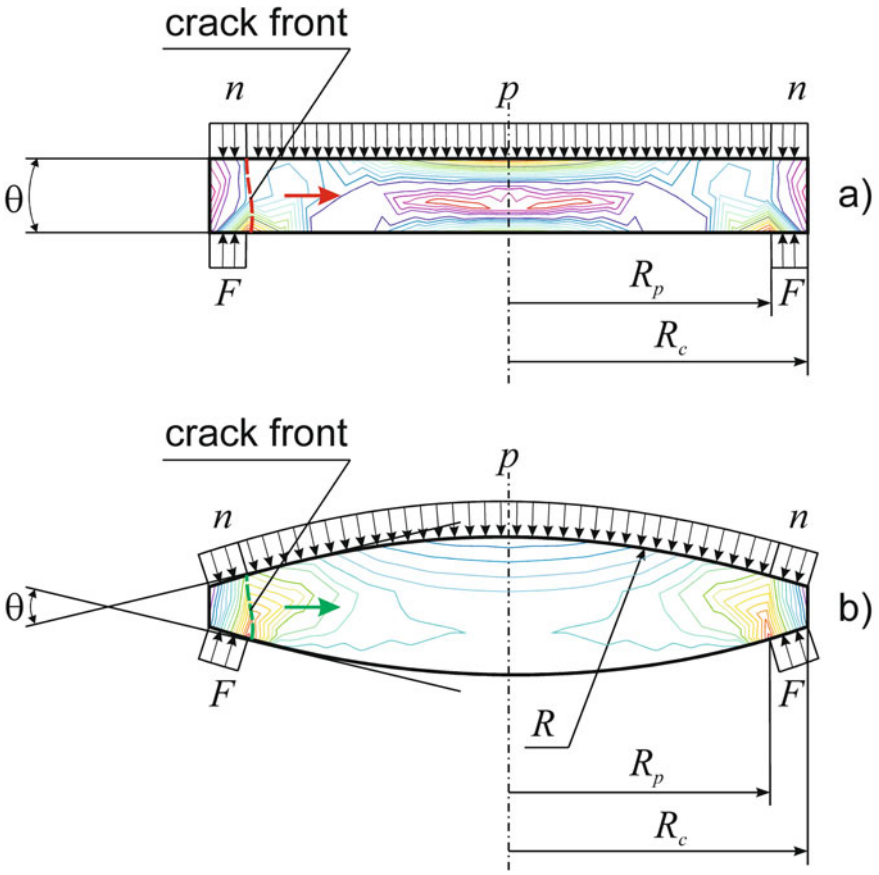

Fig. 14 Diagrams of the crack initiated at the edge of an anode-substrate with **(a)** parallel working surfaces (the profile angle $\theta = 0$) and **(b)** convex ones ($\theta > 0$). The notation is the same as in Fig. 1. A dashed line marks the crack front, and a horizontal arrow indicates the direction of crack advance for each case

correlation between K_{I} and K_{III} modes as $K_{\mathrm{III}} = \alpha K_{\mathrm{I}}$, where α is a correlation factor in the range of 0.2–0.6 [32].

We can use minimum value 0.2 of this factor to estimate ultimate stress arising in the material of an anode at equivalent conditions corresponding K_{I} mode:

$$K_{\mathrm{I}} = \frac{K_{\mathrm{III}}}{\alpha} \text{ or, } \sigma_u = \frac{p+n}{\alpha} \tag{21}$$

i.e., $\sigma_u = \frac{1+1}{0.2} = 10\,\mathrm{MPa}$

In case of a certain crack length $a = 1.5$ mm, we can calculate an equivalent value of K_{I} using a conventional formula [33] for eccentric tension of a compact precracked specimen with a straight-through notch:

$$K_{\mathrm{I}} = \sigma_u \sqrt{\pi \cdot a}, \tag{22}$$

i.e., $K_{\mathrm{I}} = 10\sqrt{0.0015\pi} = 0.7\,\mathrm{MPa\,m^{1/2}}$.

Taking into account a range of the fracture toughness K_{Ic} of 1.9–3.4 MPa $\mathrm{m}^{1/2}$ for the YSZ–Ni cermet presented in [1], we can conclude that calculated above the value of K_{I} parameter does not reach this range. That is, an initiated crack may advance subcritically at these conditions [24].

Similarly to the cylindrical shape anode, we can estimate crack growth behavior in a spheroidal shape anode. For the last having similar crack initiated at the edge, conditions of crack growth also depend on its profile and applied load. In particular, the same K_{III} value (corresponding to an equivalent value of K_{I}) is reached when a crack approaches the length of crack front 1 mm; i.e., values of the crack front length become the same for both the cylindrical and spheroidal shape anodes.

But in the case of spheroidal shape anode, a crack is already decelerated if the current value of the crack profile angle is about 10° [24].

In order to study a process of crack retardation in detail, its behavior was modeled using various R/R_{c} ratio, namely 3, 5, 15, and 20 (at constant $R_{\mathrm{c}} = 12$ mm), which allows constructing anode-substrates of four various shapes with convex working surfaces. Circumscribed figures were also drawn outside these shapes. Such modeling figures are rectangle ones with symmetrical chevron cross sections having the profile angle θ of 41.2°, 25.26°, 9.56°, and 7.55°, respectively (Fig. 15a). These profile angles correspond to the initial ones measured for the four various shapes.

The modified formula for calculating stress intensity factor K_{CN} at the crack tip in a chevron specimen can be as follows [24]:

$$K_{\mathrm{CN}} = \frac{P_X}{B}\sqrt{\frac{\pi}{W}} \cdot y_{\mathrm{STC}} \left(\frac{\alpha_1 - \alpha_0}{\alpha - \alpha_0}\right)^{0.5} \tag{23}$$

where P_{x} is the applied tensile load, B and W are the thickness and width of a specimen, respectively, a_1 is the distance from load line to the point where chevron notch intersects specimen surface, $\alpha_1 = a_1/W$, a_0 is the distance from load line to the tip of chevron notch, $\alpha_0 = a_0/W$, a is the crack length, $\alpha = a/W$ is the relative crack length (see Fig. 7); y_{STC} is determined according to Eq. (11).

The crack running load P_{x} applied to a specimen with symmetrical chevron crack profile was determined by transforming Eq. (23):

$$P_X = \frac{K_{\mathrm{CN}} \cdot B\sqrt{W}}{y_{\mathrm{STC}} \cdot \sqrt{\pi}} \cdot \left(\frac{\alpha_1 - \alpha_0}{\alpha - \alpha_0}\right)^{-0.5} \tag{24}$$

Having calculated values of P_{x} for the four profile angles, we constructed the crack running load, P_{x}, versus the crack length, a, dependences (Fig. 15b) for the modeling figures (dashed lines) with cracks of a certain length of their fronts (Fig. 15a).

Then, the stress intensity factor ratio, $K_{\mathrm{I}}/K_{\mathrm{Ic}}$, versus the crack length, a, dependences (Fig. 15c) were plotted at $P_{\mathrm{x}} = \mathrm{const}$ for corresponding shapes pointed out

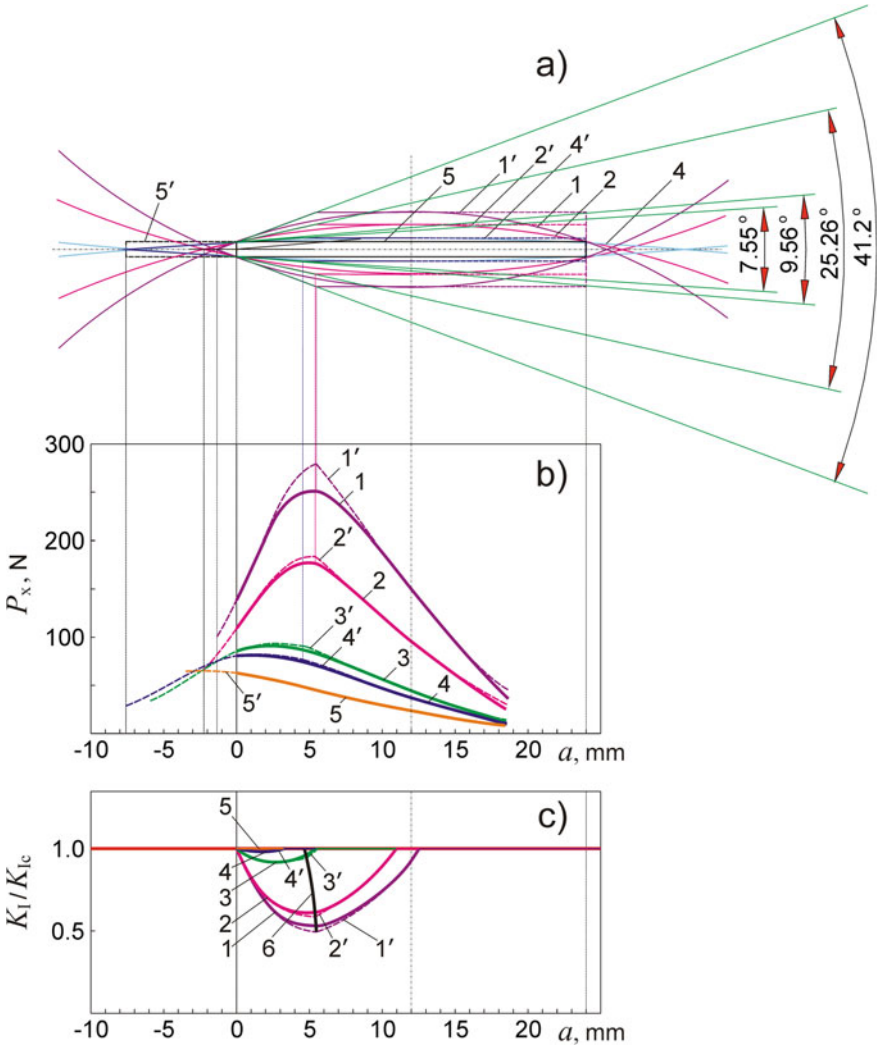

Fig. 15 Diagrams of **(a)** anode-substrates with cracks of a certain length of their fronts, and corresponding dependences of **(b)** the crack running load, P_x, versus the crack length, a, and **(c)** the stress intensity factor ratio, K_I/K_{Ic}, versus the crack length, a. The positions 1–4 (solid lines) correspond to the anodes with convex working surfaces, with the initial profile angle θ of 41.2°, 25.26°, 9.56°, and 7.55°, respectively, and parallel working surfaces ($\theta = 0$, position 5, solid lines). The positions 1′–5′ (dashed lines) correspond to circumscribed figures drawn outside the abovementioned shapes. Curve 6 marks the boundary positions where corresponding cracks put out of the chevron profiles. A horizontal line **(c)** marks the start value of the K_I/K_{Ic} ratio equal to 1, which corresponds to certain start values of P_x **(b)**. The stress intensity factor ratio, K_I/K_{Ic}, versus the crack length, a, dependences **(c)** are plotted at P_x = const for corresponding shapes

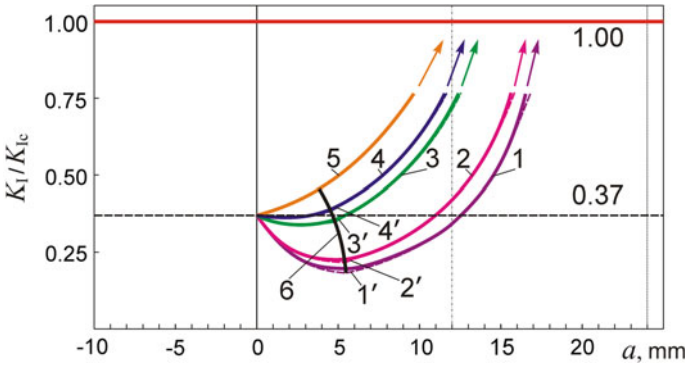

Fig. 16 Stress intensity factor ratio, K_I/K_{Ic}, versus the crack length, a, dependences for anode-substrates of various shapes (notation is the same as in Fig. 15). A horizontal dashed line marks the start value of the K_I/K_{Ic} ratio, and arrows indicate the tendencies of its change while P_x = const for corresponding shapes

above, starting from a value $K_I/K_{Ic} = 1$ which corresponds to certain start values of P_x (Fig. 15b).

Also, approximated curves for actual anode-substrate shapes (Fig. 15b, c) were constructed (solid lines) which allow predicting behavior of an initiated crack in such products. Curve 6 (Fig. 15c) marks the boundary positions where corresponding cracks put out of the chevron profiles. It can be noted that the curves for the actual shapes differ slightly from ones for the modeling figures.

When studying crack behavior at the start value of K_I/K_{Ic} equal to 0.37 (a particular case described above, $K_{Ic} = 0.7$ MPa $m^{1/2}$), one can note general tendencies of the curves for corresponding profiles (Fig. 16).

Based on Figs. 15 and 16, it can be concluded that in the case of a spheroidal shape anode, crack retardation occurs when the current value of the crack profile angle is about 10° (Fig. 15c, curve 3) or more.

So the spheroid shaped SOFC anode-substrate has a higher resistance to crack advance as compared to a conventional flat one.

Thus, a shape-dependent crack deceleration approach is a successful tool for evaluation of the resistance to crack advance in the SOFC anode-substrate of various shapes.

4 Conclusions

In this work, the improved shape of an anode-substrate for a solid oxide fuel cell has been suggested. Using the finite element analysis, the stress and strain distributions in YSZ–NiO anodes of the cylindrical and spheroidal shapes were calculated. Based on the calculations, dimensions and their ratios ranges were defined which correspond

to improved stress and strain characteristics of an anode. According to this, an anode of the cylindrical shape with top and bottom convex surfaces (a spheroidal shape anode), with an R/R_c ratio in the range from 5 to 20 is suggested. Its specific volume V/S_c is in the range from 1 to 2.5 mm. The stresses in the most dangerous areas (i.e., along the axis and the closed-loop fixing) and maximum strain, caused by the external gas pressure on the anode working surface, are decreased by 10–30% and 20–40%, respectively, as compared to an anode of the cylindrical shape of the same radius and volume features. This increases the lifetime of a solid oxide fuel cell. A three-dimensional curve of intersection of the surfaces of stress distribution in the anode along its axis and the closed-loop fixing was approximated which displays the values of balanced stresses depending on V/V_c and R/R_c parameters. The advantage of the spheroid shaped SOFC anode-substrate over conventional flat one was substantiated using a shape-dependent crack deceleration approach.

References

1. Radovic, M., & Lara-Curzio, E. (2004). Mechanical properties of tape cast nickel-based anode materials for solid oxide fuel cells before and after reduction in hydrogen. *Acta Materialia, 52,* 5747–5756. https://doi.org/10.1016/j.actamat.2004.08.023.
2. Vasyliv, B. D., Ostash, O. P., Podhurska, V. Y., et al., *Patent of Ukraine 78,992*, April 10, 2013.
3. Wang, Y., Walter, M. E., Sabolsky, K., et al. (2006). Effects of powder sizes and reduction parameters on the strength of Ni–YSZ anodes. *Solid State Ionics, 177,* 1517–1527. https://doi.org/10.1016/j.ssi.2006.07.010.
4. Vasyliv, B. D. (2009). A procedure for the investigation of mechanical and physical properties of ceramics under the conditions of biaxial bending of a disk specimen according to the ring–ring scheme. *Materials Science, 45,* 571–575. https://doi.org/10.1007/s11003-010-9215-2.
5. Vasyliv, B. D. (2010). Improvement of the electric conductivity of the material of anode in a fuel cell by the cyclic redox thermal treatment. *Materials Science, 46,* 260–264. https://doi.org/10.1007/s11003-010-9282-4.
6. Wood, A., & Waldbillig, D. (2011). *U. S. Patent 8,029,946 B2*, October 4, 2011.
7. Podhurs'ka, V. Y., Vasyliv, B. D., Ostash, O. P., et al. (2014). Structural transformations in the NiO-containing anode of ceramic fuel cells in the course of its reduction and oxidation. *Materials Science, 49*, 805–811. https://doi.org/10.1007/s11003-014-9677-8.
8. Podhurska, V., Vasyliv, B., Ostash, O., et al. (2016). Influence of treatment temperature on microstructure and properties of YSZ–NiO anode materials. *Nanoscale Research Letters*. https://doi.org/10.1186/s11671-016-1306-z.
9. Vasyliv, B., Podhurska, V., & Ostash, O. (2017). Preconditioning of the YSZ–NiO fuel cell anode in hydrogenous atmospheres containing water vapor. *Nanoscale Research Letters*. https://doi.org/10.1186/s11671-017-2038-4.
10. Song, R. H., Shin, D. R., Kim, J. H. (2007). *U. S. Patent 7,285,347 B2*, October 23 2007.
11. Bai, Y., Liu, J., Gao, H., et al. (2009). Dip coating technique in fabrication of cone-shaped anode-supported solid oxide fuel cells. *Journal of Alloys and Compounds, 480,* 554–557. https://doi.org/10.1016/j.jallcom.2009.01.089.
12. Zhang, Y., Liu, B., Tu, B., et al. (2005). Redox cycling of Ni–YSZ anode investigated by TRP technique. *Solid State Ionics, 176,* 2193–2199. https://doi.org/10.1016/j.ssi.2005.06.016.
13. Sun, B., Rudkin, R. A., & Atkinson, A. (2009). Effect of thermal cycling on residual stress and curvature of anode-supported SOFCs. *Fuel Cells, 6,* 805–813. https://doi.org/10.1002/fuce.200800133.

14. Miyazawa, T. (2011). *U. S. Patent 20110091785 A1*, April 21, 2011.
15. Ostash, O. P., Vasyliv, B. D., & Podhurska, V. Y. (2016). *Patent of Ukraine 109,256*, August 25, 2016.
16. NASA Technical Memorandum 85797. (1984). *A review of chevron-notched fracture specimens*. Hampton: Langley Research Center.
17. Nakayama, J. (1964). A bending method for direct measurement of fracture energy of brittle materials. *Japanese Journal of Applied Physics, 3,* 422–423. https://doi.org/10.1143/JJAP.3.422.
18. Nakayama, J. (1965). Direct measurement of fracture energies of brittle heterogeneous materials. *Journal of the American Ceramic Society, 43,* 583–587. https://doi.org/10.1111/j.1151-2916.1965.tb14677.x.
19. Tattersall, H. G., & Tappin, G. (1966). The work of fracture and its measurement in metals, ceramics and other materials. *Journal Materials Science, 1,* 296–301. https://doi.org/10.1007/BF00550177.
20. Pook, L. P. (1972). An approach to a quality control K_{Ic} testpiece. *International Journal of Fracture Mechanics, 8,* 103–108. https://doi.org/10.1007/BF00185202.
21. ASTM STP 410. (1966). *Plane strain crack toughness testing of high strength metallic materials*. Philadelphia: American Society for Testing and Materials.
22. Freed, C. N., & Kraft, J. M. (1966). *Journal of Materials, 1,* 770.
23. Vasyliv, B. D. (2002). In R. C. Bradt, et al. (Eds.), *Fracture mechanics of ceramics* (p. 479). New York: Kluwer Academic/Plenum Publishers.
24. Vasyliv, B. (2019). *Crack initiation and retardation in ceramics. Techniques and applications* (1st ed., pp. 143–171). Riga: LAP LAMBERT Academic Publishing.
25. Vasyliv, B. D. (2002). Initiation of a crack from the edge of a notch with oblique front in specimens of brittle materials. *Materials Science, 38,* 724–728. https://doi.org/10.1023/A:1024222709514.
26. Bower, A. F. (2009). *Applied mechanics of solids* (1st ed., pp. 27–35). Boca Raton: CRC Press, Taylor and Francis Group.
27. Barker, L. M. (1977). A simplified method for measuring plane strain fracture toughness. *Engineering Fracture Mechanics, 9,* 361–369. https://doi.org/10.1016/0013-7944(77)90028-5.
28. Munz, D., Bubsey, R. T., & Srawley, J. E. (1980). Compliance and stress intensity coefficients for short bar specimens with chevron notches. *International Journal of Fracture, 16,* 359–374. https://doi.org/10.1007/BF00018240.
29. Munz, D. (1981). Determination of fracture toughness of high strength aluminum alloys with chevron notched short rod and short bar specimens. *Engineering Fracture Mechanics, 15,* 231–236. https://doi.org/10.1016/0013-7944(81)90120-X.
30. Palmquist, S. (1962). Rissbildungsarbeit bei Vickers-Eindrücken als Mass für die Zähigkeit von Hartmetallen. *Archiw für Eisenhüttenwesen, 33,* 629–634. https://doi.org/10.1002/srin.196203379.
31. Pouvreau, C. (2007). Dissertation, Ecole Polytechnique Federale de Lausanne.
32. Pook, L. (1985). The fatigue crack direction and threshold behavior of mild steel under mixed mode I and III loading. *International Journal of Fatigue, 7,* 21–30. https://doi.org/10.1016/0142-1123(85)90004-0.
33. ASTM STP 381 (1965). *Stress analysis of cracks*. Philadelphia: American Society for Testing and Materials.

Advances in Nano-Materials Used in Photovoltaic/Thermal Systems

Ali H. A. Al-Waeli and Hussein A. Kazem

Abstract The key step for using nanoparticles for heat transfer applications is to prepare nanofluids, either through the one-step or two-step method. Among applications of nanofluids in heat transfer are to use them as working fluid for hybrid photovoltaic thermal (PV/T) systems. PV/T systems combine photovoltaic modules and solar thermal collectors to produce hot water and electricity simultaneously. This chapter presents classifications of PV/T systems, principles, and performance. Moreover, detailed introduction to nano-material is used for PV/T systems and related parameters such as volume fraction (%) and mass flow rate. Furthermore, the chapter provides a case study of three different PV/T systems which are nanofluid and nano-phase change material (nano-PCM)-based PV/T, a water-based PV/T with a PCM tank, and water-based PV/T with water tank. The findings show an overall improvement in thermo-physical properties as nanoparticles are added to base fluid (water) and phase change material (PCM). Moreover, the highest performance is attributed to the nanofluid and nano-PCM-based PV/T system.

Keywords Nanofluid · Nano-SiC · Nano-PCM · PV/T · Collectors

1 Introduction

Human population growth is expected to peak at around 9 billion in 2050, according to the predictions of the United Nations' population division [1]. With this continuous rise in the population, so does the energy demand. This is because energy is simple a proactive agent in raising the standard of living and prompting change in the social conditions as well [2]. World energy use is projected to increase from its current value

A. H. A. Al-Waeli · H. A. Kazem (✉)
Solar Energy Research Institute, Universiti Kebangsaan Malaysia, 43600 Bangi, Selangor, Malaysia
e-mail: h.kazem@soharuni.edu.om

H. A. Kazem
Faculty of Engineering, Sohar University, PO Box 44, 311 Sohar, Oman

S. J. Ikhmayies (ed.), *Advances in Energy Materials*,
Advances in Material Research and Technology,
https://doi.org/10.1007/978-3-030-50108-2_5

of 9000 million tonnes of oil equivalent to around 21,000 Mtoe/a as the population increase from 6 to 12 billion people in the twenty-second century.

Energy sources such as coal, oil, and gas or also known collectively as fossil fuels take up around 80% of global energy sources [3]. The remaining are renewable energy sources, except for uranium. The mass production and consumption of fossil fuels by human activity were known as contributor to climate change, making it a concern, as well as the depletion of fossil fuels [4]. On the other hand, renewable energy exhibits favorable characteristics as energy resources. Hence, many countries have shifted their energy policy to adopt renewable energy technologies investment and utilization for industrial, commercial, and residential purposes. Among these countries are China, the EU, and the USA.

Among renewable energy technologies is the solar cell, or photovoltaic (PV), which is the most commonly implemented by residential users. This is attributed to its relatively cheap cost, low weight, and zero noise during operation. The projected solar (PV) capacity growth from 2017 to 2022 is around 438 GW [5].

Photovoltaics are semiconductor devices that convert the sunlight into electricity by utilization of sunlight photon energy. Solar cells, PV, are made of different semiconductors including silicon such as CdS/CdTe and CIGS. PV does not utilize the infrared part of the solar spectrum; hence, the PV cell temperature increases across time of operation. Internal losses due to manufacturing and heat gained through surrounding environment lead to an increase in the cell temperature which results in a reduction in the open-circuit voltage. This means the electric power produced by this device will decrease as a result of the device heating up. Hence, every increase of 10 °C causes a decrease in PV efficiency of around 5% [6]. This is particularly the issue in hot climate and high solar irradiance areas. Moreover, this leads to shortening the lifetime of the device. Hence, several researchers and scientists have recommended the removal of the heat from the device using cooling fluids. This would involve a channel to carry a fluid which removes the temperature from the solar cell and utilize it in other applications. This design is known as photovoltaic/thermal (PV/T) hybrid collector. The heating of fluids is the function of the solar thermal collector. Hence, PV/T is essentially composed of a photovoltaic module and a solar thermal collector, attached for heat transfer purposes. The PV module will then be cooled, while fluid within the thermal collector will be heated. The type of fluid that runs through a PV/T collector is a critical factor. Given that, different fluids have different thermo-physical properties. PV/T collectors are usually classified depending on the type of base fluid [7]. Figure 1 shows the classifications of PV/T collectors.

According to Fig. 1, the types of PV/T include air-based, water-based, combi (air and water), phase change material (PCM)-based. The classifications are determined either with the number of passes within the collector, shape of pipe, type of concentrator or reflector used to maximize efficiency and working fluid.

The air-based design is considered the cheapest because of the simplicity of the system. Moreover, the use of air instead of a liquid leads to eliminate the risk of freezing, boiling, and damage (due to leak). On the other hand, the thermal performance of this type of collector is considered the lowest. This is because of its low

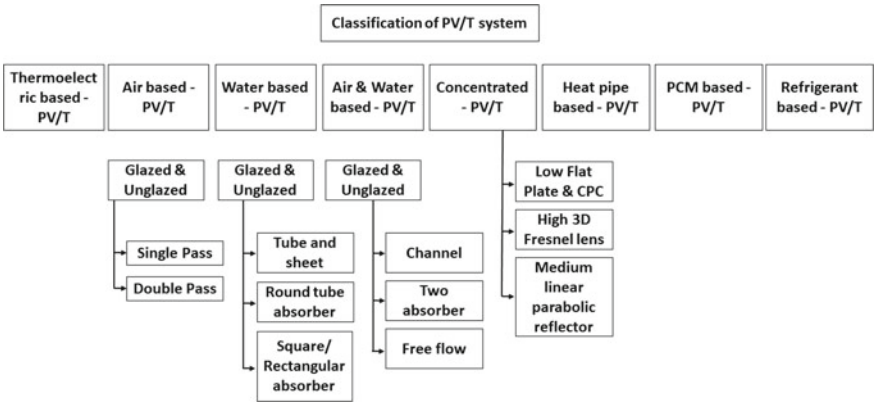

Fig. 1 Classifications of photovoltaic thermal (PV/T) collector

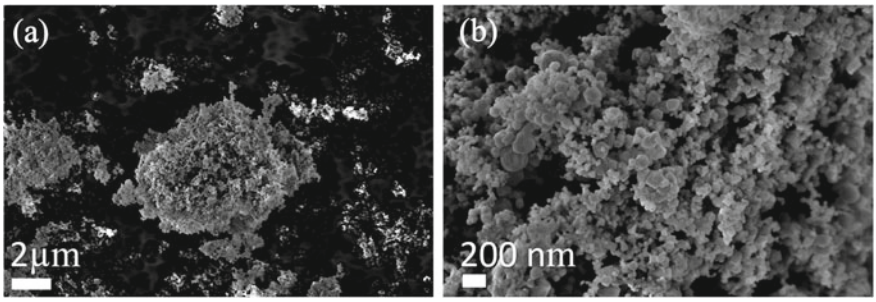

Fig. 2 **a** SiC image at 2 μm, **b** SiC image at 200 nm

heat capacity, which leads to a low heat transfer. On the other hand, water has better thermal capacity and hence better heat transfer. While water-based PV/T does exhibit better thermal performance, it is more expensive and with more risks. Water-type is most suitable for hot-water demand. Water circulates through the pipes and is supplied to the user [8]. Bi-fluid design which combines water and air is useful for cooling PV module and extracting heat. The design could be made to be thermally biased or electrically biased, depending on the consumer's needs, and/or limitations. Different refrigerants could be used for the system, e.g. R134a, such as those employed for heat pump cycles. Heat pipes on the other hand use different base fluids according to the wall and wick of the heat pipe, which are designed to operate for longer periods and minimal maintenance.

Because of the effect of base fluid thermo-physical properties on heat transfer, nanofluid was introduced as a base fluid for PV/T collectors. Nanofluids are mixtures of base fluids and nano-material.

This chapter introduces nano-material's used in PV/T collectors and provides the description of the advances of these nano-materials and PV/T collectors, mixing

process to produce nanofluids and their effect on thermal and electrical efficiencies of PV/T. Along with referenced works in the literature, actual experiments are carried out by the authors of this chapter to examine different types of nanofluids.

2 PV/T Principle and Performance

Photovoltaic component of PV/T produces electricity, while solar thermal component provides the function of cooling the PV and heating up the working fluid. Each device has an efficiency based on its output. Efficiency is a great indicator of the system's functionality and performance.

The PV efficiency is simply the ratio of its output electric energy to input solar energy. Equation (1) illustrates the electrical efficiency of PV cell [9]:

$$\eta_{\text{el}} = \frac{P_{\text{max}}}{A_{\text{c}} \times G} \tag{1}$$

where P_{max} is the maximum electrical power, A_{c} is the collector area, and G is the solar irradiance (W/m^2). On the other hand, the thermal efficiency of solar thermal collector is given in Eq. (2) [10].

$$\eta_{\text{th}} = \frac{Q_{\text{u}}}{A_{\text{c}} \times G} \tag{2}$$

where Q_{u} is the heat gain of solar collector.

The efficiency for a whole day can be calculated by integration of the solar irradiance and output power (both for electrical and thermal). As the hybrid PV/T combines both components, the efficiency of PV/T is given in Eq. 3 [11].

$$\eta_{\text{tot}} = \eta_{\text{th}} + \eta_{\text{el}} \tag{3}$$

where η_{tot} is the total efficiency of PV/T. The energy-saving efficiency offers a more accurate description of how much energy is actually produced by dividing electrical efficiency by the efficiency of the electric power generation of a conventional power plant. The power generation efficiency is usually taken as 40%.

The performance of the PV/T is affected by multiple factors including solar irradiance, ambient temperature, climate conditions, type of working fluid, mass flow rate of working fluid, and type of thermal collector material. Majority of these factors are displayed by the literature provided.

Shahsavar and Ameri [12] used air-based direct-coupled PV/T collector to investigate the effect of a thin aluminum sheet suspended at the middle of air channel. This sheet was employed to increase the heat transfer surface. The system was tested experimentally and validated with a theoretical model. Moreover, the system was tested for natural and forced convection. For the forced, various fans operating in the

model were used. The study concludes that there are an optimum number of fans to achieve maximum electrical efficiency and that increase in mass flow rate leads to better heat transfer. Finally, authors confirm that glazed PV/T has higher efficiency than unglazed. These findings are important for understanding the effect of mass flow rate, glazing, and heat transfer area has on PV/T performance.

Sopian et al. [13] performed a comparative study between double- and single-pass PV/T collectors. The study concludes that double pass exhibits higher efficiency than single. Moreover, the study affirms that increase of mass flow rate, up to a level, leads to electricity efficiency enhancement. Beyond the appropriate mass flow rate, the efficiency will in fact decline. Aside from mass flow rate, number of fluid channels has a significant effect on collector performance. Chow [14] also investigated the effect of PV/T parameters on its performance, e.g. flow rate. The investigation was carried out using an explicit dynamic model which allows for performance analysis. Chow believes that PV/T is dynamic, and that steady-state models are not favorable. Main concern for the authors is inability of steady-state model to predict PV working temperature, and heat-removal during fluctuations in irradiance and/or fluid flow.

PV/T is heavily influenced by its design. Certain design modifications could lead to higher heat transfer and hence overall total efficiency. Kumar and Rosen [15] added fins, vertical extension surfaces, to thermal collector of a double-pass PV/T system. Design, climate, and operation parameters were taken into consideration, as they have direct impact on device efficiency. Significant reduction in PV cell temperature, attributed to the addition of fins, was observed with around 16 °C drop. The design aspect is also investigated by Zondag et al. [16] where different designs were compared in terms of performance. Massive heat losses are observed for uncovered sheet and tube collector which caused the poorest performance among collectors. Fall of electrical efficiency of a sheet and tube with two covers, due to further reflection at the second cover. Authors state the importance of calculating optical efficiency as well as thermal. Hence, reducing heat losses to surroundings could be attributed to glass covers, but also reduction of energy absorption, by reflection, which is explained by Sandnes and Rekstad [17] as well. Authors see a 10% reduction in energy absorption, which is significant.

The configuration of the PV/T plays a role as well. It is important to do more research in that area. Dubey and Tiwari [18] analyzed water-based PV/T connected in series, using theoretical and analytical methods. They utilized energy balance equations to develop the analytical expression of N number of collectors. Changing the number of collectors connected in series and viewing its effect on exergy and also analyzing electrical and thermal energy, for five different cities in India. The electrical efficiency of four PV/T collectors connected in series was found to be higher than 10 connected in series.

A steady-state conditions model was used by Dupeyrat et al. [19] to study thermal and electrical performance of several glazed, water-based PV/T flat plates. The single package lamination method was used for the experiments. The focus of the experiments was on heat transfer and optical performance. With regard to optical tools, linear Fresnel concentrators are also investigated in the literature. With this type

of collectors, along with a 2D axis tracking, Rosell et al. [20] achieved an overall combined efficiency above 60% when the ratio of the concentration was above 6.

The literature in PV/T collectors is vast, and there are numerous works on the subject. This is attributed to the different fields this technology is linked to, and the number of factors associated with PV and solar thermal collectors. Table 1 shows a summary of the aforementioned research studies to provide an impression of general research in the area. It is very important for research in this field to be limited in scope. Considering, every aspect of the collector would cause too many complications to the study. It is noteworthy to mention that Table 1 does not reflect on the research field of PV/T, nor it is used as a sample representation.

Table 1 shows the year, location, type of investigated PV/T, method of investigation, investigated parameters, and the achieved maximum efficiency (theoretical or measured). The general trend in this table is the use of both experimental and theoretical modeling. Almost every single research includes investigation into mass flow rate, which is a critical factor in thermal performance of this collector. The highest thermal efficiency is around 75%, while the highest electrical efficiency 16%. These two values are merely mentioned to give an impression of the electrical and thermal outer range. Overall, the water-based PV/T designs exhibit higher thermal efficiency and better thermal performance. Optical efficiency seems to be a recurrent topic of discussion and consideration. The discussed literature proves the importance of each aspect of PV/T in terms of design, operation, and weather conditions. As explained in the introduction, nanofluids have better thermo-physical properties than water [21–25]. Hence, it is very reasonable to employ nanofluids in PV/T collector to enhance the heat transfer process. The next section provides introduction to nano-material, in-depth analysis of their thermo-physical properties and application in PV/T cooling.

3 Nano-Materials Used for PV/T Cooling

Nano-materials are nano-sized particles with a diameter between 10 and 100 nm (nano-scale). The origin of the word nano is Nanos which is Greek for dwarf, which historically implies small size. Hence, nano is commonly used as an abbreviation of nanotechnology. Nanoparticles are a product of this technology and are used for many purposes and exist in different types. Among these types are metals, alloys, semiconductors, ceramics, glasses, polymers, and inorganic carbon-based material. These nanoparticles exhibit better properties due to its high surface area-to-volume ratio, compared to large particles. This means that nano-materials will be more chemically reactive [26].

The applications of nano-materials, of different types, are immense. The following are different applications of nano-materials for different industries.

1. Template material
2. Electronics
3. Solar cells

Table 1 Summary of studies on photovoltaic thermal collectors

Reference	Year	Location	Type of investigated PV/T	Method of investigation	Investigated parameter	Max. Efficiencies
Shahsavar and Ameri [12]	2010	Iran	Direct-coupled air type	Experimental, and modeling	Glazing, mass flow rate, natural and forced convection	Thermal: around 60% Electrical: Around 10%
Sopian et al. [13]	1996	Malaysia	Single and double-pass air-based PV/T	Theoretical modeling	Packing factors, mass flow rate, absorber length, pass	Highest by double pass Electrical: 7.5% Thermal: 33%
Chow [14]	2003	China	Water-based PV/T with tube pipes	Experimental and Numerical	Mass flow rate, solar irradiance	Thermal: 60% Electrical: 10%
Kumar and Rosen [15]	2011	Canada	Double pass, air-based PV/T with/without fins	Theoretical modeling	Inlet air temperature, mass flow rate, Solar irradiance, fins, packing factor, depth of air channel	Electrical: 16% Thermal: 64%
Zondag et al. [16]	2003	The Netherlands	Free flow, two-absorber, channel, tube and sheet, PV/T designs	Theoretical, refers to some experimental studies	Collector design type, covers, insulation, opaque/transparent PV	Electrical: 7.9% (Tube and sheet) Thermal: 39% two-absorber insulated
Sandnes and Rekstad [17]	2002	Norway	Water-based PV/T	Experimental, and analytical model	Collector configuration, inlet fluid temperature	Electrical: 13.4% Thermal: 70%
Dubey and Tiwari [18]	2009	India	Water-based PV/T flat plate	Theoretical	Number of collectors series connection, solar intensity, mass flow rate	Electrical: 10.7% Thermal: 62% For 4 collector in series
Dupeyrat et al. [19]	2011	Germany	Glazed, water-based PV/T flat plate	2D theoretical model and experiments	Packing factor, inlet fluid and ambient temperatures	Thermal: 75% Electrical: 10.9%
Rosell et al. [20]	2005	Spain	linear Fresnel concentrator with a channel PV/T collector	Experiments, and theoretical model	Fresnel concentration, mass flow rate	Thermal: 65.8% Electrical: 13.5%

4. Biological sensors
5. Gas sensing nanoprobes.

There are many more applications to different nanoparticles. Heat transfer is a very important application in industry.

Nanofluids are suitable for heat transfer processes. Nanofluids are nanoparticles mixed with a base fluid. The synthesis of these nanoparticles is classified into two methods which are physical and chemical. The most popular physical method is the inter-gas evaporation technique [27]. Other physical methods include sputtering technique and mechanical deformation. The chemical method of synthesis can be divided into two:

1. Thermal and ultrasound decomposition methods.
2. Reduction methods.

However, the main issue associated with the chemical method is the chemical homogeneity of the final product.

On the other hand, the base fluid to mix with the nanoparticles is also important. There are different types of base fluid's depending on the application, final product intended. Most common base fluids used are (1) water and (2) ethylene glycol.

Water is common because it possesses the highest heat capacity per unit mass of all substances. Moreover, it is abundant and cheap. Ethylene glycol (EG) is a dihydric alcohol that is composed of two-hydroxyl-groups, making it highly soluble in water, and is connected to both sides of an aliphatic carbon chain. In addition, it can easily mix with many polar solvents. Both fluids, water and EG, are similar in being odorless, colorless, and clear [28].

Several mechanisms affect the nanoparticles as they travel through base fluid, including gravity, Brownian motion, and thermophoresis. In order to understand these concepts, it is important to understand what they affect, which is the thermo-physical properties of the produced nanofluid, or base fluid.

Thermo-physical properties are simply material properties which vary with temperature without altering the chemical identity of the material. This term is commonly used to describe the properties associated with transfer and storage of heat [29]. These properties will include thermal conductivity, viscosity, and density. Thermally, it also includes diffusivity, heat capacity, thermal expansion, and thermal radiative properties, as well as mass and thermal diffusion coefficients.

All properties are of interest in the field of nanofluids. This is because nanofluids are commonly used to transfer heat. Nanofluid-based PV/T collectors are effective due to the thermo-physical properties of the working fluid. Thermal conductivity is basically the property of a material to conduct heat. It is expressed with the general formula given by Eq. (4):

$$\vec{q} = -k \overrightarrow{\nabla} T \tag{4}$$

where $\vec{q}$ is the heat flux, k is the thermal conductivity, and $\overrightarrow{\nabla} T$ is the temperature-gradient.

Viscosity of a fluid is a measure of its resistance to gradual deformation by shear stress or tensile stress. It can be tested using different types of viscometers and rheometers. The shear viscosity formula is expressed in Eq. (5).

$$\mu = \frac{Fy}{Au} \tag{5}$$

where μ is the dynamic viscosity, F and y are the applied force into the separation distance, respectively. A and u are the area of each plate and speed, respectively.

Density of a material is its ratio of mass per volume. Equation 6 describes the density.

$$\rho = \frac{m}{v} \tag{6}$$

where ρ is the density, m and v are the mass and volume, respectively.

The effect of these thermo-physical properties is immense for solar heaters and PV/T collectors. They can affect parameters such as the heat transfer coefficient, which is the constant of proportionality between the heat flux and the thermodynamic driving force for the flow of heat. The coefficient is expressed in Eq. (7):

$$h = \frac{q}{\Delta T} \tag{7}$$

where h is the heat transfer coefficient, and q is the heat flux.

An example of the effect of thermo-physical properties is thermal conductivity's effect on the heat transfer coefficient. This is expressed in Eq. (8):

$$h = \frac{k}{l} \tag{8}$$

where h is the heat transfer coefficient of an object, k is its thermal conductivity, and l is the thickness of that object. Nanofluids have higher thermal conductivity and viscosity than water [30]; Meaning, systems utilizing nanofluids will have a better heat transfer coefficient.

Nanofluid preparation can be classified into two methods: 1-step method and the 2-step method. The most common due to its relatively cheap price is the 2-step method. The nano-materials are imported in powder form and then mixed with the base fluid. The mixing process usually involves shaking, spinning, and applying temperature. Most researchers utilize ultrasonic baths when preparing nanofluids for PV/T systems. Type, size, and volume fraction of the nano-material play major role, along with type of base fluid, in the resultant nanofluid's thermo-physical properties.

Volume fraction (φ_i) is the volume of a constituent (V_i) divided by the volume of all constituents of the mixture V prior to mixing. This is expressed in Eq. (9) [31]:

$$\varphi_i = \frac{V_i}{\sum_j V_j} \tag{9}$$

Wang and Xu [32] studied the effective thermal conductivity of alumina (Al_2O_3) and copper oxide (CuO) nanofluids with diameters of 28 nm and 23 nm, respectively. This was done by mixing the nano-material with different base fluids and measuring the thermal conductivity using steady-state parallel-plate method. The authors [32] found an increase in thermal conductivity of all base fluid's as a resultant of mixing them with nanoparticles. Moreover, the authors [32] state the decrease in the nanoparticle size leads to increase in the thermal conductivity. Finally, the dispersion method is acknowledged as an important contributor to thermal conductivity. The authors [32] used three methods for mixing the nanoparticles and base fluids: mechanical blending, coating particles with polymers, and filtration. The blending was executed using an ultrasonic bath. The filtration method resulted in the highest increase in thermal conductivity, 12% with 3 vol% particles in water, for Al_2O_3 nanofluid. However, the thermal conductivity of the same nano-material mixed with ethylene glycol, at same volume fraction, is higher. From this research, done by the authors [32], the importance of volume fraction, type and size of nano-material is highlighted, along with importance of base fluid.

According to Prasher et al. [33], increase in the viscosity is greater than thermal conductivity enhancement for nanofluids which is observed in the literature. The letter reports increase in nanofluids viscosity corresponding to increase in its volume fraction, across different types of base fluids. Moreover, the authors [33] illustrated that relative viscosity does not vary significantly with temperature. Another element to consider in the preparation of nanofluids is the stability, which is heavily linked to the type of surfactant employed, and the quality of mixing process.

Drzazga et al. [34] prepared Al_2O_3 and CuO nanofluids using the two-step method, with different stabilizers, SHMP and acetic acid, to investigate the effect of the preparation method, and stabilizers on nanofluid stability for both types. Good stability of CuO-water nanofluid was obtained for 1% mass of SHMP while poor stability of γ-Al_2O_3-water nanofluid was received for all investigated stabilizers.

The density of nanofluids decreases with the increase of the volume fraction, as illustrated by Prakash et al. [35]. The study investigated two types of nanofluids, CuO-water and TiO_2-water. Density of TiO_2 nanofluid is significantly lower than that of CuO nanofluid, for the same volume fraction. Moreover, increase in viscosity and thermal conductivity was observed, corresponding to increase in nanofluid volume fraction, for both fluids.

A common method to understanding the nano-material implemented is to utilize different scanning methods such as field emission scanning electron microscope (FESEM), X-ray diffraction (XRD) or energy-dispersive X-ray spectroscopy (EDX). FESEM images a sample surface by raster scanning over it with a high-energy beam of electrons. It allows for the characterization of size, size distribution, and measurement of height and lateral dimensions. It provides a correlation between surface appearance and morphology. Figure 1 shows an FESEM image of SiC nanoparticles at the 2 μm

range and the 200 nm range. Among important information to surmise from FESEM is the uniformity of particles or observing change in the morphology of the particles.

X-ray diffraction is a technique that is used for the structural characterization of solid and fluid materials in different ranges including the nanometer (nm) range. This method can be used to test and identify the crystallite size, shape, lattice distortions, and faulting. Also, the composition variations, orientation and phase composition [36]. Figure 3 shows XRD results for the same nano-material, SiC, used in Fig. 2.

Various research works for nanofluid-based PV/T collectors were conducted in the past decade [37–41] which addressing the nanofluid-related parameters [42, 43], PV/T design and material parameters [44, 45], and the operational parameters [46, 47]. Different system designs of nanofluid-based PV/T collectors are proposed and tested [48, 49]. The different designs include flat plate [50], nanofluid impingement jet [51], and nanofluid spectral splitting filter [52].

Yousefi et al. [53] examined the viability of Al_2O_3 nanofluid as a heat absorber medium for a flat-plate solar collector. The study investigates the impact of mass flow rate and mass fraction of nanoparticles on thermal efficiency of the collector. The mass flow rate varies from 1 to 3 L per minute for two mass fractions, 0.2% and 0.4%, respectively. The results obtained showed increase in efficiency corresponding to increase of mass flow rate, at constant nanofluid concentration.

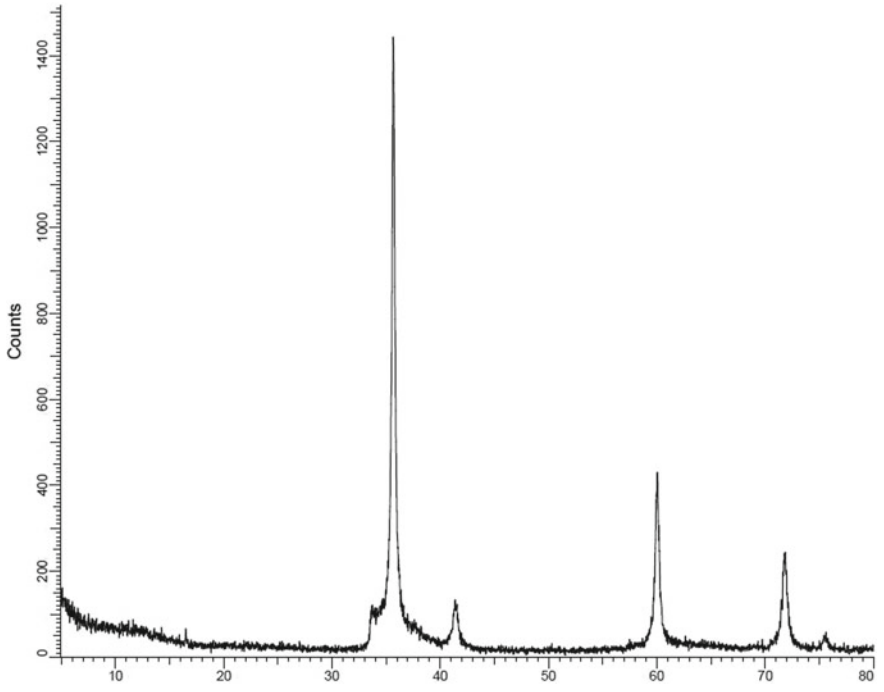

Fig. 3 X-ray diffraction of SiC

Zeinali Heris et al. [54] performed a numerical investigation on the convective heat transfer of three types of nanofluids. The channel of flow had a square cross section, with a laminar flow. The study focused on adjusting diameter and volume fraction of the nanoparticles and observing the effects on the fluid. The finds show an enhancement in heat transfer for two conditions. The first, when decreasing the nanoparticle size and fixing the volume fraction for all fluids. The second, when increasing nanoparticle volume fraction and keeping the particle size fixed.

Hwang et al. [55] also investigated multiple nanofluids in terms of conductivity. The nanofluids are multiwall carbon nanotubes (MWCNT), CuO, SiO_2. All with water is as the base fluid. The study reports a significant increase in fluid thermal conductivity (the conductivity increased more than 150% when small—about 1% of nanoparticles was added).

Sardarabadi et al. [56] experimentally studied an SiO_2 nanofluid-based PV/T. The study aimed to assess the impact different weight percentages, 1% and 3%, had on the electrical and thermal efficiencies. The authors [56] performed an uncertainty analysis to measure the inaccuracy. Adding 1% and 3% nanoparticles to water caused an increase in PV/T energy efficiency by 3.6% and 7.9%, respectively. This was done by converting produced electric power into equivalent thermal energy. As for thermal efficiency, it was increased by 7.6% and 12.8% for 1 wt% and 2 wt%, respectively. The total exergy was compared to a water-based PV/T and a conventional PV. Water-based PV/T, 1%-SiO_2-nanofluid, and 3%-SiO_2-nanofluid led to an increase in total exergy by 19.36%, 22.61%, and 24.31%, respectively.

Other methods of cooling or maintaining PV module temperature were introduced in this field. Among these methods is the use of phase change material (PCM). Organic PCM has been used to store and release temperature. PCMs are stable, non-toxic, recyclable, non-reactive, non-corrosive and available for wide phase change temperature selection. Simply, according to the required application, paraffin wax PCM is used for thermal storage to maximize thermal efficiency for PV/T collectors. PCM-based PVs and PV/Ts have massive potential for development. Ma et al. [57] presented a comprehensive review on PCM use in PV systems, for thermal regulation and electrical efficiency improvement. Various systems and emerging concepts were discussed in detail including aspects such as system development, performance evaluation, materials selection, heat transfer improvement, and numerical models. The study raises a concern on the economic-feasibility in enhancing PV efficiency only. PV/T systems utilizing PCM has a better potential, giving that the thermal storage could be extracted using a working fluid. Preet et al. [58] performed an outdoors experimental investigation of a water-based PV/T with and without PCM and compared the collectors to conventional PV system. The authors [58] integrated copper pipes to carry the water. Paraffin wax (RT-30) was used as the PCM. The study used three mass flow rates, which are 0.013 kg/s, 0.023 kg/s, 0.031 kg/s to investigate effect of mass flow rate on thermal and electrical efficiencies. The authors [58] found that overtime, the electrical efficiency of the PV/T with PCM becomes higher, while thermal efficiency of the PV/T without PCM becomes higher, which seems like a trade-off that must be taken into consideration. Nano-PCMs are preferred due to having higher heat release rates, compared to base fluids, which is attributed to

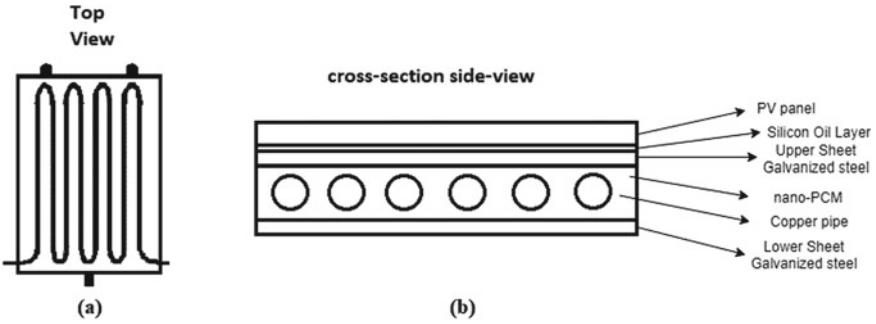

Fig. 4 **a** Top-view, **b** side-view drawings of the proposed PV/T

increase of thermal conductivity and reduction of latent heat. Fan and Khodadadi [59] performed both experimental and theoretical investigations to study freezing nano-PCM in container in vertical configuration. The experiments were used to validate the theoretical model established using a modified 1-D Stephan model. The solidification process was studied by Khodadadi and Hosseinizadeh [60] numerically using a square cavity which stores nano-PCM and is differentially heated. The results of the study show how higher rates of heat are released by the nano-PCM over the typical PCM medium and mainly attributed those outcomes to increase and reduction of thermal conductivity and latent heat, respectively.

The evolution of nano-material in PV/T systems continues to provide more innovative systems with better overall performance. In 2017, the authors of this work, Al-Waeli et al. [61], introduced a novel method and design of a hybrid nanofluid and nano-PCM-based PV/T. The collector was designed for maximum PV-cooling and thermal production. The concept was to increase the thermal conductivity of PCM by employing nanoparticles, or else known as nano-PCM. Nanofluids were added for optimum extraction of heat. The side-view and top-view drawings are given in Fig. 4.

The system was designed for optimum heat transfer. This was achieved by employing high thermal conductivity material such as nanofluids and nano-PCM. Moreover, as Fig. 4 shows, the system utilizes galvanized steel and copper as well. The copper pipes are emerged into a layer of nano-PCM which is stored at the back of PV module. The nanofluid will flow within these copper pipes. To ensure higher heat transfer, glass wool was implemented for thermal insulation. The system consisted of the proposed PV/T collector, a heat exchanger, a nanofluid tank, an expansion tank, the proper sensors, and control devices. In-between the PV and the nano-PCM tank, silicon oil was implemented to avoid air-gaps for better heat transfer. Moreover, the tank covered the whole area on the back of the PV for better cooling and heat transfer. Figure 5 shows the schematic diagram of the combined system.

The operation of the system is dependent on the nanofluid cycling through the PV/T, extracting heat, and the heat exchanger, transferring heat to water. By the start of every cycle, the nanofluid must be cooled-down for maximum heat transfer. The

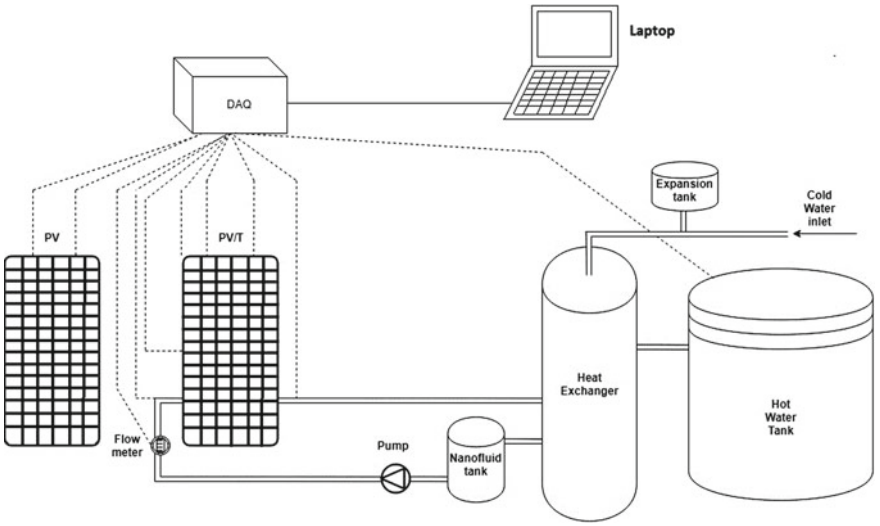

Fig. 5 Schematic diagram of the nanofluid and nano-PCM-based PV/T

nanofluid itself must be made so that it has high thermal conductivity and viscosity. This is done by performing accurate mixing and shaking of nanoparticles in the base fluid. The nano-PCM must be prepared effectively as well. Figure 6 shows the preparation of the nano-PCM.

Fig. 6 Preparation of nano-PCM using ultrasonic bath

Various mass flow rates were implemented ranging from 0.00833 to 0.0175 kg/s. The system was tested outdoors for Malaysia's tropical climate. The sensors used include flow meter, k-type thermocouples, pyranometer, and multimeter for nanofluid mass flow rate, surface temperature, solar irradiance, and electrical components—voltage and current, respectively. A data acquisition device was used to collect the data and transfer it to a portable computer. All pipes and containers were well isolated to avoid heat escape. Moreover, the proposed PV/T was compared to a water-based PV/T, a PCM-water-based PV/T, and a conventional PV.

The next section will present results from the outdoor experiments of the nano-PCM and nanofluid-based PV/T from our published works [61–64].

4 Results and Discussions

SiC nano-material was used for the nanofluid and the nano-PCM, while organic paraffin wax was used as PCM. The FESEM image and XRD analysis of the nano-PCM can be viewed in Fig. 7, while the EDS scan is provided in Fig. 8.

Figure 8 shows the map sum spectrum of the nano-PCM or SiC-Paraffin sample. It clearly shows traces of silicon (Si) and high content of carbon (C). Hydrogen (H) is not shown because it is a light element and cannot be routinely analyzed using EDX.

Four systems are considered in the results which are:

1. Nanofluid and nano-PCM-based PV/T/abbreviated (PVT cell.pcm.n.nf)
2. PCM tank, water-based PV/T/abbreviated (PVT cell.pcm.w)
3. Water tank, water-based PV/T/abbreviated (PVT cell.w)
4. Conventional PV.

To reduce the number of tests required, the experiments began with an investigation of optimum mass flow rate by testing various nanofluid flow rates. Water-based PV/T with a PCM tank was used for these tests. Figure 9 shows the observed change in PV module temperature across various flow rates throughout the day.

To form a better understanding of the system, Fig. 9 shows the recorded temperature of the PV, the solar irradiance, and time. The solar irradiance and ambient temperature behaviors are displayed in the black (diamond marker) and orange lines (square marker), respectively.

From Fig. 9, it can be observed that temperature of the PV module has decreased with increase of mass flow rate from 0.0833 to 0.175 kg/s. These results agree with the theory and literature, where increase of mass flow rate causes increase in heat exchange and enhanced heat transfer from hot to cold mediums. More increase to mass flowrate could be made, but a vibration in the PV/T system was noticed. Hence, it is important that the mechanical design works well with operational parameters. Hence 0.175 kg/s shows better cooling and is suitable for the system, and it was used for the remaining experiments. The temperature distribution across the four systems investigated and is provided in Fig. 10.

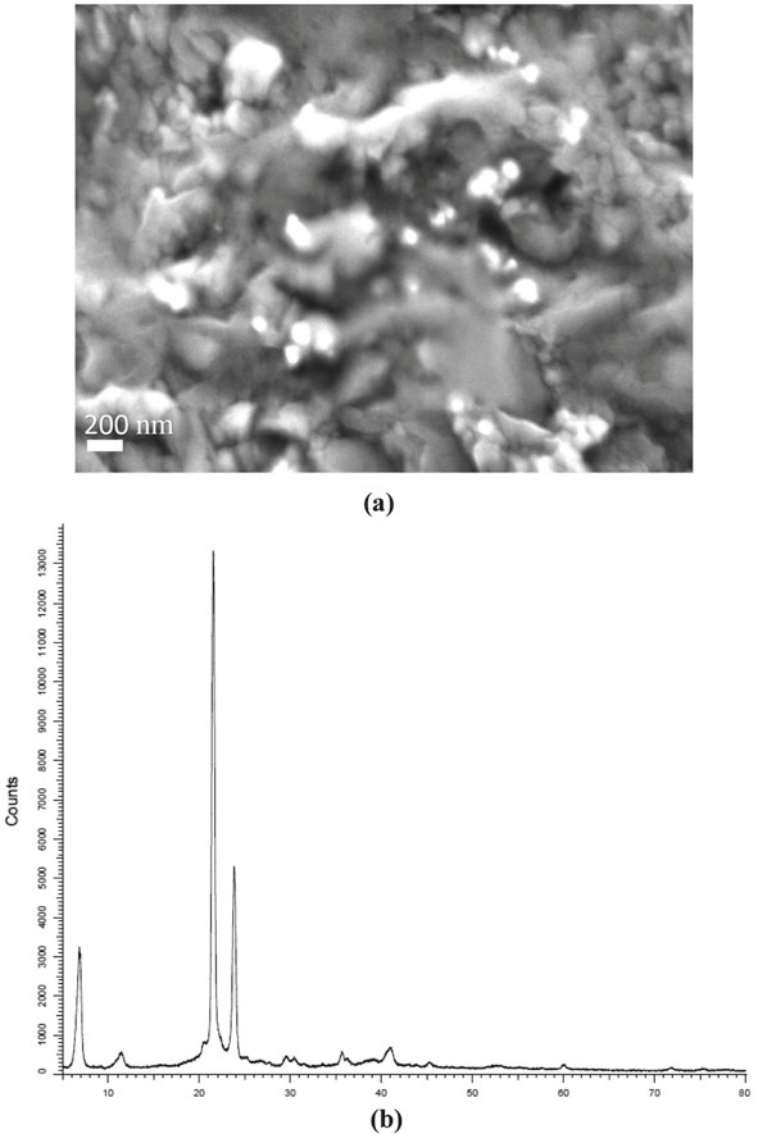

Fig. 7 **a** FESEM of SiC-paraffin, **b** XRD of SiC-paraffin

It is noticeable that temperature of all modules starts higher than the ambient. This is because measurements were taken after sunrise. As expected, the conventional PV module had the highest temperature throughout the experiments; as no method of cooling or thermal regulation was implemented. The second highest in temperature was the water-based PV/T with a water tank, then the water-based PV/T with a PCM tank. The lowest PV temperature is clearly the nano-PCM and nanofluid-based

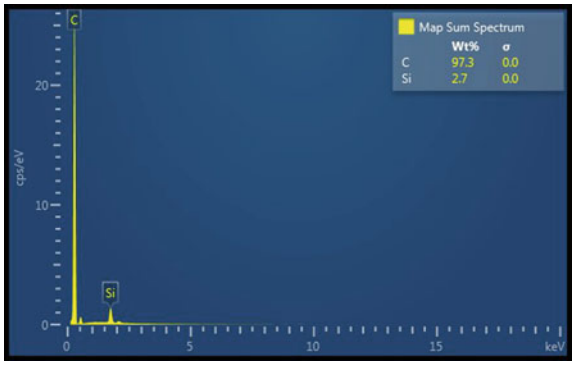

Fig. 8 EDS of SiC-paraffin sample

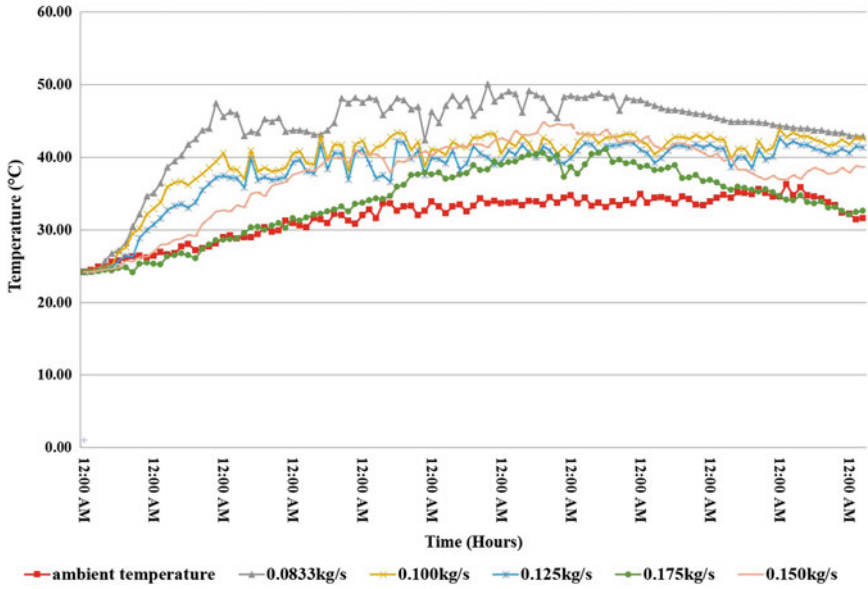

Fig. 9 Effect of mass flow rate on collector temperature for the tested systems

PV/T. Nanofluid has lower specific heat than water, but it does have higher thermal conductivity and so it led to higher reduction in PV module temperature. Using nano-PCM allowed for better utilization of PV temperature to produce more thermal energy. The nano-PCM has the advantage in heat storage as it acquired temperature and transferred it to the nanofluid more quickly. The thermal energy and thermal efficiency of the systems are provided in Figs. 11 and 12, respectively. The fourth collector, conventional PV, was excluded from these two figures given that it does not capitalize on thermal energy. Although the electricity produced can be converted into thermal energy for the sake of comparison, however, it would be counterproductive to do so, and employing a solar thermal collector would be more suitable. It is needless

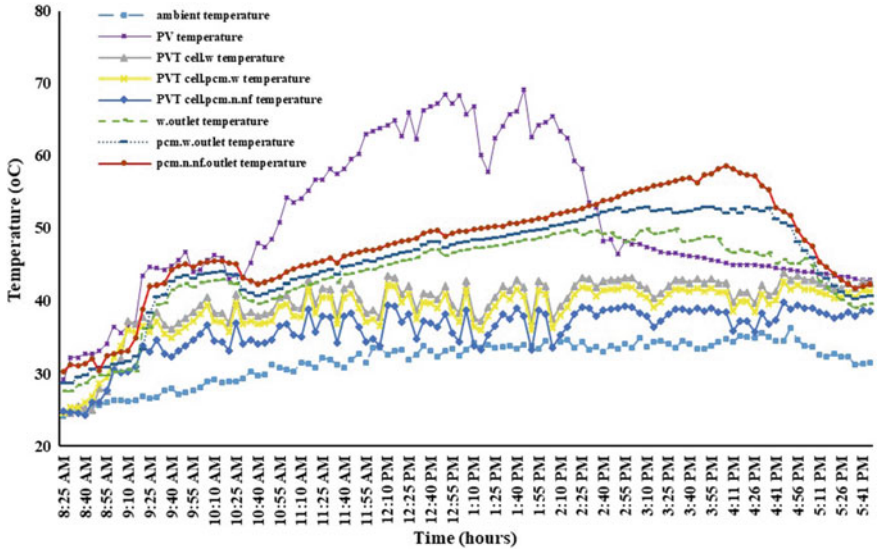

Fig. 10 Temperature distribution of all systems

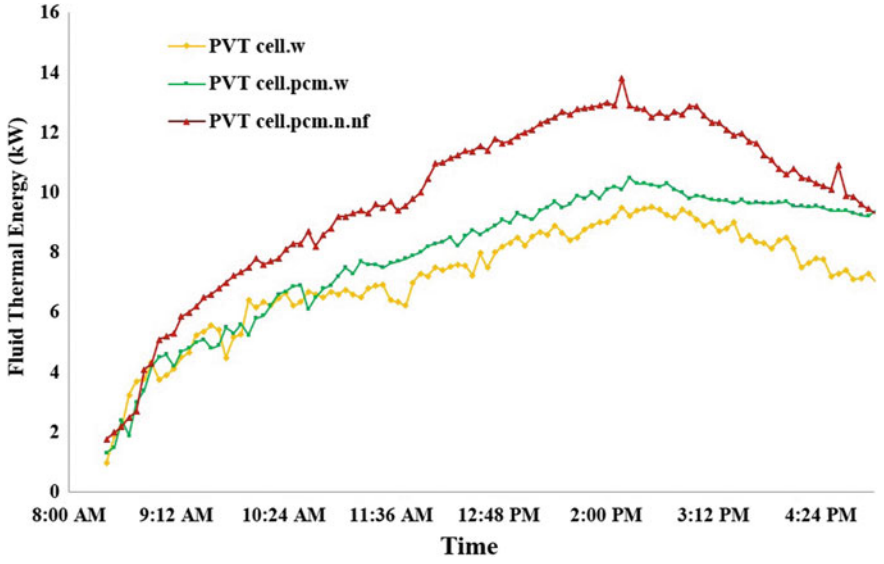

Fig. 11 Thermal energy of the PV/T collector

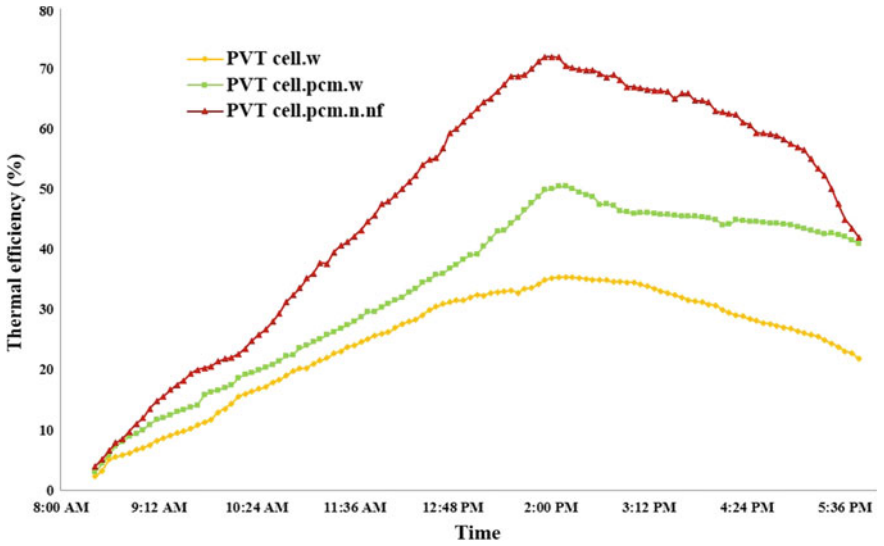

Fig. 12 Thermal efficiency of the PV/T collector

to say that other environmental variables have some effect on the performance of the module and may lead to some irregularities which are expected in tropical climate, for example, wind speed and direction, diffused and reflected solar irradiance, air mass and position of the sun.

Clearly, the highest thermal energy is produced by the nano-PCM and nanofluid-based PV/T which is mainly attributed to design material. Increase of heat transfer due to employing nano-material is the main key to this process. The better heat transfer occurs the better cooling of the module happens and hence maintaining electrical performance close to the standard conditions. It is important to note that instantaneous change of solar irradiance leads to temperature fluctuations which are dampened, or even eliminated, if PCM is used. The use of a nanofluid is particularly crucial at later time, throughout the day, typically 4–6 PM, where it is important to extract heat from the PCM or the nano-PCM as fast as possible to avoid heat returning to the module; given that module surface temperature begins to drop considerably. Because nano-PCM has higher thermal conductivity than water and PCM, it stores the heat for a longer time and hence discharges without acquiring new heat, which explains the thermal efficiency of the nanofluid and nano-PCM collector. As for thermal efficiency, Fig. 12 shows the efficiencies for the three proposed systems over time.

At the start of the testing, all three systems had similar efficiencies as not enough heat was transferred to the working fluids. Since the highest thermal efficiency is achieved by the nano-PCM and nanofluid-based PV/T, it is clear that it causes the most reduction in PV module temperature, which in turn will affect its electrical efficiency, as it is shown in Fig. 16. In general, the curves are similar with exception

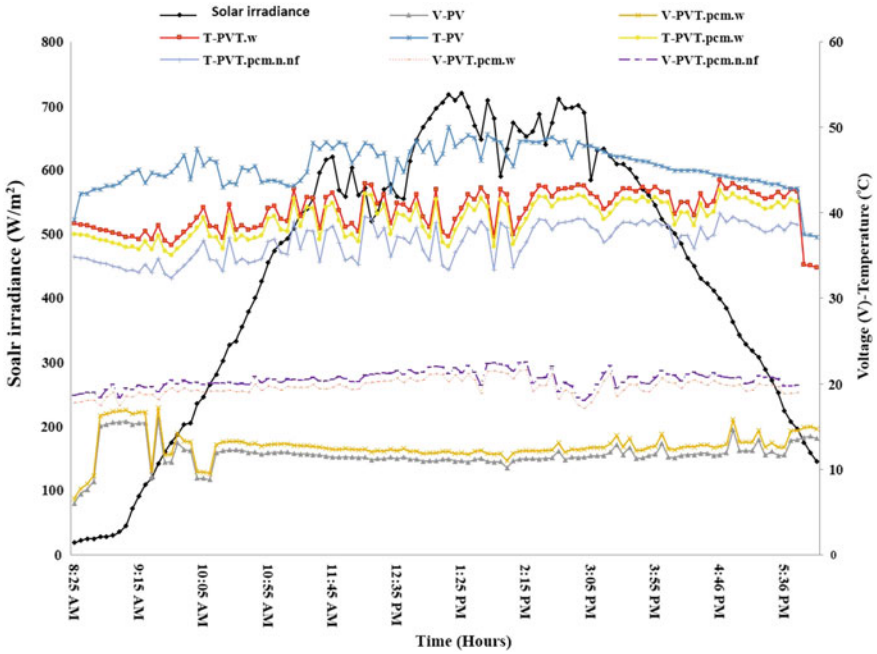

Fig. 13 Electrical voltage of PV/T collector

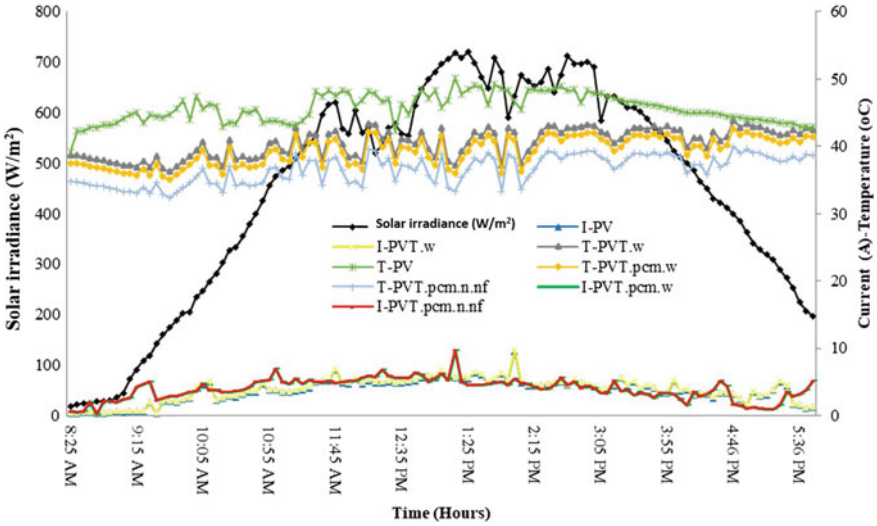

Fig. 14 Electrical current of PV/T collector

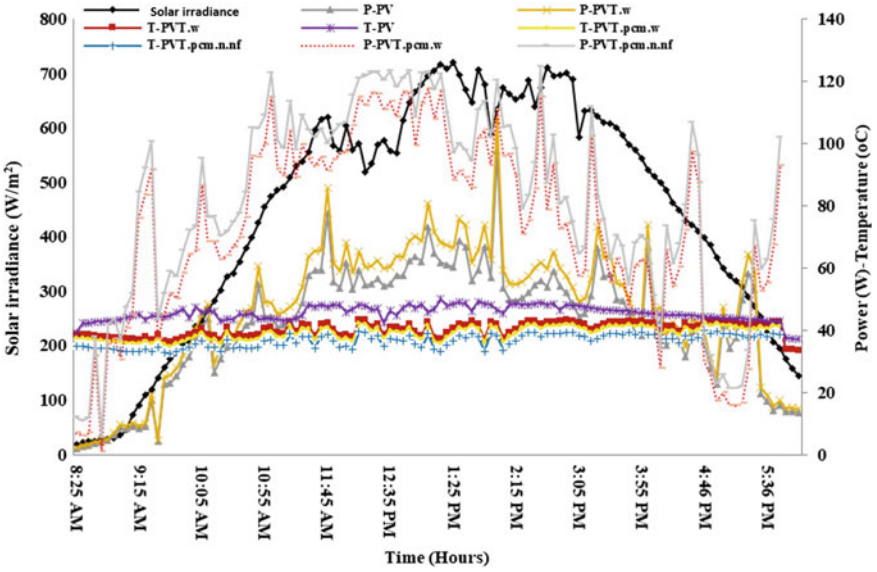

Fig. 15 Electrical power of PV/T collector

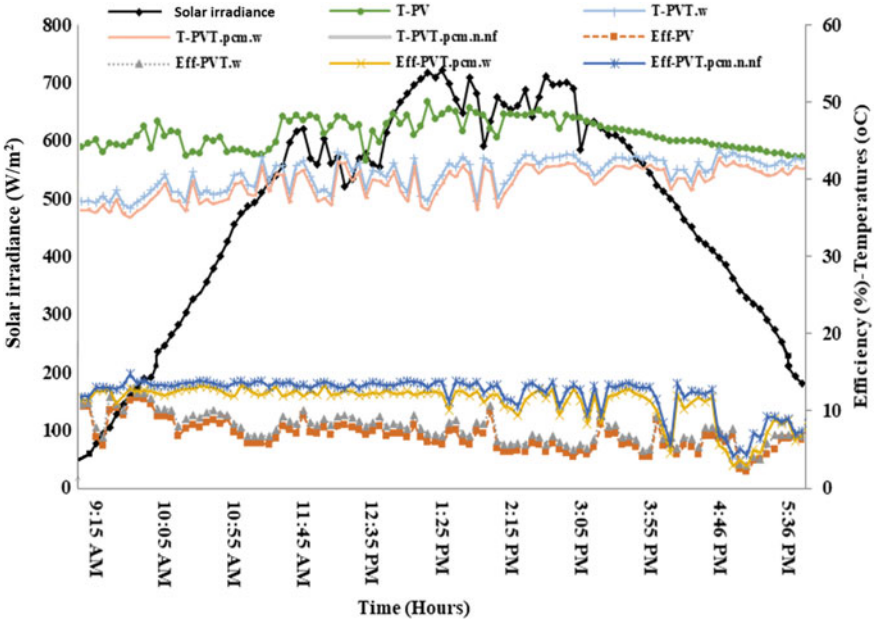

Fig. 16 Electrical efficiency of PV/T collector

to that of the proposed system which shifts due to its ability to store heat better. This heat could be utilized in many applications ranging from residential water cooling to industrial pre-heating for steam generation [65]. This system although has significant thermal efficiency, and there are multiple risks that need to be studied and considered for large-scale.

Firstly, it is the type of nanofluid and the preparation process. The performance of the system itself may vary according to the nanofluid and nano-PCM employed. Good mixing and preparation of the nanofluid and nano-PCM would lead to better thermal conductivity, while bad mixing would change that result.

Secondly, it is also important to ensure accurate pouring of nano-PCM into the nano-PCM container, or tank, to avoid gaps in the tank. Moreover, the stability analysis of the employed nanofluid over long period of times must be considered as well. Good welding of the design material must be ensured, and leaks of both liquid and heat must be avoided. Complete covering of the PV module is important to cover more area of the collector for heat transfer.

To assess the electrical performance of the collector, it is preferable to state the general properties of the PV module. The PV power, open-circuit voltage, short-circuit current, and efficiency at standard testing conditions (STC) are 120 ± 3% W_p, 21.5 V_{OC}, 7.63 $I_{SC,}$ and 14%, respectively. The elements affecting the system are solar irradiance, ambient temperature, and mass flow rate. Remaining elements such as atmospheric pressure, wind speed, and age of the PV were neglected. A source meter was used to measure the output of the module. Figures 13 and 14 show the electrical voltage and current of the different collectors, respectively.

Both figures, of voltage and current, are with respect to solar irradiance and temperature. The voltage waveform of the PV is more affected by variations in solar irradiation, given that it would affect the potential barrier of the cell itself and cell temperature. However, current waveform is consistent with solar irradiance. Given continuous changes in instantaneous solar irradiance, fluctuations, and spikes appear for both the voltage and current, as shown in Figs. 13 and 14. The highest voltages for the systems were around 18–20 V and 20–21 V for the PVT.pcm.w and PVT.pcm.n.nf, respectively. Moreover, the average voltages are around 19.7 V and 20.6 V, respectively. The current curve is highly affected by solar irradiance curve. The current increased with the increase of cell temperature, which is consistent with the theory; however, for all PV modules the current fluctuated throughout the experiments but the change is insignificant. The electric power and efficiency of the systems are presented in Figs. 15 and 16, respectively.

From Fig. 15, the highest production of electric power during the experimental period is achieved by the nano-PCM and nanofluid-based PV/T. The instantaneous peak power generation of the systems is 61.1 W, 85.7 W, 116.1 W, and 119.5 W for the PV, PVT.w, PVT.pcm.w, and PVT.pcm.n.nf, respectively. These values are subject to uncertainty of 3%.

Moreover, the electrical efficiency follows, as Fig. 16 shows the electrical efficiency, which is also a success domain for the PVT.pcm.n.nf which achieved peak instantaneous efficiency at around 13.7% that is very close to that of standard testing conditions. However, instantaneous efficiency should not be a representation of the

PV performance throughout the day, nor overtime. The second-highest efficiency is achieved by PVT.pcm.w with around 11.3%, followed by 8.6% for PVT.w, respectively. The lowest electrical efficiency is found for the typical PV module that may seem shocking; however, it is very reasonable under tropical climates. It is noteworthy to mention that one pyranometer is used in-between all four-system collector; meaning slight variation of incident solar irradiance occurs from the one shown in graph. Moreover, changing pyranometer tilt angle can affect the measurement as well. The modules are installed at a tilt angle, and the hence difference between recorded solar irradiance and actual irradiance received by PV can differ slightly.

The thermal and electrical efficiencies of the proposed system effectively showcase the importance of nano-material for solar energy development. Nano-PCMs have a massive potential for these systems. It is important to note that the water-based PV/T with a water tank is not very common, as most research only employed direct pipes with water or flat-plate designs. PV module can decrease in efficiency up to a substantial margin due to environmental elements such as heat, humidity, dust, and inner device losses [66]. Irregularities, spikes, and discontinuity are major issues associated with PV modules and need to be addressed. Establishing PV/T for cooling and heat extraction is a cost-effective method and has great potential for success in the field.

Voltage and current of the PV are majorly affected by the cell temperature as established by Figs. 13 and 14. Hence, cell temperature is the main link between PV and solar thermal to forming PV/T. Figure 13 shows an inversely proportional relationship between voltage and cell temperature. In Fig. 16, the electrical efficiency, partially as a product of PV cell temperature, is shown to be high for the proposed system in comparison with other designs. The results displayed in this section are summarized in Table 2.

It is important to differentiate between the results displayed in Table 2, maximum values, and average operational values. For comparison with other systems, the type of PV at STC must be unified for far comparison. However, in terms of thermal collector it is not necessary to compare it to a similar type, for thermal comparison. The claim is to compare the proposed type to other types of thermal collectors, of PV/T to see which holds the highest efficiency. The main challenges of this

Table 2 Summary of electric/thermal behavior of different PV/T systems

System	Peak PV temperature (°C)	Peak output cooling fluid (°C)	Max. thermal energy (kW)	Maximum electric efficiency (Wp)	Max. total PV/T efficiency (%)
PV	68.3	–	–	77.6	7.11 (no thermal)
PVT.W	45.22	49.72	9.51	85.1	45.32
PVT.PCM.W	42.22	52.52	10.5	107.4	62.82
PVT.PCM.N.NF	39.52	58.62	13.8	119.5	85.7

configuration are mainly in preserving the stability of produced material for repeated cycles and establishing cheaper and simpler methods for preparing the end-product nanofluids and nano-PCM for the end-consumer. Discharging process after sunset is also considered an issue given that more power is spent to ensure no temperature revert to the PV module. Finally, the use of PCM will lead to increased weight and hence further construction costs.

5 Summary and Conclusions

This chapter presented advances of nano-material utilized in photovoltaic thermal (PV/T) collectors. The chapter introduces solar energy, PV and solar thermal, and PV/T collectors. The concepts and classifications of PV/T are explained, and the literature work is reviewed as well. Nano-material and nanofluids were introduced and explained as working fluids for PV/T systems. PCM and nano-PCM were also introduced as thermal regulation mediums for PV and PV/T systems. The evolution of nano-material use in PV/T collectors is further summarized in Fig. 17 [61, 67, 68].

With regard to nano-material, the following conclusions summarize the information presented in this chapter:

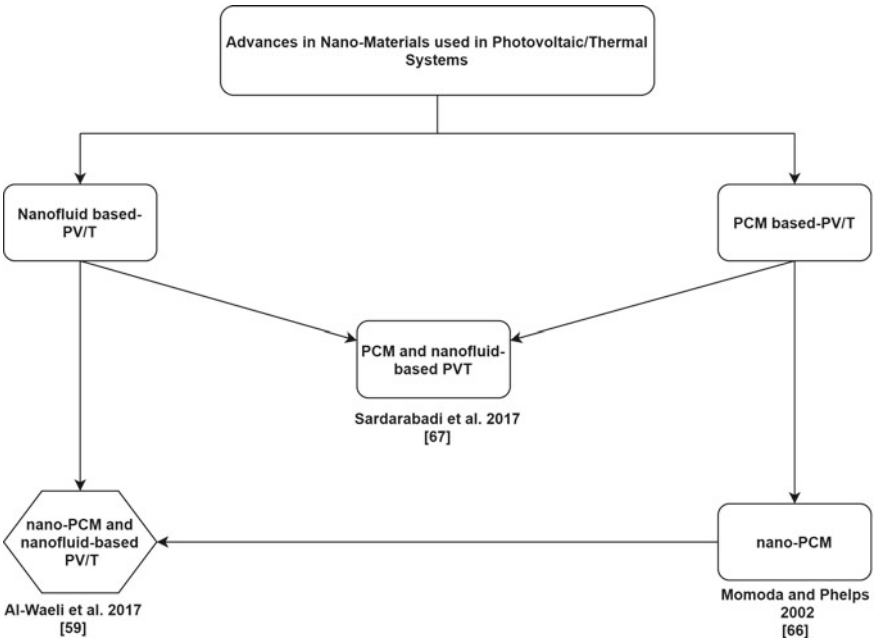

Fig. 17 Summary of PV/T classifications with nano-material innovative solutions

1. Nano-materials are special materials produced at nano-scale which have favorable properties for various industrial applications (e.g. electronics).
2. Nano-materials have a high surface area-to-volume ratio which makes them more chemical reactive than normal-sized material.
3. Nano-material synthesis is extremely important to produce them for the desired application and is classified into physical and chemical methods.
4. Nanofluids are nano-materials mixed with a base fluid. They exhibit better thermo-physical properties than water, or ethylene glycol. Hence, they are used for heat transfer applications.
5. Nanofluid preparation is a critical stage to obtain stable nanofluids. Mixing/shaking process and nano-material mass fraction have significant effect on the fluid's thermal conductivity, viscosity, and density.
6. Higher mass fraction of nano-material leads to higher thermal conductivity and lower density. However, an offset would be the cost associated with adding more nano-material.
7. The biggest issue associated with nanofluids is agglomerations and sedimentations which are bound to occur but could be minimized.
8. Stability, particle structure, and morphological properties are among characterizing factors which can be examined using various scanning methods such as FESEM, EDS, and XRD.
9. Nanofluids are considered Newtonian fluids and are affected by gravity and Brownian motion.
10. Nanofluids are used for different types of PV/T collectors, spectral splitting filters, jet impingement, and flat-plate designs.

Phase change materials (PCM) are effective tools for maintaining and thermal regulating the temperature of the PV modules. However, they lack thermal conductivity. Hence, employing nano-materials will affect this process, yielding 'nano-PCM.'

The implementation of nanofluids has massive effects on thermal and electrical behavior of PV/T systems. Highlighted below are important factors associated with nanofluid-based PV/T:

1. Nanofluid-based PV/T has higher thermal and electrical efficiency than water-based PV/T.
2. PCM-based PV and PV/T have higher thermal efficiency than conventional PV modules.
3. Nano-PCM has higher thermal conductivity than PCM and is more suitable for heat transfer applications.
4. Increase of nanofluid mass flow rate leads to better cooling and heat extraction, up to a certain point.
5. Thermal isolation and elimination of air-gaps are crucial to the successful design of PV/T.
6. Higher solar irradiance leads to higher electrical efficiency when cooling the PV modules.

Currently, the main challenges facing this technology are the high costs for producing nanofluids and nano-PCM. Other challenges extend to stability of nano-material and accurate methods of measuring latent heat change.

The design described in the results and discussion sections can be improved for future research with consideration of the following points:

1. Using the photovoltaic module frames as the nano-PCM tank buy simply placing a sheet at their back to cover it. Also, this will eliminate the need for silicon oil in the design.
2. Varying the design of the pipes to examine different configurations for improved performance.
3. Employing concentrated CPC PV/T with the nano-PCM and nanofluids to test the effect of concentration on thermal and electrical power generation.

Further, research investigations must be conducted to examine various environmental conditions and PV/T system configurations using nano-material for efficiency enhancement and offering cost-effective solutions for consumers.

References

1. Naciones Unidas. Department of International Economic, Social Affairs. Population Division, Naciones Unidas, United Nations Department of Economic, and Nations Unies. Division de la population. (2004). *World population to 2300* (Vol. 236). New York: United Nations Publications.
2. Sheffield, J. (1998). World population growth and the role of annual energy use per capita. *Technological Forecasting and Social Change, 59*(1), 55–87.
3. U.S. Energy Information Administration (Monthly energy review, Table 1.3, April 2018, preliminary data). https://www.eia.gov/energyexplained/index.php?page=about_sources_of_energy and https://www.e-education.psu.edu/earth104/node/1345.
4. Höök, M., & Xu, T. (2013). Depletion of fossil fuels and anthropogenic climate change—A review. *Energy Policy, 52,* 797–809.
5. International Energy Agency (IEA). Publications, renewables 2017 report, 4th October 2017. Link: https://www.iea.org/publications/renewables2017/. Retrieved November 8, 2018.
6. Chow, T. T., Hand, J. W., & Strachan, P. A. (2003). Building-integrated photovoltaic and thermal applications in a subtropical hotel building. *Applied Thermal Engineering, 23*(16), 2035–2049.
7. Chow, T. T. (2010). A review on photovoltaic/thermal hybrid solar technology. *Applied Energy, 87*(2), 365–379.
8. Al-Waeli, A. H. A., Sopian, K., Kazem, H. A., & Chaichan, M. T. (2017). Photovoltaic/Thermal (PV/T) systems: Status and future prospects. *Renewable and Sustainable Energy Reviews, 77,* 109–130.
9. Lorenzo, E. (1994). *Solar electricity: Engineering of photovoltaic systems*. Spain: Earthscan/James & James.
10. Duffie, J. A., & Beckman, W. A. (2013). *Solar engineering of thermal processes* (4th ed.). Hoboken, New Jersey: Wiley.
11. Radziemska, E. (2009). Performance analysis of a photovoltaic-thermal integrated system. *International Journal of Photoenergy*, *2009*.
12. Shahsavar, A., & Ameri, M. (2010). Experimental investigation and modeling of a direct-coupled PV/T air collector. *Solar Energy, 84*(11), 1938–1958.

13. Sopian, K., Yigit, K. S., Liu, H. T., Kakac, S., & Veziroglu, T. N. (1996). Performance analysis of photovoltaic thermal air heaters. *Energy Conversion and Management, 37*(11), 1657–1670.
14. Chow, T. T. (2003). Performance analysis of photovoltaic-thermal collector by explicit dynamic model. *Solar Energy, 75*(2), 143–152.
15. Kumar, R., & Rosen, M. A. (2011). Performance evaluation of a double pass PV/T solar air heater with and without fins. *Applied Thermal Engineering, 31*(8–9), 1402–1410.
16. Zondag, H. A., De Vries, D. W., Van Helden, W. G. J., Van Zolingen, R. J. C., & Van Steenhoven, A. A. (2003). The yield of different combined PV-thermal collector designs. *Solar Energy, 74*(3), 253–269.
17. Sandnes, B., & Rekstad, J. (2002). A photovoltaic/thermal (PV/T) collector with a polymer absorber plate. Experimental study and analytical model. *Solar Energy, 72*(1), 63–73.
18. Dubey, S., & Tiwari, G. N. (2009). Analysis of PV/T flat plate water collectors connected in series. *Solar Energy, 83*(9), 1485–1498.
19. Dupeyrat, P., Ménézo, C., Rommel, M., & Henning, H.-M. (2011). Efficient single glazed flat plate photovoltaic–thermal hybrid collector for domestic hot water system. *Solar Energy, 85*(7), 1457–1468.
20. Rosell, J. I., Vallverdu, X., Lechon, M. A., & Ibanez, M. (2005). Design and simulation of a low concentrating photovoltaic/thermal system. *Energy Conversion and Management, 46*(18–19), 3034–3046.
21. Hussein, A. M., Abu Bakar, R., Kadirgama, K., & Sharma, K. V. (2013). Experimental measurement of nanofluids thermal properties. *International Journal of Automotive and Mechanical Engineering, 7*, 850.
22. Yu, W., & Xie, H. (2012). A review on nanofluids: Preparation, stability mechanisms, and applications. *Journal of Nanomaterials, 2012*, 1.
23. Saini, A., Kaur, H., Sharma, S., & Gangacharyulu, D. (2016). Nanofluids: A review preparation, stability, properties and applications. *International Journal of Engineering Research and Technology, 5*(07), 11–16.
24. Liu, M., Zhou, Z., Zhang, X., Yang, X., & Cheng, X. (2016). The effect of nano-SiO_2 dispersed methods on mechanical properties of cement mortar. In *International Conference on the Durability of Concrete Structures*, January 2016. http://doi.org/10.5703/1288284316135.
25. Kalteh, M. (2013). Investigating the effect of various nanoparticle and base liquid types on the nanofluids heat and fluid flow in a microchannel. *Applied Mathematical Modelling, 37*(18–19), 8600–8609.
26. Aliofkhazraei, M. (Ed.). (2016). *Handbook of nanoparticles*. Cham: Springer.
27. Baker, C., Shah, S. I., Hasanain, S. K., Ali, B., Shah, L., Li, G., et al. (2002). Inert gas condensation of iron and iron-oxide nanoparticles. In *MRS Online Proceedings Library Archive, 746*.
28. Rebsdat, S., & Mayer, D. (2000). Ethylene glycol. Ullmann's Encyclopedia of Industrial Chemistry.
29. NPL. What are thermophysical properties? (FAQ—Thermal). http://www.npl.co.uk/reference/faqs/what-are-thermophysical-properties-(faq-thermal) (Retrieved). Accessed November 10, 2018.
30. Sarviya, R. M., & Fuskele, V. (2017). Review on thermal conductivity of nanofluids. *Materials Today: Proceedings, 4*(2), 4022.
31. McNaught, A. D., & McNaught, A. D. (1997). *Compendium of chemical terminology* (Vol. 1669). Oxford: Blackwell Science.
32. Wang, X., Xu, X., & Choi, S. U. S. (1999). Thermal conductivity of nanoparticle-fluid mixture. *Journal of Thermophysics and Heat Transfer, 13*(4), 474–480.
33. Prasher, R., Song, D., Wang, J., & Phelan, P. (2006). Measurements of nanofluid viscosity and its implications for thermal applications. *Applied Physics Letters, 89*(13), 133108.
34. Drzazga, M., Lemanowicz, M., Dzido, G., & Gierczycki, A. (2012). Preparation of metal oxide-water nanofluids by two-step method. *Inżynieria i Aparatura Chemiczna, 51,* 213–215.
35. Prakash, S. B., Ningappa Kotin, K., & Praveen, K. (2015). Preparation and characterization of nanofluid (CuO–water, TiO_2–water). *International Journal of Science and Engineering, 1*(3), 14–20.

36. Klug, H. P., & Alexander, L. E. (1974). X-ray diffraction procedures: For polycrystalline and amorphous materials. In H. P. Klug & L. E. Alexander (Eds.), *X-ray diffraction procedures: For polycrystalline and amorphous materials* (2nd ed., pp. 992). ISBN 0-471-49369-4. Wiley-VCH.
37. Sidik, N. A. C., Adamu, I. M., Jamil, M. M., Kefayati, G. H. R., Mamat, R., & Najafi, G. (2016). Recent progress on hybrid nanofluids in heat transfer applications: A comprehensive review. *International Communications in Heat and Mass Transfer, 78,* 68–79.
38. Mukherjee, S., & Paria, S. (2013). Preparation and stability of nanofluids—A review. *IOSR Journal of Mechanical and Civil Engineering, 9*(2), 63–69.
39. Li, X. F., Zhu, D. S., Wang, X. J., Wang, N., Gao, J. W., & Li, H. (2008). Thermal conductivity enhancement dependent pH and chemical surfactant for Cu-H_2O nanofluids. *Thermochimica Acta, 469*(1–2), 98–103.
40. Ali, N. A. (2010). *Preparation and characterisation of physicochemical properties of aluminium oxide (Al_2O_3)—Water nanofluids using two step methods* (Doctoral dissertation), UMP.
41. El-Salamony, R. A., Morsi, R. E., & Alsabagh, A. M. (2015). Preparation, stability and photocatalytic activity of titania nanofluid using gamma irradiated titania nanoparticles by two-step method. *Journal of Nanofluids, 4,* 442–448.
42. Castellanos, J. B. (2014). *Thermal conductivity of alumina and silica nanofluids.* Mankato: Minnesota State University.
43. Das, S. K., Choi, S. U., Yu, W., & Pradeep, T. (2007). *Nanofluids: Science and technology.* Hoboken: Wiley.
44. Das, S. K., Putra, N., Thiesen, P., & Roetzel, W. (2003). Temperature dependence of thermal conductivity enhancement for nanofluids. *Journal of Heat Transfer, 125*(4), 567–574.
45. Abdallah, S. R., Saidani-Scott, H., & Abdellatif, O. E. (2019). Performance analysis for hybrid PV/T system using low concentration MWCNT (water-based) nanofluid. *Solar Energy, 181,* 108–115.
46. Jing, D., Hu, Y., Liu, M., Wei, J., & Guo, L. (2015). Preparation of highly dispersed nanofluid and CFD study of its utilization in a concentrating PV/T system. *Solar Energy, 112,* 30–40.
47. Khanjari, Y., Pourfayaz, F., & Kasaeian, A. B. (2016). Numerical investigation on using of nanofluid in a water-cooled photovoltaic thermal system. *Energy Conversion and Management, 122,* 263–278.
48. Michael, J. J., & Iniyan, S. (2015). Performance analysis of a copper sheet laminated photovoltaic thermal collector using copper oxide–water nanofluid. *Solar Energy, 119,* 439–451.
49. Hussien, H. A., Noman, A. H., & Abdulmunem, A. R. (2015). Indoor investigation for improving the hybrid photovoltaic/thermal system performance using nanofluid (Al_2O_3-water). *Engineering and Technology Journal, 33*(4 Part (A) Engineering), 889–901.
50. Hawwash, A. A., Rahman, A. K. A., Nada, S. A., & Ookawara, S. (2018). Numerical investigation and experimental verification of performance enhancement of flat plate solar collector using nanofluids. *Applied Thermal Engineering, 130,* 363–374.
51. Hasan, H. A., Sopian, K., Jaaz, A. H., & Al-Shamani, A. N. (2017). Experimental investigation of jet array nanofluids impingement in photovoltaic/thermal collector. *Solar Energy, 144,* 321–334.
52. Imenes, A. G., & Mills, D. R. (2004). Spectral beam splitting technology for increased conversion efficiency in solar concentrating systems: A review. *Solar Energy Materials and Solar Cells, 84*(1–4), 19–69.
53. Yousefi, T., Veysi, F., Shojaeizadeh, E., & Zinadini, S. (2012). An experimental investigation on the effect of Al_2O_3–H_2O nanofluid on the efficiency of flat-plate solar collectors. *Renewable Energy, 39*(1), 293–298.
54. Zeinali Heris, S., Kazemi-Beydokhti, A., Noie, S. H., & Rezvan, S. (2012). Numerical study on convective heat transfer of Al_2O_3/water, CuO/water and Cu/water nanofluids through square cross-section duct in laminar flow. *Engineering Applications of Computational Fluid Mechanics, 6*(1), 1–14.

55. Hwang, Y., Park, H. S., Lee, J. K., & Jung, W. H. (2006). Thermal conductivity and lubrication characteristics of nanofluids. *Current Applied Physics, 6,* e67–e71.
56. Sardarabadi, M., Passandideh-Fard, M., & Heris, S. Z. (2014). Experimental investigation of the effects of silica/water nanofluid on PV/T (photovoltaic thermal units). *Energy, 66*, 264–272.
57. Ma, T., Yang, H., Zhang, Y., Lin, L., & Wang, X. (2015). Using phase change materials in photovoltaic systems for thermal regulation and electrical efficiency improvement: A review and outlook. *Renewable and Sustainable Energy Reviews, 43,* 1273–1284.
58. Preet, S., Bhushan, B., & Mahajan, T. (2017). Experimental investigation of water based photovoltaic/thermal (PV/T) system with and without phase change material (PCM). *Solar Energy, 155,* 1104–1120.
59. Fan, L., & Khodadadi, J. M. (2012). A theoretical and experimental investigation of unidirectional freezing of nanoparticle-enhanced phase change materials. *Journal of Heat Transfer, 134*, 092301–092309.
60. Khodadadi, J. M., & Hosseinizadeh, S. F. (2007). Nanoparticle-enhanced phase change materials (NEPCM) with great potential for improved thermal energy storage. *International Communications in Heat and Mass Transfer, 34*, 534–543.
61. Al-Waeli, A. H., Sopian, K., Chaichan, M. T., Kazem, H. A., Ibrahim, A., Mat, S., & Ruslan, M. H. (2017) Evaluation of the nanofluid and nano-PCM based photovoltaic thermal (PVT) system: An experimental study. *Energy Conversion and Management, 151*, 693–708.
62. Al-Waeli, A. H., Sopian, K., Kazem, H. A., Yousif, J. H., Chaichan, M. T., Ibrahim, A., et al. (2018). Comparison of prediction methods of PV/T nanofluid and nano-PCM system using a measured dataset and artificial neural network. *Solar Energy, 162*, 378–396.
63. Sopian, K., Alwaeli, A. H., Al-Shamani, A. N., & Elbreki, A. M. (2019). Thermodynamic analysis of new concepts for enhancing cooling of PV panels for grid-connected PV systems. *Journal of Thermal Analysis and Calorimetry, 136*(1), 147–157.
64. Al-Waeli, A. H., Sopian, K., Kazem, H. A., & Chaichan, M. T. (2018). Nanofluid based grid connected PV/T systems in Malaysia: A techno-economical assessment. *Sustainable Energy Technologies and Assessments, 28*, 81–95.
65. Alwaeli, A. H., Sopian, K., Ibrahim, A., Mat, S., & Ruslan, M. H. (2017). Nanofluid based photovoltaic thermal (PVT) incorporation in palm oil production process. *IJOCAAS, 3*, 292–294.
66. Alshakhs, M. (2013). *Challenges of solar PV in Saudi Arabia.* Submitted as coursework for PH240, Stanford University.
67. Momoda, L. A., & Phelps, A. C. (2002) Nanometer sized phase change materials for enhanced heat transfer fluid performance. U.S. Patent 6,447,692, issued September 10, 2002.
68. Sardarabadi, M., Passandideh-Fard, M., Maghrebi, M.-J., & Ghazikhani, M. (2017). *Solar Energy Materials and Solar Cells, 161,* 62.

Si Quantum Dots for Next-Generation Solar Energy Harvester

Mrinal Dutta

Abstract Over the last two decades, semiconductor quantum dots have attracted considerable research interest for a wide range of applications such as photovoltaics, light-emitting devices, nanoelectronics and markers for biomedicine. Among these, non-toxic silicon quantum dots (Si QDs) have grown intensive worldwide research interest because of their exciting physical properties and prospects in future electronic and optoelectronic devices. Tuning the band gap through quantum confinement by tuning the QD size and tuning the surface-related luminescence properties from UV to NIR range allow fabrication of optimized tandem photovoltaic devices in one growth run. This chapter focuses on the progress and growth of Si QD-based photovoltaic devices with the synthesis techniques as well as the broad range emission properties of these Si QDs. The issues related to p-type and n-type doping of these QDs are also discussed in this context. The performances of several photovoltaic devices reported in the literature are summarized. Finally, several routes for optimizing the performance of these Si QD cells by resolving the doping issue and other structural improvements are discussed.

Keywords Si quantum dot · Non toxic · Solar cell · Energy harvester · Multi exciton generation

1 Introduction

In the last two decades, intensive research has been focused on the synthesis of semiconductor quantum dots (QDs) having color-tunable emission properties for their potential applications in light-emitting diodes (LEDs), lasers, thermoelectric devices, solar cells and biomedical imaging [1–5]. The synthesized QDs for these applications should be compatible with the existing mature device processing technology,

M. Dutta (✉)
Inorganic Photovoltaic Devices Group, Advanced Materials Device Division, Council of Scientific & Industrial Research (CSIR)-National Physical Laboratory, K.S. Krishnan Marg, Pusa, New Delhi 110012, India
e-mail: sspmd.iacs@gmail.com

S. J. Ikhmayies (ed.), *Advances in Energy Materials*,
Advances in Material Research and Technology,
https://doi.org/10.1007/978-3-030-50108-2_6

cost-effective and environment friendly to be used in long run. The conventional direct bandgap semiconductor QDs such as CdS, CdSe and PdS QDs. are efficient emitters, and their emissions can be tuned in a long range by changing QD size only. However, they are toxic in nature and do not properly fit with the existing semiconductor processing technology, and moreover, they are not as much cost-effective as per need. The semiconductors that have all these advantages such as silicon and germanium are indirect bandgap semiconductors and have poor absorption and emission properties. The top of the valance band and the bottom of the conduction band are not at the same point in the Brillouin zone. Due to this, they are inefficient emitters as the radiative recombination across the band gap needs phonons to conserve crystal momentum [1, 6]. In 1991, Cullis and Canham for the first time showed the path and raised the hope to obtain visible emission from indirect bandgap semiconductor like Si by using porous form [7]. They showed that quantum confinement could remove this inefficiency in emission of indirect bandgap semiconductors. The report of this pathbreaking discovery in 1991 started a new dawn of production of Si nanostructures with good emission property. Bandgap enhancement and indirect-to-direct conversion of indirect bandgap semiconductors are ascribed to quantum confinement [8]. Bandgap tuning is possible in different forms of Si nanostructures such as Si nanowires, porous Si, Si nanocrystals and Si QDs.

Right after the discovery of luminescence from porous Si and up to the middle of the last decade, intensive research was focused on the synthesis of various forms of luminescent Si nanostructures and established the possible mechanism of this luminescence property. These various efforts include reports on the light emission from textured bulk Si, porous Si, electrochemically etched Si, Si nanocrystals or Si QDs embedded in dielectric (SiO_2, SiN, SiC) matrix etc. [9–12]. Here, it is to be mentioned that Si nanocrystals having size less than exciton Bohr radius are usually called Si QDs [13]. Among various nanostructures of Si, Si QDs exhibit strong quantum confinement effects. As a result electrical, optical and photovoltaic properties can be tuned by changing size, surrounding matrix, doping and crystalline structure [14–19].

However, when compared to the other luminescent Si nanostructures, colloidal Si QDs offer the highest quantum yield, full solution processing, good mechanical and chemical stability and easily tailorable optoelectronic properties. Because of these properties, research on the synthesis of high quantum yield Si QDs has been shifted to the forefront of research in Si from the middle of the last decade. The colloidal stability of the QDs has attained by surface modification and using ligands of various compositions.

2 Synthesis

Only some of the conventional Si QD synthesis techniques will be discussed in this chapter. Interested readers are referred to the review articles of Askari et al. [20], Ghosh et al. [21] and Dogan et al. [22] the references therein.

2.1 Bottom-up Approach

2.1.1 Atmospheric Pressure Plasmas

Synthesis of Si QDs by atmospheric pressure plasma technique offers simplicity, low cost and versatility. Here, gas discharge occurs between electrodes where at least one electrode dimension should be less than 1 mm. The discharge could be powered by use of direct current or by use of capacitive discharge in which gas temperature should be less than 0.2 eV with an electron temperature up to 10 eV [23]. Sankaran et al. [24] used direct-current (DC) microplasma for the first time to synthesize Si QDs. 30% quantum efficiency for the Si QDs with blue luminescence at room temperature was reported. The discharge was carried out in a metal tubing as anode in which a metal capillary was configured as cathode and powered with a DC power supply (power density was measured for the plasma as ~ 5000 W cm^{-3}). This approach could be considered as an important step toward synthesis of Si QDs, however, subjected to the limitations of high-scale production and scaling up in large surface area. Later, Barwe et al. [25] using a fast camera imaging find out that the plasma was not located inside the hollow cathode. The plasma was appeared to be moving filamentary microplasma between cathode and anode, and only a part of the gas flow was interacting with the plasma. This observation could explain the reason behind the low throughput of the process. Nozaki et al. [26] in an attempt to improve this method changed precursor chemistry as well as reactor configuration. Instead of silane, silicon tetrachloride was used as precursor, and radio-frequency (144 MHz) atmospheric-pressure microplasma sustained by two ring electrodes was used in place of micro-hollow cathode configuration. With time, the two ring configurations (Fig. 1) have been proved to be more effective in production of Si QDs at high rate. HRTEM and dark field analysis show that synthesized QDs are very well separated and have a very narrow distribution (~ 2 nm in diameter) with good crystallinity [27]. With the progress of research work more easily, scaled-up reactor configuration has come out. The geometry of such a modified configuration, called 'cross-flow' as termed by its inventors, uses the electric field across the electrodes placed normal to the direction of the flow on the contrary of the two previous configurations [28].

2.1.2 Microwave Plasma

Operating power in microwave plasma varies from hundred to thousand watts where microwave cavities decompose precursor gas and generate plasma. Wiggers group [29–32] has successfully produced crystalline Si nanocrystals with sizes 3–30 nm using $Ar/H_2/SiH_4$ gas mixture. Just after entering into the plasma zone, SiH_4 completely dissociates from free Si atoms and nucleation process starts from this supersaturated Si atoms. After formation of small Si nanoparticles, they start to sinter and reach larger sizes. However, agglomerated Si nanocrystals are formed in the cold downstream zone. The gas temperature drops quickly when Si nanocrystals go out

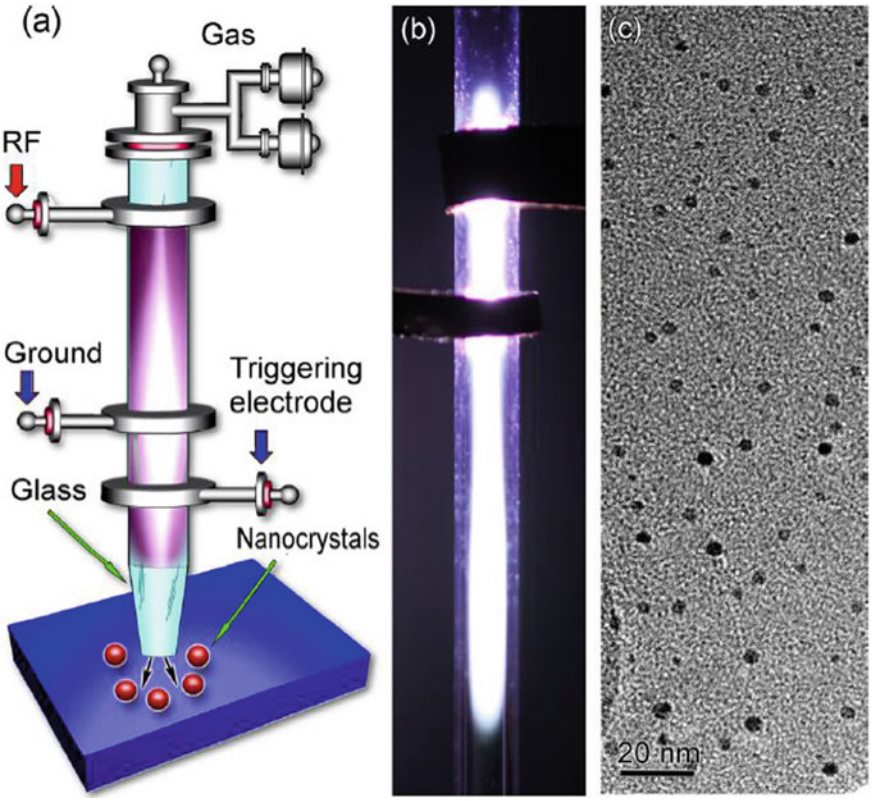

Fig. 1 **a** Schematic diagram of the 'two-ring' configuration microplasma reactor; **b** photo of the plasma inside the quartz tube; **c** representative TEM image of the silicon QDs Reproduced with permission from [27], Copyright (2014) AIP Publishing

of plasma zone after growth. In this process, the size of the Si nanocrystals can be controlled by changing SiH_4 concentration, total gas pressure in the reaction chamber and the residence time. Increase of SiH_4 concentration and total pressure increases the number of primary nanocrystals and helps in growing larger size nanocrystals by increasing their sintering rate, while increase in residence time allows more time to grow nanocrystals. In view of high scalability, microwave plasma is very attractive as it could produce in one hour of processing as high as 10 g of Si nanocrystals [3].

2.1.3 Non-Thermal Plasma

Non-thermal plasmas are composed of 'hot' electrons having energy between 2 and 5 eV, and colder ions and neutral species. In the experimental setup, two copper rings are used to produce RF power (~ tens of watts) to generate a plasma for the gas mixtures of Ar/SiH_4 [33–39] or $Ar/SiCl_4$ [40, 41] flown through a narrow quartz tube

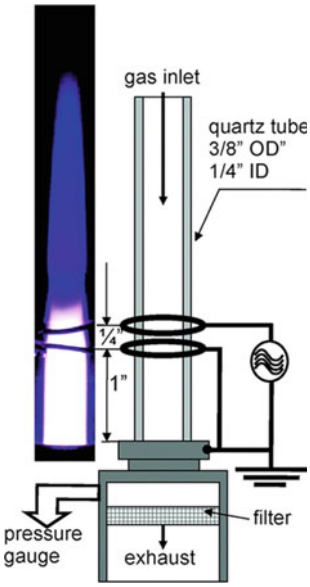

Fig. 2 Schematic diagram of the non-thermal plasma system together with a photo of the plasma Reproduced with permission from Ref. [37]. Copyright (2005) American Chemical Society

placed within these rings (Fig. 2). Dissociation of the precursor gas by hot electrons produces mainly radicals and negative ions. In non-thermal plasmas, Si nanocrystal formation occurred mainly by anion–neutral reactions. By controlling the residence time (~ <10 ms) of the nanocrystals in the plasma, size control is achieved [37, 41]. A narrow size distribution of the nanocrystals within the range of 2–20 nm could be achieved in this way. With this, partial pressure also has effect in controlling the sizes of these Si nanocrystals [37]. Using non-thermal plasma, it is possible to produce fully amorphous or fully crystalline nanoparticles by controlling the power coupled in the plasma [38, 41].

2.1.4 Thermal Plasma

Si nanocrystals could be produced in thermal plasma zone at very high rate ~ 300 gm/hour, that is, almost highest among all plasma synthesis process [42]. At high power discharges (from a few to hundred kWs having electron and gas temperature above 1 eV) and close or at atmospheric pressures, synthesis of Si nanocrystals has been reported using both RF and DC sources [42–46]. In thermal plasma region, micrometer-sized solid particles also can be used as precursor material. With the vapor phase condensation from a supersaturated vapor of Si atoms within the thermal plasma zone, nucleation occurs also in the downstream where the gas temperature is less than 0.4 eV by means of coagulation and co-condensation [42, 44]. Size control of Si nanocrystals with sizes of 5–20 nm could be synthesized by varying substrate-to-nozzle distance and the residence time [43–45].

2.1.5 Solution Phase Oxidation/Reduction

This method is most popular method to prepare nanocrystals. Heath [47] first used this method in 1992 to synthesize Si nanocrystals. The synthesis was done at high pressure and high temperature (~385 °C) in a nonpolar organic solvent in which reduction of silicon tetrachloride and $RSiCl_3$ (R = hydrogen atom or octyl group) was done by sodium metal. Use of trichlorosilane resulted nanocrystals in broad size distribution (5 nm to 3 μm), whereas use of trichlorooctylsilane provided a good control on size distribution, and the average size of the Si nanocrystals was estimated as 5.5 ± 2.5 nm. Dhas et al. [48] used sonochemical method by reducing reaction temperature and pressure of the above procedure. Ultra-sound induced reduction of tetraethyl orthosilicate at 70 °C in toluene by sodium has used to produce porous silicon nanoparticles within size range from 2 to 5 nm having an emission maximum at around 680 nm. Synthesis of alkyl-capped Si QDs has been reported by the reduction of $SiCl_4$ in appropriate solvents by using Zintl compounds like potassium silicide (KSi), sodium silicide (NaSi), etc. [49, 50]. These QDs showed strong NUV–blue luminescence property, and their sizes were measured to be in the range of 2–5 nm [50]. Later, metal silicides were replaced by sodium biphenylide and sodium naphthalenide to reduce $SiCl_4$ [51]. Chloride-capped QDs obtained through this reduction process had average size of 5.2 ± 1.9 nm. Due to slightly polar characteristic, sodium naphthalenide was found to be more useful for complete purification. In this process of alkoxylation, surface of QDs was capped with halide atoms that help in efficient surface passivation. Samara group [52, 53] used reverse micellar cage to effectively control the size of Si nanocrystal in the range of 1.8–10 nm. The nanocrystals produced by the reduction of $SiCl_4$ by $LiAlH_4$ in this method were further size selected by using high-performance liquid chromatography. Tilley et al. [54] prepared highly monodisperse nanocrystals using the above method using tetraoctylamonium bromide (TOAB) as a surfactant.

2.2 Top-Down Approach

2.2.1 Laser Ablation

In 1991, Okada and Iijima first reported the production of almost spherical Si particles within diameter 20–500 nm by laser ablation [55]. High-resolution transmission electron microscopic (HRTEM) studies confirmed a crystalline core surrounded by 1–2 nm amorphous oxide layers. Laser ablation was done under argon or oxygen environment by using a Si wafer as target. Later, in 1994, by modifying this process, Si QDs within 2–3 nm size range with emission in red region were produced [56]. Very low pressure ~ 10^{-8} Torr was used to carry out this abalation process. After this success in the synthesis of luminescent Si nanocrystals by laser ablation technique, several different types of modified approaches have been used [57–59]. Si QDs with emission in the range 1.34–1.79 eV due to change in the size of the nanocrystals

were reported by Orii et al. [60] by changing the parameters of ablation in helium gas environment. Laser ablation also carried out successfully in liquid environment instead of using gaseous ambient. Surface-passivated freestanding Si QDs could be fabricated in a one-step approach by using reactant as a solvent (liquid medium) in laser ablation [61]. The colloidal Si QD solution prepared from same Si target emitted 2.9 and 3.5 eV light when prepared by pulsed laser ablation using water and hexane as reactant solvent, respectively [62].

2.2.2 Electrochemical Etching

Synthesis of Si QDs by electrochemical etching of Si wafer used as anode of the electrochemical process also had been used extensively. The first observation of synthesis of Si nanocrystals by this method was reported by Heinrich et al. [63]. In this method, to produce colloidal suspension of Si nanocrystals, n-type or p-type Si wafers are made porous after electrochemical etching and ultrasonicate in solvents like water, methanol, methylene chloride, toluene, etc. Ultrasonically dispersed nanocrystals by this method are irregular in shape, and their sizes vary from nanometer to micrometer scale. To improve this size distribution, the thin section of the wafers was started to ultrasonicate for long time, and later, Kauzlarich group used a 20 nm sieve to filter out large size nanocrystals [64]. This process helps to separate Si nanocrystals with a very narrow size distribution within 2–11 nm.

3 Properties

Properties of crystalline bulk silicon are found to be uniform in size ranging from some tenths of nanometers up to centimeters. However, the properties of Si-QDs found to be strongly dependent on size; the interface between matrix and QDs could influence the properties, and in case of the electrical transport, strong dependence on the distance between the QDs is observed.

3.1 Optical Properties

Due to indirect bandgap nature of Si, bottom of the conductance band and top of the valence band are not aligned in k-space. By using the effective mass approximation, the effect of the confinement on the bandgap energy can be given as [65],

$$E_{\text{gap}} = E_{\text{gap\_si - bulk}} + \hbar^2\pi^2/2\left[1/L_x^2 + 1/L_y^2 + 1/L_z^2\right][1/m_e* + 1/m_h*] \quad (1)$$

where $E_{\text{gap\_si-bulk}}$ is the band gap in bulk silicon (1.12 eV), L_x, L_y, L_z are the dimensions of the nanostructure and m_e* and m_h* are the effective masses of electron

and hole in bulk silicon. In a first approximation, the hole mass is essentially half of the electron mass. This simple model predicts that the shifting of the valence band should be twice that of the conductance band. Figure 3 shows the effect of size reduction on band gap (measured from photoluminescence transition energy) [66]. Effect on band gap becomes vital by reducing the size below 5 nm, and for 2 nm size of QDs, it is predicted to be as high as 2 eV. This shifting of conduction and valance band well agrees with effective mass approximation and could be measured experimentally by x-ray and UV absorption techniques (such as x-ray or UV photoelectron spectroscopy) [67]. In addition to change of bandgap energy, the quantum confinement also influences the transition probabilities. Localization of the carriers (excitons) takes place in a very small volume due to quantum confinement, and this effect relaxes the k-selection rules, thus increasing the quasi-direct transition probabilities. Brus et al. [68, 69] investigated theoretically and experimentally to understand the size-dependent confinement effect and also surface passivation effect on photoluminescence property of Si QDs within size range 3–8 nm. They observed that the emission within 600 nm to 900 nm could be tuned by varying the size of the crystalline core of Si, and oxide passivation could lead to red shift of band gap, relatively high PL and low radiative rates. This group further suggested that the QDs have indirect band gaps by studying the broad absorbance near 3–4 eV.

Proper surface passivation by organic molecules or silica shells drastically increased the PL quantum yields (QYs) up to 40–50% [70, 71]. Holmes et al. [72]

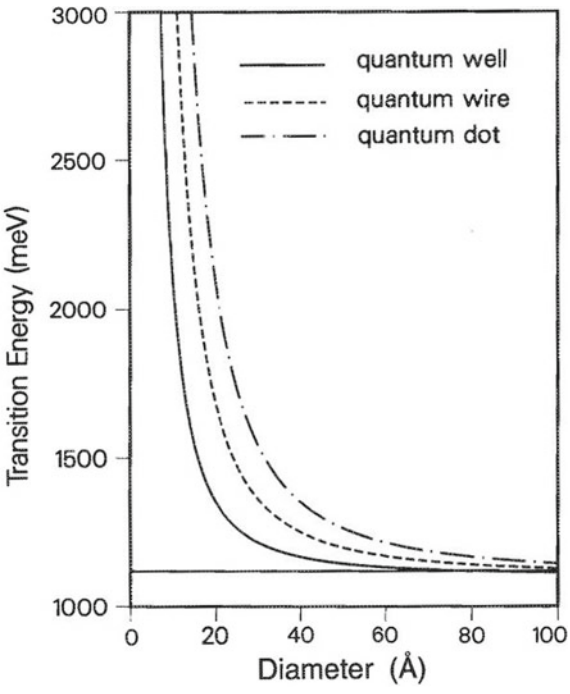

Fig. 3 Variation of transition energy with the size of the nanostructures Reproduced with permission from Ref. [66]. Copyright (2009) Canadian Science Publishing

reported high PL QY up to 23% using organic monolayers for the passivation of the silicon surface. QYs reached up to 60% when plasma-synthesized Si QDs surface was passivated by organic ligands under strict exclusion of oxygen [72]. However, for hydrogen-terminated Si QDs, maximum PL QYs reached up to 10% and decayed with ambient conditions. It is proved by both theoretical and experimental studies that the surface properties of QDs play a dominant role in controlling the band gap and the radiative decay time [73, 74]. Naturally occurring surface oxide generates oxygen-related surface/interface states inside the band gap. This causes slow relaxation of e–h carriers. Use of different ligands also creates different emissions [75]. In a study, average lifetime found to decrease from 42 to 33 μs as the emission peak maxima changed from 715 to 596 nm [75]. This blue shift could be explained by size reduction effect of QDs. Again, when green-emitting or green–yellow-emitting QDs were exposed to ambient air, red shift of luminescence occurred [33]. Surface-related states are responsible for this red shift observed in ambient air. Finally, a series of factors affects the PL properties of Si QDs like (i) differences in fabrication process, (ii) defect states or active centers at the surface of QDs or at the interface between QDs and matrix or at the matrix, (iii) different surface passivation processes and (iv) the presence of strain and stress at the interface between QDs and matrix. The last factor has been well confirmed and studied in a series of experiments [76–78].

4 Doping

To fabricate Si QD solar cell, it is necessary to dope the QDs by n- and p-type dopant. However, doping in Si QDs is totally different issue than it is for bulk Si. Direct quantitative characterization and tracking of this type of doping in nanometer resolution is really a challenge. Other some extreme difficulties include high impurity formation energy and kinetically unfavorable conditions of such type of doping. To get high power conversion from Si QD solar cells, it is necessary to gain information about the concentration of dopant impurity atoms and their positions at nanoscale. The existing characterization tools like x-ray photoelectron spectroscopy (XPS), secondary ion mass spectrometry (SIMS) and Auger electron spectroscopy are not adequate for this purpose. XPS cannot able to detect low concentration of impurity dopants. Using SIMS, relative concentrations of impurities can be estimated [79]. However, atom probe tomography, scanning transmission microscopy, electron paramagnetic resonance and high-resolution XPS might be useful for this purpose [80]. In spite of such difficulties, some research groups have succeeded in doping impurities like boron [81, 82], phosphorus [18, 83], antimony [84], etc. Impurity doping in Si QDs films has been done by using PECVD, sputtering, ion implantation, etc. [19, 85–87]. Co-sputtering of Si, SiO_2 and P_2O_5 has used to dope phosphorus atom in Si QDs [87]. A seven order of magnitude decrease in resistivity was noted for 0.1 atm.% phosphorous concentration. To calculate both the resistivity and the temperature dependence of the resistance (R), transfer length measurements of the resistance were used (Fig. 4) [88]. The activation energy E_a was calculated from the relation

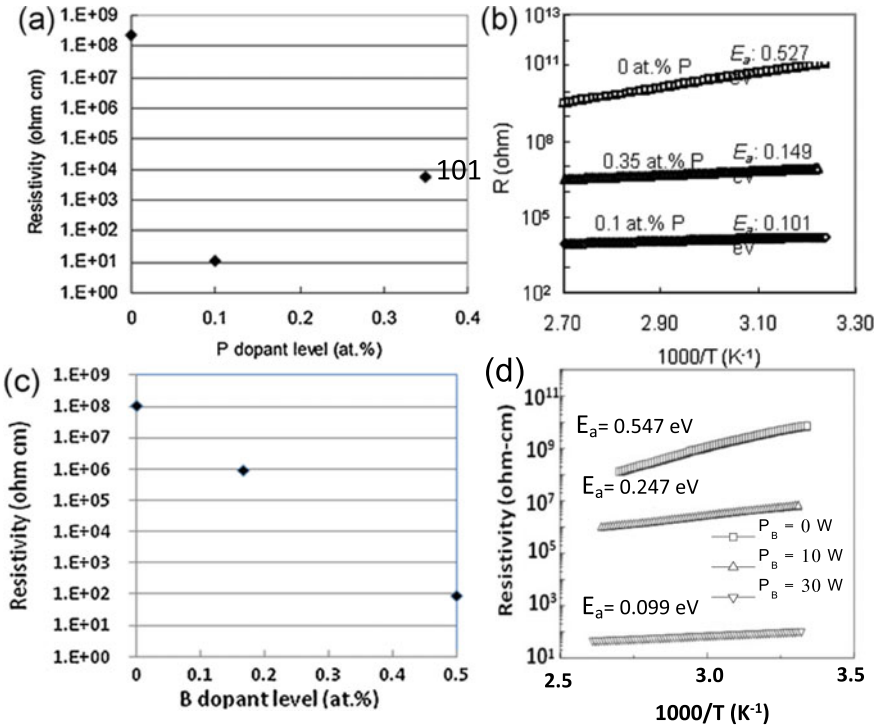

Fig. 4 Resistance obtained by transfer length measurements for different values of P and B doping concentrations using Si QDs of 5 and 4 nm sizes, respectively: **a** resistivity versus P doping level; **b** resistance versus temperature (P doping) (Reproduced with permission from Ref. [86]. Copyright (2009) Elsevier); **c** resistivity versus B dopant level; **d** resistivity versus temperature (Reproduced with permission from Ref. [88]. Copyright (2009) Elsevier)

$R \approx \exp(E_a/kT)$. The activation energy decreases from 0.527 to 0.101 eV when the P doping level increases from 0 to 0.1 atm.%. However, more increase of P doping up to 0.35 atm.% increased activation energy up to 0.149 eV and increased resistivity by three orders of magnitude. In a similar way, boron doping of 0.5 atm% resulted in six orders of magnitude decrease in resistivity. Transfer length resistivity measurement of such doping is shown in Fig. 3c. 13.4% power conversion efficiency has been achieved by depositing B-doped Si QDs/SiO_2 multilayer on n-type c-Si substrate [79]. In addition, some adverse effects of doping on the growth of Si QDs were also noted [89–92]. Acceleration in the phase separation in silicon-rich oxide layers was noted by phosphorus doping, and it also improves the crystallization of Si [90]. Doping of P atoms also enhances Si crystallization rate and phase separation in Si rich SiN_x films [92]. On the contrary, B doping slows down Si crystallization rate and has almost no effect on QD size [89]. Ni doping affected Si nanocrystal growth rate in a different way. Yoon et al. [92] have studied effects of such kind doping by thermal annealing of Ni-implanted SiO_x films. Moderate amount of Ni

favors the growth of Si nanocrystals. However, high amount of Ni accelerates the formation of $NiSi_2$ nanocrystals. Voitovych et al. [91] have studied the effect of Sn doping on the growth of Si nanocrystals in an amorphous SiO_x ($x = 1.15$) thin film. It was found that the presence of Sn favors the crystallization process by lowering the crystallization temperature by 200 °C and also lowering the size of nanocrystals. Doping of Sn also increases the crystalline phase to amorphous phase ratio.

5 Photovoltaics of Si QD Solar Cell

Use of QDs in fabricating solar cells has been shown the path to increase power conversion efficiency much higher than the present value which exists in today's state-of-the-art solar structures. To reach this goal by using quantum confinement effect in Si QDs, some distinct approaches have been taken by different research groups around the globe [93–100], such as (i) spectral conversion, (ii) all-Si QD solar cells, (iii) tandem or multi-junction solar cells, (iv) non-radiative energy transfer (NRET)-based solar cells, (v) organic/inorganic hybrid.

5.1 Spectral Conversion for Si Photovoltaics

Spectral conversion is a process design for more utilization of short wavelength (e.g., blue region) photons for which solar cell quantum efficiency is low. The spectral converters act by two basic mechanisms either by producing more than one low-energy photons by absorbing one high-energy photon or by shifting high-energy photons to a lower-energy photon. Down-conversion process minimizes thermalization losses in solar cells, and for c-Si solar cells, the maximum power conversion efficiency improvement was estimated to be 38.6% by placing spectral converter on the top of the solar cell [101]. In downshifting process for Si QD, a high-energy (blue–green region) photon is absorbed by the QD and re-emitted at lower energy (red–infrared region) that involves a radiative energy transfer from Si QD to Si solar cell underneath [64]. This process is depicted in Fig. 5. This process is a three-step process. First, a high-energy photon is absorbed by the QD, and a fast non-radiative relaxation takes place between the highest excited level and the intermediate level. Then, the emission of this lower energy photon (only one) has occurred through the radiative recombination of the electron from the intermediate level to the lowest level. Thus, with the help of this luminescence process of QDs, incident high-energy photon downshifted to lower energy high wavelength photon for which the internal quantum efficiency (IQE) of cell is high. For c-Si solar cell, IQE is very high in the range 500–1000 nm while low below 450 nm due to surface recombination. So, a downshifting of UV–blue photons to the region red–NIR could result in enhanced short-circuit current (I_{sc}). However, the open-circuit voltage (V_{oc}) and fill factor (FF)

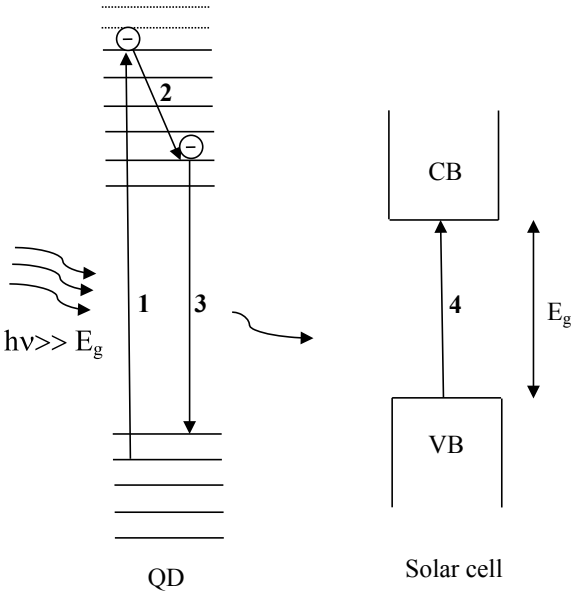

Fig. 5 Schematic for a radiative energy transfer from Si QD to Si solar cell underneath. 1. Absorption process of high-energy photon. 2. Non-radiative transition in lower energy level. 3. Radiative trasition (re-emission of lower energy photon). 4. Absorption of low-energy photon by solar cell

will not change as by downshifting. Also, there will be no effect on electronic property and resistance of the device. Simulation shows that QDs with an emission at ~ 600 nm could increase the I_{sc} of multicrystalline solar cell by nearly 10% [102]. The first reported experiment with Si QDs as a down-converter was performed in 2004 [103]. This measurement was done by applying spin-on-glass antireflecting SiO_2-based solution containing Si QDs on c-Si solar cell. This modification was increased the I_{sc} by 0.4%. However, the conclusion drawn in this study remains controversial. In a later study by a different group, it was suggested that the previous enhancement was due to the improved optical coupling of the incident light by Si QDs embedded in the spin on glass at the solar cell surface [104], and it was the porous nature of the QD film that was the origin of the performance enhancement of the cell because porous Si layer can act as antireflection layer [105]. So, the downshifting effect of Si QDs was put on doubt. The later group obtained a 0.6% efficiency improvement and proposed to use Si QD-based ink to determine the downshifting effect. By using Si QDs dispersed in organic solvent, improvement of 2.3% was observed for I_{sc}. Finally, by depositing Si QDs with either strong blue emission (1 nm diameter) or orange–red emission (2.85 nm) directly on industrial polycrystalline solar cell, efficiency improvement up to 70% using blue light and 10% improvement using visible light was obtained in 2007 [106].

5.2 All-Si QD Solar Cells (p–n or p–i–n Junction Solar Cells)

Devices containing Si QDs in forms of n-type Si QDs/p-type c-Si heterojunction, p-type Si QDs/n-type c-Si heterojunction or p–i–n junction have been reported. Table 1 summarizes the solar cell parameters of such photovoltaic devices with Si QDs. Table 1 shows that the performance of these Si QDs-based solar cells is inferior except a few. The PV device with 3 nm n-type Si QDs embedded in 2 nm thick 15

Table 1 Photovoltaic properties of Si QD-based solar cells

Device structure	V_{oc} (mV)	J_{sc}/I_{sc}	FF (%)	Efficiency (%)	Effective area	Ref.
p-type Si QDs in SiC/n-type c-Si	463	19 mA/cm^2	53	4.66	–	[110]
p-type a-SixC$_{1-x}$/intrinsic Si QDs in SiC/n-type a-SixC$_{1-x}$	282	0.339 mA/cm^2				[109]
n-type Si QDs in Si3N4/p-type c-Si	510	4.96 mA	20.5	–	1 mm^2	[17]
n-type poly-Si/intrinsic Si QDs in SiC/p-type hydrogenated a-Si	518	0.34 mA/cm^2	51	–	–	[111]
p-type Si QDs in SiO_2/intrinsic Si QDs in SiO_2/n-type Si QDs in SiO2	492	0.02 mA/cm^2			2.2 mm^2	[108]
p-type Si QDs in SiO_2/intrinsic Si QDs in SiO_2/n-type Si QDs in SiO2	373				0.12 cm^2	[107]
p-type Si QDs in SiO_2/n-type Si QDs in SiO_2	410	–	–	–	2–10 mm^2	[112]
n-type a-Si/intrinsic Si QDs in SiC/p-Si	532	24.1 mA/cm^2	48.9	6.28	0.8 cm^2	[111]
n-type Si QDs in Si_3N_4/p-type c-Si	500	26.5 mA/cm^2	65.2	8.6	1 cm^2	[113]
n-type Si QDs in SiO_2/p-type c-Si	556	29.8 mA/cm^2	63.83	10.58		[85]
n-type Si QDs in SiO_2/p-type c-Si	555.6	29.8 mA/cm^2	63.8	10.6	–	[114]
p-type Si QDs in SiO_2/n-type c-Si	525	37.7 mA/cm^2	78.5	13.4		[79]

layers of SiO_2 produced J_{sc} ~ 29.8 mA/cm^2, V_{oc} ~ 555.6 mV and FF ~ 63.8 with an overall PCE 10.6% [114]. The best one among such reports used p-type Si QDs with boron (B) concentration of 4×10^{20} cm^{-3} to fabricate p-type Si QDs/n-type Si heterojunction solar cell with PCE 13.4% (with J_{sc} 33.7 mA/cm^2, V_{oc} 525 mV and FF 78.5%) [79]. The cause of such inferior performances in other structures could be the poor charge transport properties among the QDs that lead to small J_{sc} values. The other noticeable point is that the V_{oc} values are not high as expected by incorporating higher bandgap Si QDs as active absorption layer in the solar cells. In these devices, it also becomes a challenge to estimate contribution in the PCE from only Si QDs as the performance of Si QDs is masked by that of the Si substrates. However, there are few reports where Si QD solar cells are made on insulating substrates. Figure 6 shows p–i–n PV device fabricated on quartz substrate [107] with an active area 0.12 cm^2. SIMS observation reveals that huge inter-diffusion of B and P occurred in the i-layer after high-temperature annealing and the structure changed to p–n junction. After annealing, this device showed V_{oc} around 373 mV. Later, the same group reported a photovoltaic device with same structure but with device area of 2.2 mm^2 with V_{oc} ~ 492 mV and J_{sc} 0.02 mA/cm^2 [108]. This low J_{sc} was ascribed to high series resistance 28 kΩ cm^2. In another attempt to estimate the contribution of only Si QDs layer, Si substrate was locally etched using chemical method, and the rest in form of a membrane was encapsulated after solid-phase crystallization of Si QDs to form p–i–n device structure [109]. Using doped amorphous silicon carbide (a-Si_xC_{1-x}:H) as

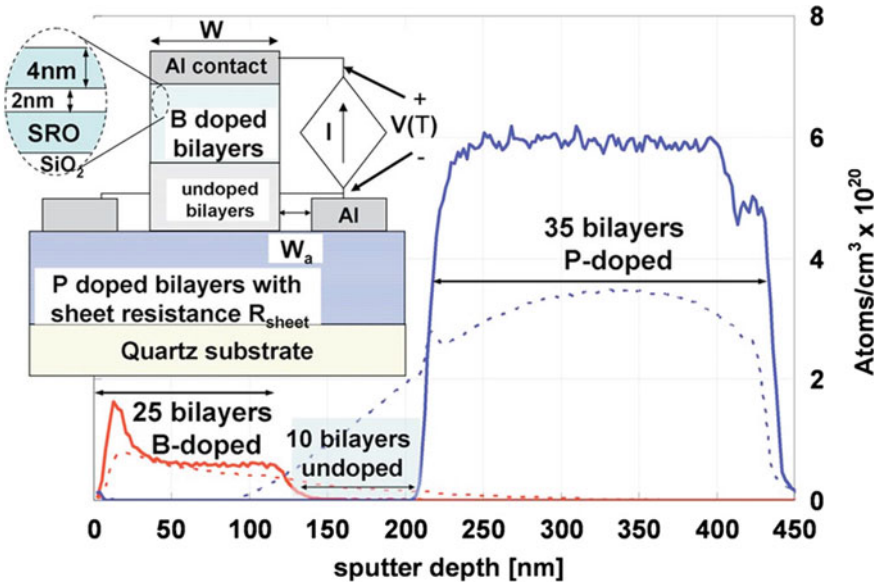

Fig. 6 SIMS profiles of annealed (dotted line) and as-deposited (solid line) p–i–n structure. Inset shows schematic of the device (p–i–n) structure Reproduced with permission from Ref. [107]. Copyright (2009) American Institute of Physics

electron and hole selective contacts, this device structure showed a V_{oc} ~ 282 mV, J_{sc} ~ 0.339 mA/cm^2. This low J_{sc} was resulted due to the presence of high recombinative defects in the depletion region.

5.3 Non-radiative Energy Transfer-Based Solar Cells

In recent years, non-radiative energy transfer (NRET) has successfully demonstrated for hybrid nanostructures combining absorbing components (e.g., quantum dots) with high-mobility semiconducting transport channels (e.g., Si). Exploiting the NRET process by using colloidal semiconductor, nanocrystals have opened new possibilities in light harvesting that provides the benefit of absorbing the solar spectrum in a wider range than Si layers are able to [97, 115–117]. Limitation of low-charge transfer efficiency in charge transfer-based devices could be overcome in NRET-based devices. In NRET process, long-range dipole–dipole interaction goes beyond that involved in both radiative energy transfer and the short-range charge transfer process. The highest NRET efficiency could be as high as ~ 65% where energy transfer occurred to the adjacent Si layer as revealed by time-resolved photocurrent measurements, and the increase in photocurrent could be as large as three times [118, 119]. Using energy transfer from nanocrystalline-Si (nc-Si) QDs (emitting in near red region and absorption in blue region), efficient exciton harvesting has been achieved in underlying radial p–n junction SiNW arrays [97, 120]. An increase of 18.5% in J_{sc} value has reported for this nc-Si QD-modified SiNW solar cells. Using time-dependent photoluminescence decay experiments, it was demonstrated that NRET rate was ~ 1.6 times faster than the radiative energy transfer rate.

5.4 Multilayer Tandem Solar Cells

Tandem solar cells are basically stacking of p–n or p–i–n diode with different bandgap materials and connect them either in series or in parallel, so that a major part of the solar spectrum could be absorbed. Hence, increasing the cell performance rapidly compare to single-junction cells. Performance limitations of the tandem cells have been studied extensively by Meillaud et al. [121]. For a single-junction radiative efficiency, limit for silicon cell is 30%, whereas for double and triple junction, this is 42.5% and 47.5%, respectively. The optimal bandgap requirement of top cell for maximum performance under an AM1.5G solar spectrum is ∼ 1.7 to 1.8 eV for a 2-cell tandem with a Si cell as bottom cell and 1.5 and 2.0 eV for the middle and upper cells for a 3-cell tandem. Figure 7 shows a 3-cell tandem stack. For the upper cell, the choice of material should be a high bandgap material, so that high-energy photon (blue region of solar spectrum) could be absorbed, whereas for the bottom cell, the choice material should be such that it can absorb well the infrared portion

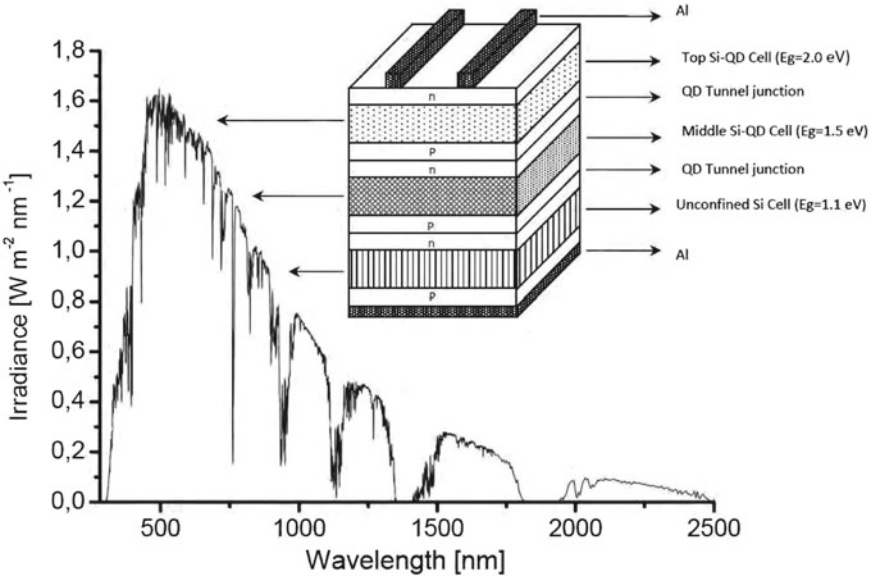

Fig. 7 Stacking of three p–n junctions to utilize three different regions of AM 1.5 solar spectrum. Reproduced with permission from Ref. [65]

of the spectrum, i.e., low-energy photons. For a series connection, these cells are connected through tunnel diodes.

In fabrication of all-Si tandem solar cells, Si QDs might be useful with the addition of Si thin-film technology. By changing the size of QDs, band could be varied from high to low which will allow fabricating from top cells to bottom cell. If the QDs could be patterned in a superlattice stack, the charge carriers can tunnel from one QD to another. So, by varying the size of the QDs and using quantum confinement effect in addition to the thin-film technology, all-Si tandem cell could be achieved by stacking Si QD layers from higher band gap to lower band gap as shown in the Figure.

5.5 Si QDs-Organic Hybrid Solar Cell

Since the first report on organic/Si heterojunction photovoltaics in 1984 where pyrene was used as the organic compound, several attempts have been done and power conversion efficiency reaches as high as 13.6% [122, 123]. The literature shows two types of such solar cell structures: (i) hole conductor and electron acceptor-based organic bulk heterojunction (OBHJ) solar cell. The mixture poly (3-hexylthiophene): 1-(3-methoxycarbonyl) propyl-1-phenyl [6, 6] C61 (P3HT: PCBM) and PEDOT:PSS is currently the most prominent material system in such organic photovoltaic, (ii) the

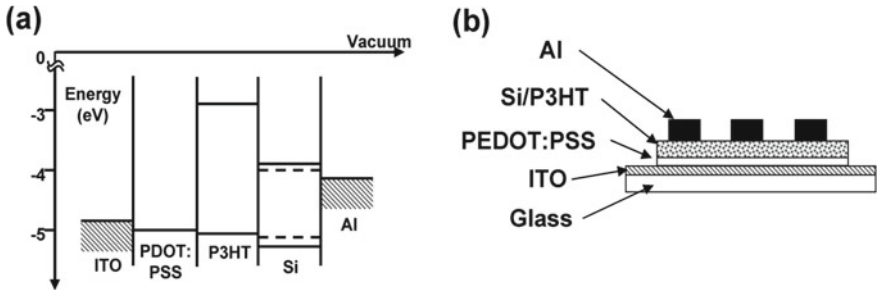

Fig. 8 **a** Energy band diagram of a Si nanocrystal/P3HT solar cell. The dotted lines represent the valence and conduction bands of bulk Si, while the solid lines are representation of 4 nm nanocrystal. **b** Schematic of a hybrid solar cell Reproduced with permission from Ref. [125]. Copyright (2009) American Chemical Society

dye-sensitized solar cell (DSSC). Use of Si QDs in such devices could increase short-circuit current and the external quantum efficiency. Characteristics of Si QDs with conducting polymer had been studied by Dietmueller et al. [124] in detail, where the charge transfer between Si QDs and the component of bulk heterojunction solar cells (P3HT and PCBM) was reported. Liu et al. reported a hybrid solar cell fabricated by spin coating blends of silicon nanocrystals (Si NCs) and poly-3(hexylthiophene) (P3HT) polymer together on PEDOT:PSS-coated ITO glass (Fig. 8) [125]. V_{oc} and I_{sc} were found to be dependent on Si nanocrystals size due to changes in the band gap and surface-area-to-volume ratio. The best performance device made with 35 wt% Si NCs 3-5 nm in size showed 1.15% power conversion efficiency.

6 Future Outlook and Challenges

Few photovoltaic devices using Si QDs in the device structure of Si QDs/opposite polarity c-Si p–n (hetero) junctions and p–i–n junctions have been reported (Table 1). Some all-Si tandem cells are also reported using the size-dependent quantum properties of these Si QDs [121]. The most efficient Si QD cell with power conversion efficiency of 13.4% so far reported was fabricated by depositing a p-type Si QDs with B concentration of 4×10^{20} cm^{-3} on n-type c-Si [79]. Although the device performance (I_{sc} 33.7 mA cm^{-2}, V_{oc} 525 mV and FF 78.5%) is not comparable to commercial crystalline Si solar cell, yet this shows a path toward realization of all-Si tandem solar cells based on Si QDs in near future. Cell performance of the Si QD-based devices constrained mainly due to the difficulty in charge transfer between the QDs and the formation of tunnel junctions which has direct effect on I_{sc} values. Again, the V_{oc} obtained from these solar cells is much lower than the expected value. Another difficulty is that Si QDs alone contributing how much to the photovoltaic performance of the device cannot be estimated as the Si substrates also contribute. Fabrication of Si substrate-free Si QD solar cells is also reported [107]. These types

of cells are discussed in Sect. 5.2. However, preparation of these type of cells is not easy as one has to deposit layer of Si QDs embedded in dielectric matrix. To improve device performance of such kind of solar cells, it is necessary to optimize Si QDs growth condition, i.e., film deposition conditions, and improve interface engineering, light trapping and passivation techniques as the Si QDs layers are very thin.

However, in a futuristic approach, use of Si nanocrystals-based energy selective electrodes could have an important potential to improve the power conversion efficiency of hot carrier solar cells (HCSCs). The experiment in this regard was done by Conibeer et al. [126] where they used a QD-based layer (with a discrete energy level) embedded between two insulating layers. This structure consists of a 4 nm thick Si-nc layer sandwiched between two 5 nm SiO_2 layers as barrier. Control over the nanocrystal size was maintained by controlling the thickness of the layer. Thus, the specific discrete energy levels could be created inside the double barrier.

The appearance of differential resistance (NDR) feature in the I-V curve at room temperature is very encouraging though it is weak (Fig. 9). This experiment has started a series of experiments on HCSCs based on Si nanocrystals layers with energy selective electrodes.

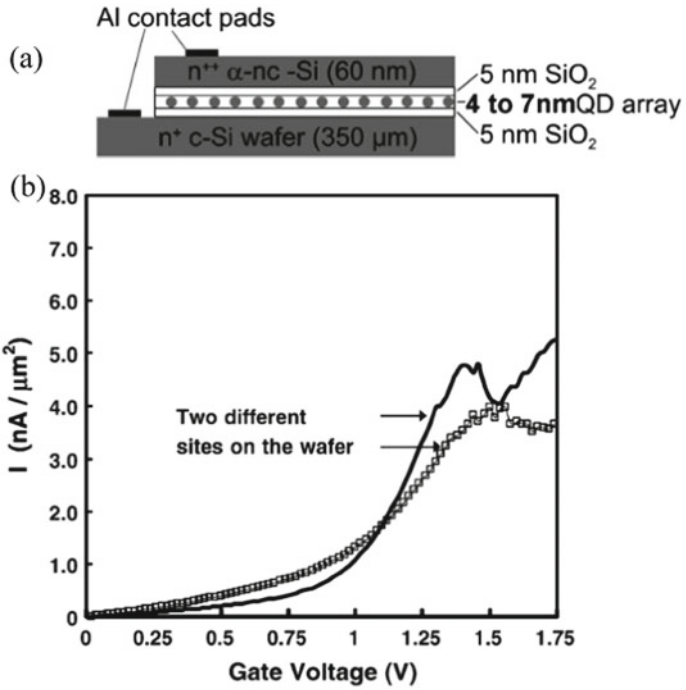

Fig. 9 **a** Schematic of selected energy contact structure and **b** I–V curves of this structure showing NDR at 300 K for two mesa devices on one wafer Reproduced with permission from Ref. [127]. Copyright (2008) Elsevier

Femtosecond transient absorption spectroscopic studies on different sizes of colloidal Si QDs showed that multiple exciton generation (MEG) occurs with much higher efficiency in Si QDs as compared to bulk Si [127]. Reports confirmed that a threshold exists for Si QDs with diameter 9.5 nm to be 2.4 $\pm$ 0.1 E_g with exciton quantum yield of 2.6 $\pm$ 0.2 excitons per absorbed photon at 3.4E_g. In a contrary to the negative impact of indirect bandgap nature of Si for photonic applications, it turns out to be beneficial for MEG-based photovoltaic applications. Because the relatively long exciton lifetime in Si QDs simplifies energy extraction compared to the direct bandgap semiconductor QDs.

References

1. Shirahata, N. (2011). *Physical Chemistry Chemical Physics: PCCP, 13,* 7284.
2. English, D. S., Pell, L. E., Yu, Z. H., Barbara, P. F., & Korgel, B. A. (2002). *Nano Letters, 2,* 681.
3. Gupta, M. T., & Wiggers, S. H. (2009). *Advanced Functional Materials, 19,* 696.
4. Shirahata, N., Tsuruoka, T., Hasegawa, T., & Sakka, Y. (2010). *Small (Weinheim an der Bergstrasse, Germany), 6,* 915.
5. Godefroo, S., Hayne, M., Jivanescu, M., Stesmans, A., Zacharias, M., & Lebedev, O. I. (2008). *Nature Nanotechnol, 3,* 174.
6. Ghosh, B., Sakka, Y., & Shirahata, N. (2013). *J Mater Chem A, 1,* 3747.
7. Cullis, A. G., & Canham, L. T. (1991). *Nature, 353,* 335–338.
8. Ciurea, M. L., & Lepadatu, A. M. (2015). *Dig J Nanomater Bios, 10,* 59.
9. Garrido, B., López, M., Pérez-Rodrıguez, A., Garcı, C., Pellegrino, P., Ferré, R., et al. (2004). *Nucl Instrum Methods Phys Res B, 216*, 213.
10. Wang, J., et al. (1992). *Phys Rev Lett, 69*, 3252.
11. Janz, S., Löper, P., & Schnabel, M. (2013). *Materials Science and Engineering B, 178,* 542–550.
12. Chen, X., & Yang, P. (2015). *Journal of Materials Science: Materials in Electronics, 26,* 4604–4617.
13. Ray, S. K., Maikap, S., Banerjee, W., & Das, S. (2013). *Journal of Physics. D. Applied Physics, 46,* 153001.
14. Kourkoutis, L. F., Hao, X., Huang, S., Puthen-Veettil, B., Conibeer, G., Green, M. A., et al. (2013). *Nanoscale, 5,* 7499.
15. Kuo, K. Y., Huang, P. R., & Lee, P. T. (2013). *Nanotechnology, 24,* 195701.
16. Lepadatu, A. M., Stavarache, I., Ciurea, M. L., & Iancu, V. (2010). *Journal of Applied Physics, 107,* 033721.
17. Di, D., Xu, H., Perez-Wurfl, I., Green, M. A., & Conibeer, G. (2013). *Prog Photovolt Res Appl, 21,* 569.
18. Wu, P. J., Wang, Y. C., & Chen, I. C. (2013). *Journal of Physics. D. Applied Physics, 46,* 125104.
19. Gutsch, S., Hartel, A. M., Hiller, D., Zakharov, N., Werner, P., & Zacharias, M. (2012). *Applied Physics Letters, 100,* 233115.
20. Askari, S., Macias-Montero, M., Velusamy, T., Maguire, P., Svrcek, V., & Mariotti, D. (2015). *Journal of Physics. D. Applied Physics, 48,* 314002.
21. Ghosh, B., & Shirahata, N. (2014). *Science and Technology of Advanced Materials, 15,* 014207.
22. van de Dogan, M. C. M. (2016). Sanden. *Plasma Process Polym, 13,* 19–53.
23. Nozaki, T., Sasaki, K., Ogino, T., Asahi, D., & Okazaki, K. (2007). *Journal of Thermal Science and Technology, 2,* 192.

24. Sankaran, R. M., Holunga, D., Flagan, R. F., & Giapis, K. P. (2005). *Nano Letters, 5,* 537.
25. Barwe, B., Stein, A., Cibulka, O. E., Pelant, I., Ghanbaja, J., Belmonte, T., et al. (2014). *Plasma Process Polym, 121,* 32–40.
26. Nozaki, T., Sasaki, K., Ogino, T., Asahi, D., & Okazaki, K. (2007). *Nanotechnology, 18,* 235603.
27. Askari, S., Levchenko, I., Ostrikov, K., Maguire, P., & Mariotti, D. (2014). *Applied Physics Letters, 104,* 163103.
28. Askari, S. (2014). Synthesis and characterization of Si-based quantum confined nanoparticles by atmospheric pressure plasmas, Dissertation, University of Ulster, U. K.
29. Wiggers, G. H. (2009). *Phys E Low-Dimens Syst Nanostructures, 41,* 1010.
30. Goller, S., Polisski, H., & Wiggers, D. (2010). Kovalev. *Applied Physics Letters, 97,* 041110.
31. Petermann, N., Stein, N., Schierning, G., Theissmann, R., Stoib, B., Brandt, M. S., et al. (2011). *Journal of Physics. D. Applied Physics, 44,* 174034.
32. Giesen, B., Wiggers, H., Kowalik, A., & Roth, P. (2005). *J Nanoparticle Res, 7,* 29.
33. Chaukulkar, R. P., De Peuter, K., Stradins, P., Pylypenko, S., Bell, J. P., Yang, Y., et al. (2014). *Mater Interface, 6,* 19026.
34. Jariwala, B. N., Dewey, O. S., Stradins, P., Ciobanu, C. V., Agarwal, S., & Appl, A. C. S. (2011). *Mater Interface, 3,* 3033.
35. Mangolini, L., & Kortshagen, U. (2007). *Advanced Materials, 19,* 2513.
36. Kortshagen, U. (2009). *Journal of Physics. D. Applied Physics, 42,* 113001.
37. Mangolini, L., Thimsen, E., & Kortshagen, U. (2005). *Nano Letters, 5,* 655.
38. Yasar-Inceoglu, O., Lopez, T., Farshihagro, E., & Mangolini, L. (2012). *Nanotechnology, 23,* 255604.
39. Lopez, T., Mangolini, L., Vac, J. (2014). *Sci Technol B, Nanotechnol Microelectron Mater Process Meas Phenom, 32*, 061802.
40. Ding, Y., Yamada, R., Gresback, R., Zhou, S., Pi, X., & Nozaki, T. (2014). *Journal of Physics. D. Applied Physics, 47,* 485202.
41. Gresback, R., Nozaki, T., & Okazaki, K. (2011). *Nanotechnology, 22,* 305605.
42. Kambara, M., Kitayama, A., Homma, K., Hideshima, T., Kaga, M., Sheem, K.-Y., et al. (2014). *Journal of Applied Physics, 115,* 143302.
43. Rao, N., Girshick, S., Heberlein, J., McMurry, P., Jones, S., Hansen, D., et al. (1995). *Plasma Chemistry and Plasma Processing, 15,* 581.
44. Rao, N. P., Tymiak, N., Blum, J., Neuman, A., Lee, H. J., Girshick, S. L., et al. (1998). *Journal of Aerosol Science, 29,* 707.
45. Rao, N. P., Lee, H. J., Kelkar, M., Hansen, D. J., Heberlein, J. V. R., McMurry, P. H., et al. (1997). *Nanostructured Mater, 9,* 129.
46. Colombo, V., Deschenaux, C., Ghedini, E., Gherardi, M., Jaeggi, C., Leparoux, M., et al. (2012). *Plasma Sources Science and Technology, 21,* 045010.
47. Heath, J. R. (1992). *Science, 258,* 1131.
48. Dhas, N. A., Raj, C. P., & Gedanken, A. (1998). *Chemistry of Materials, 10,* 3278.
49. Bley, R. A., & Kauzlarich, S. M. (1996). *Journal of the American Chemical Society, 118,* 12461.
50. Mayeri, D., Phillips, B. L., Augustine, M. P., & Kauzlarich, S. M. (2001). *Chemistry of Materials, 13,* 765.
51. Zou, J., Sanelle, P., Pettigrew, K. A., & Kauzlarich, S. M. (2006). *Journal of Cluster Science, 17,* 565.
52. Wilcoxon, J. P., & Samara, G. A. (1999). *Applied Physics Letters, 74,* 3164.
53. Wilcoxon, J. P., Samara, G. A., & Provencio, P. N. (1999). *Phys Rev B, 60,* 2704.
54. Tilley, R. D., & Yamamoto, K. (2006). *Advanced Materials, 18,* 2053.
55. Okada, R., & Iijima, S. (1991). *Applied Physics Letters, 58,* 1662.
56. Werwa, E., Seraphin, A. A., Chiu, L. A., Zhou, C. X., & Kolenbrander, K. D. (1994). *Applied Physics Letters, 64,* 1821.
57. Umezu, K., Shibata, S., Yamaguchi, A., Sugimura, Y., & Yamada, T. Y. (1998). *Journal of Applied Physics, 84,* 6448.

58. Yamada, Y., Orii, T., Umezu, I., Takeyama, S., & Yoshida Japan, T. (1996). *Journal of Applied Physics, 35*(Pt 1), 1361.
59. Makino, T., Inada, M., Umezu, I., & Sugimura, A. (2005). *J Phys D Appl Phys, 38*, 3507.
60. Orii, T., Hirasawa, M., & Seto, T. (2003). *Applied Physics Letters, 83,* 3395.
61. Shirahata, N., Linford, M. R., Furumi, S., Pei, L., Sakka, Y., Gates, R. J., et al. (2009). *Chem Commun*, 4684–4686.
62. Umezu, M., & Senoo, H. (2007). *Journal of Physics: Conference Series, 59,* 392.
63. Heinrich, J. L., Curtis, C. L., Credo, G. M., Kavanagh, K. L., & Sailor, M. J. (1992). *Science, 255,* 66.
64. Bley, R. A., Kauzlarich, S. M., Davis, J. E., & Lee, H. W. H. (1996). *Chem Mater, 8*, 1881.
65. Pucker, G., Serra, E., & Jestin, Y. (2012). Silicon quantum dots for photovoltaics: A review. In A. Al-Ahmadi (ed.). *Quantum dots—A variety of new applications* (pp. 59–92). Rijeka: Intech.
66. Lockwood, D. J., Aers, G. C., Allard, L. B., Bryskiewicz, B., Charbonneau, S., Houghton, D. C., et al. (1992). *Canadian Journal of Physics, 70,* 1184–1193.
67. Lockwood, D. J., Lu, Z. H., & Baribeau, J.-M. (1996). *Physical Review Letters, 76,* 539–541.
68. Brus, L. (1994). *Journal of Physical Chemistry, 98,* 3575.
69. Littau, K. A., Szajowski, P. J., Muller, A. J., Kortan, A. R., & Brus, L. E. (1993). *Journal of Physical Chemistry, 97,* 1224.
70. Henderson, E. J., & Kelly, J. A. (2009). *J G C Veinot Chem Mater, 21,* 5426.
71. Hessel, C. M., Henderson, E. J., & Veinot, J. G. C. (2006). *Chemistry of Materials, 18,* 6139.
72. Holmes, J. D., Ziegler, K. J., Doty, R. C., Pell, L. E., Johnston, K. P., & Korgel, B. A. (2001). *Journal of the American Chemical Society, 123,* 3743.
73. Ledoux, G., Gong, J., & Huisken, F. (2001). *Applied Physics Letters, 79,* 4028.
74. Lannoo, M., Delerue, C., & Allan, G. (1996). *Journal of Luminescence, 70,* 170.
75. Yu, W., Xu, Y. M., Li, H. M., Zhan, X. Z., & Lu, W. B. (2013). *Applied Physics A, 111,* 501.
76. Khriachtchev, L., Kilpelä, O., Karirinne, S., Keränen, J., & Lepistö, T. (2001). *Applied Physics Letters, 78,* 323–326.
77. Daldosso, N., Luppi, M., Ossicini, S., Degoli, E., Magri, R., Dalba, G., et al. (2003). *Phys Rev B, 68,* 085327–085335.
78. Zatryb, G., Podhorodecki, A., Hao, X. J., Misiewicz, J., Shen, Y. S., & Green, M. A. (2011). *Nanotechnology, 22,* 335703–335708.
79. Hong, S. H., Kim, Y. S., Lee, W., Kim, Y. H., Song, J. Y., Jang, J. S., et al. (2011). *Nanotechnology, 22,* 425203.
80. Conibeer, G., Green, M. A., König, D., Perez-Wurfl, I., Huang, S., Hao, X., et al. (2011). *Prog Photovolt Res Appl, 19*, 813.
81. Xie, M., Li, D., Chen, L., Wang, F., Zhu, X., & Yang, D. (2013). *Applied Physics Letters, 102,* 123108.
82. Ma, J., Ni, J., Zhang, J., Huang, Z., Hou, G., Chen, X., et al. (2013). *Solar Energy Materials and Solar Cells, 114,* 9.
83. Zeng, Y., Dai, N., Cheng, Q., Huang, J., Liang, X., & Song, W. (2013). *Materials Science in Semiconductor Processing, 16,* 598.
84. So, Y. H., Huang, S., Conibeer, G., & Green, M. A. (2011). *EPL-Europhys Lett, 96,* 17011.
85. Park, S., Cho, E., Song, D., Conibeer, G., & Green, M. A. (2009). *Solar Energy Materials and Solar Cells, 93,* 684.
86. Hao, X. J., Cho, E. C., Scardera, G., Shen, Y. S., Bellet-Amalric, E., Bellet, D., et al. (2009). *Solar Energy Materials and Solar Cells, 93,* 1524.
87. Nakamura, T., Adachi, S., Fujii, M., Miura, K., & Yamamoto, S. (2012). *Phys Rev B, 85,* 045441.
88. Hao, X. J., Cho, E. C., Flynn, C., Shen, Y. S., Park, S. C., Conibeer, G., et al. (2009). *Sol Energ Mater Sol Cells, 93,* 273–279.
89. Hao, X. J., Cho, E. C., Flynn, C., Shen, Y. S., Conibeer, G., & Green, M. A. (2008). *Nanotechnology, 19,* 424019.

90. Hao, X. J., Cho, E. C., Scardera, G., Bellet-Amalric, E., Bellet, D., Shen, Y. S., et al. (2009). *Thin Solid Films, 517,* 5646.
91. Voitovych, V. V., Rudenko, R. M., Kolosiuk, A. G., Krasko, M. M., Juhimchuk, V. O., Voitovych, M. V., et al. (2014). *Semiconductors (Translation of Fizika i Tekhnika Poluprovodnikov (Sankt-Peterburg)), 48,* 73.
92. Yoon, J. H. (2014). *Materials Letters, 136,* 237.
93. Klampaftis, E., Ross, D., McIntosh, K. R., & Richards, B. S. (2009). *Sol Energ Mater Sol Cells, 93,* 345–351.
94. Richards, B. S. (2006). *Sol Energ Mater Sol Cells, 90,* 1189–1207.
95. Marti, L. A. (2010). *Sol Energ Mater Sol Cells, 94,* 287–296.
96. Nozik, A. J., Beard, M. C., Luther, J. M., Law, M., Ellingson, R. J., & Johnson, J. C. (2010). *Chemical Reviews, 110,* 6873–6890.
97. Dutta, M., Thirugnanam, L., Trinh, P. V., & Fukataetal, N. (2015). *ACS Nano, 9,* 6891–6899.
98. Conibeer, G., Green, M. A., Cho, E. C., König, D., Cho, Y. H., Fangsuwannarak, T., et al. (2008). *Thin Solid Films, 516,* 6748–6756.
99. Di, D., Perez-Wurfl, I., Conibeer, G., & Green, M. A. (2010). *Solar Energy Materials and Solar Cells, 94,* 2238–2243.
100. Buhbut, S., Itzhakov, S., Tauber, E., Shalom, M., Hod, I., Geiger, T., et al. (2010). *ACS Nano, 4,* 1293–1298.
101. Trupke, T., Green, M. A., & Würfel, P. (2002). *Journal of Applied Physics, 92,* 1668–1675.
102. van Sark, W. G. J. H. M., Meijerink, A., Schropp, R. E. I., van Roosmalen, J. A. M., & Lysen, E. H. (2004). *Semiconductors, 38*, 962–969.
103. Švrcek, V., Slaoui, A., & Muller, J.-C. (2004). *Thin Solid Films, 451–452,* 384–388.
104. Pi, X., Li, Q., Li, D., & Yang, D. (2011). *Sol Energ Mater Sol Cells, 95,* 2941–2945.
105. Chaoui, R., Mahmoudi, B., & Si Ahmed, Y. (2008). *Phys Status Solidi A, 205*, 1724–1728.
106. Stupca, M., Alsalhi, M., Al Saud, T., Almuhanna, A., & Nayfeh, M. H. (2007). *Appl Phys Lett, 91*, 063107.
107. Perez-Wurfl, X., Hao, A., Gentle, D. H., Kim, G., & Conibeer, M. A. (2009). Green. *Applied Physics Letters, 95,* 153506.
108. Perez-Wurfl, L., Ma, D., Lin, X., Hao, M. A., & Conibeer, G. G. (2012). *Solar Energy Materials and Solar Cells, 100,* 65.
109. Löper, P., Canino, M., Qazzazie, D., Schnabel, M., Allegrezza, M., Summonte, C., et al. (2013). *Appl Phys Lett, 102*, 033507.
110. Song, D., Cho, E. C., Conibeer, G., Flynn, C., Huang, Y., & Green, M. A. (2008). *Solar Energy Materials and Solar Cells, 92,* 474.
111. Yamada, S., Kurokawa, Y., Miyajima, S., & Konagai, M. (2014). *Nanoscale Research Letters, 9,* 1.
112. Di, D., Perez-Wurfl, I., Gentle, A., Kim, D. H., Hao, X., Shi, L., et al. (2010). *Nanoscale Research Letters, 5,* 1762.
113. Wu, P.-J., Wang, Y.-C., & Chen, I.-C. (2013). *Nanoscale Research Letters, 8,* 457.
114. Cho, E. C., Park, S., Hao, X., Song, D., Conibeer, G., Park, S. C., et al. (2008). *Nanotechnology, 19,* 245201.
115. Lu, S., & Madhukar, A. (2007). *Nano Letters, 7,* 3443–3451.
116. Achermann, M., Petruska, M. A., Kos, S., Smith, D. L., Koleske, D. D., & Klimov, V. I. (2004). *Nature, 29,* 642.
117. Nguyen, H. M., Seitz, O., Peng, W., Gartstein, Y. N., Chabal, Y. J., & Malko, A. V. (2012). *ACS Nano, 6,* 5574.
118. Lu, S., Lingley, Z., Asano, T., Harris, D., Barwicz, T., Guha, S., et al. (2009). *Nano Letters, 9,* 4548.
119. Nguyen, H. M., Seitz, O., Aureau, D., Sra, A., Nijem, N., Gartstein, Y. N., et al. (2011). *Applied Physics Letters, 98,* 161904.
120. Dutta, M., & Fukata, N. (2015). *Nano Energy, 11,* 219–225.
121. Meillaud, F., Shah, A., Droz, C., Vallat-Sauvarin, E., & Miazza, C. (2006). *Sol Energ Mater Sol Cells, 90,* 2952–2959.

122. Mc Caffrey, R. R., Prasad, P. N. (1984). *Solar Cells, 11*, 401–409.
123. Park, K.-.T., Kim, H.-J., Park, M.-J., Jeong, J.-H., Lee, J., Choi, D.-G., et al. (2015). *Sci Rep, 5*, 12093.
124. Dietmueller, R., Stegner, A. R., Lechner, R., Niesar, S., Pereira, R. N., Brandt, M. S., et al. (2009). *Applied Physics Letters, 94,* 113301.
125. Liu, C. Y., Holman, Z. C., & Kortshagen, U. R. (2009). *Nano Letters, 9,* 449–452.
126. Conibeer, G., Jiang, C. W., König, D., Shrestha, S., Walsh, T., & Green, M. A. (2008). *Thin Solid Films, 516,* 6968–6973.
127. Beard, M. C., Knutsen, K. P., Yu, P., Luther, J. M., Song, Q., Metzger, W. K., et al. (2007). *Nano Lett, 7*, 2506.

Progress in Growth and Development of Perovskite Single Crystals and Their Potential Use in the Future Devices

Mrinal Dutta and Aishik Basu Mallick

Abstract Single crystals of organic–inorganic hybrid halide perovskites ($MAPbX_3$; MA=$CH_3NH_3^+$, X=Br^-, I^- or $FAPbX_3$ where FA (formamidinium) $NH_2CH{=}NH_2^+$, X=I^- or Br^-) have shown remarkably low trap density, high carrier mobility, large light absorption coefficient, low non-radiative recombination, and long carrier diffusion length. As a result of these properties, perovskite single crystals could be anticipated to overcome the drawbacks and bottleneck problems faced by polycrystalline perovskite thin films in several optoelectronic and photovoltaic applications. This chapter focuses on the progress and development of growth techniques of these perovskite single crystals and their applications in photovoltaics and different detectors. Finally, the enormous challenges face by the fabrication processes and possible new techniques to face the problems of this emerging field are also included.

Keywords Perovskite · Single crystal · Growth · Crystallization · Single crystal photovoltaics · Single crystal detector

1 Introduction

Technologies that have potential for higher power conversion efficiencies with lower production costs could replace silicon (Si) technology for future processing. Organic–inorganic hybrid perovskites ($MAPbX_3$ or $FAPbX_3$ where MA (methylamonium)=$CH_3NH_3^+$, FA (formamidinium) $NH_2CH{=}NH_2^+$, X=I^- or Br^-), a group of materials having layers of organic and inorganic elements in alternating form, are considered as potential material for future device applications for their

M. Dutta (✉)
Inorganic Photovoltaic Devices Group, Advanced Materials Device Division, Council of Scientific & Industrial Research (CSIR)-National Physical Laboratory, K.S. Krishnan Marg, Pusa, New Delhi 110012, India
e-mail: sspmd.iacs@gmail.com

A. B. Mallick
Department of Energy Engineering, Central University of Jharkhand, Ranchi, Jharkhand 835205, India

S. J. Ikhmayies (ed.), *Advances in Energy Materials*,
Advances in Material Research and Technology,
https://doi.org/10.1007/978-3-030-50108-2_7

cheap production. Some key features of these perovskite materials are broad and high solar light absorption, low non-radiative recombination rates with easy fabrications process. Use of these organic–inorganic hybrid perovskite materials for solar energy conversion comes with the prospect of high conversion efficiency at low fabrication cost that has grown in an exponential manner in the last few years to reach efficiency up to 25.2% [1–5]. These types of materials also have widely been used in photodetectors [6], lasing [7], and light-emitting diodes [8]. However, this fascinating material has some major drawbacks. Among this, environmental impact of using such materials has to be considered first as lead has remains to be the main constituent of high performing perovskite materials. Also these materials show rapid degradation when exposed to environment. State of art up to now shows stability for thousands of hours. However, for commercial production, stability should be minimum for 10 years. Zhou et al. have reported stability for 2000 h in dark at room temperature in air ambient for mesoporous $TiO_2/CH_3NH_3PbI_3/C$ device structure [9]. Again, for temperature higher than 60 °C, rapid degradation of active material as well as devices occurs that could find its route in either fading or new types of reactions accelerating degradation. External factors like water vapor, temperature, oxygen, UV light, etc., and internal factors such as interfacial and within lattice ion migration, electro-migrations are considered as major causes for degradation [10]. In terms of stability, relaxation should come in the form of single crystals of hybrid halide perovskites that have shown remarkably low trap state densities, long carrier diffusion lengths, and large absorption coefficient. In addition, the as-prepared perovskite single crystals exhibit a narrower band gap than the corresponding films, which means improved photocurrent generation and broader light absorption. These properties are comparable to the best photovoltaic candidate silicon (Si) [11, 12]. Different techniques have been used to produce hybrid perovskite single crystals with different cation (like MA or FA for organic cation and Pb or Sn for inorganic cation) and anion (like I or Br or Cl) in organic and inorganic parts [11, 13–26]. Fabrication of inorganic perovskite single crystals is also reported [17, 27]. These different single crystals are varied in size and growth rate depending on the method iused to grow them. Even monocrystalline perovskite films are also reported that are best suited for the fabrication devices [28, 29]. The electronic and optical properties of these perovskite single crystals and monocrystalline perovskite films are also well studied [15, 30–43]. These studies revealed long carrier diffusion lengths as a result of low trap state density for these hybrid perovskite single crystals that opens the path for the production of reliable and stable optoelectronic devices.

This chapter intends to provide recent research on the growth of perovskite single crystals, especially, different growth techniques and elaborated discussion on the fascinating properties of these single crystal perovskites that will follow by their applications in energy harvesting and high energy radiation detection.

2 Crystal Structure

Perovskites materials are described by common nomenclature formula ABX_3, where A and B are cations (size of A is bigger than B) and X is an anion. B resides at the body center position of a cubic unit cell surrounded by six anions X (face centered position) forming an octahedral $[BX_6]^{4-}$ cluster while A cation resides at the eight corners of the cube [44]. Crystallographic structure and stability of the perovskite structures could be realized by using Goldschmidt tolerance factor (t_f) defined as

$$t_f = \frac{(R_A + R_X)}{\{2(R_B + R_X)\}^{-1/2}} \quad (1)$$

where R_A, R_B, and R_X are the ionic radii of the A cation, B cation, and X anion, respectively.

For hybrid perovskites of present interest, the larger cation A is organic; such as MA ($CH_3NH_3^+$) with $R_A = 0.18$ nm, FA ($NH_2CH{=}NH_2^+$) with $R_A \sim 0.19$–0.22 nm [13, 45–47]. Cation B is Pb ($R_B = 0.119$ nm) or Sn ($R_B = 0.11$ nm) and anion X is generally halides (Br, I or Cl with $R_X = 0.196$, 0.22, and 0.181 nm, respectively). For $0.9 < t_f < 1$, ideal perovskite crystal structure with cubic phase is formed. However, for lower values in the range 0.7 to 0.9 (i.e., with smaller A or larger B), orthorhombic, rhombohedral or tetragonal crystal structures are formed. For $t_f > 1$, layered crystal structures are found to form for larger A.

3 Perovskite Single Crystal Growth Techniques

A few techniques so far have been proposed such as top and bottom seeded solution growth, inverse temperature crystallization, anti-solvent vapor-assisted crystallization, etc., for the growth of perovskite single crystals. Few of them are based on conventional crystal growth processes. The single crystal growth rates as well as sizes of crystals are varied from one type of growth technique to other. Table 1 shows a collection of these data as available in literature so far. For more details about these particular perovskite single crystal growth techniques, readers are suggested to go through the references cited therein.

3.1 Temperature-Lowering Method

The temperature-lowering method is one of the appropriate techniques for the growth of organo metallic halide perovskite single crystal. It is simple and convenient for the growth of high quality large size single crystals perovskite $MAPbX_3$ (X=Cl, Br, I). By reacting an organic halide salt and an inorganic metal salt, saturated aqueous

Table 1 Different size and type of perovskite single crystals grown by different techniques and their application area

Perovskite single crystal	Crystal growth technique	Crystal size	Application	References
$MAPbI_3$	Bottom-seeded solution growth	$10 \times 10 \times 8$ mm^3	–	[13]
$MAPbI_3$	Top-seeded solution growth	10 mm (length), 3.3 mm (height)	–	[15]
$ASnI_3$ (A=CH_3NH_3 or $CH(NH_2)_2$)	Top-seeded solution growth		–	[16]
$MAPbBr_3$, $MAPbI_3$	Inverse temperature crystallization	– 1 mm (length)	–	[19, 48]
$(CH_3NH_3)Pb(Br_{1-X}Cl_X)_3$	Inverse temperature crystallization	–	–	[49]
$FAPbX_3$ (X=I or Br)	Inverse temperature crystallization	3 mm for X=I 5 mm for X=Br	–	[21]
$FAPbI_3$	Cooling solution and inverse temperature crystallization	–	–	[24]
$CsPbBr_3$ and $CsSnI_3$	Bridgman growth	–	–	[17, 27]
$MAPbI_3$ arrays in microscale	Droplet-pinned crystallization	–	–	[52]
$MAPbBr_3$ and $MAPbI_3$	Anti-solvent vapor-assisted crystallization	–	–	[11]
$(benzylammonium)_2PbCl_4$	Slow evaporation	$5 \times 10 \times 2$ mm^2	–	[26]
$MAPbBr_3$ monocrystalline film	Cavitation triggered asymmetrical crystallization	–	Photovoltaic devices	[28]
$MAPbCl_3$	Inverse temperature crystallization	$2 \times 4 \times 4$ mm^3	Photodetector	[20]
$MAPbCl_3$	Bottom-seeded solution growth	$12 \times 12 \times 7$ mm^3	Photodetector	[14]
$MAPbBr_3$, $MAPbI_3$	Temperature-lowering method	–	Self-powered photodetector	[36, 37]
$MAPbI_3$, $FAPbI_3$ and I-treated $MAPbBr_3$	Inverse temperature crystallization	0.3–1 cm	Solid state γ ray detector	[42]
$MAPbBr_3$	Anti-solvent vapor-assisted crystallization	2–3 mm	X-ray detector	[25]
$MAPbI_3$	–	–	X-ray photon detector	[43]
$MAPbI_3$	Inverse temperature crystallization	Large size wafer	–	[29]

perovskite precursor is prepared at first step. With change in temperature, the solubility of the organic halide perovskites in their corresponding halide solvents varies considerably. However, it is moderate at room temperature. Decrease in the solution temperature induces saturation of the solute. This saturation leads to the development of perovskite single crystals.

This method could be divided in two methods depending on position of the seed crystal in crystal growth vessel: top-seeded solution growth (TSSG) and bottom-seeded solution growth (BSSG). Easy control and stable growth are the main advantages of these two methods. However, this method is not suitable for low solubility materials at high temperature region.

3.1.1 Bottom-Seeded Solution Growth Method (BSSG)

This crystal growth technique was developed for crystals that are grown from heated solutions. Figure 1a shows the schematic of a typical crystal growth system. In this process, the seed crystals were formed first by spontaneous crystallization. Optimization of the crystal growth condition was achieved by accurate control of the temperature and selecting of a high quality seed crystal; in the middle of the crystal holding tray, the seeded crystal was fixed. With the help of an electric motor, this tray along with the seed crystal was rotated during the crystal growth process. Growth of large (~centimeter size) bulk single crystal of $MAPbI_3$ by bottom-seeded solution growth (BSSG) method was first reported by Dang et al. [13]. For this, the temperature of the saturated solution was cooled down slowly from 65 to 40 °C and thus, the single crystal of $MAPbI_3$ (dimensions of 10 mm × 10 mm × 8 mm) was formed in a month. The growth rate for this crystal was found to be ~26 mm^3 per day (~1 mm^3/h). This crystal had two natural facets {100} and {112}. Lian et al. [14] also utilized same technique to grow bulk single crystals by lowering the temperature of the growth solution from 100 to 57 °C. In this process, a seed crystal was fixed to a platinum wire (Fig. 1b) and the dimensions of the grown crystals were ~ 12 mm × 12 mm × 7 mm as shown in Fig. 2.

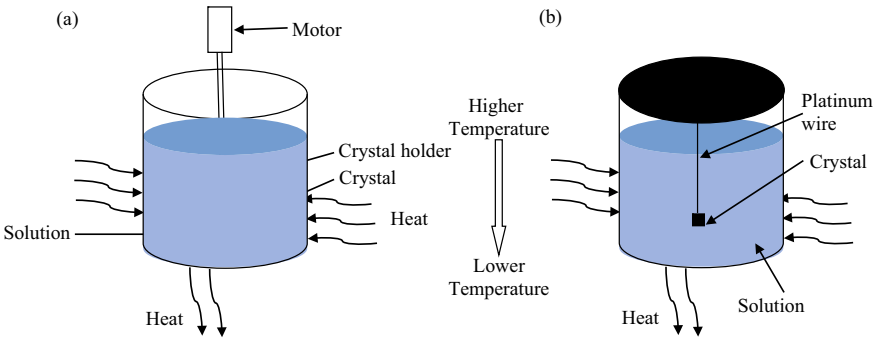

Fig. 1 Schematic representation of the bottom-seeded solution growth method

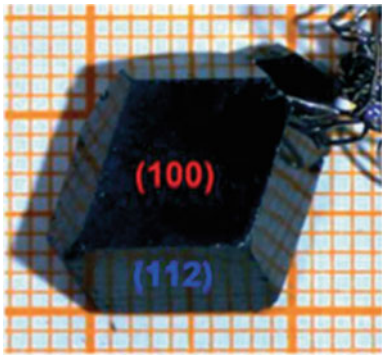

Fig. 2 Photographs of bottom-seeded solution grown bulk $MAPbI_3$ perovskite single crystal. Reproduced with permission from Ref. [14]. Copyright 2014, Nature

3.1.2 Top-Seeded Solution Growth Method (TSSG)

Growth of bulk single crystals of $MAPbI_3$ by using the top-seeded solution growth (TSSG) method was reported by Dong et al. [15]. During the growth process, a silicon (Si) substrate holds the seed crystal at the top of the solution as shown in Fig. 3. This Si substrate was air cooled on the part outside of the tube and the seed crystal remains suspended in the solution. Using the temperature discrepancy between the bottom and top of the solution and dissolution of small seed crystals at the bottom, super saturation was induced. This condition leads the growth of bulk $MAPbI_3$ single crystals with size of 10 mm (length) and 3.3 mm (height).

In recent time, the same group has reported for the first time the growth of high quality bulk hybrid $ASnI_3$ perovskite ($A=CH_3NH_3$ or $CH(NH_2)_2$) single crystals by using the top-seeded solution growth (TSSG) method [16].

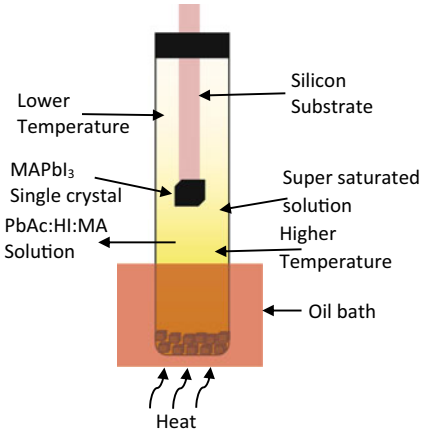

Fig. 3 Schematic representation for $MAPbI_3$ single crystal growth by TSSG method

3.2 *Inverse Temperature Crystallization (ITC)*

The inverse temperature crystallization (ITC) method is used for the particular materials whose solubility decrease with increase of temperature in specific solvent and compare to other methods, the rate of crystal growth by this method is an order of magnitude faster [11, 15, 17, 18].

Figure 4 shows the schematic of the crystal growth process. Precursor solution is kept in a bottle and the bottle is kept inside an oil bath. The temperature of the oil bath is raised. After a certain temperature, crystallization starts at the bottom of the bottle. This growth is reversible one as the crystal could dissolve in the solution when temperature of the solution again comes down to room temperature. Based on the inverse temperature or retrograde solubility of organic–inorganic hybrid halide perovskite in particular organic solvents, ITC was initially proposed by Bakr et al. [19–22]. This type of inverse solubility induced crystallization and growth occurs within several hours. So, it is widely used to grow bulk single crystal rapidly as compared to temperature-lowering method [20, 22–24].

Basically, in ITC method, the crystal growth process is a balance of dissolution and precipitation. At low temperature, concentration of unbound perovskite molecules is low as most of them are bound by molecules of the solvent. For this reason, concentration of perovskite molecules does not reach saturation. The bonding energy depends on temperature in inverse proportion. For this reason, with increase of temperature, more and more perovskite molecules are free to increase concentration of free perovskite molecules in solution. With increase of temperature at some point, super saturation occurs that enunciates nucleation and crystal growth starts. Single crystal growth by this method depends on the choice of solvent. For the growth of hybrid halide perovskites crystals solvents like g-butyrolactone (GBL), dimethylsulphoxide (DMSO) and N,N-dimethylformamide (DMF) are the most widely used. There is lot of variations in solubility of PbX_2 and MAX in these solvents. It has been found that $MAPbI_3$ crystallized more aptly from GBL while $MAPbBr_3$ crystallized better from DMF [11].

First, $MAPbI_3$ and $MAPbBr_3$ single crystals were grown by the rapid ITC method (Fig. 5a–c) [19, 48]. In later works, Zhao group [49] succeeded to grow mixed halide perovskite $(CH_3NH_3)Pb(Br_{1-X}Cl_X)_3$ single crystals.

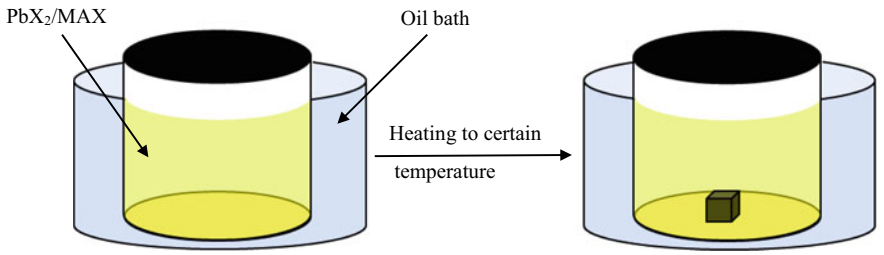

Fig. 4 Schematic for ITC method for growth of $MAPbX_3$ single crystals

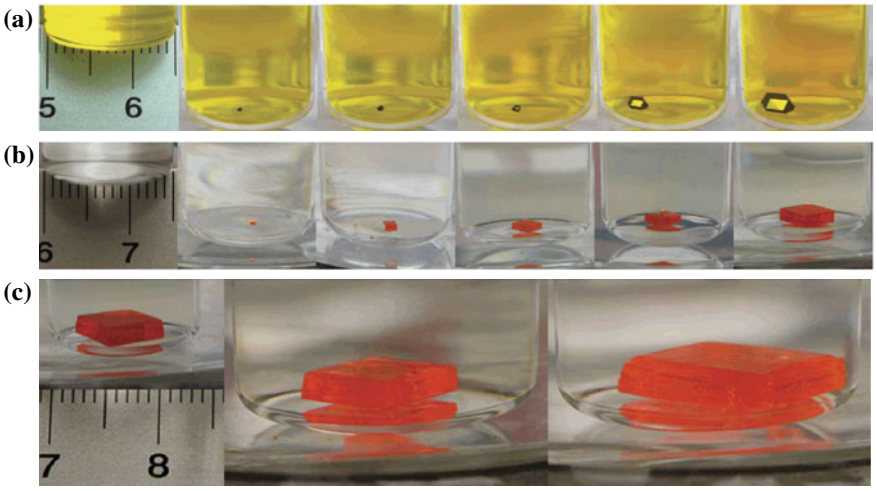

Fig. 5 Inverse temperature crystallization growth of **a** $MAPbI_3$ and **b** $MAPbBr_3$ single crystals at different time intervals. **c** Continuous growth of $MAPbBr_3$ single crystal by transferring the crystal into a larger vessel containing a fresh growth solution. Reproduced with permission from Ref. [19]. Copyright 2015, Nature

Bakr group [21] also synthesized $FAPbX_3$ single crystals using the ITC method by using proper solvent. 0.8 mol L^{-1} GBL solution was used to reach super saturation and starts crystallization at 115 °C for the growth of $FAPbI_3$ single crystals. Crack and grain boundary-free black $FAPbI_3$ single crystals were grown in 3 h. 1:1 (v/v) DMF:GBL solution (1 mol L^{-1}) was used in the growth of $FAPbBr_3$ single crystals using ITC method. Crystallization was found to occur at 55 °C. Yang's [24] group also reported growth of $FAPbI_3$ single crystal (5 mm in size) with some modification in ITC process. First, $FAPbI_3$ seed crystal was grown by a cooling solution method. This seed crystal was used to grow larger crystal by ITC method.

3.3 Bridgman Growth Method

The Bridgman growth technique is a melt crystal growth method that is mostly used to grow large-sized crystal inside the sealed ampoules [50, 51]. Organic compounds become chemically instable and attained high vapor pressure around their melting point. Single crystal of perovskite materials having definite melting point could be grown using this property. For this, a quartz ampoule was initially filled with all of the raw reactants and then sealed under the vacuum. At definite temperature, crystallization starts at the tip of the ampoule. Growth of $CsPbBr_3$ single crystals and $CsSnI_3$ polycrystalline ingots has reported by Kanatzidis group using Bridgman growth method [17, 27]. By varying the size of the ampoules, large-sized crystals could be grown by using this growth method. This method has only one limitation

that is come from the stress between the surface of the crystal and the ampoules. This stress could induce cracks and small grain boundaries in the crystals. Again as the crystals comes in touch of the crucible wall during growth, impurity level increases in the crystals grown by this method.

3.4 Droplet-Pinned Crystallization Method (DPC)

Droplet-pinned crystallization (DPC) method is used to grow micro-scale $MAPbI_3$ single-crystalline arrays and could be used to grow single-crystalline thin films [52]. In this process, first $MAPbI_3$ precursor solution is dropped on PEDOT: PSS-coated ITO glass. Over it, a small piece of Si wafer was placed. $MAPbI_3$ starts to disperse along the diminishing direction of the droplet with the evaporation of solvent. Annealing induces formation of rectangular $MAPbI_3$ single crystal arrays within minutes.

3.5 Anti-solvent Vapor-Assisted Crystallization (AVC)

In the year 2014, Seok and Chang group has shown the anti-solvent-assisted crystallization method which is also known as fast crystallization deposition [53] and solvent engineering [27] to produce high quality and dense perovskite thin films. The methods are based on the similar principle: different solubility of $MAPbX_3$ (X=Cl, Br, I) in different solvents [53–55]. The anti-solvent vapor diffusion method comes in handy to grow materials that are highly soluble in a good solvent but have poor solubility in different class of solvents. To support the above statement in general, hybrid halide perovskites show good solubility in DMF, DMSO, and GBL, while they show nonsolubility or low solubility in chlorobenzene, diethylether, benzene, etc. (the poor solubility solvents here referred as anti-solvent). The anti-solvent could accelerate the crystallization of these perovskites during spin coating and facilitates to attain uniform film formation. Using this same strategy, the Bakr group [11] developed a new method to grow large-sized millimeter-scale $MAPbBr_3$ and $MAPbI_3$ single crystals.

Figure 6 shows the schematic of crystal growth arrangement. Powders of $PbBr_2$ and MABr (molar ratio 1:1) were dissolved in DMF to form the precursor solution. Dicholoromethane (DCM) as an antisolvent and the precursor solution (yellow color in Fig. 6) was sealed in a closed vessel and stored. Slowly, the evaporation of DCM occurs and its vapor will diffuse into the precursor solution because the DCM mixes well with DMF. The diffusion of DCM in DMF will consume some DMF solvent. Since MABr and $PbBr_2$ cannot dissolve in DCM solvent, the consumption of DMF by DCM will result an increase in the concentration of MABr and $PbBr_2$ in the solution. And finally lead to the formation of $MAPbBr_3$ crystals. Huang group found that it was difficult to get high quality $MAPbBr_3$ with a 1:1 mol ratio of MABr and $PbBr_2$

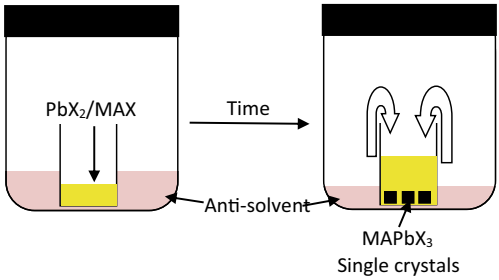

Fig. 6 Schematic representation of the anti-solvent vapor-assisted crystallization process

because of their different solubility's in DMF [25]. $PbBr_2$ and MABr molar ratio of 0.8 can produce high quality crystals with higher carrier mobility and lifetime.

3.6 Slow Evaporation Method

Slow evaporation technique in solution growth processes is a simple method for obtaining single crystals. Xiong et al. [26] have reported growth of hybrid perovskite in analogous $(\text{benzyl ammonium})_2PbX_4$ (X=Cl, Br) materials. In this process, a stoichiometric mixture of benzylammonium chloride and $PbCl_2$ in a concentrated HCl aqueous solution was prepared. Upon slow evaporation of N,N-dimethylformamide (DMF) solution at 90 °C bulk crystals size ~(5 mm × 10 mm × 2 mm) were obtained. In spite of simplicity and efficiency in crystal growth by slow evaporation method, sometimes, it becomes hard to accurately control.

3.7 Cavitation-Triggered Asymmetrical Crystallization (CTAC)

Gorwth of monocrystalline hybrid perovskite films by using CTAC method was first proposed by Bakr group [28]. This group has shown growth of monocrystalline perovskite films on various types of substrates such as Si wafers, ITO-coated glass, FTO-coated glass, and sputter-coated metal on silicon. Ultrasound has been used in crystal growth process since 1927 [56, 57]. Without seed crystal, only the use of ultra sound promotes nucleation under a low super saturation level. The basic idea of this growth process lies in the fact that if successive cycles of compression and rarefaction sound waves are sending through a solution, then these waves creates and collapse cavities repeatedly inside the liquid. Release of ultrahigh energy during the collapse of these cavities could induce nucleation by overcoming nucleation barrier by increasing local pressure, accumulation of energy, and rapid cooling [58]. High-speed jets of fluid called microjetting occur through the asymmetric collapse of cavities near a solid surface [59]. Due to the induced strong shearing force, this

process has been used in film thinning and reducing the particle size from long past [60]. In the growth of monocrystalline perovskite thin film, this force plays a major role. Thickness of the perovskite films depends on the concentration of the precursor solution. When ultrasonic pulses are targeted toward supersaturated precursor solution, excessive nucleation occurs that results in the growth of plenty amount of tiny crystals.

4 Optical and Optoelectronic Properties

Morphology strongly affects the carrier diffusion length in organometal trihalide perovskite material. Charge carrier diffusion lengths >100 nm in the hybrid polycrystalline perovskite (e.g., $MAPbI_3$) are necessary and vital for the fabrication of high efficiency solar cells. However, recently Dong et al. [15] has reported more than 175 μm diffusion lengths in $MAPbI_3$ single crystals are grown by a solution growth method under 1 sun (100 mW cm^{-2}). Even this could exceed 3 mm under weak light for both types of carriers. The reason behind this long diffusion length was ascribed to longer lifetime, higher carrier mobility, and much smaller trap densities compare to polycrystalline $MAPbI_3$ thin films. Thin film showed an absorption cutoff at 800 nm whereas the absorption of single crystal extended up to 850 nm. The shorter wavelength (~770 nm) emission in single crystals than the excitonic absorption peak position (~790 nm) indicates dissociation of all excitons in free electron and hole charge carriers in single crystal with a bandgap of 1.61 eV. The narrower and blue-shifted PL peak of the single crystals suggests the presence of low trap density. For measuring the optoelectronic properties, a single crystal device was fabricated by depositing 25 nm thick gold (Au) film on one facet of the crystal that acts as an anode and for cathode, gallium (Ga) was connected on the opposite facet. The EQE of a 3 mm thick single crystal-based solar cell is ranged from 12.6 to 15.8% for wavelengths from 520 to 810 nm. The red shift (~50 nm) of the EQE up to 850 nm for the single crystal device compare to polycrystalline thin films increased the upper limit of the short-circuit current density (J_{SC}) for single-crystal-based solar cells from 27.5 to 33 mA/cm^2. The decrease of EQE for the single crystal device at shorter wavelengths indicates that the metal–single crystal interface contains a large defect density. The reason for this large defect density was ascribed to the formation of Pb^{2+} clusters due to the partial loss of the more soluble methylammonium iodide during the removal of the single crystal from solution. In a separated work, the same group has shown theoretically that Pb^{2+} clusters tend to form charge traps on the surface of $MAPbI_3$ [30]. A near unity internal quantum efficiency (IQE) (95 ± 7%) was obtained for 3 mm thick single crystal device.

Diffusion length L_D is related to carrier mobility (μ) and carrier lifetime τ by the following relation

$$L_{\mathrm{D}} = \left(\frac{\mu k_{\mathrm{B}} T \tau}{e}\right)^{\frac{1}{2}} \tag{2}$$

where k_{B} is Boltzmann's constant, T is the absolute temperature, and e is electronic charge. To estimate μ and τ, dark current (J_{D}) versus voltage characteristics of the device was studied. Two types of devices were made: one hole-only device with the structure Au/MSC/Au and other electron only with the structure Ga/phenyl-C61-butyric acid methyl (PCBM):C60/MSC/PCBM:C60/Ga. Three regions were indentified. (1) At low bias, the current increases linearly with applied bias (with $n = 1$), (2) at higher bias voltage $J \alpha V^2$, i.e., trap free space-charge-limited current (SCLC) regime (with $n = 2$), (3) an intermediate regime identified (a trap-filled regime) by the rapid increase of current with bias. In the SCLC regime above 10.7 V, the J_{D} of the device was well fitted by the Mott–Gurney law

$$J_{\mathrm{D}} = \frac{9\varepsilon\varepsilon_0 \mu V^2}{8L^3} \tag{3}$$

A large hole mobility ~164 ± 25 cm^2 V^{-1} s^{-1} was obtained by curve fitting. The trap-filled limit voltage V_{TFL} defined as the voltage at which all the traps are filled is directly proportional to the trap density by the relation

$$V_{\mathrm{TFL}} = \frac{e n_t L^2}{2\varepsilon\varepsilon_0} \tag{4}$$

where L is the thickness of the single crystal, ε (=32) is relative dielectric constant of $MAPbI_3$, and ε_0 is the vacuum permittivity. The trap density n_{t} was estimated to be 3.6×10^{10} cm^{-3} which is five orders of magnitude lower than that of polycrystalline thin films of $MAPbI_3$. Similarly, the electron mobility and electron trap density for the electron-only device were measured to be 24.8 ± 4.1 cm^2 V^{-1} s^{-1} and 4.5×10^{10} cm^{-3}.

In a different work, on organolead trihalide $MAPbX_3$ ($MA=CH_3NH_3^+$; $X=Br^-$ or I^-) perovskites single crystals of volume larger than 100 cc grown by anti-solvent vapor-assisted crystallization approach, it was found that the trap densities are exceptionally low on the order of 10^9 to 10^{10} per cc which is comparable to the best quality Si [31]. The absorption spectra of $MAPbX_3$ single crystals show a clear cutoff at band edge with no excitonic absorption. This feature arises due to subsequent reduction in the number of in-gap defect states. However, absorption spectra of polycrystalline $MAPbX_3$ thin films show excitonic features near band edge [32]. The optical band gap was determined to be 2.21 and 1.51 eV for $MAPbBr_3$ and $MAPbI_3$ single crystals, respectively. Both types of single crystals show a sharp transition at band edge that could enhance photon harvesting and photocurrent generation compare to their thin film counterpart. Similarly, single crystals show narrow PL peak corresponding to band gap. For determining the carrier diffusion length L_{D}, carrier life time (τ) and carrier mobility (μ) were separately measured using time of flight technique [33] and PL decay in addition to transient absorption spectroscopy, respectively. For

$MAPbBr_3$ single crystal, the transient current for various driving voltages (V) and the transit time τ_t, (defined as the position of the kink in the time traces) were plotted as a function of V^{-1}. Using the transit time τ_t, sample thickness d, and applied voltage V, mobility μ was estimated to be 115 cm^2 V^{-1} s^{-1} by linear fit of τ_t versus V^{-1} using the equation

$$\mu = \frac{d^2}{V\tau_t} \tag{5}$$

This estimation of mobility was higher than the value measured from Hall Effect measurement (20–60 cm^2 V^{-1} S^{-1}). The disagreement was attributed to the surface effects that are negligible for time of flight measurement. Carrier lifetime t was estimated from transient absorption (TA) and PL spectra. Bi-exponential fits prove the presence of two types carrier dynamics: the fast ($t \approx 74$ ns) and the slow ($t \approx 978$ ns) carrier dynamics. For $MAPbI_3$ single crystals, mobility was estimated by measuring the current–voltage characteristics (space-charge-limited current (SCLC) technique) where a quadratic dependency of the current was observed at 300 K. From this, dependency μ was obtained as 2.5 cm^2 V^{-1} s^{-1}.

The time-dependent PL measurements for $MAPbBr_3$ and $MAPbI_3$ single crystals were carried out for the wavelength of the main PL peak (i.e., $\lambda = 580$ nm and $\lambda = 820$ nm for $MAPbBr_3$ and $MAPbI_3$, respectively). Through bi-exponential fits, the bromide- and iodide-based perovskite single crystals showed a combination of fast and slow dynamics ($t \approx 41$ and 357 ns for $MAPbBr_3$, and $t \approx 22$ and 1032 ns for $MAPbI_3$). These two very different time scales were assigned to the presence of a surface component (fast) in addition to a bulk (band to band recombination) component (slow). By combining the longer (bulk) carrier lifetimes with the higher measured bulk mobility and shorter carrier lifetime with lower mobility, L_D was estimated [by using Eq. (1)] to be ~17 and ~3 μm in $MAPbBr_3$ single crystals, respectively. Similarly, for $MAPbI_3$ single crystals L_D was found to be ~8 and ~2.

The current–voltage responses of these hybrid perovskite crystals in the SCLC regime were further investigated in order to find trap density that plays a crucial role in determining μ, τ, and L_D. The I–V curves were divided in three regions: at low voltages, the I–V response was ohmic (i.e., linear); at intermediate voltages, non-linear behavior evidenced transition into trap-filled limit (TFL) where injected carriers filled all trap states ($V_{TFL} = 4.6$ V for $MAPbBr_3$ and 24.2 V for $MAPbI_3$); At high voltages, a quadratic dependence in the Child's regime was observed. As the density of trap states is linearly proportional to the onset voltage V_{TFL}, for $MAPbBr_3$ and $MAPbI_3$ single crystals trap densities were found to be 5.8×10^9 cm^{-3} and 3.3×10^{10} cm^{-3}, respectively.

In a separate study on $FAPbI_3$ and $FA_xMA_{1-x}PbI_3$ crystals formed by hydroiodic (HI) acid-assisted inverse temperature crystallization method, it was found that substitution of 15% MA^+ on $FAPbI_3$ crystals stabilizes the phase and gives best charge transport characteristic [34]. Using slower component of time-resolved photoluminescence (TRPL) curves, the carrier lifetime of $FAPbI_3$ and $MAPbI_3$ single crystals were estimated to be 839.31 ns and 145.5 ns, respectively. All the

Table 2 Lifetimes obtained from the analysis of PL spectra of $FA_{(1-x)}MA_xPbI_3$ single crystals with $x = 0, 0.05, 0.1, 0.15, 0.2, 0.8, 0.85, 0.9, 0.95, 1$ [34]

$FA_{(1-x)}MA_xPbI_3$	$x = 0$	$x = 0.05$	$x = 0.1$	$x = 0.15$	$x = 0.2$
τ_1 (ns)	91.26	61.43	52.11	27.26	31.58
τ_2 (ns)	839.31	689.92	381.86	579.75	236.74
$FA_{(1-x)}MA_xPbI_3$	$x = 1$	$x = 0.95$	$x = 0.9$	$x = 0.85$	$x = 8$
τ_1 (ns)	7	32.45	122	88.05	105.3
τ_1 (ns)	145.65	557.5	1074.78	926.39	956.8

$FA_{(1-x)}MA_xPbI_3$ ($x = 0.1$–0.2) single crystals showed shorter carrier lifetime than that of $FA_{(1-x)}MA_xPbI_3$ ($x = 0.8$–0.9) single crystals. The carrier lifetime of the single crystals with different compositions are listed in Table 2. The cut-off absorption wavelength of $FA_{0.85}MA_{0.15}PbI_3$ and $FA_{0.15}MA_{0.85}PbI_3$ crystals were found at 872 nm and 851 nm, respectively, that reflects a bandgap of 1.42 eV and 1.46 eV, respectively, for the crystals. PL emission peak for these two types of crystals were found to be centered at 827 nm and 807 nm, respectively. Using Indium (In)/perovskite single crystal/In (electron-only) device and Au/perovskite single crystal/Au (hole-only) device current–voltage characteristics were studied to estimate both types of charge carrier mobility. By fitting Eq. (2) and using the values of $\varepsilon = 46.9$ for $FA_{0.85}MA_{0.15}PbI_3$ [24] and 32 for $FA_{0.15}MA_{0.85}PbI_3$ single crystal [15], electron and hole mobility were estimated to be 10.19 $cm^2\ V^{-1}\ s^{-1}$ and 5.31 $cm^2\ V^{-1}\ s^{-1}$, 0.77 $cm^2\ V^{-1}\ s^{-1}$ and 0.66 $cm^2\ V^{-1}\ s^{-1}$, respectively. Interestingly, when the hole mobility of $FA_{0.15}MA_{0.85}PbI_3$ was measured in vacuum, it increased to 17.12 $cm^2\ V^{-1}\ s^{-1}$ which is much higher the mobility measured in air. This indicates that atmosphere interacts with the single crystal and could increase the surface defects.

5 Applications

5.1 Photovoltaics

The characteristics features of the inorganic–organic hybrid perovskite single crystals, such as long carrier diffusion length, very low trap density, absence of grain boundary, etc., if could be transported to perovskite films may overcome the challenges in the development of perovskite solar cells (PSC). In this regard, transition from bulk perovskite single crystals to perovskite single crystal films could provide the potential solution. Up to now, there are few attempts to fabricate bulk single crystal perovskite solar cells as discussed in Sect. 4. Bakr group [28] has reported PSC based on monocrystalline perovskite ($MAPBr_3$) film grown by CTAC strategy. One set of solar cells were fabricated by depositing Au electrode on the surface of monocrystalline films grown on ITO glass. In another set of cells, monocrystalline film was grown on compact TiO_2-coated FTO glass and Au was deposited on the

perovskite monocrystalline film to get a comparison with PSC devices that made from perovskite polycrystalline film of the same device structure. The cell with 1 μm thick monocrystalline film showed a J_{SC} ~ 7.39 mA/cm^2, V_{OC} ~ 1.25 V, and fill factor (FF) ~0.59 with over all conversion efficiency of 5.49%. However, the cell with 4 μm thick monocrystalline film showed a little lower performance with J_{SC} ~ 7.42 mA/cm^2, V_{OC} ~ 1.24 V, and FF ~ 0.58. The large J_{SC} value of the cells is further confirmed by calculating the integrated current density from the EQE curve. IQE of the device is more than 90% over a broad spectral range with maximum 97% at 507 nm and onset at 550 nm. By considering IQE to be 100% (only loss through the reflection and absorption by ITO), upper limit of this current density was estimated to be 7.64 mA/cm^2. Using the *C–V* measurement (Mott–Schottky plot), built-in potential was estimated to be 1.21 which is close to the experimental value obtained for V_{OC}. For FTO/TiO_2/$MAPbBr_3$ monocrystalline film (thickness: 1 μm)/Au structure solar cell, the power conversion efficiency was improved to 6.53% (with V_{OC} of 1.36 V, a J_{SC} of 6.96 mA cm^{-2} and an FF of 0.69). The behavior is similar to the ITO/$MAPbBr_3$/Au-structured solar cell with a sharp decrease in EQE and IQE beyond 350 nm in UV region due to strong absorption of UV irradiation by FTO/TiO_2.

5.2 Detectors

Low trap density (~10^9 to 10^{10} per cc), long carrier diffusion length, narrower bandgap with high light absorption, and improved photocurrent suggest huge potential of these hybrid perovskite single crystals to be used as photodetectors [35]. Bakr group has reported a UV detector (rise time: 24 ms; decay time: 62 ms) based on $MAPbCl_3$ single crystals (thickness 350 μm) whose performance is comparable to the performance of TiO_2 thin films and ZnO nanoparticles-based UV-detectors [20]. The detector was fabricated by depositing 20 nm thick platinum (Pt) layer of transparency 20% at 365 nm as a top electrode and 20 nm Ti/100 nm Au layer as a back electrode. This detector showed a low dark current (4.15 × 10^{-7} A) and high photocurrent (4.7 × 10^{-4} A) at 15 V with an ON–OFF ratio 1.1 × 10^3. The responsivity of photodetector was estimated as 46.9 mA/W by using the formula

$$R = \frac{I_{\text{light}} - I_{\text{dark}}}{P_{\text{light}} \times S} \tag{6}$$

where I_{light} is the photocurrent, I_{dark} is the dark current, and P_{light} is the power of incident light, and S is effective area. Detectivity of the same detector was estimated to be 1.2 × 10^{10} Jones by using the formula

$$D = \frac{R}{(2q\,J_{\text{dark}})^{1/2}} \tag{7}$$

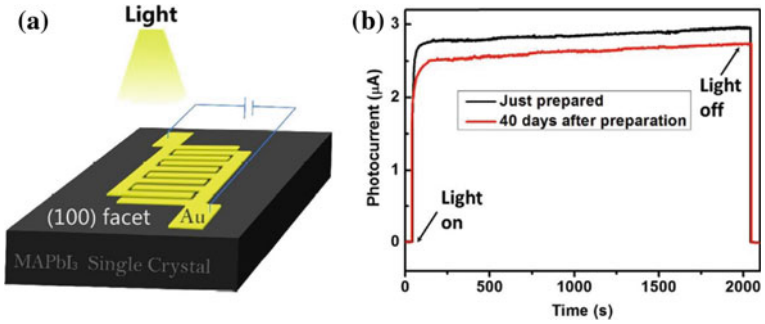

Fig. 7 **a** Schematic diagram of the planar-type photodetector produced on the (100) facet of a $MAPbI_3$ single crystal. **b** Durability and stability of the $MAPBI_3$ single crystal photodetector. Reproduced with permission from Ref. [14]. Copyright 2014, Nature

where q is the elementary charge and J_{dark} is the dark current density. Without any encapsulation, the $MAPbCl_3$ single crystal photodetector showed photostability up to 8000 s biased at 15 V under continuous light (365 nm, 1 W/cm^2) illumination in ambient condition with humidity 55–60%. The same device shows high photostability over 12 h under blue light (1 Sun excitation density) which is attributed to the low trap density.

Figure 7a shows a schematic of $MAPBI_3$ single-crystal-based photodetector (effective illuminated area 1.19×10^{-7} m^2) where a pair of interdigitized Au film electrodes, with bridging gap of about 20 μm were deposited on the (100) facet of the single crystal [14]. The dark current of this device was found to be very low as 11 nA at 4 V bias. Current–voltage characteristics revealed that a Schottky contact was formed between Au electrode and the crystal. The incident power density was varied from 0.11 to 3.22 mW cm^{-2} by using a 532 nm laser as the light source. Responsivity (R) was estimated by using formula (6) and external quantum efficiency (EQE) by using the formula

$$\mathrm{EQE} = R \times \left(\frac{hc}{e\lambda}\right) \tag{8}$$

where h represents the Planck's constant, c is the velocity of light, e is the electronic charge, and λ is the wavelength of incident light. From this, the lowest detectable irradiance power density of the single crystal device was estimated to be 2.12 nW cm^{-2} with R value of 953 A W^{-1}. For polycrystalline film of $MAPBI_3$ below 120 nW cm^{-2}, irradiance power could not be detected as it was covered by noise. The highest R and EQE for the photodetector based on polycrystalline film were estimated to be 0.28 A W^{-1} and 64.64%, respectively, at 1 V bias. Again, under a relative strong light irradiance of 1 mW cm^{-2}, the single crystal device showed about 100 times higher R value of 2.55 A W^{-1} compared with the similar photodetector based on polycrystalline film (R: 0.0197 A W^{-1}). For this single crystal photodetector, a peak photocurrent of 7.6 μA was achieved at 3 V bias with ON–OFF ratio of 224 (rise

time: 74 μs and decay time: 58 μs). Figure 7b shows the stability and durability of this single crystal photo-detector in a time scan of 2000 s for the same device before and after 40 days storage at room temperature. A 6% decay in photocurrent value was notice after 40 days storage.

By using the improved photocurrent generation and exciton separation by built-in electric field in the hybrid perovskite single crystals (achieved either by choosing proper asymmetric electrode material or fabricating heterojunction), self-powered photodetectors have been proposed [35]. This self-powered photodetectors eventually works as photovoltaic devices. A self-powered photodetector, achieved by exploiting Pt (thickness: 20 nm, transparency: 20% in visible region)/$CH_3NH_3PbBr_3$ single crystal Schottky junction has shown photodetectivity of 1.4×10^{10} Jones at zero bias [36]. This device showed stable performance in air ambient for over 45 days with rise time of 70 μs and decay time of 150 μs. In another similar type of work by using asymmetric electrodes of Au–Al (with channel length of 30 mm between the electrodes), self-powered photodetector based on $CH_3NH_3PbI_3$ single crystal has been realized [37]. The photovoltaic effect comes into play in this device depending on the formation Schottkey contacts between the semiconducting single crystal surface and metal electrode that creates the built-in electric field to separate photogenerated electron–hole pairs. This self-powered single crystal photodetector or rather single crystal photovoltaic device produced short circuit current density (J_{sc}) of 6.86 mA cm^{-2}, open-circuit voltage (V_{oc}) of 0.7 V, and fill factor (FF) of 16.5% with a overall efficiency of 0.79%. The photocurrent showed by this device is 2 orders of magnitude higher than its polycrystalline perovskite film-based device with similar device architecture. The lowest incident power detected by this device was 1×10^{-8} W cm^{-2} with responsivity (R) 0.24 A W^{-1} at zero bias. The rise and decay times of this device were estimated to be 71 and 112 μs. In another report, Cao et al. [38] showed that photodetector made of a core–shell heterojunction based on the $MAPbBr_3$ single crystal renders the feature of self powered due to the built-in electric field at the junction. The perovskite heterojunction is made of a single-crystalline $MAPbBr_3$ core and a crystalline $MAPbI_xBr_{3-x}$ shell with sharp frontier and interface between each pure component. The perovskite heterojunction photodetector was constructed on FTO glass over which Au was deposited as anode. This device showed peak responsivity up to 11.5 mAW^{-1} under 450 nm irradiation at zero bias and a maximum EQE of 3.17% with a rise time of 2.3 s and a fall time of 2.76 s. Both this values are higher than self-powered device based of pure $MAPbBr_3$ single crystal. This self-powered photodetector produced a short-circuit photocurrent of 0.1961 mA cm^{-2}, an open-circuit voltage of 0.61 V, and a fill factor of 0.413.

Detection of high energy photons having energy ~50 keV to 10 MeV (like gamma (γ) ray, X-ray, etc.) emitted from decay of various radioactive isotopes has importance in several fields of research and also in non-destructive testing of industrial products, medical diagnostics, and defense [39, 40]. High charge carrier lifetime, mobility, low density of charge traps, high absorption of hard radiation by heavy metals present in hybrid perovskite single crystals allow the fabrication of low-cost hard radiation detectors that are highly sensitive and could be operated at room temperature [41]. Yakunin et al. [42] have demonstrated that semiconducting single crystals (SCs) of

hybrid lead halide perovskites ($MAPbI_3$, $FAPbI_3$, and I-treated $MAPbBr_3$) of size 0.3–1 cm could work as solid state γ ray detecting material due to the high $\mu\tau$ product of 1.0–1.8 $\times$ 10^{-2} cm^2 V^{-1}, a low charge trap density of 10^9 to 10^{10} cm^{-3} [15, 31], a low dark carrier density of 10^9 to 10^{11} cm^{-3} [23, 31], and a high absorptivity of hard radiation by the lead and iodine atoms. Single crystal of $MAPbI_3$ gives rise to a sensitivity of 0.65 μC $mGyair^{-1}$ cm^{-2} for a photon flux of ~5.6 $\times$ 10^7 cm^{-2} s^{-1} and a photocurrent of 22 nA. If the full penetration depth ~30 μm is considered, then the sensitivity goes to ~220 μC $mGyair^{-1}$ cm^{-3} that is one order of magnitude higher than polycrystalline perovskite film detector [43]. Wei et al. [25] reported a highly sensitive X-ray detector based on $MAPbBr_3$ single crystal with a record-high mobility–lifetime product of 1.2 $\times$ 10^{-2} cm^2 V^{-1} and surface charge recombination velocity of 64 cm s^{-1}. Detectors based on 2–3 mm thick single crystal showed detection efficiency up to 16.4% at near zero bias under the irradiation of X-ray up to 50 keV. For this type of detectors can detect X-ray dose rate as low as 0.5 μGyair s^{-1} with a sensitivity of 80 μC Gy^{-1}air cm^{-2}.

6 Future Aspects

In a very short span, these metal organic halide perovskites have shown unique properties. Superior semiconducting properties with low-cost deposition techniques open new paths for the metal hybrid halide perovskite applications. Properties like long carrier diffusion length and low trap state density make these hybrid single crystals comparable to best photovoltaic quality Si. This book chapter focuses on the different growth methods for the hybrid halide perovskite with an outlook for possible applications.

Around the globe, researchers from all genres are making continuous efforts to unlock the full potential of these versatile materials. Apart from these, some demerits like toxicity due to presence of heavy metal (e.g., Pb) is needed to be addressed. One such option is to go for fully inorganic halide perovskite like $CsPbBr_3$ which can be grown using solution processes.

Most studied application of single crystal halide perovskite is photodetectors that have shown brilliant performance. Another application of these could be in solar cells based on single crystal but to date, the application is not flourished properly. This is due to unavailability of high quality monocrystalline films along with appropriate thickness to be used as perovskite solar cells. Though, the deposition of monocrystalline perovskite films by CTAC method has shown a path toward this goal [28]. However, a lot has to be remaining to achieve. Other methods should be explored in this direction so as the fascinating properties of bulk single crystals could be incorporated in the geometry of thin films [61]. Nevertheless, Liu group [29] has developed a process for the production of thin and shape controlled large size single crystal perovskite wafers for mass production based on ITC growth method. Figure 8 shows the similar schematic of the arrangement used for this type of large size thin single crystal wafer growth. Two slides of glass are kept parallel and aligned with

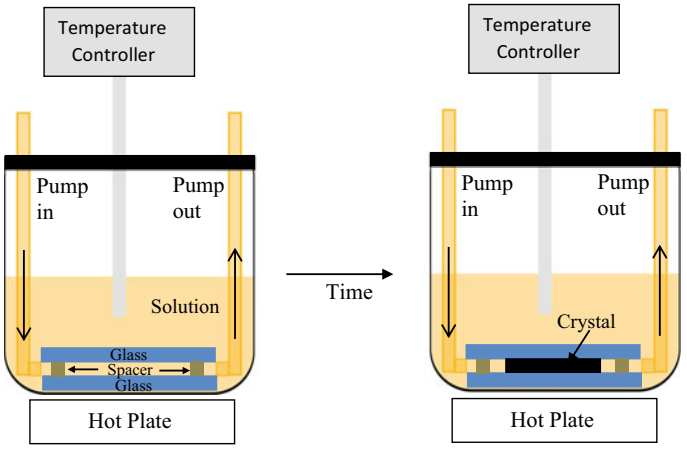

Fig. 8 Schematic representation for large size single crystal perovskite wafer growth by ITC method

each other by using two spacers. Thickness of the spacers defines the thinness of the grown perovskite single crystal wafer. Growth of the single crystal confines within the gap between the glass slides. Shape of the single crystal wafers is decided by the design of the channel between the two glass slides. To maintain the flow of fresh precursor solution during growth inside the channel, peristaltic pump is used.

In the near future, prospects of creating single crystal of high quality with controlled thickness and orientation would fulfill the requirements of this application.

References

1. Park (2013). *The Journal of Physical Chemistry Letters, 4*, 2423.
2. Snaith, H. J. (2013). *The Journal of Physical Chemistry Letters, 4,* 3623.
3. Kim, H., Im, S. H., & Park, N. (2014). *The Journal of Physical Chemistry C, 118,* 5615.
4. Hodes, G., & Cahen, D. (2014). *Nature Photonics, 8,* 87.
5. Best Research-Cell Efficiencies-NREL. (2019, November 5). https://www.nrel.gov/pv/assets/pdfs/best-research-cell-efficiencies.20191105.pdf. Accessed March 22, 2020.
6. Dou, L., Yang, Y. M., You, J., Chang, W., Li, G., Hong, Z., et al. (2014). *Nature Communications, 5,* 1.
7. Xing, G., Mathews, N., Lim, S. S., Yantara, N., Liu, X., Sabba, D., et al. (2014). *Nature Materials, 13,* 476.
8. Tan, Z., Moghaddam, R. S., Lai, M. L., Docampo, P., Higler, R., Deschler, F., et al. (2014). *Nature Nanotechnology, 9,* 687.
9. Zhou, H., Shi, Y., Dong, Q., Zhang, H., Xing, Y., Wang, K., et al. (2014). *The Journal of Physical Chemistry Letters, 5,* 3241.
10. Berhe, T. A., Su, W.-N., Chen, C.-H., Pan, C.-J., Cheng, J.-H., Chen, H.-M., et al. (2016). *Energy & Environmental Science, 9,* 323.
11. Shi, D., Adinolfi, V., Comin, R., Yuan, M., Alarousu, E., Buin, A., Chen, Y., Hoogland, S., Rothenberger, A., Katsiev, K., Losovyj, Y., Zhang, X., Dowben, P. A., Mohammed, O. F., Sargent, E. H., & Bakr, O. M. (2015). *Science, 347*, 519. (80).

12. Dang, Y., Ju, D., Wang, L., & Tao, X. (2016). *CrystEngComm, 18,* 4476.
13. Dang, Y., Liu, Y., Sun, Y., Yuan, D., Liu, X., Lu, W., et al. (2015). *CrystEngComm, 17,* 665.
14. Lian, Z., Yan, Q., Lv, Q., Wang, Y., Liu, L., Zhang, L., et al. (2015). *Scientific Reports, 5,* 16563.
15. Dong, Q., Fang, Y., Shao, Y., Mulligan, P., Qiu, J., Cao, L., & Huang, J. (2015). *Science, 347*, 967 (80).
16. Dang, Y., Zhou, Y., Liu, X., Ju, D., Xia, S., Xia, H., et al. (2016). *Angewandte Chemie, 55,* 3447.
17. Stoumpos, C. C., Malliakas, C. D., & Kanatzidis, M. G. (2013). *Inorganic Chemistry, 52,* 9019.
18. Baikie, T., Fang, Y., Kadro, J. M., Schreyer, M., Wei, F., Mhaisalkar, S. G., et al. (2013). *Journal of Materials Chemistry A, 1,* 5628.
19. Saidaminov, M. I., Abdelhady, A. L., Murali, B., Alarousu, E., Burlakov, V. M., Peng, W., et al. (2015). *Nature Communications, 6,* 7586.
20. Maculan, G., Sheikh, A. D., Abdelhady, A. L., Saidaminov, M. I., Banavoth, M., Alarousu, E., et al. (2015). *The Journal of Physical Chemistry Letters, 6,* 3781.
21. Saidaminov, M. I., Abdelhady, A. L., Maculan, G., & Bakr, O. M. (2015). *ChemComm, 51,* 17658.
22. Abdelhady, A. L., Saidaminov, M. I., Murali, B., Adinol, V., Voznyy, O., Katsiev, K., et al. (2016). *The Journal of Physical Chemistry Letters, 7,* 295.
23. Zhumekenov, A. A., Saidaminov, M. I., Haque, A., Alarousu, E., Sarmah, S. P., Murali, B., et al. (2016). *ACS Energy Letters, 1,* 32.
24. Han, Q., Bae, S., Sun, P., Hsieh, Y., & Yang, Y. M. (2016). *Advanced Materials, 28,* 2253.
25. Wei, H., Fang, Y., Mulligan, P., Chuirazzi, W., Fang, H.-H., Wang, C., et al. (2016). *Nature Photonics, 10,* 333.
26. Liao, W.-Q., Zhang, Y., Hu, C.-L., Mao, J.-G., Ye, H.-Y., Li, P.-F., Huang, S.-D., & Xiong, R.-G. (2015). *Nature Communications, 6*, 7338, 1.
27. Chung, I., Lee, B., He, J., Chang, R. P. H., & Kanatzidis, M. G. (2012). *Nature, 485,* 486.
28. Peng, W., Wang, L., Murali, B., Ho, K., Bera, A., Cho, N., et al. (2016). *Advanced Materials, 28,* 3383.
29. Liu, Y., Zhang, Y., Yang, Z., Yang, D., Ren, X., Pang, L., et al. (2016). *Advanced Materials, 28,* 9204.
30. Dong, R., Fang, Y., Chae, J., Dai, J., Xiao, Z., & Dong, Q. (2015). *Advanced Materials, 27,* 1912.
31. Shi, D., Adinolfi, V., Comin, R., Yuan, M., Alarousu, E., Buin, A., et al. (2015). *Science, 347,* 519.
32. Stranks, S. D., Stranks, S. D., Eperon, G. E., Grancini, G., Menelaou, C., Alcocer, M. J. P., Leijtens, T., Herz, L. M., Petrozza, A., & Snaith, H. J. (2014). 341.
33. Haynes S. W. & J. R. *American Physical Society, 81*, 835 (1951).
34. Huang, Y., Li, L., Liu, Z., Jiao, H., He, Y., Wang, X., et al. (2017). *Journal of Materials Chemistry A, 5,* 8537.
35. Fang, H., Li, Q., Ding, J., Li, N., Tian, H., Zhang, L., et al. (2016). *Journal of Materials Chemistry C, 4,* 630.
36. Shaikh, P. A., Shi, D., Retamal, J. R. D., Sheikh, A. D., Haque, M. A., Kang, C. F., et al. (2016). *Journal of Materials Chemistry C, 4,* 8304.
37. Ding, J., Fang, H., Lian, Z., Li, J., Lv, Q., Wang, L., et al. (2016). *CrystEngComm, 18,* 4405.
38. Cao, M., Tian, J., Cai, Z., Peng, L., Yang, L., & Wei, D., (2016). *Applied Physics Letters, 109*.
39. Milbrath, B. D., Peurrung, A. J., Bliss, M., & Weber, W. J. (2008). *Journal of Materials Research, 23,* 2561.
40. del Sordo, S., Abbene, L., Caroli, E., Mancini, A. M., Zappettini, A., & Ubertini, P. (2009). *Sensors, 9,* 3491.
41. Heiss, W., & Brabec, C. (2016). *Nature Photonics, 10,* 288.
42. Yakunin, S., Dirin, D. N., Shynkarenko, Y., Morad, V., Cherniukh, I., Nazarenko, O., et al. (2016). *Nature Photonics, 10,* 585.

43. Yakunin, S., Sytnyk, M., Kriegner, D., Shrestha, S., Richter, M., Matt, G. J., et al. (2015). *Nature Photonics, 9,* 444.
44. Sum, T. C., & Mathews, N. (2014). *Energy & Environmental Science, 7,* 2518.
45. Nh, C. H., Im, J., Chung, J., Kim, S., & Park, N. (2012). *Nanoscale Research Letters, 7,* 353.
46. Eperon, G. E., Stranks, S. D., Menelaou, C., Johnston, M. B., Herz, L. M., & Snaith, H. J. (2014). *Energy & Environmental Science, 7,* 982.
47. Green, M. A., Ho-Baillie, A., & Snaith, H. J. (2014). *Nature Photonics, 8,* 506.
48. Kadro, J. M., Nonomura, K., Gachet, D., Grätzel, M., & Hagfeldt, A. (2015). *Scientific Reports, 5,* 1.
49. Zhang, T., Yang, M., Benson, E. E., Li, Z., Van De Lagemaat, J., Luther, J. M., et al. (2015). *ChemComm, 51,* 7820.
50. Bridgman, P. W. (2015). *Proceedings of the American Academy of Arts and Science, 60,* 305.
51. Jiang, H., & Kloc, C. (2013). *MRS Bulletin, 38,* 28.
52. Ye, T., Fu, W., Wu, J., Yu, Z., Jin, X., Chen, H., et al. (2016). *Journal of Materials Chemistry A, 4,* 1214.
53. Jeon, N. J., Noh, J. H., Kim, Y. C., Yang, W. S., Ryu, S., & Il Seok, S. (2014). *Nature Materials, 13*, 897 (2014).
54. Yang, M., Zhou, Y., Zeng, Y., Jiang, C., Padture, N. P., & Zhu, K. (2015). *Advanced Materials, 27,* 6363.
55. Padture, N. P., Zhou, Y., Yang, M., Wu W., Vasiliev, A. L., & Zhu, K. (2015). *Journal of Materials Chemistry A, 3*, 8178.
56. Kapustin, A. P. (2012). *The effects of ultrasound on the kinetics of crystallization*. New York: Springer Science & Business Media.
57. Thompson, L. H. & Doraiswamy, L. K. (1999). *38*, 4, 1215.
58. Ruecroft, G., Hipkiss, D., Ly, T., Maxted, N., & Cains, P. W. (2005). *Organic Process Research & Development, 9*, 923.
59. Plesset, M. S., & Chapman, R. B. (1971). *Journal of Fluid Mechanics, 47*, 283.
60. Elder, A. S. (1959). *Journal of the Acoustical Society of America, 443,* 54.
61. Xiao, M., Huang, F., Huang, W., Dkhissi, Y., Zhu, Y., Etheridge, J., et al. (2014). *Angewandte Chemie, 53,* 9898.

Perovskite Oxides as Advanced Energy Materials for Solid Oxide Fuel Cell and Supercapacitor Applications

P. Muhammed Shafi

Abstract The present chapter reveals a detailed explanation of ABO_3-type perovskite oxides with their physiochemical properties. The crystallographic structure and its impact on stability and properties are well discussed in various sections of this chapter. Even though the perovskite oxides exhibit a wide range of applications owing to their unique crystallographic and physiochemical property, here the electrochemical energy conversion/storage applications are mainly focused. The importance of electronic and ionic conductivities of ABO_3-type perovskite oxide materials and their impacts on electrochemical conversion and storage properties are elucidated with suitable schematic representations and theoretical backgrounds. Particularly, application toward the supercapacitor as electrode material and toward all the three components (cathode, anode, and electrolyte) of solid oxide fuel cells (SOFCs) is addressed. The possibility of anionic as well as cationic storage mechanism in perovskite-based supercapacitors are discussed as well. Moreover, the role of these perovskite materials for oxygen ion conducting electrolyte as well as the proton-conducting electrolytes for the SOFCs is schematically illustrated. The chapter also covers a broad literature survey to understand the current scenario and development of these materials to the given applications.

Keywords Perovskite oxide · Tolerance factor · Cationic array · Oxygen vacancy · Mixed ionic electronic conductivity · Fuel cell · Supercapacitor

1 Introduction

Compared to common binary (rutile structure) oxides, the complex or mixed oxides have attracted great interest in material science owing to their wide range of applications. Multiple numbers of cations together formed to a single oxide material is usually referred as mixed oxide. However, an oxide material with one single cation

P. Muhammed Shafi (✉)
School of Chemical Engineering, Yeungnam University, Gyeongsan, Gyeongbuk 38541, Republic of Korea
e-mail: shafiparasseri@gmail.com

S. J. Ikhmayies (ed.), *Advances in Energy Materials*,
Advances in Material Research and Technology,
https://doi.org/10.1007/978-3-030-50108-2_8

of different oxidation states is also often considered as mixed oxide material. But, in a general perceptive, unlike rutile oxides, a mixed oxide consists of two or more cations with different oxidation states, ionic sizes and co-ordination numbers [1–3]. The spinel and perovskite are well-known examples for complex oxide structures. In both the cases, the diversity of ions, oxidation states and sizes offer different properties depending upon the ions present. Hence, these types of complex oxides are explored to a variety of applications. There are two types of spinel structures namely: normal spinel and inverse spinel. The normal spinel has a structure of AB_2O_4 where A cations occupy the 1/8 tetrahedral hole and B cation occupy the 1/2 of the octahedral hole. The inverse spinel has a common formula of $B[AB]O_4$ where B cations occupy the 1/8 tetrahedral hole and the second B and A cations occupy the cation occupy the 1/2 of the octahedral hole. Moreover, the rutile oxide (AO_2) comprises of only one cation and an oxygen, which are octahedrally coordinated. Unlike these binary rutile structured oxides and complex spinel structured oxides, the perovskite oxide structure follows a general formula of ABO_3, where A and B are cations of different atomic and mass numbers, and O is the oxygen anion in the ratio of 1:1:3 [3–5]. The history of these types of materials start from the discovery of $CaTiO_3$ in 1839 by Gustav Rose, a famous geologist and is named as perovskite after a renowned Russian mineralogist, Lev Alexevich von Perovski (1792–1856). A site is usually occupied by lanthanides/alkaline earth elements of larger ionic radius and B site by transition metal of comparatively smaller radius. The A cation usually has a 12-fold dodecahedral co-ordination and B cation has sixfold co-ordination [5]. The spatial structure of a perovskite material is given in Fig. 1a. The choice of cations and anion, oxidation state of cation, and ionic radii of A and B site cations affect the structure and properties of perovskite material. The diversity of cations and anions of these structures provide a wide variety of applications including photovoltaic, ferroelectric, dielectric, pyroelectric, piezoelectric, magnetic, catalytic, and energy storage/conversion. The synthesis route and controlling morphology of the perovskite material are very crucial and have a strong impact on their properties.

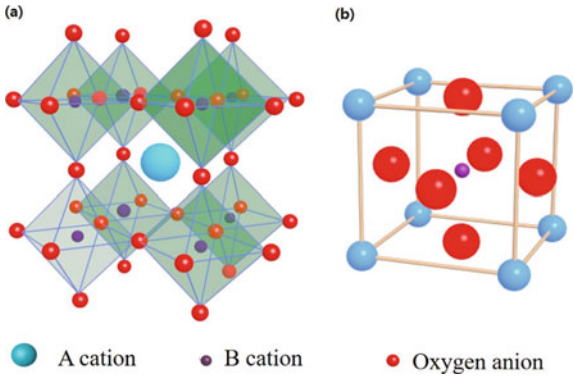

Fig. 1 **a** Spatial arrangement of atoms in perovskite structure and **b** unit cell for an ideal cubic perovskite

2 Material Properties

2.1 Structural Stability

The stability of a perovskite structured material is usually defined by tolerance factor, τ. The first explanation on perovskite tolerance factor was made by Victor Moritz Goldschmidt, mineralogist, and now the formula of tolerance factor calculation is often called as Goldschmidt tolerance factor (Eq. 1). Here, r_A, r_B and r_O are radii of A cation, B cation, and oxygen anion, respectively. The tolerance factor range $0.7 < \tau < 1$ is considered as a stable structure.

$$\tau = \frac{r_A + r_O}{\sqrt{2}(r_B + r_O)} \tag{1}$$

The perfect crystal structure is considered as cubic ($\tau = 1$) and by further lowering the τ value, the structure tilts to rhombohedral and then to orthorhombic and so on. The decrease in r_A or increase in r_B definitely lowers the τ value and will result in a decrease in the symmetry. For a τ value greater than unity, the crystal tends to stabilize with hexagonal structure [1]. Hence, the calculation of τ can be used to opt cations for A and B sites in order to tailor the property without losing structural stability. The ideal perovskite structure, that is the cubic phase belongs to the $pm\bar{3}m$ (221) space group [2]. Figure 1b shows the pictorial representation of a unit cell of an ideal cubic structure, where the A cations are occupied at the corners, B cation at the body center and the oxygen ions are located at the center of each face of the cube. The packing factor of these perovskites is usually high and is 0.76 for $LaMnO_3$ [3]. Generally, the packing factor for perovskite structure lies around 0.75 [1, 2]. For a perfect cubic structure, the B–O–B bond forms a linear chain with 180° bond angle. The reduction in τ value induces deviation from the cubic phase by tilting the BO_6 octahedra, resulting in a reduced B–O–B bond angle (<180°). Hence, opting choice of cations is very crucial in order to maintain the stable phase of perovskite oxide. Despite considering the oxidation state and radii of A and B site cations as important factors to decide the material properties, their role in upholding the stable phase also should be taken care of.

2.2 Electronic and Ionic Conductivity

The electronic and ionic conductivity of the perovskite adapts them to various applications like superconductivity, electrodes for energy storage, and catalytic applications. Cu-based perovskite achieved great potential toward superconductivity, where Cu occupies the B site. There are many examples of superconducting perovskite oxides with Cu as B cation. $YBa_2Cu_3O_7$, $Bi_2Sr_2Ca_2Cu_3O_{10}$, and $HgBa_2Ca_2Cu_3O_{8+\delta}$ are some examples. Apart from these superconducting materials, there are many

perovskite materials that exhibit nearly metallic behavior, and hence they are used as electrodes for solid oxide fuel cells and metal-air batteries. $LaMnO_3$ and $LaCoO_3$ are commonly used electrode materials. The BO_6 octahedra play a major role in the electronic conductivity of the ABO_3 perovskites. The anion polarization induces to form a covalent bond between B cation and oxygen anion, which facilitates the electronic conductivity. Electrons of n-type and holes of p-type perovskites are transported through B–O–B chains. The electronic conductivity of these materials could be further improved by partial substitution of A or B site cation with different oxidation states. Furthermore, it is believed that the perovskite oxide has an inherent property of having oxygen vacancy. This oxygen vacancy will play as a medium for ionic mobility and result in an improved ionic conductivity. Hence, these types of materials are largely used as ion-conducting electrolytes for solid-state fuel cell SOFCs. Similar to electronic conductivity, the ionic conductivity of the perovskite oxides could effectively improve by cationic substitution. Therefore, the electron/hole conduction along chains of B–O–B bond and vacancy mediated oxygen ion mobility, having played a major role in bringing the material as a mixed ionic and electronic conduction application, is being explored for electrodes as well as ion-conducting electrolytes of various conversion and storage devices.

3 Tuning Electronic and Ionic Conductivities in ABO_3-Type Perovskite Materials

The extensive array of cationic selection possibility of perovskite structure over A and B sites is well known to tailor the specific properties. Though the critical properties of the perovskite materials are defined by the B site cation, A site cation plays a vital role in tuning these properties. Furthermore, this class of material allows a wide range of cationic substitution over A and B sites without affecting the structural stability factor. This offers intriguing possibilities for further improvement of material properties. The electronic and ionic conductivities or mixed ionic and electronic conductivity of these materials are effectively tuned depending upon the application by such cationic substitutions.

For instance, consider an ABO_3-type perovskite oxide where the electric neutrality is maintained with charge distribution of $A^{3+}B^{3+}O_3$. Now let us see how the cationic substitution at A site affects the conductivity of the material.

Let us consider another cation, À of similar ionic radii, (so that it may not affect the tolerance factor) with an oxidation state of +2 (a divalent acceptor, $À^{2+}$) and is substituted partially for trivalent A cation (A^{3+}).

Now, in order to maintain the electron neutrality, the effective negative charge induced by À substitution should be compensated either by electronic compensation or ionic compensation [4].

3.1 Electronic Compensation

- The extra electron left at the A site lattice by À substitution will be balanced by converting an equal amount trivalent B transition metal to tetravalent state.
  i.e. $x\text{À} + A_{(1-x)}BO_3 \rightarrow \text{À}_x^{2+}\, A_{(1-x)}^{3+}\, B_x^{4+}\, B_{(1-x)}^{3+}\, O_3$
  (substitution of xÀ induces a conversion xB^{3+} to xB^{4+}).
- As a consequence, the divalent cationic substitution at the A site causes to form an electron hole (h˚) at the tetravalent B site as p-type.
- Hence, the electronic conductivity through the B–O–B chains will be due to the transportation of holes, i.e., the electronic conduction occurs through the migration of hole associated with the tetravalent B site cation to the nearest trivalent B site cation.
- The amount of transition metal B^{4+}/B^{3+} couple is proportional to the amount of divalent acceptor À substitution at trivalent host cation, A.
- Higher the B^{4+}/B^{3+} couple, higher the electronic conductivity expected. Theoretically, 50% of mole percentage divalent acceptor substitution is expected to have a maximum electronic conductivity.
- Electronic conductivity,

$$\sigma = \frac{C}{T} e^{-E_a/kT} \tag{2}$$

where the pre-exponential constant C includes the carrier concentration along with other material-dependent parameters, T is the absolute temperature, E_a is the activation energy and k is the Boltzmann constant.

Figure 2 shows the schematic representation of electronic conductivity exerted by the partial substitution of a divalent acceptor cation.

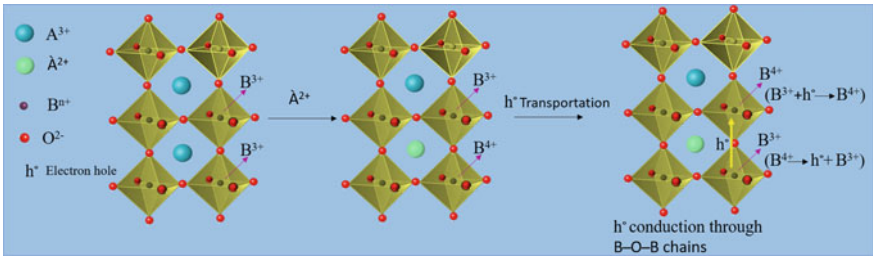

Fig. 2 Electronic conduction through electron hole migration from B^{4+} to B^{3+} state. The B^{4+}/B^{3+} couple formed due to the introduction of divalent cation (À) to the A site

3.2 Ionic Compensation

- If the B cation is not multivalent, the extra negative charge occurred at the host lattice by divalent À acceptor cation is balanced by reducing the oxygen stoichiometry.
- Consequently, charge imbalance due to each 2À substitution is compensated by forming an oxygen vacancy at anionic sites.

(i.e., two electron holes are eliminated by removal of single oxygen from the lattice)

$$2\delta\text{À} + A_{(1-2\delta)}BO_3 \rightarrow \text{À}_{2\delta}A_{(1-2\delta)}BO_{3-\delta} + \frac{\delta}{2}O_2$$

- The ionic conductivity in ABO_3-type oxides occurs due to the oxygen vacancy mediated oxygen ion transport. The oxygen vacancy of any vacancy site will be filled by an adjacent oxygen ion. This diffusive jump of O^{2-} ion from the adjacent oxygen site by exchanging their position facilitates the ionic conductivity.
- Hence, the ionic conductivity of any ABO_3 perovskite oxide is directly proportional to their measure of oxygen vacancies [5].
- Nonetheless, the electronic conductivity is limited due to the decreased amount of B^{4+}/B^{3+} couple, which leads to decreased amount of available hopping sites. Hence, the modified electronic conductivity is,

$$\sigma = \left(\text{Á} - 2\delta\right)\frac{C}{T}\text{e}^{-E_a/kT} \tag{3}$$

The new term included in the pre-exponential factor represents the oxygen vacancy limited carrier concentration.

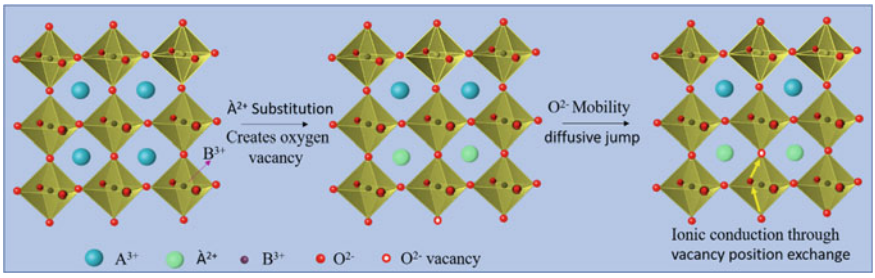

Fig. 3 Ionic conduction through diffusive jump of adjacent O^{2-} ion due to the divalent acceptor cationic substitution induced oxygen vacancy

Figure 3 shows the schematic representation of ionic conductivity through oxygen mobility through the perovskite lattice exerted by the partial substitution of a divalent acceptor cation.

However, the simultaneous presence of transition metal B^{4+}/B^{3+} couple and oxygen vacancies can perform a mixed ionic and electronic conductivity.

4 Perovskite Oxides as Advanced Energy Materials

Since the perovskite oxides are structurally stable even at elevated temperatures and have the mixed ionic electronic conductivity, these materials are traditionally used for multiple applications. More importantly, these materials have great potential insight in energy conversion and storage applications. Though there many energy applications for perovskite oxide materials (photovoltaic, fuel cell, secondary batteries, and supercapacitor), this chapter mainly focused on solid oxide fuel cell and supercapacitor applications.

4.1 As Advanced Energy Conversion Materials

For a conversion device like the so-called fuel cell, perovskite oxides have been studied for all the three components (anode, cathode, and electrolyte). Especially, in the case of SOFC, perovskite has been used for electrodes (cathode and anode) as well as for electrolytes. The cathode material should have high electrochemical activity toward oxygen reduction reaction (ORR), high oxygen ion diffusivity to transfer the reduced oxygen ion through the bulk cathode material. Hence, perovskite materials of mixed ionic electronic conductivity along with high ORR activity are favorable to cathode application. The properties required for anode material are similar to the cathode material properties except for one additional property of high catalytic activity toward the hydrogen oxidation reaction. The mixed ionic electronic conductivity is a must for electrolytes of SOFC so as to transport the reduced oxygen ion from cathode to anode where the combustion reaction or hydrogen oxidation takes place.

- **Components of SOFC**

A solid oxide fuel cell is a solid-state electrochemical device that converts chemical energy to electrical energy and heats by the efficient combustion of fuels or oxidants. Generally, SOFC is a bipolar conversion device with three basic components such as cathode, anode, and electrolyte. Figure 4a represents the scheme for the basic structure of a SOFS device. The cathode and anodes are made up of porous ceramics as it should sustain higher temperatures. The porous structure of anode material enables the easy diffusion of fuel gases to and from the electrode–electrolyte interface. The reduction of oxygen at cathode and oxidation of fuel/oxidant

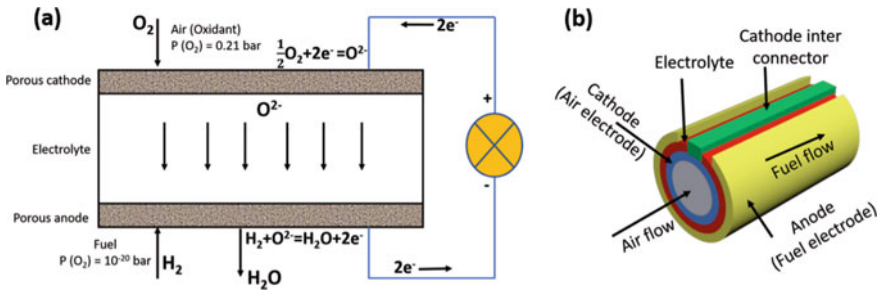

Fig. 4 **a** Basic structure of a solid oxide fuel cell and **b** the tubular SOFC design from Siemens–Westinghouse

at the anode are spatially separated and the electrons are directed to flow through an external circuit. The movement of oxygen ion from the cathode to anode through the solid electrolyte is controlled and driven by the oxygen chemical potential gradient between the cathode and anode. The oxygen partial pressure exerted at the cathode is very high and at the anode is very low due to the consumption of oxygen ion by the fuel combustion. The critical component of a SOFC is the gas-tight solid electrolyte, which separates the cathode and anode safely. A light crack or presence of a pinhole will lead to diffusion of fuel gas from anode to cathode. Such leakages cause a direct reaction of fuel with oxygen ions at cathode, and the device then becomes inefficient. According to the design and spatial arrangement of these components, there are planar, tubular, and single chamber SOFCs [6]. Figure 4b represents the famous tubular design of SOFC developed by Westinghouse and taken over by Siemens.

a. **Cathode materials**

Numerous perovskite oxides have been developed as efficient cathode materials for SOFC in recent years [7–15]. The cathode material for SOFC should be catalytically active toward the ORR activity. Besides, it should be conductive electrically as well as ionically in order to transport the oxygen ion through the bulk. The chemical stability of cathode material is also a critical parameter for the SOFC to work effectively. Because, the cathode side will be oxygen ion rich always, the material should be highly stable even in this oxidizing environment. Moreover, the thermo-mechanical property of the cathode material should be well-matched with the electrolyte; otherwise, the possibility of stress development is maximum upon heating and cooling conditions. The state-of-the-art of cathode material for SOFCs generally comprises of a highly ORR catalytic with electrically conducting or with mixed ionic electric conductive material and an ionic conductor (Y_2O_3 stabilized ZrO_2, so-called YSZ) [16]. There are two types of cathode materials based on the conducting nature.

1. Electrically conducting cathode materials:

Here, the electrode acts as electron supplier and the ORR activity will take place at the triple phase boundary (TPB), where the cathode catalyst, oxygen gas, and

Table 1 Perovskite oxide materials used as cathode material for SOFCs with their operating temperature (°C), electronic and ionic conductivities (S cm^{-1}) and TEC (K^{-1})

Cathode materials	Temperature (°C)	Electronic conductivity (S cm^{-1})	Ionic conductivity (S cm^{-1})	TEC [× 10^{-6} K^{-1}]	References
$La_{0.65}Sr_{0.35}MnO_{3-\delta}$	800	102	1.7×10^{-4}		[7]
$(La_{0.8}Sr_{0.2}MnO_3)$	700	180		11.8	[8]
$La_{0.7}Sr_{0.3}MnO_3$	800	240		11.7	[9, 10]
$La_{0.8}Sr_{0.2}FeO_3$	700	90		12.2	[11]
$La_{0.6}Sr_{0.4}FeO_3$	800	129	5.6×10^{-3}	16.3	[12]
$La_{0.6}Sr_{0.4}Co_{0.2}Fe_{0.8}O_3$	800	302	8×10^{-3}		[7]
$Ba_{0.5}Sr_{0.5}Co_{0.8}Fe_{0.2}O_{3-\delta}$		15		19.95	[13, 14]
$La_{0.6}Sr_{0.4}CoO_3$	800	1600	0.22	20.5	[7, 15]
$Pr_{0.8}Sr_{0.2}Co_{0.2}Fe_{0.8}O_3$	800	76	1.5	12.8	[7]
$Sr_{0.9}Ce_{0.1}Fe_{0.8}Ni_{0.2}O_3$	800	87	0.04	18.9	[7]

electrolytes meet. Hence, in this case, the TPB length plays a critical role in the cathode performances toward high current density and lower overpotential.

2. Mixed ionic and electronic conducting cathode materials:

Here, the cathode material is a mixed ionic electronic conductor, and hence the ORR activity will take place at the surface of cathode material and it will diffuse through the bulk. Thus, the surface and bulk pathways coexist in parallel. Mostly, these two are in competition with each other, the fastest will determine the overall kinetics of SOFC cathode. Few important perovskite-based cathode materials are listed in Table 1.

Considering these parameters, the widely used cathode materials are $La_{1-x}Sr_xMnO_3$ (LSM) materials and $La_{1-x}Sr_xCo_{1-y}Fe_yO_3$ (LSCF). However, the LSM perovskites are still struggling due to its relatively lower ionic conductivity and larger activation energy for ORR activity. The ORR activity happening at SOFC cathode is as follows:

$$\frac{1}{2}O_2 + 2e^- = O^{2-} \tag{4}$$

b. **Anode materials**

Anode is an important component of SOFC device since it serves as an electrochemical active site for oxidation of fuel gas. Anode also requires higher electronic conductivity as the electron released after the fuel oxidation should transport to the connecting component of the fuel cell. Moreover, the anode should support a good catalytic activity toward the fuel gas oxidation. The oxidation reaction for a hydrogen fuel SOFC is as follows;

$$H_2 + O^{2-} = H_2O + 2e^- \quad (5)$$

In the early stages of anode material development for SOFCs, noble metals such as platinum, gold, silver, palladium, and rhodium were used. In addition, some transition metals were also examined such as manganese, copper, nickel, cobalt, and iron [17]. The nickel in its pure metal form achieved great attraction owing to its high electrochemical activity, redox stability, and low cost. However, the sintering problem, carbon surface deposition, sulfur poisoning, and the thermal expansion coefficient mismatch from the usual electrolytes lead to the reduced life span of SOFCs, and thus it hinders its commercialization [6, 18–21]. In this context, perovskite oxide materials have gained much attention to develop efficient anode for SOFCs and to replace the traditional anodes. The mixed ionic electronic conductivity of these materials can overcome the confinement of electrochemical oxidation activity at the TPB by extending its solid-gas two-phase boundaries [22]. Besides, some perovskite oxides provide few additional properties, which are important to the SOFC anode. They are listed below;

- High thermal stability
- Compatibility with a solid-state electrolyte
- Excellent electronic conductivity (>100 S cm^{-1}), preferably n-type conductivity
- Better oxygen surface exchange kinetics
- Highly porous structure to ease the fuel gas transportation
- Inherent property of oxygen vacancy to enhance oxygen ion diffusion
- Tunable ionic conductivity by choosing proper B cation.

Based on the crystalline nature, the perovskite cathode materials are classified as chromite, titanate, and vanadate. Among the chromite perovskite oxides, Ca doped $LaCrO_3$ or Sr doped $LaCrO_3$ are widely used owing to their reduced sinterability to YSZ electrolyte, no carbon formation and excellent thermal expansion coefficient (TEC) match with YSZ electrolyte. Further to enhance the electrocatalytic activity, numerous efforts were made by various material scientists by doping the A and B sites cations [23–27]. S Feir et al. investigated an array of dopant cations for the A and B site substitution and found Sr and Ni are the best for SOFC anodes to enhance the electrochemical catalytic activity [28]. $LnSrTiMO_3$ is another class of successful anode materials, where Ln stands for lanthanides like La, Nd, and Sm elements, and M stands for Mn and Fe transition metal. It is observed by jeong et al. that the substitution of Mn or Fe to the B site enhances both the structural stability as well as catalytic activity [29]. Among the various doped $LnSTMO_3$, the Nd-doped material is found to be promising due to its improved conductivity. The Nd substitution at the A site induces some Ti molecules to exhibit metallic behavior [30]. Some of the commonly studied materials for SOFC cathode application are tabulated in Table 2 [31–45].

Recently, double perovskite structured ($A_2B_2O_6$) materials are also being examined for anodes of SOFC devices due to their promising electrochemical property, rich active sites, excellent defense capability toward carbon deposition and sulfur poisoning [43, 46–48]. $Sr_2Fe_{1.5}Mo_{0.5}O_{6-\delta}$, $Sr_2MgMoO_{6-\delta}$, and layered

Table 2 Perovskite oxide materials used as anode material for SOFCs with their operating temperature in °C and conductivity in S cm^{-1}

Anode materials	Temperature (°C)	Conductivity (S cm^{-1})		References
		Reducing	Oxidizing	
$La_{0.7}Mg_{0.3}CrO_3$	800	0.17	3.35	[31]
$La_{0.75}Sr_{0.25}CrO_3$	800	7.07	59.1	[31]
$La_{0.7}Ca_{0.3}CrO_3$	800	1.6	50.1	[31]
$La_{0.75}Sr_{0.25}Cr_{0.5}Mn_{0.5}O_3$	900	1.5	38	[32]
$La_{0.9}Ca_{0.1}Fe_{0.95}Nb_{0.05}O_{3-\delta}$	850	42.55	3.52	[33]
$La_{0.75}Sr_{0.25}Cr_{0.3}Fe_{0.2}Mn_{0.5}O_{3-\delta}$	750	1.04	15.42	[34]
$SrFe_{0.9}Ti_{0.1}O_{3-\delta}$	600	2.53	4.19	[35]
$Sr_{0.9}Ce_{0.1}Co_{0.2}Fe_{0.8}O_{3-\delta}$	600	22	180	[36]
$La_{0.3}Sr_{0.7}Ti_{0.8}Cr_{0.2}O_3$	800	53	8	[37]
$La_{0.9}VO_3$	800	2.9		[38]
$La_{0.8}Sr_{0.2}VO_3$	800	45		[38]
$La_{0.7}Sr_{0.3}VO_3$	800	120		[38]
$Ce_{1-x}Ca_xVO_3$ ($x = 0.1, 0.2, 0.3, 0.4$)	700	2-13	$\sim 10^{-3}$	[39]
$Sr_2FeNb_{0.2}Mo_{0.8}O_{6-\delta}$	800	5.3	19.5	[19]
$Sr_2FeMoO_{6-\delta}$	800	186.9		[40]
$Sr_{1.8}Sm_{0.2}Fe_{1.5}Mo_{0.5}O_6$	850	25		[41]
$Sr_2Fe_{1.4}Ni_{0.1}Mo_{0.5}O_{6-\delta}$	800	20.6		[42]
$PrBaMn_2O_5$	800	8.16	91.5	[43]
$PrBaMn_{1.5}Fe_{0.5}O_{5+\delta}$	800	7.4	112.5	[44]
$(PrBa)_{0.95}(Fe_{0.9}Mo_{0.1})_2O_{5+\delta}$	800	59.2		[45]

$PrBaMn_2O_{5+\delta}$ are few of the excellent double perovskite anode materials having superior electrochemical activity and resistance toward sulfur poisoning and carbon deposition [43, 47, 48]. Both $A_2BB'O_3$ and $AA'B_2O_3$ type double perovskites were investigated for the SOFC anode by various people. Few of these materials are listed in Table 2.

c. **Electrolytes**

The electrolyte of a SOFC device is another important component, which categorizes the SOFC depending upon the nature of the electrolyte's conductivity. The primary requirement for a SOFC electrolyte is the ionic conductivity rather than electronic conductivity. The electrolyte with maximum ionic conductivity and minimum electronic conductivity is believed to be the best choice [6]. Moreover, the electrolyte should be dense enough to prevent the gas mixing possibility. So far, YSZ is the most commonly used SOFC electrolyte since the trivalent yttrium doping creates a large amount of oxygen vacancies and thus ionic conductivity to the zirconia lattice [6]. However, the substantial growth of its grain size at high-temperature calcination

and not being cost-effective to practical use brought researchers to think about alternate options. Ceria-based (CeO_2) electrolytes are also largely used for SOFCs due to its much higher ionic conductivity. Gd_2O_3 doped ceria (CGO) has exhibited large oxygen vacancies and thus show a much better ionic conductivity. These results drive the attention of researchers to the ABO_3-based perovskite materials as it contains large number of inherent oxygen vacancies, and further the vacancies are tunable by proper substitutions at A and B sites. Based on the conductivity nature, there are two types of electrolyte.

(i) **Oxygen ion conducting electrolyte**

In the case of SOFC with oxygen ion conducting electrolyte, the O^{2-} diffuses to anode and the fuel combustion takes place at anode. Hence, the oxygen ion mobility is a must for proper functioning of this type of SOFCs. Since ABO_3-type perovskites have already drawn much attention by its capability of oxygen ion diffusion through the lattice, the property is much explored in SOFC electrolyte field. Lanthanum gallate ($LaGaO_3$) is one of the hot materials being examined well in this application. The intermediate operating temperature range and excellent ionic conductivity even higher than stabilized zirconia made $LaGaO_3$ a promising candidate for SOFC electrolyte application [49]. Furthermore, doped $LaGaO_3$ exhibits exciting advantages over YSZ and other competing electrolytes. Partial substitution for trivalent La and Ga by divalent acceptor cations drastically improved the oxygen vacancies and thus oxygen ion conductivity of the material. For example, the divalent Sr and Mg co-doped $La_{1-x}Sr_xGa_{1-y}Mg_yO_{3-x/2-y/2}$ showed significant improvement in ionic conductivity and stability than CGO-based electrolytes [50]. Thus, this electrolyte material is explored well in intermediate operating temperature range (600–800 °C) SOFCs [51]. However, the complexity of preparing this material without impurities formation and instability under oxidizing and reducing conditions suppressed the applications [52, 53]. Similarly, perovskite oxides of structure $LnBO_3$ (Ln = La, Dy and B = Al, In, Sc, Y) were also examined by various people as an ion-conducting electrolyte. $LnAlO_3$ received considerable interest owing to their high stability, relatively low cost, and moderate thermal expansion [54, 55]. Few oxide ion conducting perovskite electrolyte materials are listed in Table 3 [56–60].

(ii) **Proton-conducting electrolyte**

The role of perovskite in SOFC electrolyte became more relevant while focus was on proton-conducting electrolyte. Here, the SOFC can be used at lower operating temperature due to the lower activation energy of proton. Again, the possibility of using high conductive material for proton-conducting electrolyte applications allows an array of materials to be used for this application. Iwahara et al. [61, 62] analyzed this ABO_3 perovskite material ($SrCeO_3$) for proton conduction first, after that the topic gained popularity for SOFC electrolyte application. Once this material comes in contact with water molecule, it starts proton conduction. The mechanism can be explained using Kröger–Vink notation as Eq. 6 [63] where, $V_0^{\bullet\bullet}$, O_0^x, and $OH_0^{\bullet}$ are an oxygen vacancy, a lattice oxygen ion, and a hydroxyl ion. The proton defect formation happens when water vapor is incorporated with the oxygen vacancy and

Table 3 Some perovskite-based oxygen ion conducting electrolyte material for SOFCs with their operating temperature (°C), electronic and ionic conductivities (S cm^{-1}) and TEC (K^{-1})

Electrolyte materials	Temperature (°C)	Electronic conductivity (S cm^{-1})	Ionic conductivity (S cm^{-1})	TEC [× 10^{-6} K^{-1}]	References
$La_{0.9}Sr_{0.1}Ga_{0.8}Mg_{0.2}$ $O_{2.85}$	800		0.1	10.7	[56]
$LaSc_{0.9}Mg_{0.1}O_{3-\delta}$	800	200	2×10^{-4}		[57]
$La_{0.9}Sr_{0.1}AlO_{3-\delta}$	800	60	2×10^{-3}		[58]
$La_{0.9}Sr_{0.1}Al_{0.9}Mg_{0.1}O_{3-\delta}$	800	70	2×10^{-4}	11.2	[59, 60]
$La_{0.9}Sr_{0.1}ScO_{3-\delta}$	800	46	7×10^{-3}		[58]
$La_{0.9}Sr_{0.1}InO_{3-\delta}$	800	23	7×10^{-3}		[60]

lattice oxygen ion of the electrolyte material.

$$H_2O + V_0^{\bullet\bullet} + O_0^x \leftrightarrow 2OH_0^{\bullet} \tag{6}$$

At the anode side, the hydrogen from fuel will incorporate the electrolyte lattice oxygen ion as shown in Eq. 7. When the number of protonated oxygen ions is sufficiently high, the proton will migrate to the adjacent oxygen ion in the lattice since it is not bounded to any particular oxygen and is quasi-free to diffuse. Hence, the protonic conductivity in these types of electrolytes occurs through this proton migration [64]. Consequently, the protons continuously transport to the cathode side and there the oxygen gas consumes and leaves electrons and water molecules according to Eq. 8. The major advantage of the proton-conducting electrolyte SOFC is that it will not release water at anode like oxygen ion conducting SOFC, which helps to keep the fuel in pure form.

$$H_{ads} + O_0^x \rightarrow OH_0^{\bullet} + e^- \tag{7}$$

$$2OH_0^{\bullet} + \frac{1}{2}O_2(g) + 2e^- \rightarrow H_2O_{ads} + 2O_0^x \tag{8}$$

Figure 5 represents the schematic illustration of a SOFC with proton-conducting electrolyte. The protonic conductivity by the proton defect diffusion through the electrolyte lattice is balanced by oxygen vacancies as a counterpart to keep the neutral charge. Hence, oxygen vacancy plays a major role here too, similar to oxygen ion conducting SOFC. Consequently, perovskite oxides materials, well known by its inherent and tunable oxygen vacancies, were studied for the proton-conducting electrolyte applications. $BaCeO_3$-based materials received much attention in this field due to its higher protonic conductivity [6]. Further, doping with acceptor cation at Ce^{4+} site of $BaCeO_3$ leads to promising improvement in proton defect formation, where the charge neutrality is maintained by forming oxygen vacancy. It is found that the trivalent cations (M^{3+}) result in more protonic conduction than divalent

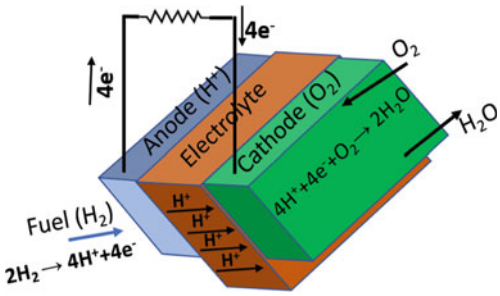

Fig. 5 Schematic illustration of a proton-conducting electrolyte

Table 4 Some perovskite-based proton-conducting electrolyte material for SOFCs with their operating temperature (°C), ohmic and polarization resistances (Ω)

Electrolyte materials	Operating temperature (°C)	Ohmic resistance (Ω)	Polarization resistance (Ω)	References
$BaZr_{0.8}Y_{0.2}O_{3-\delta}$ (BZY20)	800	1.4	1.3	[65]
$BaZr_{0.7}Pr_{0.1}Y_{0.2}O_{3-\delta}$ (BZPY10)	–	1.33	1.3	[66]
$BaCe_{0.7}Nb_{0.1}Sm_{0.2}O_{3-\delta}$ (BCNS)		1.1	1.2	[67]
$BaCa_{0.9}Nd_{0.1}O_{3-\delta}$ (BCNO)	700			[68]
$BaCe_{0.7}Ta_{0.1}Y_{0.2}O_{3-\delta}$ (BCTY)		1.08	0.95	[69]
$BaCe_{0.9}Sm_{0.1}O_{3-\delta}$ (BCS)	620			[68]

cation, since it produces protonic defect more effectively. The partial substitution results to form $BaCe_{1-x}M_xO_{3-\delta}$. Similarly, the B site partial substitution on $SrCeO_3$ ($SrCe_{1-x}M_xO_{3-\delta}$) also received much interest. Some excellent proton-conducting electrolytes are listed in Table 4.

4.2 As Advanced Energy Storage Materials

The rapid growth of electronic industries and increased use of fossil fuels requires urgent implementation of sustainable energy conversion/storage devices. Hence, there is an increased demand for developed and cost-effective high-performance storage devices. Batteries and supercapacitors are the two major devices in this field. There are countless efforts paid by researchers to develop efficient electrodes for these devices. Perovskite oxides received considerable attention owing to their unique tenability of composition and thus their functionalities. The array of cation sites and their possible substitutions, and the multiple oxidation states of B site cation along with inherent and tunable property of lattice oxygen vacancies brought them to a special space in the field of electrode material development for batteries and supercapacitors. Though there are many reports available on perovskite oxide materials

used for electrodes of different types of batteries, this chapter discusses the application toward supercapacitor electrode fabrication. While coming to energy storage application, ternary metal oxides with two different metal cations are found to be suitable for advanced electrode materials owing to their multiple oxidation states and improved electronic conductivity. Similarly, perovskite oxides with ABO_3 structure have achieved tremendous attention in replacing metal oxides as electrode material in electrochemical energy storage devices. The availability of A site and B site, where A site is usually occupied by lanthanides and B site by transition metal which provides enough sites for cationic intercalation. Further, their properties strongly vary depending on A and B ion's nature and oxidation states. In majority of the cases, ion A (rare-earth) is catalytically inactive and merely provides thermal stability, while ion B (transition metal) is the active component.

4.2.1 Electrochemical Capacitor/Supercapacitor Application

With the high-power capability and relatively large energy density as compared to conventional capacitors, electrochemical capacitors offer a promising approach to meet the increasing power demands of energy storage systems in the twenty-first century. Thus, supercapacitors have achieved great attention among energy storage devices due to their ability to bridge the gap between power density and energy density. High energy batteries (deliver energy consistently for a prolonged period) and high-power capacitors (quick delivery and charging) are equally important in energy storage/conversion field. Hence, obtaining high energy density at larger power density becomes a great challenge to the researchers. Coming to the charge storage mechanism in a supercapacitor device, there are electric double-layer capacitance and pseudocapacitors depending up on the materials used as its active electrodes. Figure 6 represents the schematic illustration of the electrode–electrolyte interface for a supercapacitor at its discharged and charged conditions. A supercapacitor stores energy using either ion adsorption (electrical double-layer capacitors, EDLCs) or fast and

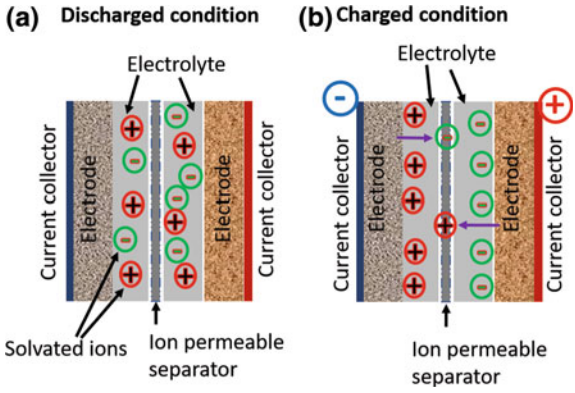

Fig. 6 Schematic illustration of charge storage mechanism in supercapacitors; **a** before charging and **b** in charged condition

reversible faradaic reactions (pseudocapacitors). These two mechanisms can function simultaneously depending on the nature of the electrode material. Progress in supercapacitor technologies can be credited to the continuous development of nanostructured electrode materials. For EDLCs, proper control over the pore size and the specific surface area of the electrode for an appropriate electrolyte solution is crucial to ensure good performance of the supercapacitor in terms of both power delivery rate and energy storage capacity. To further enhance the specific capacitance of the electrode, the pseudocapacitance, due to the intercalation of foreign electro-active species on the electrode material, can be coupled with the electrical double-layer capacitance. The material which is used to fabricate electrode presents its own benefits and challenges as this technology moves toward the next generation of supercapacitor devices. Generally, carbons or carbon derivatives belong to EDLCs, which provide physical charge storage at the interface between electrode and electrolyte. Activated carbon (AC) is the most popular and well-established EDLC electrode so far. Pseudocapacitive materials undergo redox reactions to store more than one charge per reactive surface site and hence usually deliver higher energy density than EDLCs. The pseudocapacitance is a bulk storage mechanism unlike EDLC, which is constrained to only the surface of the material. Transition metal oxides or conducting polymers (CPs) are well known to depict this type of storage mechanism owing to their switching ability between different oxidation states and the potential to store charges along reactive groups in their polymer backbones, respectively.

As we already know the electrochemical properties of perovskite oxide, which is being utilized for the electrodes and electrolytes of SOFCs, the application as pseudocapacitor electrode is unquestionable. The availability of multivalent transition metal (B cation) and inherent property of oxygen vacancy at the perovskite oxide lattice was first explored by Mefford et al. in 2014 [5], and then the idea of anion intercalation became more relevant in perovskite-based pseudocapacitors. The strategy they followed was just analogous to Hahn B. P. et al. where the cation vacancy is utilized to have cationic charge storage [70]. There are numerous reports on perovskite oxides based on $LaMnO_3$, $LaCoO_3$, $LaNiO_3$, $LaFeO_3$, etc., being used for pseudocapacitor electrode applications [5, 71–84], and few are tabulated in Table 5. However, the storage mechanism based on anionic intercalation was explored more after the Mefford et al. [5] findings. They prepared both the oxygen-deficient as well as oxygen excess $LaMnO_3$ electrodes and investigated the storage mechanisms. Interestingly, their findings proved that the anionic intercalation is not only confined to oxygen-deficient perovskite but also to oxygen excess compound though the rate is maximum for oxygen-deficient structure. Thus, the anion intercalation-based storage mechanism in perovskite oxide led to a new strategy to enhance the energy density and performances of the pseudocapacitors. The anionic intercalation by the oxygen ion diffusion through the bulk can be understood more clearly from the schematic representation as shown in Fig. 7. Here, the oxygen ion from electrolyte intercalates to the oxygen vacancy or surface leaving the proton to the electrolyte, where it combines with hydroxyl ion and forms water. The mechanism can be explained as follows:

Table 5 Some perovskite-based supercapacitor with their specific capcitances, energy and power densities, and life span

Material	Specific capacitance	Energy density	Power density	Cycle stability	References
$La_{0.7}Sr_{0.3}NiO_{3-\delta}$	719.5 F g^{-1} at 2 A g^{-1} 1 M Na_2SO_4 as electrolyte	81.4 W h kg^{-1}	500 W kg^{-1}	90% after 2000 cycles at 5 A g^{-1}	[71]
$Sr_{0.8}Ba_{0.2}MnO_3$	446.8 F g^{-1} at 0.5 A g^{-1} 0.5 M Na_2SO_4 as electrolyte	37.3 W h kg^{-1}	400 W kg^{-1}	87% after 5000 cycles at 10 A g^{-1}	[72]
$LaMnO_3$	609.8 F g^{-1} at 2 mV s^{-1} 1 M KOH as electrolyte	23.4 Wh kg^{-1}	4214 W kg^{-1}	–	[5]
$SrCo_{0.9}Nb_{0.1}O_{2.418}$	108.125 mA h g^{-1} (778.5 F g^{-1}) at 5 A g^{-1}	37.6 W h kg^{-1}	433.9 W kg^{-1}	95.7% after 3000 cycles at 5A g^{-1}	[73]
$SrCo_{0.9}Mo_{0.1}O_{2.5092}$	168.88 mA h g^{-1} at 1 A g^{-1} 6 M KOH as electrolyte	74.8 W h kg^{-1}	734.5 W kg^{-1}	97.6% after 10,000 cycles at 10 A g^{-1}	[75]
$La_{0.85}Sr_{0.15}MnO_{2.25}$	102 F g^{-1} at 1 A g^{-1} 1 M KOH as electrolyte	3.6 W h kg^{-1}	at 120 W kg^{-1}	about 50% after 3000 cycles at 2 A g^{-1}	[76]
$La_{0.8}Na_{0.2}Fe_{0.8}Mn_{0.2}O_3$	21.15 mA h g^{-1} (56.4 F g^{-1}) at 3 mV s^{-1} 1 M H_2SO_4 as electrolyte	1.8 W h kg^{-1}		–	[77]

(continued)

Table 5 (continued)

Material	Specific capacitance	Energy density	Power density	Cycle stability	References
Reduced $LaNiO_3$ powder	28.75 mA h g^{-1} (230 F g^{-1}) at 1 A g^{-1} 6 M KOH as electrolyte			3500 cycles at 5A g^{-1}	[78]
$LaMnO_3$	520 F g^{-1} at 1 A g^{-1} 0.5 M $N_{a2}SO_4$ as electrolyte	52.5 W h kg^{-1}	1000 W kg^{-1}	117% after 7500 cycles at 10 A g^{-1}	[79]
$LaNiO_3$	139.2 mAh g^{-1} at 1.0 A g^{-1} 6 M KOH	65.8 Wh kg^{-1}	1.8 kW kg^{-1}	92.4% after 10,000 cycles	[74]
Y_2NiMnO_6	77.76 F g^{-1} at 30 mA g^{-1}	0.89 W h kg^{-1}	19.27 W kg^{-1}	70.17% after 1800 cycles	[80]
$BiFeO_3$ nanowire/reduced graphene oxide	116.05 mA h g^{-1} (928.43 F g^{-1}) at 5 A g^{-1} 3 M KOH as electrolyte	18.62 W h kg^{-1}	950 W kg^{-1}	87.51% after 1000 cycles at 5 A g^{-1}	[81]
$La_{0.7}Sr_{0.3}CoO_{3-\delta}$/Ag composite	118.59 mA h g^{-1} (517.5 F g^{-1}) at 1 mA cm^{-2} 1 M KOH as electrolyte	21.9 mW h cm^{-3}	90.1 mW cm^{-3}	85.6% after 3000 cycles at 50 mA cm^{-2}	[82]

(continued)

Table 5 (continued)

Material	Specific capacitance	Energy density	Power density	Cycle stability	References
$La_{0.85}Sr_{0.15}MnO_3/NiCo_2O_4$ Core–shell architecture	260.75 mA h g^{-1} (1341 F g^{-1}) at 0.5 A g^{-1} 6 M KOH as electrolyte	63.5 W h kg^{-1}	900 W kg^{-1}	200% after 10,000 cycles at 20 A g^{-1}	[83]
$CaTiO_3$/active carbon	270 F g^{-1} at 1 A g^{-1} 6 M KOH as electrolyte	26.3 W h kg^{-1}	375 W kg^{-1}	Constant over 5000 cycles at 1 A g^{-1}	[84]
$LaMnO_3/Mn_3O_4$	540 F g^{-1} at 1 A g^{-1} 0.5 M $N_{a2}SO_4$ as electrolyte	75 W h kg^{-1}	1000 W kg^{-1}	No change up to 50,000 cycles	[85]
Porous $LaMnO_3$	58 F g^{-1} at 1 A g^{-1} 0.5 M $N_{a2}SO_4$ as electrolyte	43 W h kg^{-1}	770 W kg^{-1}	Stable for > 100,000 cycles	[86]

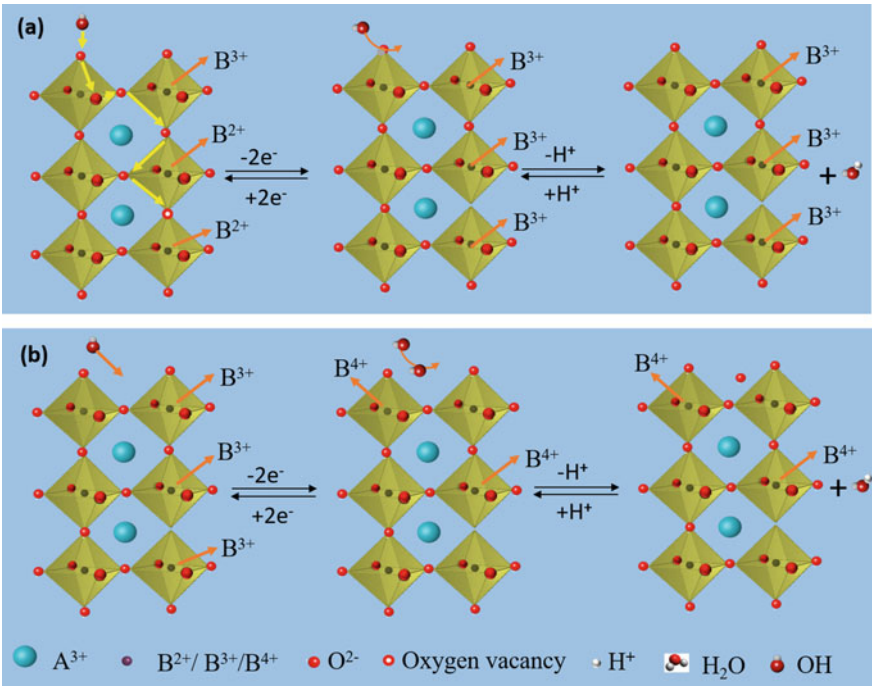

Fig. 7 Schematic illustration of oxygen ion intercalation in ABO_3-type perovskite oxides **a** with oxygen vacancy and **b** with oxygen excess material

(a) **For the material with oxygen vacancy ($ABO_{3-\delta}$)**

- The charge imbalance due to the presence of oxygen vacancy in the $ABO_{3-\delta}$ is neutralized by reduction of 2δ amount of B^{3+} cations to B^{2+} state.

$$A^{3+}B^{3+}O_3 \rightarrow A^{3+}[B^{2+}_{2\delta}B^{3+}_{(1-2\delta)}]O_{3-\delta}$$

- The oxygen ion from electrolyte OH^- will intercalate to the oxygen vacancy by leaving the proton (H^+) to the electrolyte, where it combines with another hydroxyl ion to form water and the filling of oxygen site oxidize B^{2+} to B^{3+}.

$$A^{3+}[B^{2+}_{2\delta}B^{3+}_{(1-2\delta)}]O_{3-\delta} + 2\delta OH^- \leftrightarrow A^{3+}B^{3+}O_3 + 2\delta e^- + \delta H_2O$$

The mechanism is schematically illustrated in Fig. 7a.

- Then, the diffusion of O^{2-} ion will take place along the octahedral edges and fill the vacancies with the oxidation of two B^{2+} to two B^{3+} per one oxygen ion.

(b) **For the material without any oxygen anion (ABO_3)**

- Here, the perovskite oxide is in perfect form ($A^{3+}B^{3+}O_3$).
- The excess oxygen is intercalated to the surface through diffusion of B cation to the surface and oxidizing two B^{3+} to two B^{4+} states per one oxygen ion intercalation.

$$A^{3+}B^{3+}O_3 + 2\delta OH^- \leftrightarrow A^{3+}[B^{4+}_{2\delta}B^{3+}_{(1-2\delta)}]O_{3+\delta} + 2\delta e^- + \delta H_2O$$

  The mechanism is schematically illustrated in Fig. 7b.
- Thus, the diffusion of OH^- is possible even into oxygen excess perovskite structure by oxidizing 2δ amount of B^{3+} cations to B^{4+} state for a δOH^- concentration.

5 Conclusions

The thermal and electrochemical stability, tunable functionality and cost-effective availability of perovskite oxides propelled the material to possess numerous applications. These include applications in all type of battery electrodes, especially of metal-air batteries, all components of SOFCs, solar cell, photoelectrochemical cell, and supercapacitor electrode applications. An array of cations can be placed in the A or B site of the ABO_3-type perovskite oxide with maintaining the tolerance factor, such that there is no hindrance to structural stability. Further, these cation arrays can also tune the catalytic activity and control oxygen ion mobility by electrical polarization, making it a potential candidate for various energy applications. Though there are many components of different energy devices, which have been fabricated using perovskite oxides, the direct applications to SOFC's components and supercapacitor electrodes are discussed and scientifically demonstrated in detail in this chapter. This chapter mainly focused on the material science view of applications rather than device engineering or technological developments. The tunable functionality of perovskite oxides by upholding the stability factor (tolerance factor) through proper cationic substitutions and oxygen vacancy creation and also its role in oxygen ion mediated ionic conductivity is further scientifically elucidated.

References

1. Richter, J., Holtappels, P., Graule, T., Nakamura, T., & Gauckler, L. J. (2009). *Monatshefte für Chemie-Chemical Monthly, 140,* 985.
2. Vyshatko, N., Kharton, V., Shaula, A., Naumovich, E., & Marques, F. (2003). *Materials Research Bulletin, 38,* 185.
3. Muller, O. (1974). The major ternary structural families.

4. Stevenson, J., Armstrong, T., Carneim, R., Pederson, L., & Weber, W. (1996). *Journal of the Electrochemical Society, 143,* 2722.
5. Mefford, J. T., Hardin, W. G., Dai, S., Johnston, K. P., & Stevenson, K. J. (2014). *Nature Materials, 13,* 726.
6. Gauckler, L. J., Beckel, D., Buergler, B. E., Jud, E., Muecke, U. P., Prestat, M., et al. (2004). *CHIMIA International Journal for Chemistry, 58,* 837.
7. Ullmann, H., Trofimenko, N., Tietz, F., Stöver, D., & Ahmad-Khanlou, A. (2000). *Solid State Ionics, 138,* 79.
8. Tietz, F., Raj, I. A., Zahid, M., & Stöver, D. (2006). *Solid State Ionics, 177,* 1753.
9. Yamamoto, O., Takeda, Y., Kanno, R., & Noda, M. (1987). *Solid State Ionics, 22,* 241.
10. Kharton, V., Viskup, A., Marozau, I., & Naumovich, E. (2003). *Materials Letters, 57,* 3017.
11. Tai, L.-W., Nasrallah, M., Anderson, H., Sparlin, D., & Sehlin, S. (1995). *Solid State Ionics, 76,* 259.
12. Sun, C., Hui, R., & Roller, J. (2010). *Journal of Solid State Electrochemistry, 14,* 1125.
13. Jun, A., Yoo, S., Gwon, O.-H., Shin, J., & Kim, G. (2013). *Electrochimica Acta, 89,* 372.
14. Wei, B., Lü, Z., Huang, X., Miao, J., Sha, X., Xin, X., et al. (2006). *Journal of the European Ceramic Society, 26,* 2827.
15. Teraoka, Y., Zhang, H., Okamoto, K., & Yamazoe, N. (1988). *Materials Research Bulletin, 23,* 51.
16. Rehman, S. U., Song, R.-H., Lim, T.-H., Park, S.-J., Hong, J.-E., Lee, J.-W., et al. (2018). *Journal of Materials Chemistry A, 6,* 6987.
17. Setoguchi, T., Okamoto, K., Eguchi, K., & Arai, H. (1992). *Journal of the Electrochemical Society, 139,* 2875.
18. Da Silva, F. S., & de Souza, T. M. (2017). *International Journal Of Hydrogen Energy, 42*, 26020.
19. Ding, H., Tao, Z., Liu, S., & Yang, Y. (2016). *Journal of Power Sources, 327,* 573.
20. Feng, J., Qiao, J., Sun, W., Yang, P., Li, H., Wang, Z., & Sun, K. (2015). *International Journal Of Hydrogen Energy, 40*, 12784.
21. Neagu, D., & Irvine, J. T. (2010). *Chemistry of Materials, 22,* 5042.
22. Ge, X. M., Chan, S. H., Liu, Q. L., & Sun, Q. (2012). *Advanced Energy Materials, 2,* 1156.
23. Simner, S., Hardy, J., Stevenson, J., & Armstrong, T. (2000). *Solid State Ionics, 128,* 53.
24. Metcalfe, I. S., & Baker, R. T. (1996). *Catalysis Today, 27,* 285.
25. Baker, R., Metcalfe, I., Middleton, P., & Steele, B. (1994). *Solid State Ionics, 72,* 328.
26. Primdahl, S., Hansen, J., Grahl-Madsen, L., & Larsen, P. (2001). *Journal of the Electrochemical Society, 148,* A74.
27. Vernoux, P., Guillodo, M., Fouletier, J., & Hammou, A. (2000). *Solid State Ionics, 135,* 425.
28. Sfeir, J., Buffat, P. A., Möckli, P., Xanthopoulos, N., Vasquez, R., Mathieu, H. J., et al. (2001). *Journal of Catalysis, 202,* 229.
29. Jeong, J., Azad, A. K., Schlegl, H., Kim, B., Baek, S.-W., Kim, K., et al. (2015). *Journal of Solid State Chemistry, 226,* 154.
30. Abdalla, A. M., Kamel, M., Hossain, S., Irvine, J. T., & Azad, A. K. (2019). *International Journal of Applied Ceramic Technology.*
31. Liu, L., Ong, K. P., Wu, P., Li, J., & Pu, J. (2008). *Journal of Power Sources, 176,* 82.
32. Tao, S., & Irvine, J. T. (2003). *Nature Materials, 2,* 320.
33. Wu, X., Zhou, X., Tian, Y., Kong, X., Zhang, J., Zuo, W., et al. (2016). *Electrochimica Acta, 208,* 164.
34. Liu, Y., Wang, S., Qian, J., Xin, X., Zhan, Z., & Wen, T. (2013). *International Journal of Hydrogen Energy, 38,* 14053.
35. Cowin, P. I., Lan, R., Petit, C. T., & Tao, S. (2015). *Solid State Sciences, 46,* 62.
36. Choi, H., Fuller, A., Dogu, D., Binkley, K. E., Davis, J., & Ozkan, U. S. (2015). *Topics in Catalysis, 58,* 359.
37. Du, Z., Zhao, H., Zhou, X., Xie, Z., & Zhang, C. (2013). *International Journal of Hydrogen Energy, 38,* 1068.
38. Hui, S., & Petric, A. (2001). *Solid State Ionics, 143,* 275.

39. Petit, C. T., Lan, R., Cowin, P. I., Kraft, A., & Tao, S. (2011). *Journal of Materials Science, 46,* 316.
40. Ammal, S. C., & Heyden, A. (2015). *Journal of Materials Chemistry A, 3,* 21618.
41. Yang, X., Chen, J., Panthi, D., Niu, B., Lei, L., Yuan, Z., et al. (2019). *Journal of Materials Chemistry A, 7,* 733.
42. Feng, J., Yang, G., Dai, N., Wang, Z., Sun, W., Rooney, D., et al. (2014). *Journal of Materials Chemistry A, 2,* 17628.
43. Sengodan, S., Choi, S., Jun, A., Shin, T. H., Ju, Y.-W., Jeong, H. Y., et al. (2015). *Nature Materials, 14,* 205.
44. Ding, H., Tao, Z., Liu, S., & Zhang, J. (2015). *Scientific Reports, 5,* 1.
45. Zhao, L., Chen, K., Liu, Y., & He, B. (2017). *Journal of Power Sources, 342,* 313.
46. Shu, L., Sunarso, J., Hashim, S. S., Mao, J., Zhou, W., & Liang, F. (2019). *International Journal of Hydrogen Energy.*
47. Liu, Q., Dong, X., Xiao, G., Zhao, F., & Chen, F. (2010). *Advanced Materials, 22,* 5478.
48. Huang, Y.-H., Dass, R. I., Xing, Z.-L., & Goodenough, J. B. (2006). *Science, 312,* 254.
49. Kharton, V., Marques, F., & Atkinson, A. (2004). *Solid State Ionics, 174,* 135.
50. Ormerod, R. M. (2003). *Chemical Society Reviews, 32,* 17.
51. Steele, B. C., & Heinzel, A. (2011). *Materials for sustainable energy: A collection of peer-reviewed research and review articles from Nature Publishing Group* (p. 224). World Scientific.
52. Brandon, N. P., Skinner, S., & Steele, B. C. (2003). *Annual Review of Materials Research, 33,* 183.
53. Weitkamp, J., & Wiemhöfer, H.-D. (2002). *Solid State Ionics, 154,* 597.
54. Hayashi, H., Inaba, H., Matsuyama, M., Lan, N., Dokiya, M., & Tagawa, H. (1999). *Solid State Ionics, 122,* 1.
55. Takahashi, T., & Iwahara, H. (1971). *Energy Conversion, 11,* 105.
56. Ishihara, T., Matsuda, H., & Takita, Y. (1994). *Journal of the American Chemical Society, 116,* 3801.
57. Fujii, H., Katayama, Y., Shimura, T., & Iwahara, H. (1998). *Journal of Electroceramics, 2,* 119.
58. Nomura, K., & Tanase, S. (1997). *Solid State Ionics, 98,* 229.
59. Lybye, D., Poulsen, F. W., & Mogensen, M. (2000). *Solid State Ionics, 128,* 91.
60. Nguyen, T. L., & Dokiya, M. (2000). *Solid State Ionics, 132,* 217.
61. Iwahara, H., Esaka, T., Uchida, H., & Maeda, N. (1981). *Solid State Ionics, 3,* 359.
62. Iwahara, H., Uchida, H., Ono, K., & Ogaki, K. (1988). *Journal of the Electrochemical Society, 135,* 529.
63. Turnbull, D. (1956). *Solid state physics*; *Vol. 3* (p. 225). Elsevier.
64. Hung, I.-M., Peng, H.-W., Zheng, S.-L., Lin, C.-P., & Wu, J.-S. (2009). *Journal of Power Sources, 193,* 155.
65. Sun, W., Yan, L., Shi, Z., Zhu, Z., & Liu, W. (2010). *Journal of Power Sources, 195,* 4727.
66. Fabbri, E., Bi, L., Tanaka, H., Pergolesi, D., & Traversa, E. (2011). *Advanced Functional Materials, 21,* 158.
67. Xie, K., Yan, R., Chen, X., Dong, D., Wang, S., Liu, X., et al. (2009). *Journal of Alloys and Compounds, 472,* 551.
68. Li, Z., Liu, R., Wang, J., Xu, Z., Xie, Y., & Wang, B. (2007). *Science and Technology of Advanced Materials, 8,* 566.
69. Magrasó, A., Fontaine, M. L., Larring, Y., Bredesen, R., Syvertsen, G., Lein, H., et al. (2011). *Fuel Cells, 11,* 17.
70. Hahn, B. P., Long, J. W., & Rolison, D. R. (2013). *Accounts of Chemical Research, 46,* 1181.
71. Cao, Y., Lin, B., Sun, Y., Yang, H., & Zhang, X. (2015). *Electrochimica Acta, 174,* 41.
72. George, G., Jackson, S. L., Luo, C. Q., Fang, D., Luo, D., Hu, D., et al. (2018). *Ceramics International, 44,* 21982.
73. Zhu, L., Liu, Y., Su, C., Zhou, W., Liu, M., & Shao, Z. (2016). *Angewandte Chemie, 128,* 9728.
74. Li, Z., Zhang, W., Wang, H., & Yang, B. (2017). *Electrochimica Acta, 258,* 561.
75. Tomar, A. K., Singh, G., & Sharma, R. K. (2018). *Chemsuschem, 11,* 4123.
76. Lang, X., Mo, H., Hu, X., & Tian, H. (2017). *Dalton Transactions, 46,* 13720.

77. Rai, A., & Thakur, A. K. (2017). *Ionics, 23,* 2863.
78. Ho, K. H., & Wang, J. (2017). *Journal of the American Ceramic Society, 100,* 4629.
79. Shafi, P. M., Joseph, N., Thirumurugan, A., & Bose, A. C. (2018). *Chemical Engineering Journal, 338,* 147.
80. Alam, M., Karmakar, K., Pal, M., & Mandal, K. (2016). *RSC Advances, 6,* 114722.
81. Moitra, D., Anand, C., Ghosh, B. K., Chandel, M., & Ghosh, N. N. (2018). *ACS Applied Energy Materials, 1,* 464.
82. Liu, P., Liu, J., Cheng, S., Cai, W., Yu, F., Zhang, Y., et al. (2017). *Chemical Engineering Journal, 328,* 1.
83. Lang, X., Zhang, H., Xue, X., Li, C., Sun, X., Liu, Z., et al. (2018). *Journal of Power Sources, 402,* 213.
84. Cao, X.-L., Ren, T.-Z., Yuan, Z.-Y., & Bandosz, T. J. (2018). *Electrochimica Acta, 268,* 73.
85. Shafi, P. M., Nisar, N., & Bose, A. C. (2018). *ChemistrySelect, 3*(23), 6459.
86. Shafi, P. M., Bose, A. C., & Vinu, A. (2018). *ChemElectroChem, 5*(23), 3723.

Phase Change Materials

Rabab Jarrar

Abstract The world's rapid increase of energy consumption and demand with the environmental bad effects of fossil and traditional fuels prompted scientists and researchers to search for methods of storing and reducing energy consumption. Phase change materials (PCMs) are substances that have the ability to store and release energy at constant temperature during their change of state and have been widely investigated and used as thermal energy storage TES and thermal regulator. This chapter discusses the main types of PCMs with their advantages and disadvantages, some of the efforts and methods used by scientists to overcome these disadvantages during the last three decades and to improve their performance and demonstrate their most common thermal applications.

Keywords Phase change material · Latent heat · Thermal conductivity · Thermal energy storage (TES) · Supercooling

List of Abbreviations

bcm	Billion cubic meters
CNTs	Carbon nanotubes
CSP	Concentrating solar power systems
DSC	Differential scanning calorimetry
DTA	Differential thermal analysis
EG	Expanded graphite
GO	Grapheme oxide
GR	Grapheme
HDPE	High density polyethyelene
IEA	International Energy Agency
LDPE	Low density polyethyelene

R. Jarrar (✉)
Palestine Technical University—Kadoorie, Tulkarm, Palestine
e-mail: r.jarrar@ptuk.edu.ps

S. J. Ikhmayies (ed.), *Advances in Energy Materials*,
Advances in Material Research and Technology,
https://doi.org/10.1007/978-3-030-50108-2_9

LHS	Latent heat storage
NG	Nanographite
PCMs	Phase change materials
PEG	Polyethylene glycol
PMMA	Polymethyl methacrylate
SEM	Scanning electron microscopy
SHS	Sensible heat storage
TES	Thermal energy storage
TWh	Tera Watt -hour

1 Introduction

The intensive and exaggerated use of traditional energy, which depends on fossil fuels as petroleum, its derivatives, coal and natural gas, causes extremely serious problems to human beings as environmental pollution, global warming and acid rain. In addition, these resources will vanish sooner or later. These facts led to the search for sources of clean and renewable energy and methods of decreasing energy consumption which achieve sustainable development and does not adversely affect human health and the environment [1].

Figure 1 from International Energy Agency (IEA) shows the increase in word natural gas production in the period of 1971–2018 as a traditional source of energy, and at the same time Fig. 2 illustrates the increase of wind and photovoltaic electricity production as a renewable energy sources from 2005 to 2018, while Fig. 3 shows the percentage participation of types of traditional and renewable energy sources in electricity generation for two years 1973 and 2017.

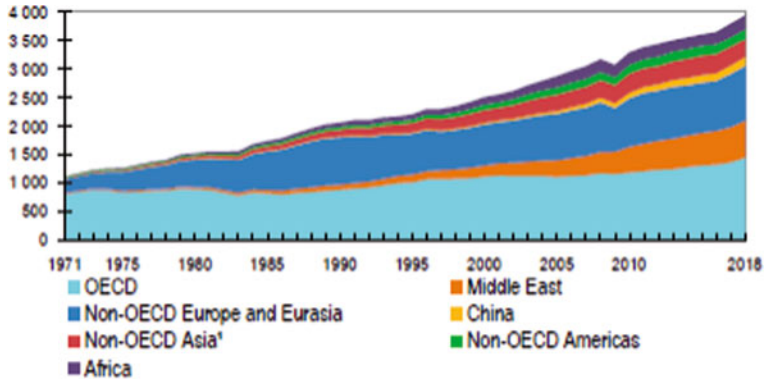

Fig. 1 World natural gas production from 1971 to 2016 by region (billion cubic meters, bcm.). *Source* IEA (2018) World Energy Outlook. All rights reserved [2]

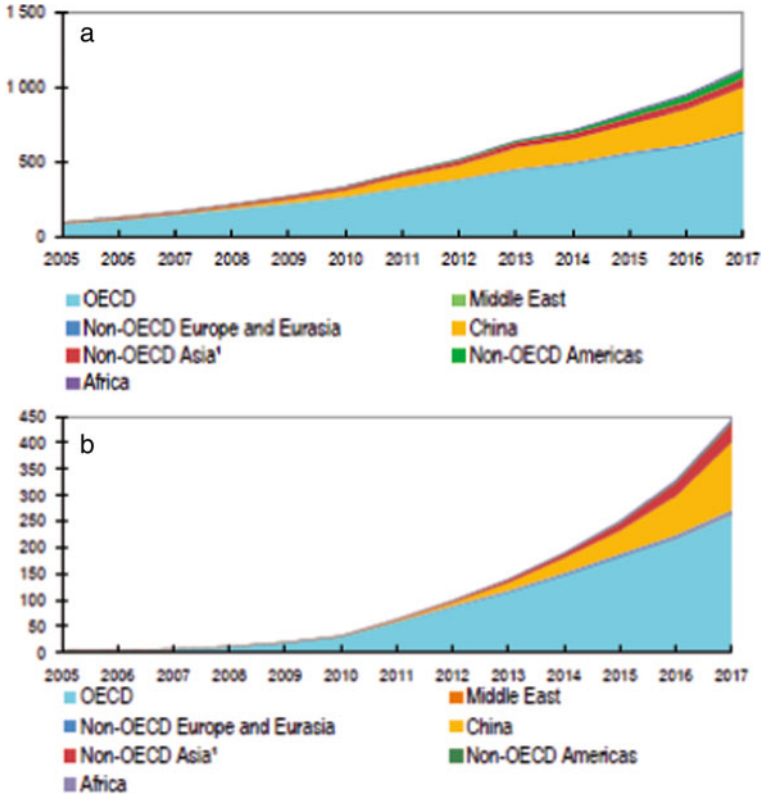

Fig. 2 World electricity production from 2005 to 2017 by region (TWh): **a** by wind and **b** by solar photovoltaic PV. *Source* IEA (2018) World Energy Outlook. All rights reserved [2]

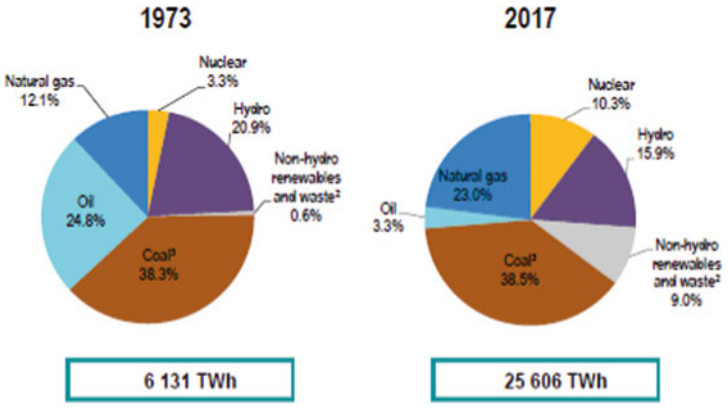

Fig. 3 Source shares of electricity generation in (TWh) at the two years 1973 and 2017. *Source* IEA (2018) World Energy Outlook. All rights reserved [2]

These figures and curves which are based on real data emphasize two facts: The first one is the increase in the world consumption and demand of energy with time, and the second fact is the attitude and continuous search for alternative and clean energy sources which is obvious from the increase of the percentage participation of renewable energy sources in the year 2017 compared with 1973.

Energy storage helps to optimize the use of energy and preserve it from being lost, to be used when needed. Phase change materials (PCMs) are one of the most important methods of thermal energy storage (TES), and the last three decades have shown huge research activity in this field to study, discover and improve the properties of different types of PCMs that can be used in many thermal applications.

2 Phase Change Material Definition

When heat is added to a solid material below its melting point, the temperature starts to increase until the melting point is reached and then the temperature will remain constant until all the solid material is melted. When more heat is added, an increase in liquid temperature will occur until reaching the boiling point and again the temperature will not increase by adding heat until all the material evaporates; then, the temperature will continue in increasing as more heat is added [3]. This behavior is illustrated in the heating curve of a typical substance as shown in Fig. 4.

The added heat in these portions of constant temperature is used to increase the potential energy of the atoms or molecules of the material by increasing the separation distance between them, so in both melting and evaporation, the distance between molecules or atoms is changing to reduce the attractive forces and affect the potential energy. This amount of heat absorbed at constant temperature by a material during melting and boiling is called latent heat of fusion and latent heat of vaporization, and the same amount of heat is released by cooling; the cooling curve is the opposite of heating curve shown in Fig. 4.

The process of melting and the process of evaporation are called changes of state or phase changes of a material, and in general changes of phase or state are:

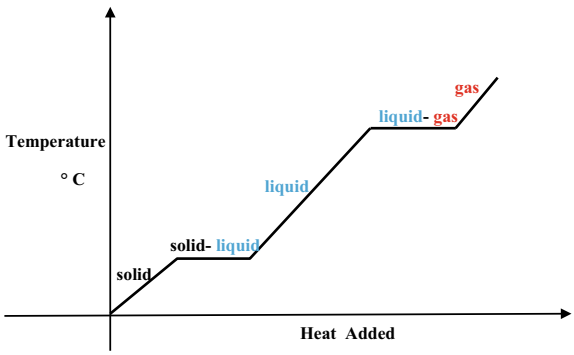

Fig. 4 Heating curve of a typical substance

- From solid to liquid and from liquid to solid (solid ↔ liquid)
- From liquid to gaseous state and vice versa (liquid↔ gas)
- From solid to gaseous state directly by a process called sublimation and from gaseous state to solid by a process called deposition (solid ↔ gas)

Another type of phase change or state change may happen in some solid materials when heat is used to change the crystal structure of the solid material from one crystal structure to another (solid ↔ solid).

All these changes of state involve absorbing or releasing energy, and this is the scientific principle or idea of phase change material.

So **phase change materials (PCMs)** are substances that absorb or release large amounts of latent heat when they go through a change in their state or phase at nearly constant temperature and are considered as thermal energy storage (TES) [4, 5].

To explain more heat is absorbed when the material changes from solid to liquid as an example without raising temperature, and the same amount of heat is released when solidified. This regulates and reduces changes in temperature in the environment surrounding the phase change material [6].

TES is classified into two main types [7]:

- The first one is latent heat storage (LHS) or phase change materials
- The second type is sensible heat storage (SHS).

The two types are well described by Fig. 4. Latent heat is represented by the horizontal portions and given by the equation:

$$Q = m \times L$$

where

Q is the amount of heat
m is the mass of the material
L is the latent heat of fusion or evaporation in units of energy per unit mass.

Sensible heat is represented by the linear non-constant portions in which energy stored in the material depends on the temperature difference, mass and specific heat capacity of the material and given by the equation

$$Q = m\, c\, \Delta T$$

where

c: is the specific heat of the material in units of energy per unit mass per unit temperature
ΔT: is change in temperature.

Latent heat energy storage is considered more efficient than sensible heat storage as the second type needs more amount of material to store the same amount of energy.

The most commercial applicable PCMs are those involving solid–liquid transitions as liquid ↔ gas, and solid ↔ gas transitions need larger volume for containers due to big volume changes upon transition of state; solid ↔ solid transitions have got attention by researchers [8], but in general the heat exchange in this transition is smaller than that in solid–liquid transition.

3 Properties of Ideal Phase Change Materials (PCMs)

PCMs used in thermal applications should have specified properties to make them suitable for these applications. These properties are classified as thermal or physical, kinetic, chemical and economical properties [9, 10].

3.1 Thermal—Physical Properties

- Melting temperature fits or matches the operating temperature range of the application. So if PCMs are used in building applications, we choose PCMs of melting temperature range (20–32 °C) and according to the geographic region of use.
- High latent heat (ΔH) of fusion so as to obtain large quantities of heat with reasonable volume of PCMs containers.
- Small volume change upon phase transformation (solid ↔ liquid) and small vapor pressure at operating temperature to reduce the containment problem.
- Thermal stability after many cycles of heating and cooling of the PCM with no significant changes in melting temperature and latent heat.
- High thermal conductivity of both solid and liquid phases to assist the charging and discharging energy of the storage system, and this point is one of the challenges in this field as nearly most PCMs have low thermal conductivity nearly in the range of (0.13–0.33 W/m K) for organic PCMs and (0.5–0.9 W/m K) for inorganic ones as reported by Nazir et al. [8] in his review depending on many articles [11–17], and as a result intensive research efforts and developments are being conducted to improve thermal conductivity of PCMs.

3.2 Kinetic Properties

- No or very little supercooling, where supercooling is the presence of a material in liquid state in spite of having a temperature below its freezing point [5, 18], is expressed by degree of supercooling which is the difference between the melting and freezing temperature.
- High rate of crystal growth and reproducible crystallization.

3.3 Chemical Properties

- Non-degradable or chemical stability after many cycles of heating and cooling.
- Non-corrosiveness.
- Safety issues as non-toxic, non-flammable and non-explosive.

3.4 Economical Properties

- Low cost in production and abundant.

4 Types of PCMs

Phase change materials are classified according to their chemical nature into two main groups: organic PCMs and inorganic ones, a third and not a main group is eutectic which is a homogenous mixture of two (binary), three (ternary) or more from the two main groups. Figure 5 is a schematic representation of groups and types of PCMs [7, 8, 19].

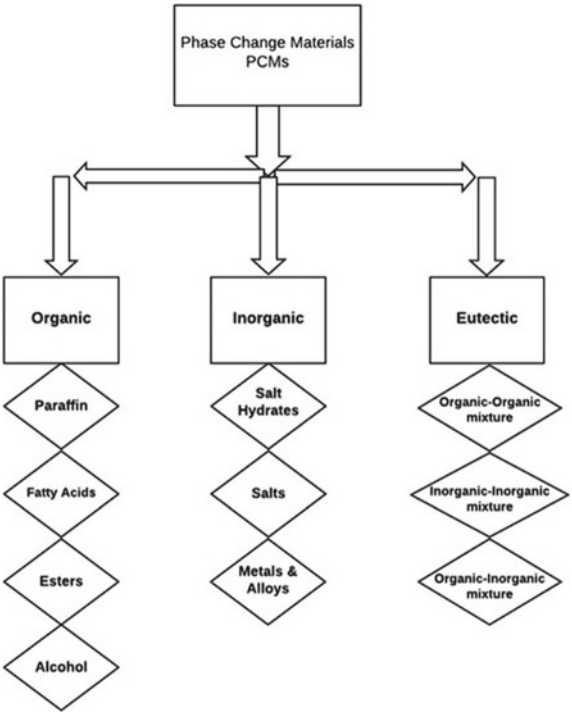

Fig. 5 Schematic representation of PCM types

Each type of PCMs has its own properties with advantages and disadvantages; none of them has all the physical, chemical and kinetic properties of an ideal PCM mentioned before, and as a result, researchers are in continuous search to develop and enhance the desired properties to fit different thermal applications. Table1 summarizes properties, advantages and disadvantages of selected types from different groups with some examples on each type [7, 8, 10, 13, 19–21].

Commercial paraffin waxes are less expensive than pure paraffins with moderate latent heat, and they are obtained as by-products from the process of refining oil and consisting of straight hydrocarbon chains with carbon atoms greater than 15 and contain also volatile compounds as toluene, ketone, formaldehyde which may cause cancer so care must be taken when they are used in thermal applications. Their melting temperatures are within the range of 5–67 °C, and they are widely used because of their low cost and availability [7, 22].

The most important disadvantages of organic PCMs are their low thermal conductivity and their cost while for inorganic ones as salt hydrates are their thermal instability and supercooling taking into consideration that both groups suffer from their low thermal conductivity except metals and metal alloys.

Metals and metal alloys with low melting temperatures are promising type of PCMs due to their desirable properties mentioned in Table 1 [10].

Eutectic mixtures are widely investigated by researchers and scientists; these include eutectic mixtures of organic materials alone [23–27], inorganic mixtures [28] and organic–inorganic eutectic mixtures [29]. A decrease in melting temperature of binary and ternary mixtures is usually observed in comparison with single components of the mixture.

Mixing different types of PCMs will produce a new material with modified melting temperature and smaller in most cases than the single types, and this will provide a melting temperature that may match with specific thermal application. The mixing process also may improve or solve some of the problems or limitations in some types of PCMs [28]. Mixing $Na_2HPO_4.12H_2O$ salt hydrate with $Na_2CO_3 \cdot 10H_2O$ [30] produces novel thermal stable eutectic mixture of salt hydrates with decrease in phase separation and a decrease in both supercooling and melting temperature in comparison with mentioned single salt hydrates.

Nazir et al. [8] in their review of energy storage applications gathered information and data from many research articles about melting temperatures of organic [11–13, 31], inorganic [12, 13, 15–17, 31, 32] and eutectic PCMs [11, 13–17, 32, 33] and represented them in histograms shown in Figs. 6, 7, 8. Figures 6a–c are for organic compounds including paraffin, polymers, fatty acids, sugar alcohols and others, while Figs. 7a–c are for inorganic compounds as salt hydrates, salts and metals with melting temperatures up to 1000 °C for some salts and Fig. 8 for eutectic PCMs.

Table 1 Properties, advantages/disadvantages and examples of selected types from different groups of PCMs [7, 8, 10, 13, 19–21]

	Properties	Advantages	Disadvantages	Examples
Paraffin	– Linear alkanes of 8–40 carbon atoms of chemical formula C_nH_{2n+2} – May have solid/solid transition between different crystalline structures - Density around 900 kg/m^3 – Obtained from petroleum	– Stable – Non-corrosive – Congruent melting – No or very small supercooling	– Low thermal conductivity around 0.2 W/m K – High cost – Flammable	Octadecane $C_{18}H_{38}$ Eicosane $C_{20}H_{42}$
Fatty Acids	– Derived from vegetable oils – Have chemical formula $CH_3(CH_2)_nCOOH$ – Melting temperatures between 30–65 °C – Latent heat nearly in the range of (130–225 J/g)	– Non-toxic – No supercooling – Stable and good behavior of melting and solidification	– Moderately corrosive – Expensive with higher cost than paraffin – Large change in volume upon melting	Lauric acid Capric acid Palmitic acid Myristic acid

(continued)

Table 1 (continued)

	Properties	Advantages	Disadvantages	Examples
Salt Hydrates	– Chemical formula M.nH_2O where M is a metal salt – Latent heat nearly in the range of (150–250 J/g) - Wide range of melting temperatures (5 – 130 °C) – Density 1500–2000 kg/m^3	– Cheap and abundance -Non-flammable – High energy density (high latent heat/unit mass) – Non-toxic – Small change in volume upon melting	– Corrosive – Low thermal conductivity but higher than Paraffin and fatty acids – Unstable after cycles of melting and solidification with phase segregation and incongruent melting. – They lose some water during heating cycles and degrade. – Supercooling	$KF \cdot 4H_2O$ $CaCl_2 \cdot 6H_2O$ $MgCl_2 \cdot 6H_2O$ $Na_2SO_4 \cdot 10H_2O$ $Na_2CO_3 \cdot 10H_2O$ $Na_2HPO_4 \cdot 12H_2O$
Metals and metal alloys	– Some metals have low melting temperature as Gallium Tm = 29.76 °C – High density	– High thermal conductivity – High thermal reliability – Low vapor pressure – Small volume changes upon phase transition – High boiling points – Thermal stability After millions of cycles of melting and solidification	– Cost – Some metals in liquid state as gallium is corrosive to some containers as aluminum containers	Al, Mg, Zn, Ga $Bi_{44.7}Pb_{22.6}In_{19} \cdot {}_1Sn_{8.3}Cd_{5.3}$
Salts	– Have high melting temperatures up to 1000 °C – Used for high temperature thermal energy storage applications	– Low cost – High latent heat	– Low thermal conductivity – Thermal instability – High corrosive to containers	Na_2CO_3

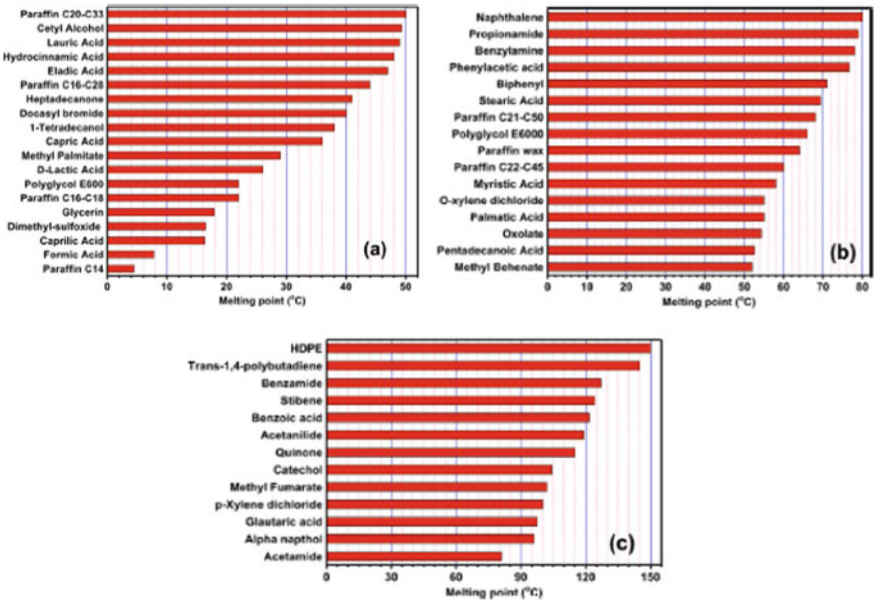

Fig. 6 Melting temperatures T_m of some organic PCMs: **a** $T_m < 50$ °C, **b** 50 °C $< T_m <$ 80 °C, **c** $T_m > 80$ °C. Reprinted from International Journal of Heat and Mass Transfer 129, Nazir et al. [8]: Recent developments in phase change materials for energy storage applications: A review, 497, 2019, with permission from Elsevier

5 Applications of PCMs

This section demonstrates some of the most common applications of phase change materials PCMs.

5.1 PCMs in Buildings

Phase change materials as a thermal storage in buildings are the most commonly used application. PCMs with melting temperature in the range of 20-32 °C are widely used in both passive (self-absorbing, storing and releasing heat) and active (depends on pumps and fans in heat transfer) heating and cooling in buildings. PCMs may be incorporated in building walls, floors, ceilings and may be used as a heat and cold storage units [9].

The presence of PCMs in building walls or any building component participate in reducing sharp changes of indoor temperatures which in turn will reduce energy consumption in heating and cooling. The incorporation of PCMs in buildings decreases the temperature peaks by 3–5 °C inside the building, and this will decrease energy consumption by air conditioning systems up to nearly 30% [34].

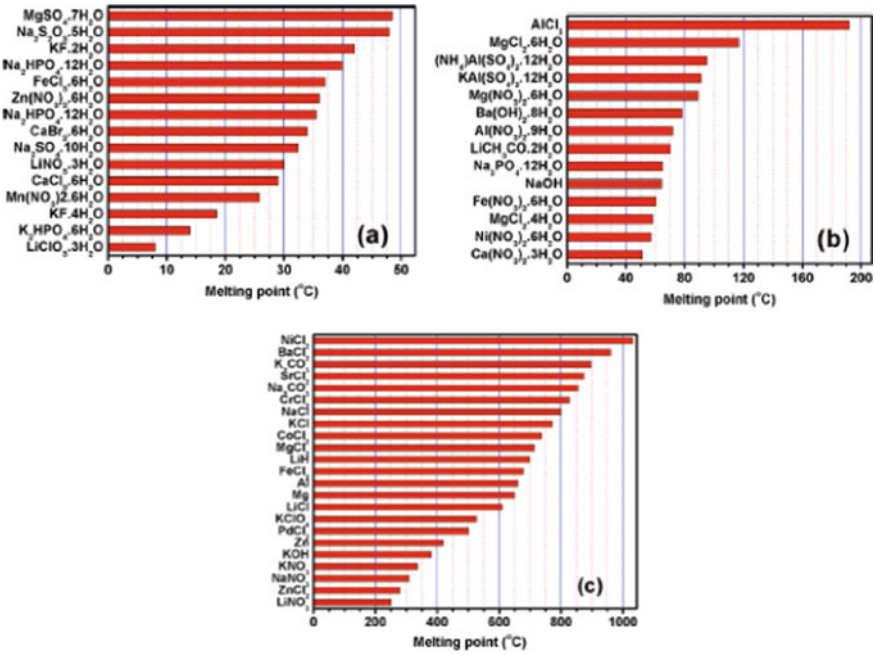

Fig. 7 Melting temperatures T_m of some inorganic PCMs: **a** $T_m < 50$ °C, **b** 50 °C < T_m < 220 °C, **c** $T_m > 220$ °C. Reprinted from International Journal of Heat and Mass Transfer 129, Nazir et al. [8]: Recent developments in phase change materials for energy storage applications: A review, 498, 2019, with permission from Elsevier

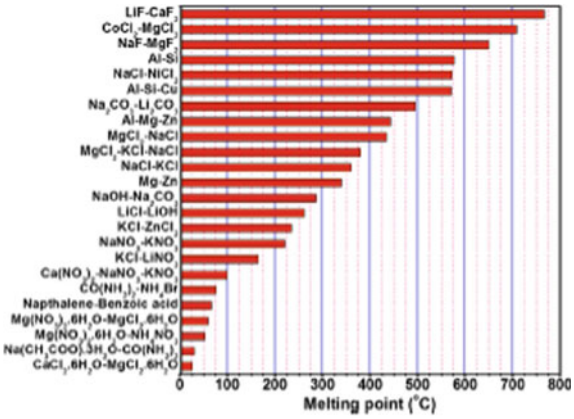

Fig. 8 Melting temperatures T_m of some eutectic PCMs. Reprinted from International Journal of Heat and Mass Transfer 129, Nazir et al. [8]: Recent developments in phase change materials for energy storage applications: A review, 497, 2019, with permission from Elsevier

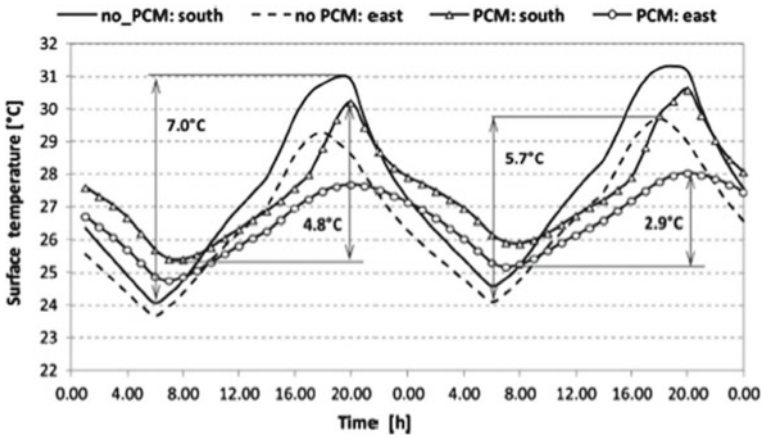

Fig. 9 Effect of incorporation of PCM on south and east surface wall temperature. Reprinted from Build Environ 59, G. Evola et al. [36]: A methodology for investigating the effectiveness of PCM wallboards for summer thermal comfort in buildings. p. 523, with permission from Elsevier

PCMs may be directly mixed with construction materials as concrete and gypsum or immersed in brick blocks by capillary phenomenon, but these methods suffer some drawbacks as the leakage problem and bad effects as corrosion on the construction materials so macro- or and microencapsulation may be used to prevent leakage and corrosion, and this is a process which will be explained later in Sect.6 [35]. Another method used to avoid leakage is by the aid of a supporting material in a process known as shape stabilization and will be explained later also in Sect. 6.

Organic PCMs as paraffins, fatty acids and inorganic ones as salt hydrates are widely and commercially used in building applications.

Figure 9 illustrates and represents the effect obtained numerically [36] of inserting PCM wall board on the inner surface of the building walls; the peak surface temperature of south wall was reduced by1 °C, and the fluctuation of the temperature was reduced from 7 °C to 4.8 °C for the south wall and reduced from 5.7 °C to 2.9 °C for the east wall.

5.2 PCMs in Textiles

When PCMs are incorporated in textiles, they will provide comfort to human body by absorbing excess heat from body and storing this heat as latent heat that will return back to the body and environment when the temperature decreases and the PCMs solidify. The change of state from solid to liquid and vice versa is nearly the most common change of state used in textiles as this type of change occurs with small volume change and vapor pressure. PCMs may be incorporated as microcapsules in the synthetic fibers, or these microcapsules will be embedded in a coating compound

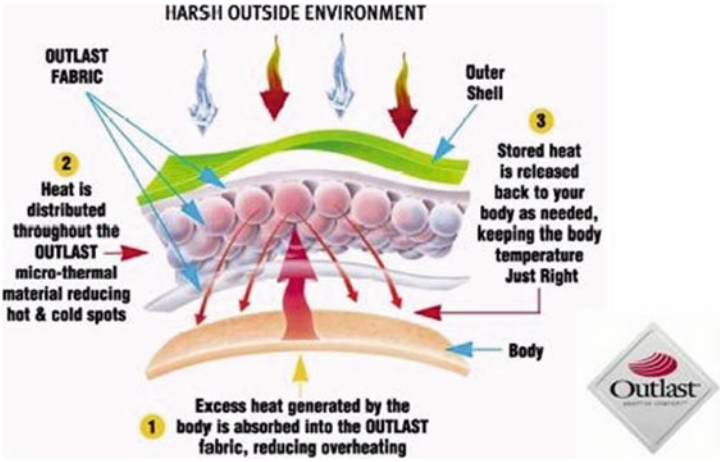

Fig. 10 PCM microcapsules in smart textile [Outlast Technologies Company] [38]

to coat the textiles or included in the structure of a foam which will be added to the textile in lamination process, and hollow fibers may be used also and filled with these microcapsules [37]. These capsules must have properties that suit and fit this application as resistant to heat, chemicals and mechanical failure. Methods of encapsulation of PCMs will be discussed later in this chapter. Figure 10 from Outlast Technologies Company [38] illustrates the shape and working principle of these capsules.

In addition of absorbing excess heat from body, these microcapsules will achieve thermal insulation by building thermal barrier which will reduce heat transfer from body to environment, as a result choosing PCMs with melting temperatures ranges near body temperature will provide the thermal protection and maintain a constant temperature at a comfortable level. The first incorporation of PCMs in textiles was in suits for astronauts to protect them from temperature fluctuations in space and then expands to sports clothing as athletes are exposed to generate lot amount of heat during exercising and playing and need to get rid of this excess heat to feel comfort. Nowadays, PCMs are being incorporated in jackets, sleeping bags, curtains, shoes skiwear and others [38].

5.3 PCMs in Rechargeable Batteries

Phase change materials are used for cooling of rechargeable batteries as lithium-ion batteries. Their low cost and high energy densities make these batteries widely used in cell phones, laptops and electric vehicles. But the generation of excess heat during discharging is one of challenges that need to be treated to prevent them from aging [39].

PCMs with suitable selected melting temperature in contact of the battery pack will absorb the excess heat during discharging as latent heat of fusion at constant temperature which controls the temperature of the battery.

As an example, Nasehi et al. [40] located three PCM shells with different thermal properties (capric acid, eicosane and sodium sulfate decahydrate) around a battery pack with different arrangements to choose the best arrangement leading to the lowest battery temperature during discharge. They concluded that the best arrangement was by locating the PCM with highest thermal conductivity closer to the battery and the lowest in thermal conductivity as the outer shell by this arrangement they obtained the smallest battery maximum temperature after 7200 s heat discharge.

5.4 PCMs in Photovoltaic PV Solar Modules

Another interesting application of PCMs is reported by Nazir et al. [8] in his review in which phase change materials are integrated in PV modules to control and limit the increase in the temperature of PV module which in turn lead to an improvement in efficiency of the system [41, 42], and the heat removed from the PV module may be used for water heating [43].

5.5 PCMs in Concentrating Solar Power Systems (CSP)

Concentrating solar power systems (CSP) concentrate sunlight using mirrors to a small area to be used later after being converted to heat [44]. Thermal energy storage of both types of latent heat and sensible heat can be used to store this heat energy and shift its use to a later time of no solar radiation. PCMs absorb the concentrated heat and store it as latent heat of fusion or evaporation during their phase transition, and these amounts of heat can be obtained later or released during the reverse phase transition.

Due et al. [1] in his review, related to the applications of phase change materials, classified these applications according to the melting temperature ranges of PCMs to four categories:

1. Low-temperature range applications [−20–5 °C]
2. Medium-low-temperature range applications [5–40 °C]
3. Medium-temperature range applications [40–80 °C]
4. High-temperature range applications [80–200 °C]

Incorporation of PCMs on the condenser and evaporator sides of refrigerators is one of the applications in low temperature range which improves the removal and heat transfer and enhances the coefficient of performance of the refrigerator by nearly 15% leading to a decrease in electrical energy consumption [45, 46].

Another application in this range is related to storing and transporting of food and medicine products by refrigerated trucks to protect these sensitive products from damage due to heat. The incorporation of paraffin as a PCM in the insulating walls of a refrigerated truck reduced the heat flow by 16.3% per day as reported by Ahmad et al. [47]. Paraffin, salt hydrates and eutectic mixtures of both types are used in these applications [48, 49].

Building and textiles mentioned before are commonly used applications in the range (5–40 °C), while cooling electrical devices is one of the applications in medium range (40–80 °C). Electricity generation by solar energy is an example of the high range of melting temperature greater than 80 °C. Sugar alcohol, salt hydrates, binary and ternary mixtures of salts of alkali and alkaline nitrate metals are used as storage unit for generating steam [50] in electricity generation at concentrating solar plants CSP.

Metallic alloys of high melting temperature ranges are also used in concentrating solar power plants CSP as heat storage units with high energy density and small storage volumes in comparison with sensible heat storage units.

The role of PCMs in all above applications may be classified into two categories: the first is thermal regulator and the second is thermal energy storage (TES) [19].

Incorporating PCMs in buildings, textiles, rechargeable batteries, electrical devices and photovoltaic solar panels are examples of the first role or category as the presence of PCMs prevents the fluctuating of temperature when choosing suitable PCMs with melting temperatures in comfort zone for humans in building and textiles and within the working range of the other applications.

PCMs with high melting temperatures as salts and alloys can be used as heat or thermal energy storage units (TES) in concentrating solar plants (CSP) and represent an example of the second category that stores available energy from daily solar radiation to be used later when it is not available. Also PCMs can be used to store excess heat or waste heat resulting from industrial and chemical processes to be used later in heating applications [51].

6 Recent Developments and Improvements on PCMs

As mentioned before, both main groups of PCMs (organic and inorganic) do not have all the required properties of an ideal PCM.

This section is devoted to discuss the main disadvantages and problems facing the use of phase change materials and some of the most commonly used techniques in solving these problems and improving the performance of PCMs.

The most important problems and disadvantages needed to be modified and solved are:

- Low thermal conductivity
- Supercooling
- Thermal instability

– Leakage of molten PCMs
– Volume and pressure variations during the phase change

6.1 Low Thermal Conductivity

The most important problem that restricts using PCMs is their low thermal conductivity for organic and inorganic ones, although the thermal conductivity of inorganic PCMs is a little bit better than organic ones; anyhow for both types increasing thermal conductivity will reduce the heat time of charging and discharging and improve the performance of PCMs in all applications.

Kant et al. [52] in their review about advancement in phase change materials for thermal energy storage applications and Kenisarin et al. [5] in their review about solar energy storage using phase change materials reported most of the improvements conducted by scientists to address the limitations and to improve the thermo-physical properties of PCMs.

The methods used to increase the thermal conductivity are [5, 52]:

1. Metallic structures and metallic fins

The attachment of fins in the PCM container will increase the area of heat transfer and improve the thermal conductivity. Figure 11 shows aluminum fins used by Singhet.al [53] to improve thermal conductivity of polyethylene glycol (PEG 1000) which is an organic phase change material with a melting temperature of 37.1 °C. The thermal conductivity increases from 0.22 W m^{-1} K^{-1} for pure PEG to 9.4 W m^{-1} K^{-1} by introducing the aluminum fin stack, i.e., an increase of more than 42 times by using the fins.

Many researchers investigated the effect of finned structures [54–56]. Other researchers carried out numerical and simulation studies [57–59] to obtain best fins configuration and dimensions for best results.

Metallic slags and chips were embedded in paraffin wax PCM to improve its thermal conductivity [60]. Aluminum, stainless steel metallic structure and coils' effect on thermal properties of paraffin were studied by Hafner and Schwarzer [61].

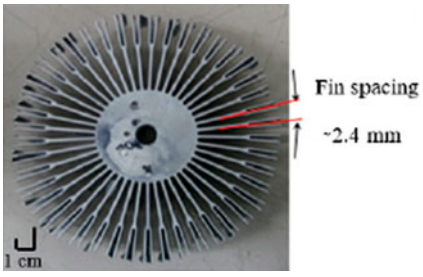

Fig. 11 Aluminum fin stack in R. Singh experimental setup to improve thermal conductivity of polyethylene glycol (PEG) [53]

One of these structures is shown in Fig. 12 [6]. A six times improvement in thermal conductivity of this structure with respect to pure paraffin was reported.

2. Carbon Additives to enhance thermal conductivity

Carbon powder, graphite, graphene, carbon fibers and carbon nanotubes (CNTs) as materials with high thermal conductivity may be added to both organic and inorganic phase change materials to obtain high thermal conductivity for PCMs. Carbon and its derivatives (powder, graphite) are non-toxic, cheap, lightweight, non-aggressive and cause no corrosion to PCMs containers and to construction materials; for these properties, they have been investigated by many researchers [62, 63].

Li et al. [64] used mechanical agitation and ultrasonic vibrations to prepare composites of paraffin with expanded graphite EG, graphene GR and graphene oxide GO with 0.5–2% concentration ranges, and thermal conductivity and heat charge rates were improved for all the composites with different types of additives and were the best for graphene as shown in Fig. 13.

3. Metallic and Oxide metallic nanoparticles

Fig. 12 Aluminum filling structure. Reprinted from Renewable and Sustainable Energy Reviews 11(9), Kenisarin and Mahkamov [5]: Solar energy storage using phase change materials, p. 1939, 2007, with permission from Elsevier

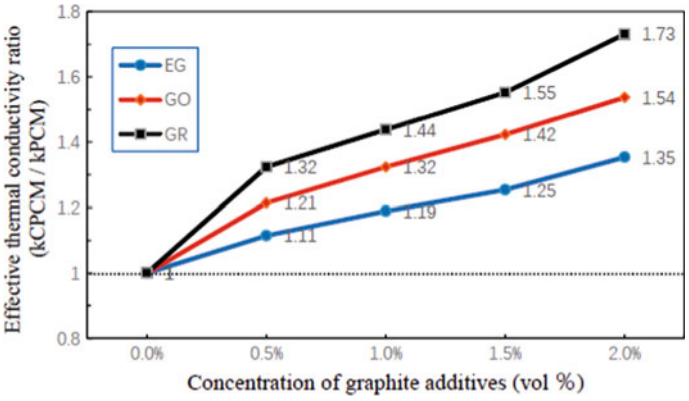

Fig. 13 Effective thermal conductivity ratio as a function of the concentration of graphite additives [64]

Nanoparticles have high surface area-to-volume ratio; this aspect increases the thermal conductivity of PCMs if nanoparticles being incorporated in them [65].

Copper (Cu), gold (Au), silver (Ag) metallic nanoparticles and other nanoparticle metallic oxides as copper oxide CuO, aluminum oxide Al_2O_3, titanium oxide TiO_2 and others are used to enhance thermal conductivity.

One of the problems facing this method of thermal conductivity enhancement is the dispersion of these nanoparticles in PCMs due to their high density and the weak chemical/thermal interaction [56]. Some scientists used surfactants during preparation as Nouani et al. [66] who used sodium stearoyl lactylate in addition to vacuum pump to get rid of air bubbles and ultrasonic vibrations to ensure a homogeneous distribution of nanoparticles. An increase of 31% and 13% in thermal conductivity of solid and liquid state respectively was obtained after the addition of 10 wt% of nano-Al_2O_3 to the paraffin sample.

The addition of nanoparticles to PCMs contributes also to solving the super cooling problem as reported by Li et al. [67] as these nanoparticles play the role of additional nucleating agent. They compared the effect of adding 0.5 wt% of different types of nanoparticles, namely ɣ-Al_2O_3, TiO_2, Cu and SiO_2 to calcium chloride hexahydrate $CaCl_2.6H_20$ on supercooling and obtained the best value in decreasing of supercooling from 5 °C supercooling in $CaCl_2.6H_20$ with a normal surfactant to 0.2 °C for $CaCl_2.6H_20$/0.5 wt% ɣ-Al_2O_3 PCM nanocomposite, after that they studied the effect of different weight concentration of ɣ-Al_2O_3 from 0.5 wt% to 2 wt% in steps of 0.5. A decrease in supercooling, time of melting and time of solidification was observed for all concentrations, and an excellent thermal reliability of 1 wt% concentration upon cycling was registered.

4. Porous metals and metallic foams

Porous metals are metals that have large volume of porosities, and this expression is more general than metallic foam expression which is porous metals but is produced by foaming processes. Some of metallic foams are open celled as a sponge and have very large surface area per unit mass, and some of them are closed cell foams [68]. These cellular structures have large number of porosities nearly 76–95% porosity as shown in Fig. 14 [69].

Their light weight, huge surface area and their ability to conduct heat and electricity make them widely used in industrial and thermal applications.

One of these thermal applications is using PCMs incorporated in metallic foams as passive cooling of electronic devices. The presence of these cellular structure will decrease the time of melting of the PCM and accelerate the process of cooling of the electronic device, i.e., enhance heat transfer between PCM and electronic device as heat is considered a very important cause of electronic devices failure. The decrease of time of discharging and charging of the PCM is due to enhancement in latent heat transfer by this metallic structure which has large surface area in contact with PCM.

Chen et al. [70] used paraffin embedded in an aluminum foam and reported the increase in rate of heat transfer during melting of paraffin due to the presence of the foam.

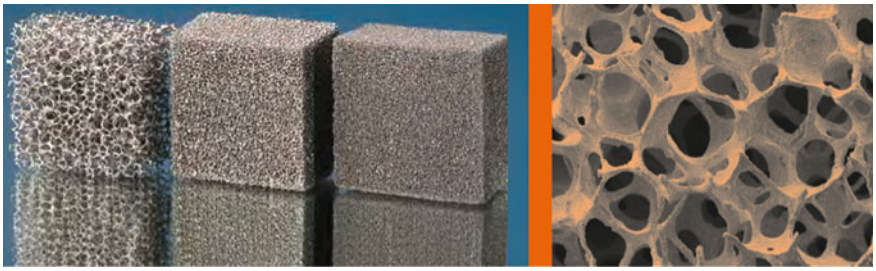

Fig. 14 Open cell structures with various cell sizes (left) *SEM image of an open cell stainless steel foam*(right) [from Fraunhofer Institute for Manufacturing Technology and Advanced Materials IFAM, Branch Lab Dresden] [69]

Numerical and experimental investigations of the effect of copper foam and porosity on rate of heat transfer for sodium nitrate [71], paraffin wax and other commercial PCMs [72] were conducted, and all results emphasize the enhancement behavior of heat transfer by foams.

5. Encapsulation of PCMs.

Encapsulation is the process of surrounding, covering or coating the PCMs by a suitable shell in which the PCM is being the core. It is most likely as M&M sweat with PCMs as the chocolate core, and the crispy candy part is the shell or cover.

Encapsulation is classified into three types depending on size of the final product:

1. Macroencapsulation > 1 mm
2. Microencapsulation (0–1000 μm)
3. Nanoencapsulation (0–1000 nm)

This process has many advantages. It prevents leakage of the PCM when being in liquid state and avoids the interaction of the PCM with surroundings which may cause corrosion of construction materials in building applications as an example, safety issues by avoiding contamination of other materials as food and blood by direct contact with PCM which may have some health hazards in addition to increase in heat transfer especially when micro- and nanoencapsulation are used due to the great surface area-to-volume ratio.

In macroencapsulation, the phase change material is filled or stored in packages of spheres, tubes, pouches and panels to be incorporated in buildings products [73]. Plastic bottles of high and low density polyethylene (HDPE, LDPE), mild steel and tin plated containers are commercially used. The temperature of the application determines the type of the container or capsule such that plastic bottles are not used in high-temperature applications, other required properties of capsules are related to yield strength, non-flammability and thermal conductivity [74]. Figure 15 displays some commercially macrocapsules [5].

In micro- and nanoencapsulation, the improvement in heat transfer is more pronounced due to the increase in surface area-to-volume ratio. Polymers as

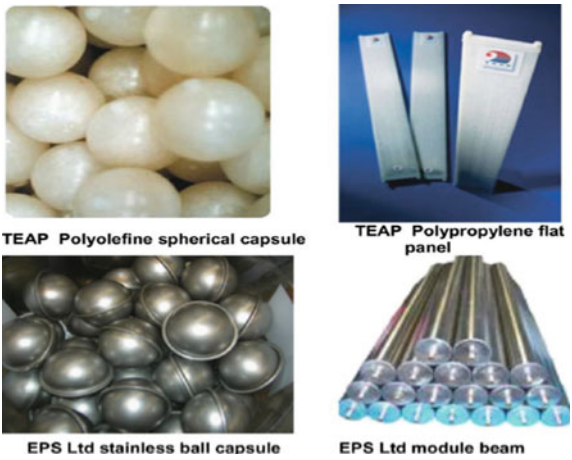

Fig. 15 Some commercially macrocapsules from TEAP and EPS companies. Reprinted from Renewable and Sustainable Energy Reviews 11(9), M. Kenisarin, K. Mahkamov [5]: Solar energy storage using phase change materials, p. 1939, 2007, with permission from Elsevier

polystyrene [75], polymethyl methacrylate (PMMA) are used as shell materials for microencapsulation of paraffin, but because of this polymer low thermal conductivity it will have worse effects when used with PCMs with low thermal conductivity such as paraffins. Some researchers [76] added nanographite NG to improve thermal conductivity of the core material. Others used calcium carbonate as a shell [77], and composites materials are also used for microencapsulation as silicon dioxide—PS [78]. Gum Arabic is recorded and used as shell material for fatty acids [79]. The encapsulation of salt hydrates with their corrosion to metals and their chemical instability is very preferred [80, 81]. Other desired properties must be found in the shell material in addition to their resistance of corrosion are: flexibility, thermal stability, low cost, non-flammability, non-toxic especially when used in food and blood cooling applications and the ability of forming bonds with PCMs as mentioned by Hassan et al. [43].

Methods of microencapsulation are divided into two main categories:

– Chemical methods

In this method, the shell is built around the core which is the PCM by chemical reaction as in situ polymerization and interfacial polymerization.

– Physical methods

The core PCM material is being coated by mechanical or physical process as spray drying and centrifugal methods. Details of both main methods are found in [43, 82]. Nanoencapsulation of PCMs is the most recent area of research in PCMs; nowadays, nanoencapsulation is also used in drug delivery.

Nanocapsules of PCMs have shown better stable structure than macro- and microcapsules [83] and better heat transfer due to decreasing capsule size which will increase surface area-to-volume ratio. Some methods of nanoencapsulation are similar to microencapsulation mentioned before as spray drying and polymerization,

but the recent and future development will focus on nanosize multilayer shells as reported and explained by Shchukina [19]. But still more efforts must be carried out by researchers to transfer these attempts of manufacturing and preparing nanocapsules from research work in laboratories to commercial applications.

6.2 Thermal Instability

One of the drawbacks of salt hydrates as mentioned before is their instability after heating cycles as a result of losing some of their water content. As an example, heating of $Na_2SO_4 \cdot 10H_2O$ salt hydrate above 32.35 °C will cause phase separation and precipitation of the anhydrous salt Na_2SO_4. The addition of 2.9 wt% of acrylic acid copolymer as a thickener prevent phase separation of $Na_2SO_4 \cdot 10H_2O$ up to 100 cycles of heating and cooling [84]. Some researchers reported that the addition of other salts up to 10 wt% did not change the melting temperature and latent heat of the salt hydrate and enhanced thermal stability. The addition of 7wt% manganese chloride hexahydrate with purity > 98% to magnesium hexahydrate with purity > 99.48% made the mixture stable after 1000 heating cycles with no change in melting temperature and heat of fusion as reported by Nagano et al. [85].

6.3 Supercooling

As mentioned before, supercooling is one of the problems in some types of phase change materials in which there will be delay in the beginning of the solidification process, and additional cooling is needed to initiate it, as a result a delay in obtaining the stored latent heat will occur which is not preferable in short term applications, but it is useful in long-term applications. Water is a very common example of this phenomenon. Pure water can be found in liquid state at very low temperatures below 0 °C (18).

Salt hydrates are the most common type of PCMs that suffer from supercooling. Some of the methods used to decrease the degree of supercooling are [18]:

1. Addition of nucleating agents with similar crystal structure that will provide nuclei to initiate crystallization and solidification, and this will decrease the supercooling degree.
2. Using thickening agents which also contribute in reducing phase separation and incongruent melting
3. Using rough surfaces of containers and capsules to provide heterogeneous nucleation. It was found that as the roughness increases, the supercooling degree decreases [86].

Acrylic acid copolymer (3–5 wt%) was used as a thickener agent for different types of high Na-salt hydrates, while carbon powders, copper and titanium oxide in

the micro range were used as nucleating agents. These nucleating agents were found to decrease the degree of supercooling of a thickened $Na_2HPO_4 \cdot 12H_2O$ salt hydrate with acrylic acid copolymer from 20 °C to (0–1 °C) for carbon and titanium oxide and to (0.5–1 °C) for copper [87]. The role of the thickener was to prevent phase separation, and the nucleating agents provide the essential nuclei for crystallization and solidification.

Mixing PCMs with nanoparticles is also considered a solution to supercooling as these nanoparticles will play the role of nucleating agents for solidification process in addition to enhancement of thermal conductivity as mentioned in the subsection 6.1.

6.4 Leakage of Molten PCMs

Encapsulation of PCMs mentioned before is the major method of preventing leakage when PCMs are in liquid state. Shape stabilization is another process used to solve this problem [88] in this process a supporting material as high-density polyethylene HDPE is mixed with the PCM by melting the mixture at a high temperature and then cooling it below the glass transition temperature of the polymer to become a solid. PCMs incorporated in porous materials or metallic foams are shape-stabilized PCMs; the metallic foam or the porous structure play the role of supporting material that prevent leakage of phase change material if loaded or embedded in the structure with suitable amount or weight percentage [89, 90]. Expanded graphite EG, single and multiple carbon nanotubes CNTs with PCMs are all examples of shape-stabilized PCMs that enhance the thermal conductivity, heat transfer and thermal properties in addition to preventing leakage of the PCM in liquid state.

6.5 Volume and Pressure Variations During the Phase Change

Volume and pressure changes during melting and solidification of PCMs are considered to be one of the problems facing the use of PCMs in thermal applications [91]. Encapsulation process by suitable shell materials with good mechanical properties and flexibility to be able to withstand stresses resulting from volume changes and pressure is considered to be a major solution of this problem. Inorganic shells have good mechanical properties, good thermal properties but poor flexibility, while polymeric shells are more flexible with good mechanical properties but unfortunately low thermal conductivity [78].

The addition of nanoparticles of good thermal conductivity to the polymeric shell is expected to improve mechanical and thermal properties.

Graphene oxide (GO) nanosheets with poly(melamine-formaldehyde) shell were prepared by Chen et al. [92] to encapsulate dodecanol PCM by in situ polymerization,

while a double shell of polystyrene and graphene oxide nanosheets were prepared as a shell to encapsulate n-hexadecane PCM by Zhang et al. [93]. Both Chen and Zhang succeeded in complete encapsulation of these PCMs, but thermal conductivity was not greatly enhanced by Chen and was not reported by Zhang.

Stearic acid as a core PCM material was successfully encapsulated with reduced graphene oxide multilayer nanosheets by Advincula et al. [94] by using a pickering-type emulsion technique. The thermal conductivity of encapsulated stearic acid by this method was enhanced in comparison with stearic acid, but a wider range of melting and crystallization temperature were reported.

7 Experimental Methods Used to Determine PCMs Thermal Properties

Thermal properties of PCMs are determined by four principal methods: conventional calorimetry, differential scanning calorimetry (DSC), differential thermal analysis (DTA) and T-History method [95]

The most common technique used to determine the latent heat and the melting temperature is differential scanning calorimetry (DSC). Samples of small amount (5-10 mg) of the PCM under investigation and a reference sample are used in sealed aluminum pans. The samples will be heated above the melting point, then cooled and heated again at constant rate under nitrogen atmosphere. The latent heat is determined from the area under the melting peak, and the melting temperature is taken to be the intersection of the steepest line at leading edge of the melting peak with the temperature horizontal axis.

Differential thermal analysis (DTA) was the earliest thermal measurement technology used. The temperature difference between the PCM sample and a reference material is recorded when both were given the same amount of heat this temperature difference is due to their difference in thermal properties. This method could be used to measure the specific heat capacity and the phase change latent heat but DSC is more accurate than DTA as both samples in DSC are kept at the same temperature, and the difference in heat flow between the PCM sample and the reference is recorded. Both DSC and DTA use small size samples, and this sometimes lead to differences compared to results of large sample size of PCMs as a result scientists sometimes use the T-history method to obtain thermal properties of larger samples. In this method, the temperature versus time curves of the PCM and a reference are recorded under natural convection condition and from these curves and using the calculations and the method proposed by Yinping et al. [96] heat of fusion, specific heat and thermal conductivity of PCMs may be determined. An explanation and comparison between most techniques used to obtain thermal properties of PCMs are found in the review article of Xie et al [97].

8 Future Work and Interests

The encapsulation process described above was used to solve more than one problem or limitations in PCMs such as low thermal conductivity, leakage problem and volume expansion of the PCM during phase transition. This process enhances the heat exchange and thermal properties due to large ratio of surface area to volume especially in nanocapsules. So I think future work should focus on improving methods of encapsulation and using nanoparticles and nanostructures both in core and shell to enhance thermal, mechanical properties of capsules and decrease supercooling by providing nucleating agents which will participate in solving another problem.

Metals and metal alloys are good candidates for both high and low thermal applications, overcoming the gap between global energy needs and available resources.

Finally, more efforts in translating research and developments in phase change technology to more commercial products and applications are definitely needed.

References

1. Du, K., Calautit, J., Wang, Z., Wu, Y., & Liu, H. (2018). *Applied Energy, 220,* 242.
2. IEA. (2019). *Key world energy statistics*. https://www.connaissancedesenergies.org/sites/default/files/pdf-actualites/Key_World_Energy_Statistics_2019.pdf. Accessed Oct 30, 2019.
3. Brady, J. E., & Humiston, G. E. (1986). *General chemistry: Principles and structure* (4th ed., pp. 375–377). New York, Chichester: Wiley.
4. Sharma, S. D., & Sagara, K. (2005). *International Journal of Green Energy, 2,* 1.
5. Kenisarin, M., & Mahkamov, K. (2007). *Renewable and Sustainable Energy Reviews, 11,* 1913.
6. Kürklü, A. (1997). *Energy Conversion and Management, 38*(4), 333.
7. Rahman, M., Hamja, A., & Chowdhury, H. N. (2013). Phase change materials: Characteristics and encapsulation. Paper presented at the International Conference on Mechanical Engineering and Renewable Energy (ICMERE), Chittagong, Bangladesh, December 24–27, 2013.
8. Nazir, H., Batool, M., Osorio, F. J., Ruiz, M. I., Xu, X., Vignarooban, K., et al. (2019). *International Journal of Heat and Mass Transfer, 129*, 491.
9. Tyagi, V. V., & Buddhi, D. (2007). *Renewable and Sustainable Energy Reviews, 11,* 1146.
10. Ge, H., Lia, H., Mei, S.,& Liu, J. (2013). *Renewable and Sustainable Energy Reviews, 21*, 331.
11. Cunha, J. P., & Eames, P. (2016). *Applied Energy, 177,* 227.
12. Sharma, S. D., Kitano, H., & Sagara, K. (2004). *Res Rep Fac Eng Mie Univ, 29,* 31.
13. Zalba, B., Marin, J. M., Cabeza, L. F., & Mehling, H. (2003). *Applied Thermal Engineering, 23,* 251.
14. Hoshi, A., Mills, D. R., Bittar, A., & Saitoh, T. S. (2005). *Solar Energy, 79,* 332.
15. Pincemin, S., Olives, R., Py, X., & Christ, M. (2008). Solar Energy Mater. *Solar Cells, 92,* 603.
16. Xu, B., Li, P., & Chan, C. (2015). *Applied Energy, 160,* 286.
17. Agyenim, F., Hewitt, N., Eames, P., & Smyth, M. (2010). *Renewable and Sustainable Energy Reviews, 14,* 615.
18. Safaria, A., Saidurb, R., Sulaimanb, F. A., Xua, Y., & Donga, J. (2016). A review on supercooling of phase change materials in thermal energy storage systems. *Renewable and Sustainable Energy Reviews*. http://doi.org/10.1016/j.rser.2016.11.272.
19. Shchukina, E. M., Graham, M., Zheng, Z., & Shchukin, D. G. (2018). *Chemical Society Reviews, 47,* 4156.
20. Abhat, A. (1983). *Solar Energy, 30,* 313.

21. Jiang, Y., Sun, Y., Liu, M., Bruno, F., & Li, S. (2016). *Solar Energy Materials and Solar Cells, 152,* 155.
22. Ukrainczyk, N., Kurajica, S., & Šipušiæ, J. (2010). *Chemical and Biochemical Engineering Quarterly, 24*(2), 129.
23. Sarı, A., Sarı, H., & Önal, A. (2004). *Energy Conversion and Management, 45,* 365.
24. Costa, M. C., Sardo, M., Rolemberg, M. P., Coutinho, J. A. P., Meirelles, A. J. A., Claro, P. R., et al. (2009). *Chemistry and Physics of Lipids, 160,* 85.
25. Gandolfo, F. G., Bot, A., & Flöter, E. (2003). *Thermochimica Acta, 404,* 9.
26. Jarrar, R., Qabaja, G., & Sawafta, R. (2016). *American Scientific Research Journal for Engineering, Technology, and Sciences (ASRJETS), 17*(1), 52.
27. Jarrar, R., & Sawafta, R. (2018). *Palestine Technical University Research Journal, 6*(3), 16.
28. Xie, N., Huang, Z., Luo, Z., Gao, X., Fang, Y., & Zhang, Z. (2017). *Appl Sci, 7,* 1317.
29. Fauzia, H., Metselaar, H. S., Mahliab, T. M., Silakhoria, M. (2014). Thermal reliability of myristic acid/palmitic acid/sodiumlaurate eutectic mixture: A feasibility study of accelerate daging for thermal energy storage application. Paper presented at the 6th International Conference on Applied Energy—ICAE. *Energy Procedia, 61*, 49.
30. Liu, Y., & Yang, Y. (2017). *Applied Thermal Engineering, 112,* 606.
31. Sharma, A., Tyagi, V. V., Chen, C. R., & Buddhi, D. (2009). *Renewable and Sustainable Energy Reviews, 13,* 318.
32. Mohamed, S. A., Al-Sulaiman, F. A., Ibrahim, N. I., Zahir, M. H., Al-Ahmed, A., Saidur, R., et al. (2017). *Renew Sustain Energy Rev, 70*, 1072.
33. Gong, Z.-X., & Mujumdar, A. S. (1997). *Applied Thermal Engineering, 17,* 583.
34. Madad, A., Mouhib, T., & Mouhsen, A. (2018). *Buildings, 8,* 63.
35. Cuia, Y., Xiea, J., Liua, J., & Pana, S. (2015). *Procedia Engineering, 121,* 763.
36. Evola, G., Marletta, L., & Sicurella, F. (2013). *Building and Environment, 59,* 517.
37. Khalil, E. (2015). *International Journal of Research & Review, 2*(5).
38. Outlast Technologies Company, (US, Colorado, 1990). www.outlast.com.
39. Khan, M., Swierczynski, M., & Kaer, S. (2017). *Batteries, 3,* 9.
40. Nasehi, R., Alamatsaz, A., & Salimpour, M. R. (2016). *Thermal Science, 20*(2), 391.
41. Ma, T., Yang, H., Zhang, Y., Lu, L., & Wang, X. (2015). *Renewable and Sustainable Energy Reviews, 43,* 1273.
42. Browne, M. C., Norton, B., & McCormack, S. J. (2015). *Renewable and Sustainable Energy Reviews, 47,* 762.
43. Hasan, A., Alnoman, H., & Shah, A. (2016). *Energies, 9,* 782.
44. Kuravi, S., Goswami, Y., Stefanakos, E. K., Ram, M., Jotshi, C., Pendyala, S., et al. (2012). *Technology and Innovation, 14,* 81.
45. Azzouz, K., Leducq, D., & Gobin, D. (2008). *International Journal of Refrigeration, 31*(5), 892.
46. Azzouz, K., Leducq, D. (2009). *Int J Refrig, 32*(7), 1634.
47. Ahmed, M., Meade, O., Medina, M. A. (2010). *Energy Convers Manage, 51*(3), 383.
48. Liu, Z. B., Zhao, D.F., Wang, O. H., Chi, Y. Y., Zhang, L. F. (2017). *Int J Refrig, 79*, 130.
49. Wu, X. H., Li, W. P., Wang, Y. L., Chang, Z. J., Wang, C. X., & Ding, C. (2017). *Int J Heat Mass Transfer, 110*, 789.
50. Bauer, T., Laing, D., Tamme, R. (2011). Recent progress in alkali nitrate/nitrite developments for solar thermal power applications. Paper presented at Molten Salts Chemistry and Technology, Trondheim, Norway, June 5–9, 2011.
51. Maruoka, N., Mizuochi, T., Purwanto, H., & Akiyama, T. (2004). *ISIJ International, 44,* 257.
52. Kant, K., Shukla, A., & Sharma, A. (2017). *Solar Energy Materials and Solar Cells, 172,* 82.
53. Singh, R., Sadeghi, S., & Shabani, B. (2019). *Energies, 12,* 75.
54. Padmanabhan, P. V., & Murthy, M. V. (1986). *International Journal of Heat and Mass Transfer, 29,* 1855.
55. Sadasuke, I., & Naokatsu, M. (1991). *Trans ASME J Sol Energy Eng, 113,* 223.
56. Liu, L., Su, D., Tang, Y., & Fang, G. (2016). *Renewable and Sustainable Energy Reviews, 62,* 305.

57. Pakrouh, R., Hosseini, M. J., Ranjbar, A. A., & Bahrampoury, R. (2015). *Energy Conversion and Management, 103,* 542.
58. Velraj, R., Seeniraj, R. V., Hafner, B., Faber, C., Schwarzer, K. (1997). *Sol Energy* 60281.
59. Youssef, W., Ge, Y. T., Tassou, S. A. (2018). *Energy Convers Manag, 157*, 498.
60. Tayeb, A. M. (1996). Use of some industrial wastes as energy storage media. *Energy Conver Manage, 37*(2), 127–133.
61. Hafner, B., Schwarzer, K. (1999). Improvement of the heat transfer in a phase-change-material storage. In *Proceedings of the 4th workshop of IEA ECES IA annex 10*, Bendiktbeuern, Germany.
62. Johansen, J. B., Dannemand, M., Kong, W., Fan, J., Dragsted, J., & Furbo, S. (2015). *Energy Procedia, 70,* 249.
63. Mao, C., Wood, M., David, L., An, S. J., Sheng, Y., Du, Z., et al. (2018). *J Electro Chem Soc, 165*, 1837.
64. Li, W., Dong, Y., Zhang, X., & Liu, X. (2019). *Processes, 7,* 447.
65. Kaviarasu, C., & Prakash, D. (2016). *Journal of Engineering Science and Technology Review, 9*(4), 26.
66. Nourani, M., Hamdami, N., Keramat, J., Moheb, A., & Shahedi, M. (2016). *Renew Energy, 88,* 474.
67. Li, X., Zhou, Y., Nian, H., Zhang, X., Dong, O., Ren, X., et al. (2017). *Energy & Fuels, 31*(6), 6560.
68. Lefebvre, L. P., Banhart, J., & Dunand, D. C. (2008). *Advanced Engineering Materials, 10*(9), 775.
69. Open-cell Metal Foams, Fraunhofer Institute for Manufacturing Technology and Advanced Materials IFAM, Branch Lab Dresden. https://www.ifam.fraunhofer.de/content/dam/ifam/en/documents/dd/Infobl%C3%A4tter/open_cell_metal_foams_fraunhofer_ifam_dresden.pdf. Accessed Sept 30, 2019.
70. Chen, Z., Gao, D., & Shi, J. (2014). *International Journal of Heat and Mass Transfer, 72,* 646.
71. Yang, J., Yang, L., Xu, C., & Du, X. (2015). *International Journal of Heat and Mass Transfer, 84,* 1008.
72. Rehman, T., Ali, H. M., Saieed, A., Pao, W., & Ali, M. (2018). *International Journal of Heat and Mass Transfer, 127*, 381.
73. Pendyala, S. (2012). Dissertation, University of South Florida.
74. Höhlein, S., Haagen, A. K., & Brüggemannn, D. (2018). *Materials (Basel), 11*(9), 1752.
75. Sarı, A., Alkan, C., Dogüscü, D. K., & Kızıl, C. (2015). *Sol Energy, 115*, 195.
76. Li, M. (2013). *Applied Energy, 106,* 25.
77. Yu, S., Wang, X., & Wu, D. (2014). *Applied Energy, 114,* 632.
78. Yin, D., Ma, L., Liu, J., & Zhang, Q. (2014). *Energy, 64,* 575.
79. Özonur, Y., Mazman, M., Paksoy, H. Ö., & Evliya, H. (2006). *International Journal of Energy Research, 30,* 741.
80. Zhong, L., Zhang, X., Luan, Y., Wang, G., Feng, Y., & Feng, D. (2014). *Solar Energy, 107,* 63.
81. Huang, J., Wang, T., Zhu, P., & Xiao, J. (2013). *Thermochimica Acta, 557,* 1.
82. Salunkhe, P. B., Shembekar, P. S. (2012). *Renewable and Sustainable Energy Reviews, 16*, 5603.
83. Sukhorukov, G., Fery, A., Möhwald, H. (2005). *Prog Polym Sci (Oxf), 30*, 885.
84. Shin, B. C., Kim, S. D., & Park, W.-H. (1989). *Energy, 14,* 921.
85. Nagano, K., Ogawa, K., Mochida, T., Hayashi, K., & Ogoshi, H. (2004). *Appl Therm Eng, 24*(2), 221.
86. Faucheux, M., Muller, G., Havet, M., & LeBail, A. (2006). *International Journal of Refrigeration, 29*(7), 1218.
87. Ryu, H. W., Woo, S. W., Shin, B. C., & Kim, S. D. (1992). *Solar Energy Materials and Solar Cells, 27,* 161.
88. Huang, X., Chen, X., Li, A., Atinafu, D., Gao, H., Dong, W., & Wang, G. (2019). *Chemical Engineering Journal, 356*, 641.
89. Xu, Y., Ren, Q., Zheng, Z. J., & He, Y. L. (2017). *Applied Energy, 193,* 84.

90. Zhang, P., Meng, Z. N., Zhu, H., Wang, Y. L., & Peng, S. P. (2017). *Applied Energy, 185*(2), 1971.
91. Tyagi, V. V., Kaushik, S. C., Tyagi, S. K., & Akiyama, T. (2011). *Renewable and Sustainable Energy Reviews, 15,* 1373.
92. Chen, Z., Wang, J., Yu, F., Zhang, Z., Gao, X., Balandin, A. A., et al. (2015). *J Mater Chem A, 3,* 11624.
93. Zhang, Y., Zheng, X., Wang, H., & Du, Q. (2014). *J Mater Chem A, 2,* 5304.
94. Advincula, P. A., de Leon, A. C., Rodier, B. J., Kwon, J., Advincula, R. C., & Pentzer, E. B. (2018). Accommodating volume change and imparting thermal conductivity by encapsulation of phase change materials in carbon nanoparticles. *Journal of Materials Chemistry A, 6*. https://doi.org/10.1039/c7ta09664j.
95. Jansone, D., Dzikevics, M., & Veidenbergs, I. (2018). *Energy Procedia, 147,* 488.
96. Yinping, Z., & Yi, J. (1999). Jiang Yi. *Measurement Science and Technology, 10,* 201.
97. Xie, J., Li, Y., Wang, W., Pan, S., Cui, N., & Liu, J. (2013). *Advances in Mechanical Engineering, 2013,* 1.